Investigation of Graphene-based materials for their application in wastewater treatment and energy storage

A thesis submitted for the degree of Doctor of Philosophy (science)

in Physics

to

Jadavpur University

Submitted by

Bidisha Mandal, **M.Sc.**

Under the guidance and supervision of

Dr. Bharati Tudu
Associate Professor
&
Ex-Prof. Aparajita Bhattacharya (Co-Supervisor)
Department of Physics, Jadavpur University
Kolkata-700032

February 2024

To the ultimate source of love, care and support

My beloved family

JADAVPUR UNIVERSITY

KOLKATA-700032, INDIA

CERTIFICATE FROM THE SUPERVISORS

This is to certify that the thesis entitled "***Investigation of Graphene-based materials for their application in wastewater treatment and energy storage***" submitted by **Bidisha Mandal**, who got her name registered on 10.05.2016 for the award of Ph.D. (Science) degree at Jadavpur University, is absolutely upon her own work under the supervision of **Dr. Bharati Tudu, Associate Professor, Department of Physics, Jadavpur University and Prof. Aparajita Bhattacharya (co-supervisor), Professor (Retired), Department of Physics, Jadavpur University** and that neither this thesis nor any part of it has been submitted for either any degree/diploma or any other academic award anywhere before.

Bharati Tudu 09/02/2024

Dr. Bharati Tudu
Associate Professor
Department of Physics
Jadavpur University
Kolkata - 700032

Dr. Bharati Tudu

(Supervisor)

Associate Professor

Department of Physics

Jadavpur University, Kolkata – 32

Aparajita Bhattacharya 09.02.2024

Dr. Aparajita Bhattacharya
Professor
Department of Physics
JADAVPUR UNIVERSITY
Kolkata – 700 0

Prof. Aparajita Bhattacharya (Retired)

(Co-Supervisor)

Department of Physics

Jadavpur University

Kolkata – 32

Declaration

*I hereby declare that this thesis entitled "**Investigation of Graphene-based materials for their application in waste water treatment and energy storage**" contains my original research work as a part for the degree of **Doctor of Philosophy (Science)** during academic session 2016-2024. Neither the thesis nor any part thereof has been presented anywhere earlier for any degree/diploma or academic award whatsoever.*

09. 02. 2024

Date

Bidisha Mandal

Bidisha Mandal

(Research Scholar)

Department of Physics

Jadavpur University

Preface

*This dissertation gives an account for a part of my research work on "**Investigation of Graphene-based materials for their application in waste water treatment and energy storage**" at the department of Physics, Jadavpur University, Kolkata-700032.*

During the period of my Ph.D work I learned several topics on nanoscience. On the experimental side , I got experienced in working with various chemical synthesis routes like co-precipitation , hydrothermal and different Physio chemical characterization techniques like PXRD, VSM, SQUID, FESEM, HR-TEM, FTIR, Raman, XPS, UV-vis absorption, PL spectroscopy etc. I also gained experience in three electrode electrochemical station along with interpreting the data for CV, GCD and EIS techniques. Moreover, I learned to interpret and explain the results of the characterization technique such as XRD using data banks such as JCPDS and software like MAUD 2.70, image J, Origin and representing the data are also added experience. This thesis presents the study of structural, morphological, and the application in the field of waste water treatment of organic dye (MB) by graphene-based manganese ferrite and cobalt ferrite composite through photocatalysis and adsorption technique. Also energy storage application through the investigation of electrochemical properties of nitrogen doped graphene and graphene manganese ferrite have been presented. This dissertation work is presented systematically in the form of chapters for all the different studies done.

***Chapter-1** contains a brief overview about waste water treatment and energy storage applications along with graphene and its composite in respective fields. **Chapter-2** includes comprehensive information of synthesis techniques, and methodology for the study of this present work. **Chapter-3** reports the synthesis of Graphene Manganese Ferrite ($MnFe_2O_4$) composite in co-precipitation method for the Methylene blue dye degradation in Photocatalytic method. **Chapter -4** presents the synthesis of Nitrogen doped Graphene (N-RGO) in single step solvothermal method in DMF for the application of energy storage as an electrode. **Chapter-5** deals with solvothermal synthesis and electrochemical properties of Graphene- Manganese Ferrite ($MnFe_2O_4$.). **Chapter-6** presents the synthesis, structural and dye adsorption efficiency of Graphene Cobalt Ferrite ($CoFe_2O_4$.) towards MB. **Chapter-7** deals with the concluding remarks and future prospects of the present work. **Appendix-I** reports the synthesis of Graphene Oxide (GO) supported α-Fe_2O_3 composite in co-precipitation method for the Methylene blue dye degradation in Photocatalytic method**. Appendix-II** contains the list of my scientific journal publications and conerences. Finally, **Appendix-III** includes the cover pages of the reprints of my scientific publications.*

Acknowledgment

*It is a great opportunity to thank and acknowledge a number of people through this submission of my Ph.D. dissertation titled "**Investigation of Graphene-based materials for their application in waste water treatment and energy storage**" carried out under the supervision of Dr. Bharati Tudu and Prof. Aparajita Bhattacharya in the Dept. of Physics in Jadavpur University. Let me start by conveying my sincerest gratitude to my guide/supervisor, Dr. Bharati Tudu for introducing me to scientific research and providing me with a chance to accelerate my research skills. Without her proper guidance, regular supervision and constant encouragement the accomplishment of this work was impossible. I'm grateful to my co-supervisor Prof. Aparajita Bhattacharya, for her guidance, invaluable suggestions and constant encouragement.*

I would also like to thank Dr. Ratan Sarkar, Assistant Professor in Physics, Jogesh Chandra Choudhuri College, Kolkata for his comments and suggestions on my work. I'm thankful to our collaborators Dr. Sachindranath Das, Department of Instrumentation, Jadavpur University, and Dr. Pabitra Kumar Pal, Department of Physics, Jadavpur University, for their constant help. Without their help and support, it would not have been possible for me to complete my present work.

I would like to make a special mention of Samik for sharing his skill and knowledge through many fruitful discussions and valuable suggestions for the electrochemical part. Of course, I would like to thank my fellow lab mates in this lovely group: Jnanranjan, Krishnendu, Dipanwita, Indrajit, Gopanggona and Arnab. They have lent their helping hand in each step of my research. I express my deepest gratitude to Sangita and Chetana for their heart-warming love, and support that gave me mental peace during my Ph.D period.

For financial support during the execution of the research work, I would like to express my profound sense of gratitude to Government of West Bengal. Their financial support through 'State Fellowship' helped me a lot to complete my work successfully.

At this precious moment, I convey my gratitude to my mother (Karuna Mandal), and my elder sister (Baishali Mandal). Their exceptional support, love and sacrifices gave me the courage

and strength to struggle in my life and achieve the goals which was once beyond imagination. In addition to them, I am grateful to my husband Manoj, who supported me with his unconditional love, patience and adjustability during various ups and downs in this period.

In the last but not the least, I must acknowledge my special gratitude to my school Dhuturdaha Kalyan Parishad high school for allowing to write and submit this thesis.

Date 09.02.2024

Bidisha Mandal

Bidisha Mandal

Jadavpur University,

Kolkata-700032,India

Synopsis

One of the major environmental concerns in pollution control is the removal of hazardous materials from water resources. The pollution of water resources by industrial effluents containing toxic dyes like, Congo red, Methyl orange, Methyele Blue etc. have been a serious problem to the human health and environment. Most of the dyes are harmful due to the high toxicity and carcinogenicity from their non-biodegradable aromatic structure . Therefore, to control the pollution of water, elimination of these dyes from water is of utmost importance. Among several methods to treat waste water photocatalysis and adsorption have gained a huge interest in last few decades due to its low cost and simple execution. On the other side, to achieve ever-increasing desired energy due to the fast gradual decrement of fossil fuel, global warming and pollution, researchers are forced to explore sustainable energy and efficient energy storage devices. One of the different energy storage systems, supercapacitors are drawing huge attention because of their high power density, environmental friendliness, long operating life and product safety.

Graphene-based spinel ferrite composite materials have recently been characterized in multiple investigations as an incredibly effective material for wastewater treatment due to their excellent catalytic and adsorptive capabilities. Among its many unique properties, two-dimensional substance graphene possesses great thermal and chemical stability, a huge specific surface area, fast electron transport, and excellent conductivity. The addition of graphene improved the photocatalytic performance of spinel ferrite nanoparticles by reducing the recombination of photogenerated charge carriers. Moreover, the synergistic advantages like increased active surface area, less particle agglomeration, and simpler magnetic separation for reusability of composite materials can also be credited with improved photocatalytic efficiency as well as adsorption for dye degradation. In addition, Graphene, being a single-atom thick sheet with hexagonal honeycomb sp^2 -hybridized carbon atom network has been extensively used as EDLC material as it possesses good conductivity and a large surface area. Also introducing pseudocapacitive spinel ferrites along with graphene has been effectively developed to achieve high-performance energy storage devices.

*The dissertation entitled '**Investigation of Graphene-based materials for their application in wastewater treatment and energy storage'** gives an account for a part of my research work at the Department of Physics, Jadavpur University, Kolkata-700032.*

This thesis presents the study of Graphene-based spinel ferrite composite materials for photocatalytic and adsorptive dye degradation of Methylene blue. Also, graphene along with nitrogen-doping has been explored as electrode material for energy storage applications. This dissertation work is presented systematically in the form of chapters for all the different studies done.

Chapter-1 *introduces the basic concepts and a brief overview of the relevant parts needed to understand the research work presented in this thesis. It highlights the importance of the studies and a general introduction to graphene and graphene-based materials for wastewater treatment and energy storage applications. A brief overview of the wastewater treatment and energy storage application as well as their theoretical interpretation have been presented. It also focuses on the properties and different synthesis procedures of graphene as well as it's application. Moreover, the structures of spinel ferrites and their application in the field of photocatalysis and adsorption as well as application in the field of electrochemical energy storage are also discussed. Finally, the motivation and objective of the thesis are presented*

Chapter-2 *represents the comprehensive information regarding instrumentations that are utilized for the study of this present work. To fulfill the research aim, experimental work was performed in the laboratory, followed by the characterization of the synthesized and spinel ferrite nanoparticles. A brief description of the various techniques for the determination of crystal structure, morphology, chemical composition, magnetic properties, optical properties, and other electrochemical properties is also presented. This includes instrumental techniques, their theories, operational procedures, and methods of analysis that are used for the study of the present thesis work.*

Chapter-3 *deals with the investigation of photocatalytic degradation of methylene blue dye (MB) using bare manganese ferrite ($MnFe_2O_4$) nanoparticles and $MnFe_2O_4$ nanoparticles-decorated reduced graphene oxide heterostructures ($MnFe_2O_4$/rGO) under ultra-violet irradiation. The $MnFe_2O_4$ nanoparticles were prepared using a facile coprecipitation method showed single-phase cubic spinel structure and superparamagnetic property. The $MnFe_2O_4$/rGO heterostructures showed the formation of sphere-like $MnFe_2O_4$ nanoparticles well-attached on rGO nanosheets with reduced agglomeration. The photocatalysis study shows that $MnFe_2O_4$/rGO had higher photocatalytic activity compared to bare $MnFe_2O_4$ nanoparticles. MB degraded by 84% in presence of $MnFe_2O_4$ after UV irradiation of 290 min, while 97% of it degraded in merely 60 min in case of $MnFe_2O_4$/rGO heterostructures. This is*

further confirmed by the well-fitted Langmuir-Hinshelwood Kinetics equation. Hydroxyl radicals play the crucial role in the $MnFe_2O_4$-graphene system for MB photodegradation. Thus, $MnFe_2O_4$ nanoparticles-decorated reduced graphene oxide heterostructures can act as potential photocatalyst for degradation of hazardous organic dyes present in water.

Chapter-4 *reports a single-step dymethyleformamide (DMF) assisted solvothermally synthesized nitrogen-doped reduced graphene oxide (N-rGO) as a novel electrode material.. The highest specific capacitance of N-rGO is found to be 516 Fg^{-1} at a scan rate of 2 mVs^{-1} along with a good cyclic stability and stable coulombic efficiency. Such a remarkable capacitive performance is attributed to its porous structure and effective nitrogen doping which facilitates the migration of electrolyte ions and provides abundant active sites for such electrochemical behaviour. The electrochemical impedance spectroscopy study showed a typical capacitive behavior of the N-rGO and a faster frequency response with a relaxation time constant of 0.4 s. Thus, the synthesized N-rGO using this simple, cost-effective, environment friendly method could be a potential candidate for high performance energy-storage applications.*

Chapter-5 *A single-step solvothermal method has been employed to synthesize $MnFe_2O_4$ composite nanoparticles where graphene sheets have been incorporated into spherical, ultra-small $MnFe_2O_4$ nanoparticles of size ~57 nm. This method aided the $MnFe_2O_4$/reduced graphene oxide (rGO) composite nanoparticles with increased porosity, surface area and conductivity leading to improved electrochemical properties. FTIR, RAMAN and X-ray photoelectron spectroscopic studies confirmed the reduction of GO and a successful formation of $MnFe_2O_4$/rGO composite. When used as an electrochemical electrode, the $MnFe_2O_4$/rGO composite nanoparticles showed an enhanced specific capacitance of 253 Fg^{-1} compared to 133 Fg^{-1} corresponding to the bare nanoparticles, at a current density of 10 Ag^{-1} within the potential range of -0.3 to 1.2V. Thus, the unification of 2D graphene structure and $MnFe_2O_4$ nanoparticles led to enhanced electrochemical performance with excellent cyclic stability of 96% (after 5000 cycles) and hence provides a good strategy for improving future supercapacitor electrode materials.*

Chapter- 6 *contains, the synthesis of spinel cobalt ferrite with graphene adsorbents (CF-rGO) by solvothermal method. By using X-ray diffraction, scanning electron microscopy (SEM), FTIR, XPS, and VSM, the properties of the produced samples were investigated. The high*

saturation magnetization value of the sample may be used by the external magnetic field, which is advantageous for the recycling procedure in the adsorption application. The analyses show that CF-rGO with an adsorption capacity of 15.5 mg g^{-1} has successfully removed 93% of MB from water. The produced composite of graphene and cobalt ferrite is promising since it is simple to separate, has a high adsorption capacity, and is inexpensive.

Chapter- 7 *contains the concluding remarks and future directions of the present work.*

Appendix-I *deals with the synthesis of composite of Graphene Oxide (GO) supported α-Fe_2O_3 nanoparticles (GF) via a simple co-precipitation method. GF composite was explored as photocatalyst towards the degradation of MB. The efficiency of dye removal of the prepared GF composite has been measured by the degradation of methylene blue (MB) in an aqueous solution. The degradation of the dye has been evaluated by UV-visible spectroscopy, by a decrease in the intensity of absorbance and concentration. The degradation efficiency of GF is found to be 90% towards MB.*

Appendix-II *contains the list of journal publications and the conference presentation. Finally,* ***Appendix-III*** *contains the cover pages of the reprints of publications.*

Date: 09.02.2024

Bidisha Mandal

(Bidisha Mandal)

Jadavpur University,

Kolkata-700032,India

Table of Contents

List of Figures

Chapter 1

Chapter-2

Chapter-3

Chapter-4

Chapter-5

Chapter-6

Appendix I:

List of Tables

CHAPTER 1

INTRODUCTION

This chapter introduces the basic concepts and a brief overview of the relevant parts needed to understand the research work presented in this thesis. It highlights the importance of the studies and a general introduction to graphene and graphene-based materials for wastewater treatment and energy storage applications. A brief overview of the wastewater treatment and energy storage application as well as their theoretical interpretations have been presented. It also focuses on the properties and different synthesis procedures of graphene as well as its various applications. Moreover, the structures of spinel ferrites and their applications in the field of photocatalysis and adsorption as well as application in the field of electrochemical energy storage are also discussed. Finally, the motivation and objectives of the thesis are presented.

1.1. Overview

Technological advancements are crucial for meeting human needs across numerous areas. However, industrial growth releases hazardous chemicals into the environment, contaminating it. Water contamination is a global environmental hazard, with dangerous pollutant concentrations exceeding WHO and EPA guidelines. Discharging hazardous dyes through industrial effluents into water is one of the main environmental concerns across the world. Photocatalytic degradation and adsorption have been regarded as very promising two methods among several dye contamination water treatment techniques. On the other hand, due to the increasing demand for energy in industrialized countries as well as the fast-growing need in emerging economies, energy scarcity and the use of fossil fuels have also emerged as significant and pressing worldwide issues. Given the concerns, it is imperative to create energy storing systems that are high-performing, affordable, and environmentally friendly. In this situation, supercapacitors are a type of energy storage technology that has been gaining a lot of interest in recent years due to their high-power density, long operational life, environmental friendliness, and product safety.

Due to their superior catalytic and adsorptive properties, graphene-based spinel ferrite composite materials have recently been described in numerous investigations as an extremely effective material for wastewater treatment. Two-dimensional substance graphene has exceptional conductivity, a large specific surface area, rapid electron transport, and strong thermal and chemical stability, along with other special qualities. Spinel ferrite nanomaterials became better photocatalysts when graphene is added because it lessens the recombination of photogenerated charge carriers. Moreover, the synergistic advantages like increased active surface area, less particle agglomeration, and simpler magnetic separation for reusability of composite materials can also be credited with improved photocatalytic efficiency as well as adsorption for dye degradation. In addition, Graphene, being a single-atom thick sheet with hexagonal honeycomb sp^2 -hybridized carbon atom network has been extensively used as EDLC material as it possesses good conductivity and a large surface area. Also introducing pseudocapacitive spinel ferrites along with graphene has been effectively developed to achieve high-performance energy storage devices. The hybrid materials can enhance the electrochemical performance due to the synergistic effect with graphene which provides not only a conductive backbone to promote the transportation of electrons but also

a mechanical strength which offers the integrity of the electrode through the electrochemical processes.

1.1.1. Wastewater Treatment

In our Earth, the 'Water' is very commonly available and easily accessible natural resource amongst many resources. Water plays a very important role in nourishing the Earth's ecology as none of living species can survive without it. On the other hand, there are several problems associated with Water pollution across our globe. From various data collections by Scientists/Authorities and other statistics, a millions of people die without seeing sunrise the next day including 3900 children from various human diseases that are caused by forcefully drinking polluted water and near about 1.2 billion people are positively looking for drinking water security [1, 2]. Hence on one part, continuously increasing of demand for water and a growing population on other part, no control in properly usage of water, rapid climate change, uneven distribution of expected rainfall, water pollution became primary reason behind the water scarcity. In modern days, polluted and contamination water are considered as most of the substantial threats that demand an immediate and effective solution [3]. The water body's Pollutant Contamination due to industrial effluents affects the balance of eco-friendly environment. Organic dyes are identified amongst major pollutants discharged into the environment by various industries like leather, textile, food and printing[4]. The ingredient color contains in textile dyes are not only increasing aesthetic damage to the water bodies [5, 6] but also building a layer from penetration of light into water that minimize the rate of photosynthesis process [7], as well as dissolved oxygen levels that affecting the overall aquatic biota. However, textile dyes may also act as toxic substances, mutagenic agents, and carcinogens[8] [9]. They can also persist as biological pollutants and cross entire food chains, causing biomagnification, which causes higher trophic levels of organisms to exhibit higher contamination levels than their prey. Hence, it's very essential to introduce treatment strategies and defined goals aiming to ensure the sustainability of the fresh water for upcoming generations. To deal with contaminated water, a number of techniques have been discovered and created, including sedimentation, coagulation, flocculation, membrane filtration, distillation, ion exchange, crystallization, ultrafiltration, reverse osmosis, electrodialysis, and electrolysis (**Fig. 1.1**). The majority of these techniques, however, are unable to totally

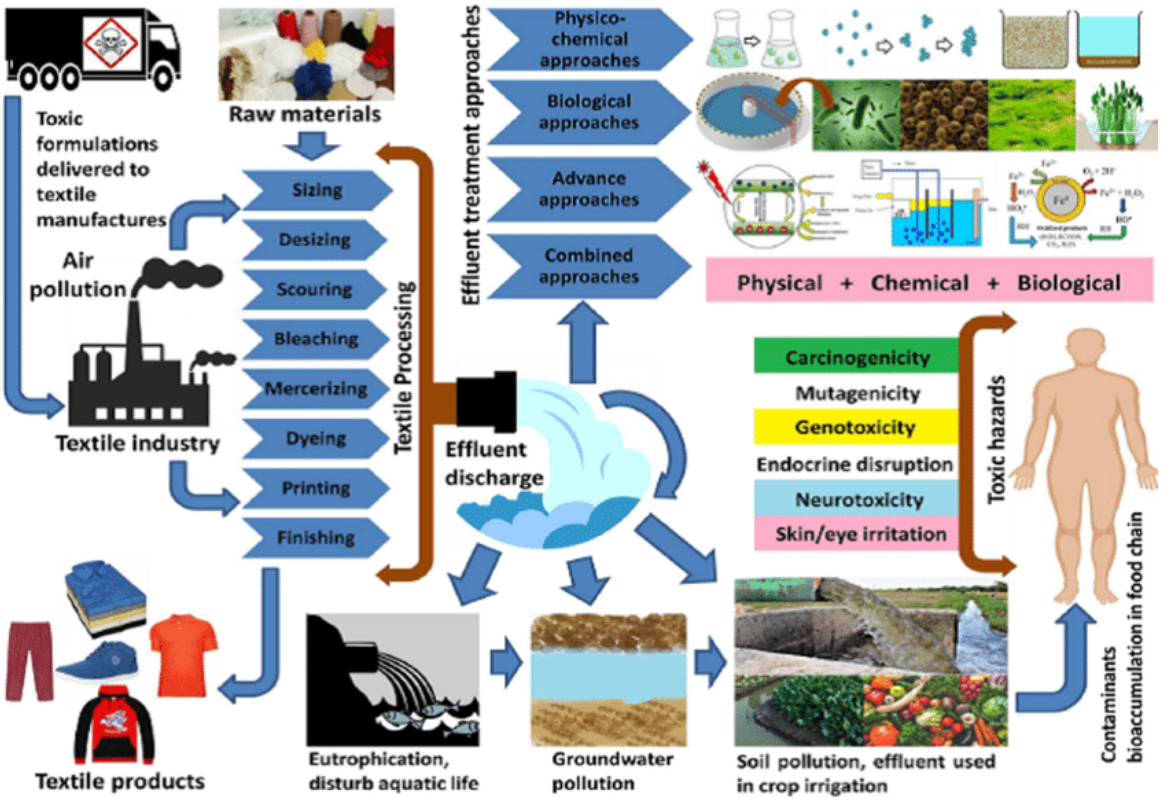

Fig. 1.1. Processing in textile industry, wastewater generation, its toxicity and various treatment approaches **[**11**].**

breakdown the contaminants in wastewater or produce secondary polluting chemicals that are indistinguishable from primary pollutants [10].

Introduction to Methylene Blue (MB)

The molecular weight of MB, an aromatic heterocyclic basic dye, is 319.85 g mol^{-1}. MB is a well-known primary thiazine dye that is cationic and has a chemical formula of $C_{16}H_{18}N_3CIS$ (**Fig. 1.2**). Its maximum absorption occurs at ~ 663 nm (λ_{max}). Due to its high-water solubility, it can be dissolved in water to create a stable solution at room temperature. MB is a positively charged molecule that belongs to the polymethine dye class and has an amino autochrome unit. MB dyes are often released in considerable quantities by the textile industry into natural water sources, endangering the health of both humans and microorganisms. Because of its significant toxicity, MB dye is hazardous to human health above a specific concentration. Because MB is toxic, carcinogenic, and non-biodegradable, it poses a major risk to public health and has a negative

impact on the ecosystem. Human health is at danger from MB for a number of conditions, including respiratory discomfort, stomach problems, eyesight, mental and digestive diseases. Along with premature cell death in tissues and skin/eye irritations, it also causes nausea, vomiting, diarrhea, cyanosis, shock, gastritis, jaundice, methemoglobinemia, tissue necrosis, and elevated heart rate.

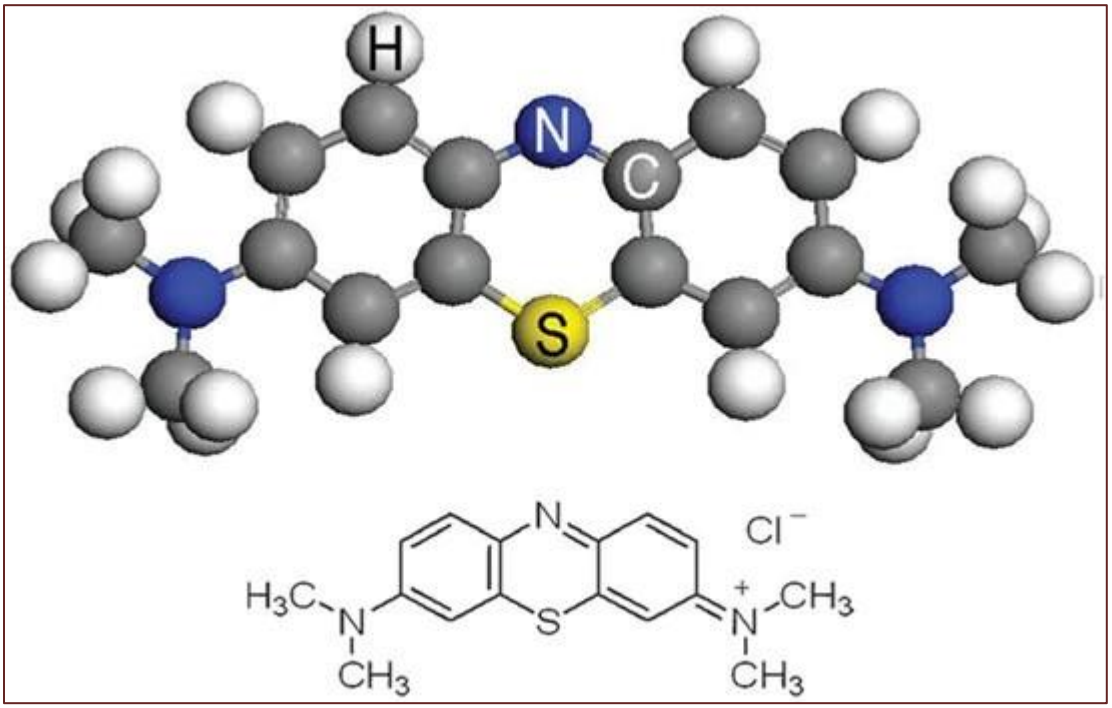

Fig. 1.2 The model and the structure of MB dye molecule [12]

1.1.1.1. Photocatalysis

One of the main global concerns is how to dispose of dye-contaminated wastewater, and numerous methods, including biological and physicochemical methods, are employed to do so. Alternative treatment methods for dye-contaminated wastewater include advanced oxidation processes (AOP), which are thought to be cutting-edge and promising.

AOP are typically able to take advantage of the hydroxyl radical's high level of reactivity in oxidation processes, which set off a series of reactions that transform aqueous pollutants into harmless byproducts [13, 14]. Among various AOP, photocatalysis is extensively researched for

the treatment of wastewater. Accordingly, over 16,000 scientific articles containing "photocatalysis" or "photocatalyst" have been published over the past 10 years (Scopus), and the number of publications is growing yearly.

In general, a semiconductor's photocatalytic activities are highly influenced by its unique electronic structures, which consist of a filled valence band (VB) and an empty conduction band (CB). It is well known that heterogeneous photocatalysis can occur only when the relevant thermodynamic parameters are met, such as the appropriate wavelength of incident light and matched levels of conduction/valance bands with the redox potentials. More specifically, with adequate light irradiation with incident photon energies equal to or greater than that of the semiconductor's band gap, E_g, the electrons in a particular semiconductor can be photochemically excited to their CB, leaving a positive hole in the VB. In other words, incoming light having a wavelength lower than $1246/E_g$ eV can only be used by a semiconductor with a band gap of E_g. These photoinduced positive holes and electrons undergo a number of reactions before forming hydroxyl radicals. These species can break down a wide range of compounds, including synthetic dyes, due to their strong oxidizing ability [15, 16]. The frequent occurrence of electron-hole recombination, however, may prevent oxidation and reduction events from occurring on the surface of photocatalytic material. Accordingly, an enhanced or suppressed electron-hole recombination is frequently linked to an increase or decrease in reaction rate [17]. Mechanism of the Photocatalysis method has been represented in **Fig. 1.3**.

The following are a few advantages that photocatalysis have over other waste water treatment methods.

1. Since the ultimate products of the Photocatalysis are H_2O, CO_2, and tiny inorganic ions, they do not produce secondary pollutants.

2. Because the photocatalysis process is non-selective, it can be employed to treat a variety of contaminants, including pathogens, organic and inorganic compounds.

3. Also in this method total deterioration of the pollutant can occur and possibly in the less expensive method.

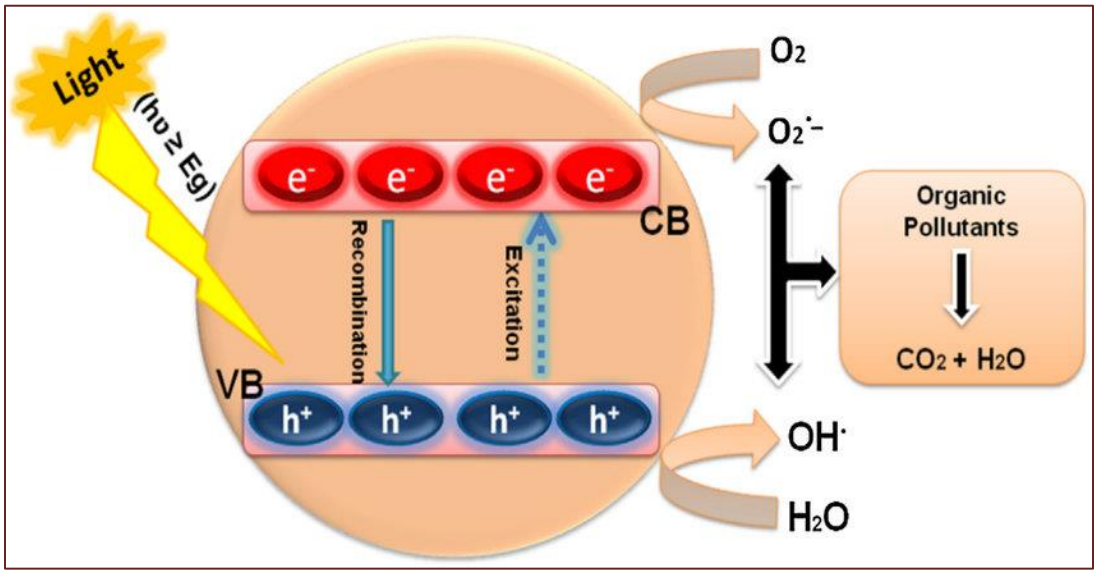

Fig. 1.3 Schematic diagram of the basic mechanism of photocatalysis [18]

1.1.1.2. Adsorption

Adsorption is a highly efficient modern wastewater treatment technique utilized by various sectors to reduce the presence of dangerous inorganic and organic pollutants in wastewater [19]. Adsorption is the process by which a material accumulates at the interface between two phases, either gas-solid or liquid-solid. Adsorbate is the material that accumulates at the interface, whereas adsorbent is the solid on which adsorption occurs.

The two primary forms of adsorption are chemical sorption and physical sorption. Chemical adsorption, also known as chemisorption, is usually irreversible because the exchange of electrons forms strong chemical bonds between molecules or ions of the adsorbate and the surface of the adsorbent. Physical adsorption, also referred to as physisorption, is usually reversible because it results from weak van der Waals intraparticle interactions between the adsorbent and the adsorbate. Most adsorption processes, including those involving agricultural byproducts, are controlled by physical forces, with the exception of chemisorption (**Fig. 1.4**).

The main physical forces affecting adsorption are hydrogen bonding, van der Waals forces, polarity, and the dipole-dipole π- π interaction. In case the sorbent is inexpensive and does not require an

additional pretreatment phase prior to application, this method presents a strong substitute for cleaning up contaminated waters. Adsorption methods are widely used in environmental remediation to eliminate specific chemical pollutants from streams, particularly those that are mostly unaffected by conventional biological wastewater treatment methods. Adsorption, in the field of waste, water treatment has been found to perform better than alternative methods in terms of ease of operation, sensitivity to hazardous pollutants, startup cost, and design flexibility. Adsorption produces no new dangerous compounds.

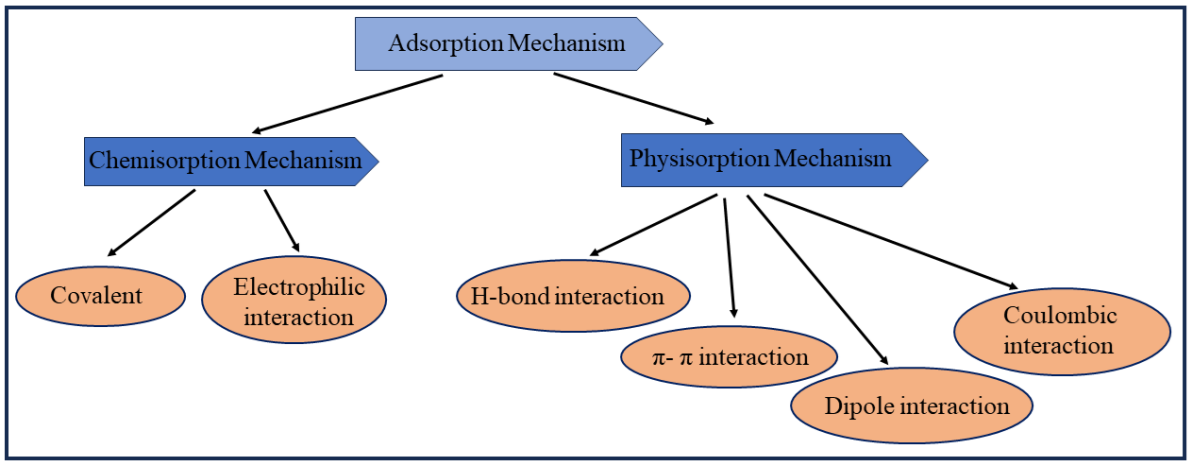

Fig. 1.4. Diagrammatic representation of types of adsorption mechanisms.

Factors affecting adsorption of dye

There are numerous parameters that influence dye adsorption, including pH, temperature, and initial dye concentration. Therefore, the consequences of these characteristics must be taken into account. The optimization of such settings will substantially aid in the creation of an industrial-scale dye removal treatment procedure. The next section discusses some of the elements that affect dye adsorption.

(a) Effect of amount of adsorbent dosage

It is an important process parameter for determining an adsorbent's capacity for a given amount of adsorbent under given operating conditions. In general, the proportion of dye removal increases with increasing adsorbent dosage, as does the number of sorption sites on the adsorbent's surface.

The effect of adsorbent dose provides insight into a dye's ability to be adsorbed with the shortest amount of adsorbent, allowing us to recognize a dye's economic potential [20].

(b) Effect of initial dye concentration

The amount of dye removed through adsorption is strongly dependent on the initial dye concentration. The effect of initial dye concentration is determined by the direct relationship between the dye concentration and accessible sites on an adsorbent surface. In general, when the initial dye concentration increases, the proportion of dye removed decreases, which could be due to saturation of adsorption sites on the adsorbent surface. On the other hand, increasing the initial dye concentration increases the capacity of the adsorbent, which could be related to the high driving force for mass transfer at a high initial dye concentration [21].

Zhang et al. investigated the adsorption of Methyl Orange by the Chitosan/Alumina interface and discovered that when the methyl orange concentration grew from 20 to 400 $mg.l^{-1}$, the percentage of dye removal fell from 99.53% to 83.55% while maintaining the same MB concentration [22]. Yagub et al. investigated the effect of initial dye concentration on methylene blue (MB) adsorption by pine leaves [23]. They discovered that as the initial dye concentration increased from 10 to 90 $mg.l^{-1}$, the percentage of dye removal decreased from 96.5 to 40.9% after 240 minutes.

(c) Effect of temperature

Another important parameter is temperature, which affects the adsorbent's adsorption ability [24]. If the amount of adsorption increases as the temperature rises, the process is endothermic. This could be owing to the dye molecules' increased mobility and the number of active adsorption sites as temperature rises. Adsorption capacity decreases with increasing temperature, indicating that the process is exothermic. This could be due to increasing temperature, which reduces the adsorptive forces between the dye species and the active sites on the adsorbent surface, hence decreasing the quantity of adsorption [20].

(d) Effect of solution pH

One of the most critical parameters influencing adsorbent capacity in wastewater treatment is solution pH. Adsorption efficiency is affected by solution pH, as variations in pH affect the degree of ionization of the adsorptive molecule as well as the surface characteristics of the adsorbent [25].

Chowdhury et al. investigated the influence of solution pH on the adsorption of Basic Green 4 dye by Ananas comosus leaf powder and discovered that at pH 10, the dye removal ratio was at its highest [26]. Dawood and Sen investigated the influence of solution pH on Congo red adsorption by pine cones and discovered that adsorption was most efficient at pH 3.5 [27].

1.1.2. Energy storage application

Due to the ongoing rise in global energy consumption and the development of advanced economies in developed countries, the over use of fossil fuels and energy shortages have evolved into extremely serious issues [28-30]. The development of high-performance, low-cost, and environmentally friendly energy systems is necessary to address the identified warnings. In these regions, emerging technologies for producing electrical energies and corresponding storages are key factors in meeting the rising demand in the energy and economic fields [31-33]. Electrical energies play a significant role in everyday life. They can be used for a variety of things, and are easily turned into the necessary light, heat, or mechanical energy. But the biggest problem with electrical energies is that they can hardly be stored [34, 35].

Therefore, the emphasis is on effectively storing energy for effective consumption or utilization. Indeed, the production of renewable energy from the most abundant resources-the sun and wind-is currently growing quickly. However, due to the unpredictable nature of solar and wind energy, there is a significant need for such energy devices that are safe to run, cost-effective, have little impact on the environment, and can also store the energy when there is an excess and release it when there is a high demand. As a result, energy storage technologies like batteries, fuel cells, and supercapacitors are becoming increasingly important in our daily lives. Due to its high conversion efficiency and ability to be recycled for a large number of cycles, electrochemical energy conversion has received a lot of interest [36]. An electrical charge works as a clean, efficient and versatile oxidizing or reducing agent for several electrochemical reactions [37]. Due to their high energy density, batteries and fuel cells are typically utilized for energy storage in industrial and consumer electronic equipment. Large amounts of electricity can be stored in batteries, but charging them takes a long time. Energy density is low in fuel cells. Capacitors, on the other hand, charge instantly but can only hold a minimal quantity of power.

Therefore, it is required to store and release enormous amounts of electricity extremely quickly, depending on the demand. Electrochemical capacitors, for example, are useful energy storage technologies because of their high-power density, long cycle life, low cost, and small size. Electrochemical capacitors, commonly referred to as supercapacitors, have an extremely high capacitance density.

1.1.2.1. Basics of Supercapacitors

Conventional commercial capacitors which come in a wide variety of types, forms, and shapes, and have varied capacities, include two conducting plates that are kept near to one another and separated by an insulating spacer. By adding such an insulating sheet, the permittivity of empty space is improved and the capacity for charge storage is increased.

An electrostatic field is created when a potential is supplied across its two terminals, causing the positive and negative charges to flow in the direction of the plates with the opposite polarity. It is now claimed that the capacitor is charged. This charged capacitor uses the electrostatic energy contained in the electric field to drive a load when linked through an external circuit. When there is no more charge in the capacitor after this action, it is considered to have been discharged. The relationship between electric charge and the potential difference between the terminals determines a capacitor's capacitance, which is a measurement of how much charge can be held on a certain device. Farad (F), its SI unit, is provided by the following equation (1.1)

$$Farad = \frac{Coulomb}{Volt} \qquad (1.1)$$

The equation $C = \varepsilon_0 \varepsilon_r \frac{A}{D}$, is the formula for conventional capacitors, where C is capacitance, or the capacity of the capacitor to store charges, ε_0 is the dielectric constant of free space, and ε_r is the dielectric constant of the insulating material between the electrodes. As a result, capacitance C is inversely proportional to the distance D between the electrodes and directly related to the electrodes' surface area A. The supercapacitor achieves its high capacitance and energy storage by having an electrode with high surface area and a distance D between the electrodes that is much narrower.

Supercapacitors function similarly to traditional capacitors. However, the additional charge can be held by the numerous pores inside the electrodes' high surface area, and the charge separation occurs across a relatively short distance, i.e. between the electrolyte and an electrode, which allows the

supercapacitors to store more charge. The basic components of a supercapacitor are two electrodes with high surface areas, an electrolyte made of a mixture of positive and negative ions dissolved in water, and a separator.

1.1.2.2. Types of electrochemical supercapacitors

Supercapacitors can be mainly classified into two types: electrochemical double-layer capacitors and pseudocapacitors, which will be covered in more detail later. The former primarily stores energy as an electric double layer and uses porous carbon material as the electrode. The conductive polymer and metal oxide are preferred by the pesudocapacitor. The highly reversible oxidation-reduction reaction occurring in two dimensions on the surface of the active material is the basis for energy storage. However, because of the increased surface-to-volume ratio, redox-active materials in nano size can store charges both electrostatically and faradically. In this instance, these supercapacitors are known as hybrid capacitors and have a very high-capacity value due to the involvement of both mechanisms.

EDLC

Similar to a parallel plate capacitor in terms of its basic charge storage methods, EDLCs use active materials (such as porous carbons) to replace the conducting plates and the dielectric substance is replaced by a polymeric separator submerged in electrolyte. In the theory of EDLC, the capacitance is created by the generation of electrostatic charge at the interface of the electrode and electrolyte, which is a non-faradaic approach for charge storage [38]. With the application of external voltage, at the electrode and electrolyte interface, impulsively two opposed charges are created when the electrode is dipped in the electrolyte and then attracted to the oppositely charged electrode surface leading to the charging process (**Fig. 1.5a**). Eventually two opposite charge layers formed: one with one polarity (positive/negative) on the electrode surface and the other with the opposite polarity in the electrolyte solution and they are represented as double layer (**Fig. 1.5b)**. However, when the external voltage is removed, the discharge process starts until all ions drift back to the equilibrium position (**Fig. 1.5c).**

Von Helmholtz introduced the idea of an electrochemical double layer (EDL) and modelled it for the first time in 1853. According to this model, two layers of opposing charges form at the electrode-electrolyte interface and are separated by an atomic distance *d*. This model implies that the electric

potential has a maximum value of ψ_0 on the surface and progressively decreases to zero in the electrolyte solution. This potential change from a maximum to zero is found on the

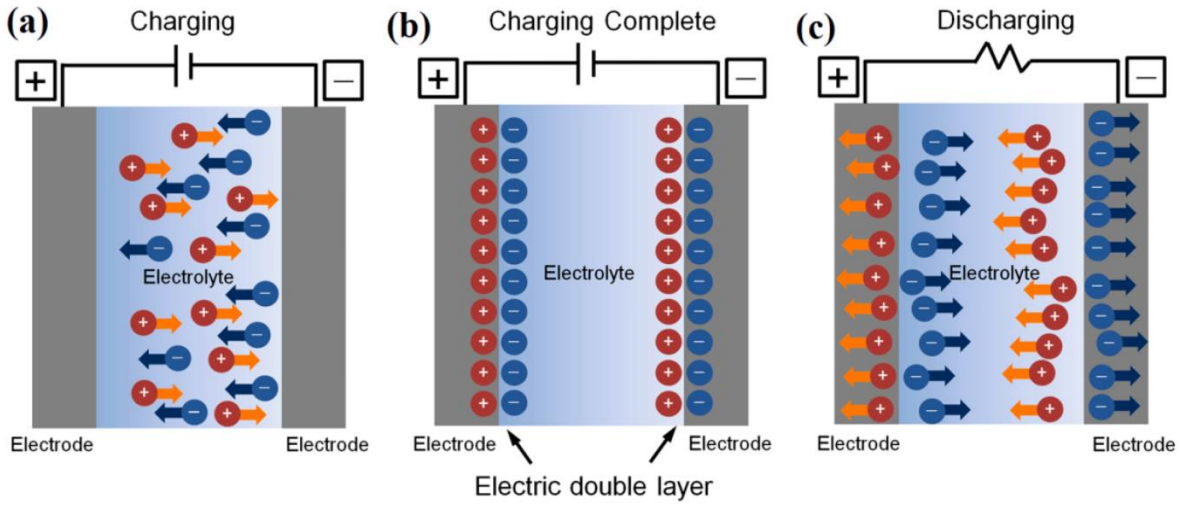

Fig. 1.5. Schematics showing the (**a**) charge process in EDL formation under an external voltage. (**b**) formation of EDL capacitors at the electrode/electrolyte interfaces, and (**c**) discharge process of EDL capacitors. Adapted from [39]

atomic dimension *d*. This variation is depicted in **Fig. 1.6a.** Helmholtz therefore proposed that electrostatic attraction is the reason why layers with opposing charges become immobile on the surface.

Later, a diffuse model of the electrolyte (EDL) was proposed by Gouy in 1910 and Chapman in 1913. This model considered that ions in the electrolyte (both cations and anions) are mobile as they are continuously in thermal motion which results in the production of a relatively thick diffuse layer (**Fig. 1.6b**). Over the diffuse layer and into the bulk of the electrolyte, the potential drops exponentially. However, the double layer capacitance value is overestimated by this approach. As a result, neither of these two models adequately describes the double layer that forms.

Stern integrated the two models. In Stern's model, the dispersion of ionic charges was thought to occur in two layers. As seen in **Fig. 1.6c**, the layer closest to the surface is referred to as the Stern layer, while the other layer is referred to as the diffuse layer. The Helmholtz model's postulated formation layer is similar to the Stern layer. As a result, the electrode has a great affinity for the ions in this layer, making them stationary. Two imaginary planes that are used to differentiate

between the two types of adsorbed ions are the outer Helmholtz plane (OHP) and the inner Helmholtz plane (IHP). The diffuse layer or outer layer closely resembles the one suggested by the Gouy-Chapman model. With the Stern model, the capacitances originating from the outer diffusion layer (C_{diff}) and the Stern layer (C_H) can be used to estimate the total double layer capacitance (C_{dl}) using equation (1.2) [40]:

$$\frac{1}{C_{dl}} = \frac{1}{C_H} + \frac{l}{C_{diff}} \qquad (1.2)$$

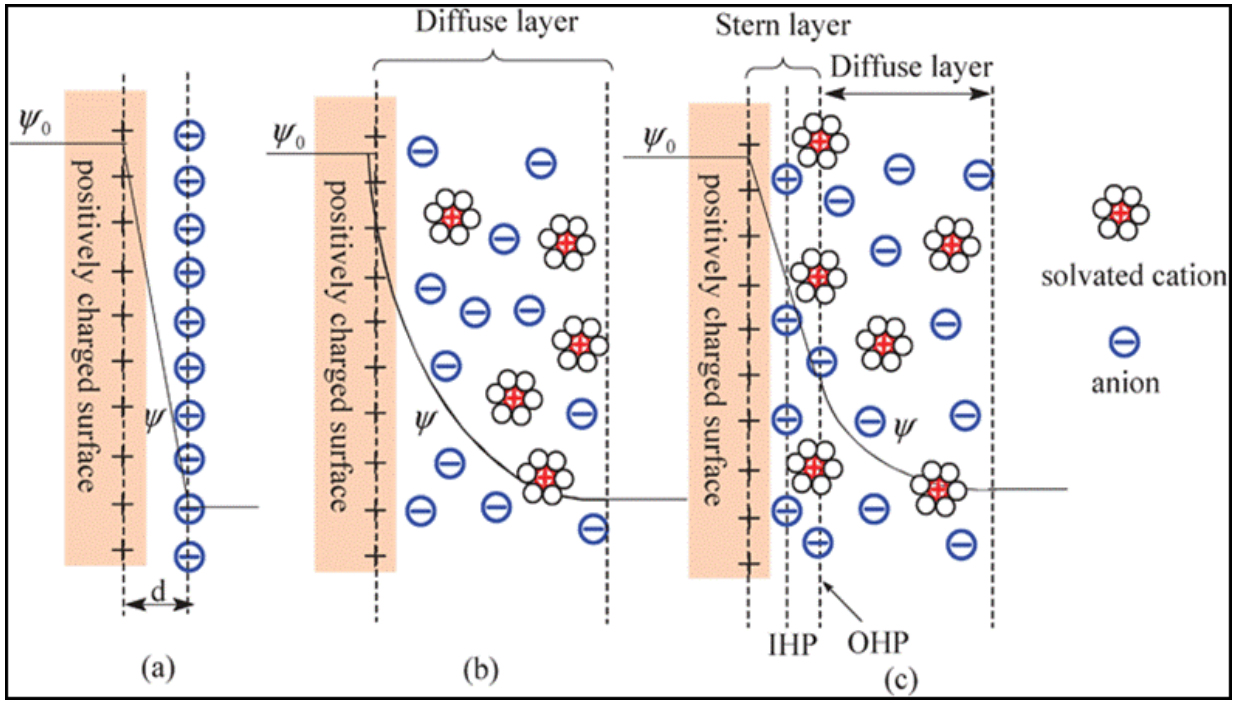

Fig. 1.6 Schematics of double layer formation at a charged surface. (a) Helmholtz model (b) Gouy-Chapman and (c) Stern model [41]

High surface area carbon-oriented materials are the main component of the electrodes utilized in EDLC [42]. Specific measures of surface areas, pore shape and structure, pore size distribution, surface functionality, and electrical conductivity are catalyst characteristics that affect the electrochemical performances [43, 44]. Greater surface area in carbon-based materials leads to a greater capacity for charge accumulation at the electrode-electrolyte interface. Aside from pore size, which includes a high specific surface area, surface functionalization must be taken into account while attempting to improve specific capacitance for carbon materials. Examples of different carbon compounds that are utilized as electrode materials include graphene, carbon

nanotubes, activated carbon, and carbon aerogels. Ion exchanges do not take place between the electrolyte and electrode [38]. To summarize, the way EDLCs store charges is by creating an electric double layer at the interface between the electrolyte and the high surface area carbon electrode. Because of the huge surface area electrode, its storage capacity can be much higher (from a few farads to thousands of farads) than that of a normal capacitor (from few μF to few mF).

Pseudocapacitors

The charge storage mechanism of the pseudocapacitor electrode is not the same as that of the EDLC. When an external potential is applied to the electrode, the active materials go through a fast and reversible redox reaction that is also referred to as a faradic reaction. Charges move through the electrolyte and over the double layer during this process. This kind of redox reaction also serves the purpose of storing energy in batteries. However, this redox reaction occurs quickly in a pseudocapacitor, which gives it a better power density than batteries [45].

Many transition metal oxides, including RuO_2, MnO_2, V_2O_5, and others, as well as a number of conducting polymers, including PANI, PEDOT: PSS, polypyrrole, etc., are now being investigated for usage as electrode materials. The redox reaction of these electrode materials can be completed rapidly if the right electrolytes are used. The storage method of the pseudocapacitor is slow due to the chemical reaction involved. As a result, the pseudocapacitor usually shows poorer power density in comparison to the EDLC. The phenomenon of pseudocapacitive charge storage can be caused by a number of different faradaic mechanisms. The type of active substance is the main factor influencing this. These mechanisms are [46]:

a) Underpotential Deposition:

Adsorption pseudocapacitance, also known as underpotential deposition, occurs when metal ions from the electrolyte solution build a monolayer on the current collector through adsorptive processes[47]. This happens when a potential for the metal's reduction is less negative than the equilibrium or Nernst potential. One example of such deposition is the deposit of lead on the surface of gold, as demonstrated by the reversible chemical reaction.

$$2e+xPb^{2+} + Au \leftrightarrow Au.xPb$$

Fig. 1.7a shows such a mechanism of charge storing.

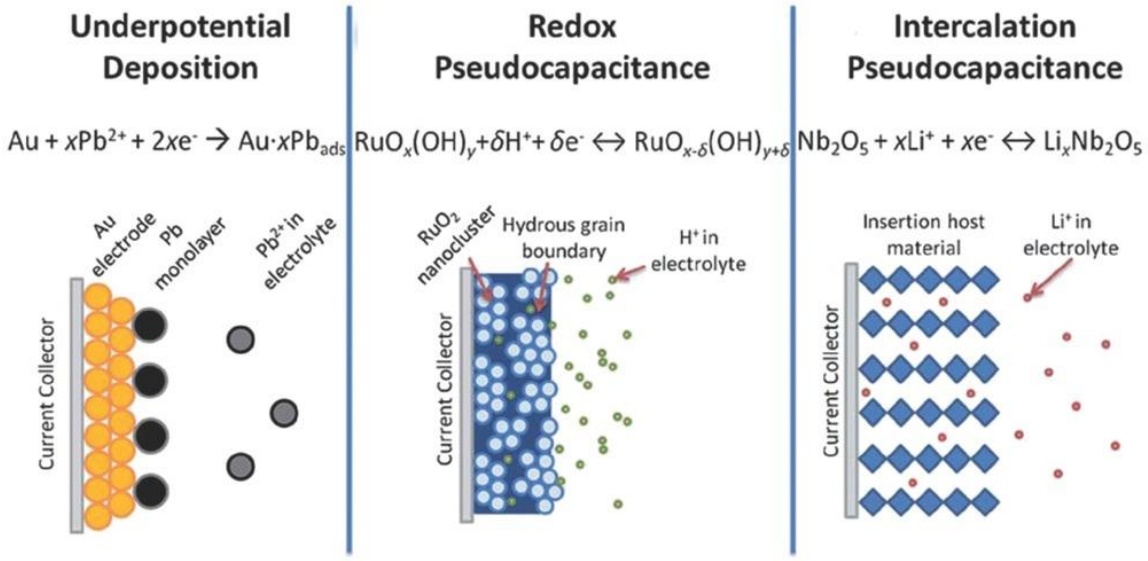

Fig. 1.7. Schematics showing different mechanisms of pseudocapacitive charge storage: (a) Underpotential deposition (b) Redox pseudocapacitance (c) Intercalation pseudocapacitance [50].

b) *Redox Pseudocapacitance:*

Redox pseudocapacitance is the result of quick and reversible faradic charge transfer that adsorbs ions from the electrolyte surface close to the surface of the active material. Such a pseudocapacitance is demonstrated by Hydrous RuO_2. Protons from the electrolyte are taken up by the RuO_2 during charging and released again during discharge. Protons from the electrolyte solution only interact with the active material's surface (within 10 nm of its surface), and the active material does not undergo a phase shift during this faradic process. [48]. **Fig. 1.7b** shows the redox pseudocapacitance mechanism.

c) *Intercalation Pseudocapacitance:*

When ions from the electrolyte solution enter the active material deeply and carry out reversible redox processes, pseudocapacitive charge storage via intercalation of ions in the bulk of the material takes place. Only in cases when the active material has a structure resembling a tunnel or layer is intercalation pseudocapacitance achievable. Because of this, only a small number of materials, such as t-Nb_2O_5, δ-MnO_2, etc., exhibit this kind of charge storage [49]. **Fig.1.7c** shows the charge storage mechanism due to intercalation pseudocapacitance.

Hybrid Supercapacitors:

Hybrid supercapacitor electrode materials store charges using both physical and pseudocapacitive charge storage techniques. For these kinds of materials, energy density and power density increase significantly as a result of the contributions from these two methods. This class of hybrid electrode material consists of composites made of several carbonaceous and redox-active components. The redox-active material stores charges by reversible faradic interactions with the electrolyte, whereas the carbon-based components in these composites store charges through double layer formation. By giving the redox-active material a backbone, carbon-based components also stabilize it against the significant volumetric strain experienced during the redox reaction. In addition, materials containing carbon give electrons a high path, which raises the sample's conductivity. Typically, the carbon-based material increases the composite's power density while the redox-active material increases the composite's energy density. Composites of NiO-CNT, MnO_2-Graphene, PANI-CNT, and so forth are instances of hybrid materials for supercapacitor electrodes.

1.2. Literature Review

The preceding section focused on the significance of developing electrode materials possessing favorable electrochemical characteristics for the purpose of energy storage devices and as effective materials for the elimination of dyes via photocatalysis and adsorption. Materials should have both a high surface area and good electronic conductivity in order to attain desirable electrochemical properties, such as high specific capacity and steady cycling life. As a layer of only one carbon atom, graphene has a potential surface area of up to 2600 m^2g^{-1}. Because of the electron adsorption and desorption on the graphene surface, it has the ability to achieve high specific capacity and steady cycle performance.

The fast and reversible Faradaic reactions take place in metal and metal oxides like spinel ferrite can contribute to a higher specific capacity. As a significant member of the spinel ferrite family, $MnFe_2O_4$ nanoparticles have drawn much attention in the field of photocatalytic dye removal and supercapacitors owing to their low cost, high electrochemical activity, environment friendliness and abundant resources. In addition, due to their outstanding qualities, including high saturation magnetization; and shape- and size-dependent magnetic behavior, cobalt ferrite ($CoFe_2O_4$)

nanocrystals with spinel structure have received a lot of attention for environmental remediation like adsorption.

In this section, the structure and properties of graphene and spinel ferrite were reviewed. The electrochemical and dye removal efficiency of graphene and graphene-based spinel ferrite composite compound were summarized.

1.2.1. Review of graphene

Graphene was introduced as the first laboratory made 2-D material. Owing to it's unique physical and chemical properties-like mechanical strength and elasticity, and exceptionally high electrical and thermal conductivity, graphene is described to be a smart alternative to various traditional materials in many applications [51]. Commonly, graphene is a single 2D layer of carbon atoms, with an average thickness of 0.34 nm. It is sp^2 hybridized, where carbon atoms are covalently bonded to three other atoms in a hexagonal lattice structure[52]. Recently, graphene has been extensively investigated, both in terms of fundamental research and R&D applications. Graphene was isolated for the first time by K. Novoselov et al. [53]what was worth to them the 2010 Nobel Prize in Physics for their groundbreaking work. Their unprecedented structural and physicochemical properties (especially its mechanical and electrical behaviors) in addition to its carrier mobility-the highest know to date, at room temperature, makes the research on graphene one of the most important topics in all materials science fields [54] . Graphene, on the other hand, provides the fundamental form for nearly all other carbonaceous materials, such as graphite, which is essentially several layers of graphene, fullerene and single- and multi-walled carbon nanotube [55].

1.2.1.1. Properties of Graphene:

Structural properties of Graphene:

Graphene is a two-dimensional carbon allotrope [51]. It is made of carbon atoms arranged in a hexagonal honeycomb arrangement [51]. Carbon happens to be the sixth element in the periodic table, which has the ground-state electronic structure $1s^2\ 2s^2\ 2P_x^1\ 2P_y^1\ 2P_z^0$, as seen in **Fig. 1.8b**. Though it is equal to the energy levels of $2p_x$ and $2p_y$, the energy level of $2p_z$ is maintained electron-free for convenience's sake. As seen in **Fig. 1.8a**, a carbon atom's nucleus is surrounded

by six electrons, four of which are valence electrons. There are three types of hybridization that these electrons in a carbon's valence shell can form: *sp*, sp^2 and sp^3. The construction of sp^2 hybrids is seen in **Fig. 1.8c**.

When carbon atoms share sp^2 electrons with three adjacent carbon atoms, they form a honeycomb network with a planar structure, also known as monolayer graphene. **Fig. 1.8d** shows the unit cell of a graphene crystal, represented by a purple parallelogram. The unit-cell vectors $\mathbf{a_1}$ and $\mathbf{a_2}$ share the identical lattice constant of 2.46 Å. The planar ring's stability is achieved through electron resonance and delocalization.

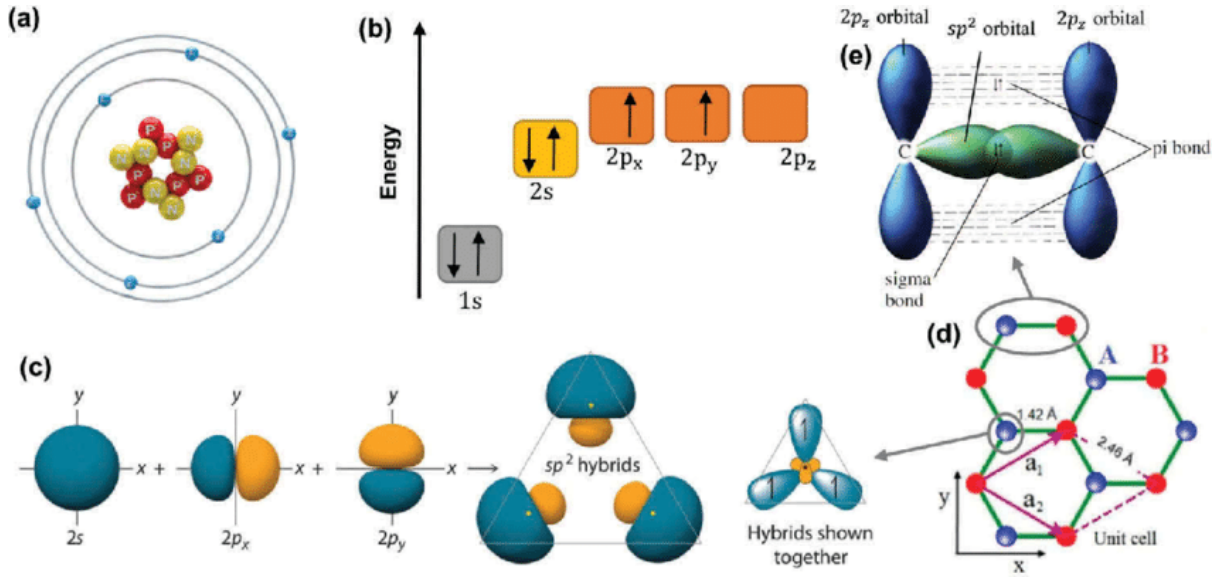

Fig. 1.8. (a) Atomic structure of a carbon atom. (b) Energy levels of outer electrons in carbon atoms. (c) The formation of sp^2 hybrids. (d) The crystal lattice of graphene, where A and B are carbon atoms belonging to different sub-lattices, $\mathbf{a_1}$ and $\mathbf{a_2}$ are unit-cell vectors. (e) Sigma bond and pi bond formed by sp^2 hybridization.[56]

Electrical properties of Graphene

Because it is a zero gap semi-conductor and has conduction and valance bands which touch at the Dirac points, graphene has incredibly high electrical conductivity [57]. A typical carbon atom has six total electrons, two of which are in the inner shell and four of which are in the outermost shell, which can be used to form chemical bonds. However, in the case of graphene, each carbon atom is connected to three additional atoms as a result of sp^2-hybridization. And the fourth is now freely accessible in the third dimension. The electronic mobility of graphene is quite high, even at

ambient temperature. Its electron mobility has been demonstrated to be practically temperature independent [58].

Mechanical properties of Graphene:

The inherent strength of graphene is another one of its exceptional qualities. Due to the strength of its carbon bonds, graphene is the strongest substance yet known. With a tensile strength of 13 $\times 10^{10}$ Pascals (or 130 giga Pascals), as compared to 4 $\times 10^{8}$ for steel, graphene is 200 times stronger than steel. Not only is graphene incredibly strong, but it is also the lightest material—lighter even than paper. It weighs 0.77 mg per square metre; to put this into perspective, one square metre of paper weighs almost 1000 times as much. Graphene exhibits elastic properties as well; after being stretched, it may return to its original size.

It is frequently said that a single sheet of graphene would be large enough to cover an entire football pitch and weigh less than one gramme. AFM investigations were performed in 2007 on graphene sheets that were placed outside of silicone dioxide cavities. These studies revealed that graphene sheets differ from three-dimensional graphite in that they had spring constants in the range of 1-5 N/m and a Young's modulus of 0.5 TPa. According to Changgu Lee, Graphene is the strongest material ever tested, with a tensile strength of 130 GPa and a Young's Modulus (defines stiffness) of 1 TPa [59]. According to a Nobel announcement which illustrates that 1 m^2 of Graphene hammock would support a 4 kg cat, but would weigh only as much as one of the cat's whiskers [57].

1.2.1.2. Methods of synthesis of Graphene

Following its discovery by micromechanical exfoliation of graphite, graphene has become a prospective material in a number of study fields. Though it is crucial to develop a large-scale synthesis process of good grade graphene to have a significant impact on research and development. Liquid exfoliation and ultrahigh vacuum procedures are now popular ways to produce graphene.

Mechanical exfoliation of Graphene:

In the development of graphene, the mechanical or micromechanical exfoliation process has been a major turning point. Due to its ability to produce high-quality graphene films with a size range of 5 to 10 m, it is still the primary synthesis method for producing high-quality graphene for

research [60]. However, the uneven thickness of the films produced by this method and the high production costs brought on by the low yield restrict its use in the field of research for mass production. These procedures are a perfect illustration of the top-down strategy, in which a precursor material for graphene (such as graphite, GO, etc.) is disassembled layer by layer to create graphene sheets. Geim and Novoselov, two Nobel Prize winners, were part of the Manchester University team that developed graphene through the micromechanical alleviation of graphite. The graphite crystals were continually divided into thinner pieces using "the scotch tape" or peel-off method. After dissolving the optically transparent flakes-containing tape in acetone, the flakes-which included both multilayer and monolayer graphene-were subsequently settled on a silicon wafer for microscopic examination. Researchers eventually updated this method to get around the phase in which graphene floated in a liquid. These advancements eventually produced naked-eye observable graphene flakes larger than 1 mm in size [61].

The current research surge was sparked by the ability to isolate graphene. Free-standing atomic planes were formerly believed to be nonexistent [62]. The general consensus among scientists was that such structures would be unstable at nanoscales and would be predicted to scroll and buckle [63, 64]. Some researchers also think that the stability of 2D crystals may be influenced by intrinsic microscopic roughening on the order of 1 nm. [65]. Similar experimental techniques were used by Novoselov et al. to generate free-standing atomic planes of boron nitride, mica, dichalcogenides, and complicated oxides, but none of them have so far been as well-received [66].

Chemical Vapor Deposition:

Chemical vapor deposition is a technique used to produce high-quality graphene by decomposing hydrocarbon gases (such as methane (CH_4), acetylene (C_2H_2), ethylene (C_2H_4), and hexane (C_6H_{14}) in order to grow graphene sheets on metallic catalysts (such as Cu and Ni films) at higher temperatures (650-1000 °C) [67, 68]. After contacting the hot surface of metal catalyst, the carbon precursor degrades into free carbon and hydrogen atoms. The carbon atom then scattered through the surface and the bulk of metal catalyst, and eventually constructs graphene sheet on the metal surface after achieving the carbon solubility limit [69, 70]. In order to enhance CVD procedures, graphene was synthesized on a variety of substrates, including glass, silicon, quartz, silicon oxide, sapphire, and boron nitride. Paper by Chen et al. describes the mechanisms in depth [71].

High-quality graphene with minor imperfections, interconnected structure, and a huge surface area may be produced via CVD [68]. Its drawbacks include high production costs, low throughput, additional purification to get rid of catalyst residue, and the transfer of graphene to different substrates [72]. Schematic diagram of CVD process has been represented in **Fig. 1.9**.

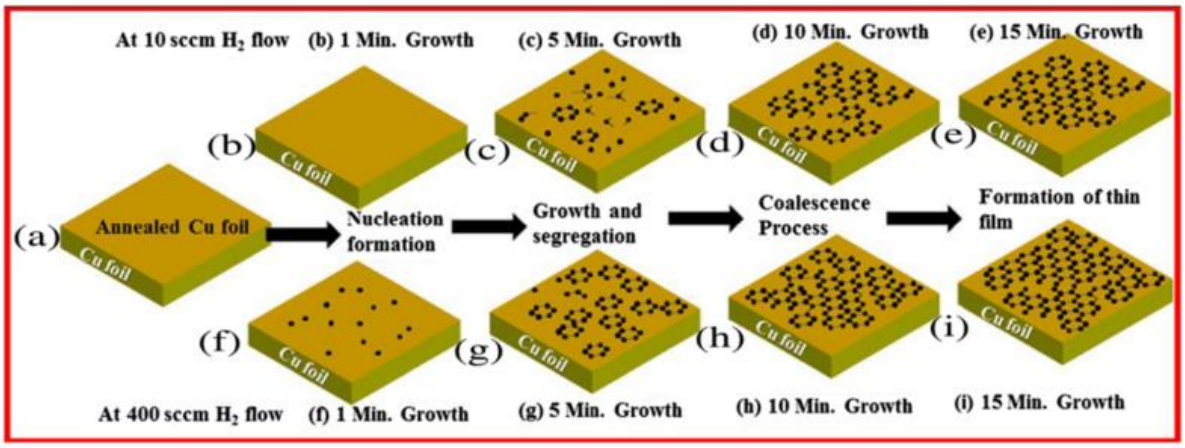

Fig. 1.9. Illustration of synthesis procedure of Graphene on Cu [73].

Graphene Oxide (GO) and Reduced Graphene Oxide (rGO)

Although graphene can be directly extracted from graphite by mechanical cleavage or solution-assisted exfoliation, the graphite oxide route yields a functional form of graphene that is desirable for applications like adsorption. Through the use of acids and oxidants in the solution oxidation/intercalation of graphite, GO is generated through the exfoliation of graphite powder. Brodie's 1958 report is the first on the production of graphite oxide using nitric acid and potassium chlorate. At the moment, the Hummer's approach [74], the modified Hummer's method [75], and Tour's method [76] are the most often utilized techniques for producing graphite powder.

The layered structure of graphite is preserved in graphene oxide (GO), while the inclusion of polar oxygen groups like hydroxyl, epoxy, carbonyl, and carboxylic leads to increased interlayer separation. When these groups are introduced, the carbon hybridization in graphite changes from being sp^2 to being a mixture of sp^2 and sp^3 in GO. The C/O ratio, which varies from 1:1 in highly oxidized graphite oxide to 4:1 in less oxidized graphite oxide based on the oxidation process and environmental factors, defines the oxygen content in graphite oxide. Because of these oxygen groups, graphite oxide is highly hydrophilic and easily exfoliates to graphene oxide (GO) in

aqueous solution. The oxygen concentration was lowered to around a C/O ratio of 10 by the conversion of GO to rGO.

Despite having defects in its surface, rGO is the least expensive way to get comparable quality to graphene sheets. One of the common critical reaction reduction techniques is the reduction of GO, which works as follows: Thermally-mediated reduction, electrochemical reduction, and chemical reduction using hydrazine monohydrate, hydrazine, and sodium borohydride are the three methods. The structure of GO and rGO as well as the schematic for their preparation is shown in **Fig. 1.10**.

1.2.1.3. Photocatalytic dye degradation by Graphene

Due to its potential for use in energy and environmental-related applications, semiconductor-mediated photocatalysis has garnered worldwide interest in recent years. Its low efficiency, however, is caused by the rapid recombination rate of photogenerated electron-hole pairs within photocatalytic materials, which restricts its practical uses. Thus, improving the photocatalytic activity of semiconductor photocatalysts requires suppressing the recombination of charge carriers [78].

Owing to the long-range pi conjugation, graphene has drawn attention of numerous theoretical studies and has become a promising area for researchers in recent time. Graphene potentially incorporate with various components such as metal (Ag, Au Pt, Pd etc.), metal oxide (ZnO, TiO_2, MnO_2, Co_2O_4, Fe_2O_3 etc.) and polymer to construct a hierarchical catalytic system [79]. The availability of oxygen groups and flaws in GO were discovered to be the main reasons why graphene support derived from GO exhibits crucial anchoring sites. The formation of rGO included the regulation of oxygen levels as well as the determination of the degree and timing of the reduction and oxidation situation [80]. In this regard, graphene supported nanocomposites are thought of as a developing area of study for environmental cleanup and water purification systems. Graphene-based nanocomposites are constructed to improve the absorptivity of pollutants, to increase light energy absorption, to facilitate charge carrier migration, to eliminate the rate of recombination, and consequently to increase the photocatalytic efficiency. Moreover, when graphene used as a support material nanocomposite, it decreases aggregation, restricts re-stacking, increases surface area, offers mechanical strength, supports material, inhibits leaching, corrosion, and electron scavengers, acts as a photosensitizer, and does other things that improve the practical use of photocatalysts.

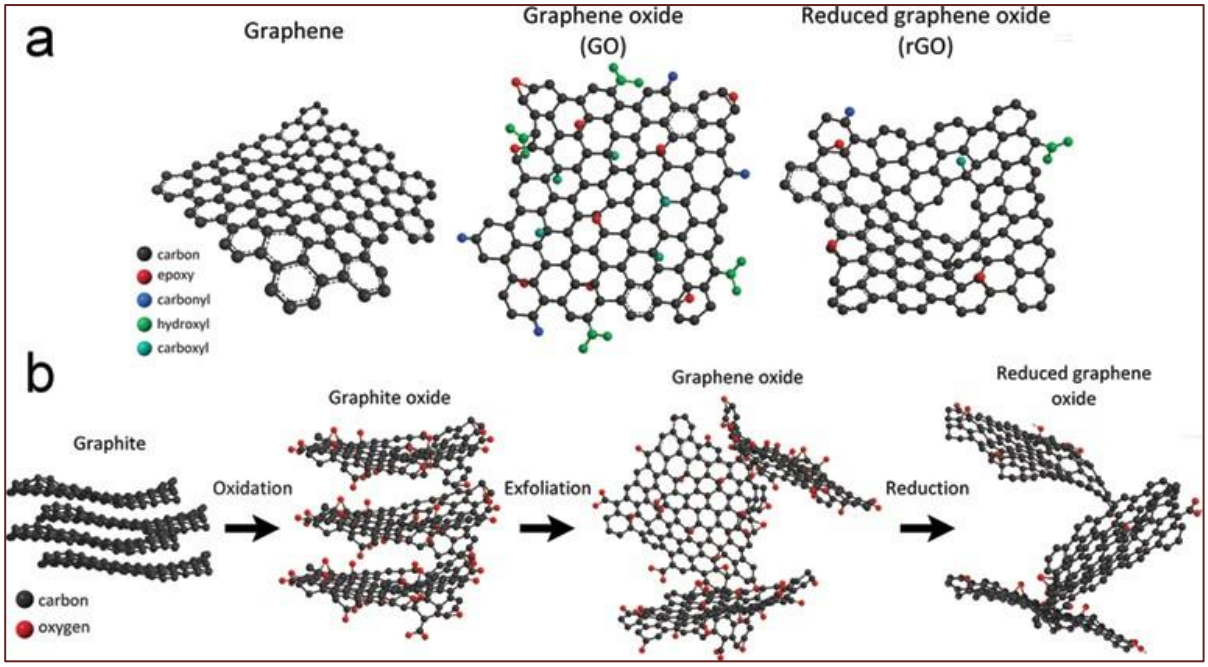

Fig. 1.10. (a) Schematics of the chemical structure of graphene, graphene oxide and reduced graphene oxide. (b) Route of graphite to reduce graphene Oxide [77].

Nano-composites based on graphene are advantageous because they offer characteristics including good water dispersion, simple chemical functionalization, and biocompatibility. Furthermore, as they are not powerful oxidants, no hazardous secondary byproducts are anticipated to be produced [81].

Many visible-light photocatalysts have been constructed and evaluated for water decontamination, and graphene-supported UV-visible light assisted photocatalysis has recently emerged as an efficient, affordable, and environmentally acceptable technique [82]. According to studies, using graphene as a support material to anchor catalyst nanoparticles (NP) offers up new opportunities for creating a new generation of catalysts [81].

Consequently, photocatalytic degradation of organic molecules has made considerable use of semiconductor photocatalysts based on graphene. These composites have improved charge separation and transportation characteristics, a large dye adsorption capacity, and a wider light absorption range. The P25 TiO_2-graphene compound, for instance, was described by Zhang et al. as a high performance photocatalyst [83]. When compared to the bare P25, this composite

photocatalyst demonstrated a notable improvement in the photocatalytic degradation of methylene blue (MB) in water under both UV and visible light irradiation. Adsorption of dyes increases compared to that on the bare P25 because MB molecules can be transported from the solution to the surface of TiO_2 and adsorbed with offset face-to-face orientation via *pi–pi* conjugation between MB and aromatic areas of graphene.

1.2.1.4. Adsorption of pollutant dye by graphene

It has been reported that activated carbon is a conventional adsorbent of pollutant in the field waste water treatment owing to it's versatility, benign nature, but its application is limited as it has high regeneration cost and chemical rigidness [84]. Graphene has opened up new possibilities for managing pollutants through adsorption. Adsorption occurs on the surface of graphene composites due to their ultra-large surface area and strong π–π interaction [85]. Physical adsorption is caused by both the π–π interaction and the electrostatic interaction of oppositely charged functional groups on the adsorbent and adsorbate [86]. Additionally, studies have shown that the adsorption is highly sensitive on ionic strength and pH, suggesting an ion exchange process.

Graphene has been enhanced with a lot of oxygen-containing functional groups to form reduced graphene oxide (rGO) and graphene oxide (GO). The surface functions of GO make it a material with great potential for use in environmental applications. The preferred materials for the adsorption of charged species are graphene and GO due to the adsorbate's electrostatic interactions with them. Dye removal has been achieved through the use of three-dimensional reduced graphene oxide macrostructures. Orange G (OG) was eliminated using exfoliated graphene oxide (EGO) and reactive graphene oxide (RGO) [87]. The charge on the dye determines whether to use GO or rGO for efficient adsorption.

RGO-Fe_3O_4 nanoparticles were used to remove RB, R6G, acid blue 92 (AB 92), MG, and other pollutants, addressing the need for a better carbon-based replacement. Annealing allowed the dye to be easily renewed without significantly reducing its regeneration capacity. It also displayed the ability to adsorb several dyes concurrently without being impacted by pH or temperature [88].

1.2.1.5. Graphene as electrode material for electrochemical supercapacitor application

Considering the need for energy conversion and storage, graphene offers a highly adjustable specific surface area (SSA) of 2630 m^2g^{-1}, as well as a remarkably high electronic conductivity because of the free, high-mobility pi (π) electrons present in its orbitals. [89]. Furthermore, graphene has 4.5×10^3 times better electronic conductivity than copper (theoretical: 200,000 cm^2 V^{-1} s^{-1}) and is temperature-independent [90]. Graphene is classified as an electrochemical double layer capacitor (EDLC) due to its charge storage process, which involves ions accumulating charges electrostatically on the material surface [91]. This type of supercapacitor has a quick charge/discharge rate and great cycle life performance [92]. A specific capacitance of 111 Fg^{-1} was achieved with ultrathin graphene paper with 25 nm thickness [93]. Exfoliating graphene under high vacuum at 200 °C results in a high capacitance of 200 Fg^{-1} [37]. Researchers also began experimenting using graphene oxide(GO) and its reduced counterpart to fabricate inexpensive, high-yield graphitic materials that can be easily attached on a flat flexible substrate [94, 95]. However, the capacitance values of graphene reported in the literature are substantially lower than its predicted value of 550 Fg^{-1} [96]. This is because graphene sheets are easily stacked back together, making it harder for ions in electrolytes to reach [97]. Therefore, by decorating graphene with imperfections, impurities, or electroactive elements, such as metals or metal oxides, additional active sites are produced, and high specific capacitance values can be attained [96]. Recently, Sun et al. obtained NDG nanosheets with a high nitrogen level via a hydrothermal reaction of GO and urea that exhibited excellent capacitive behaviors (326 Fg^{-1} at 0.2 Ag^{-1}) [98].

1.2.2. Spinel ferrite nanoparticles (SFNP)

Ferrites are mixed metal oxides with iron (III) oxides as their main component that crystallize in three crystalline structures; spinels, garnet ($A_3Fe_5O_{12}$) and magneto plumbite ($AFe_{12}O_{19}$) where A and B are metal ions. The physically simplest of these, spinel ferrites, crystalize into the spinel structure, which is essentially governed by the oxygen ion lattice [99]. Spinel ferrite is a structure. MFe_2O_4, where M is the name of the metal, is a cubic, tightly packed arrangement of oxygen atoms, with M^{2+} and Fe^{3+} at two separate crystallographic sites.

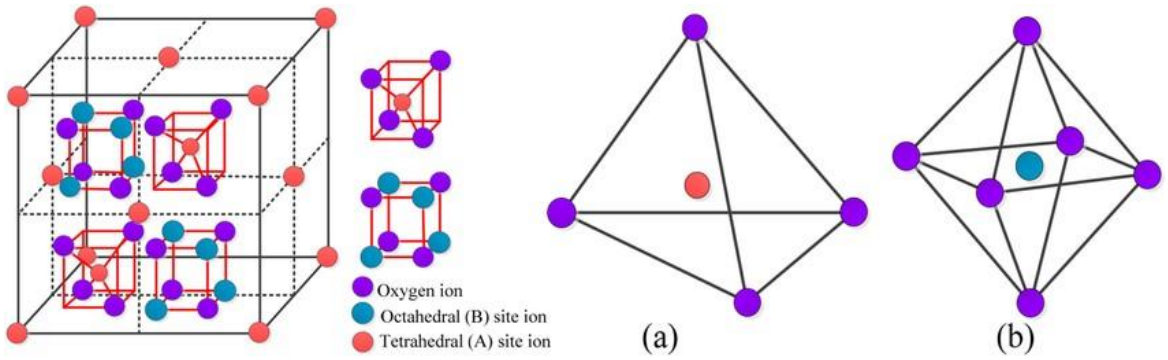

Fig. 1.11. The crystal structure of spinel ferrite and the distribution of metal ions.

These sites, designated as A and B-sites, respectively, exhibit tetrahedral and octahedral oxygen coordination. The spinel structure contains two places where metal cations can occupy cations. It has sixteen B-sites with octahedral coordination and eight A-sites where the metal cations are tetrahedrally coordinated with oxygen. The term "normal spinel" refers to ferrite in which the A-sites are occupied by M^{2+} cations and the B-sites by Fe^{3+} cations. If M^{2+} and Fe^{3+} cations occupy the B-sites randomly but Fe^{3+} cations completely occupy the A-sites, the resulting structure is called an inverse spinel. Most spinels have an intermediate degree of inversion in their cation distribution, with some M^{2+} and Fe^{3+} cations present at both locations. The magnetic characteristics of spinel ferrites display ferrimagnetic ordering. The magnetic moments of the cations at the A and B sites are parallel to one another. Between the A and B-sites the arrangement is antiparallel and as there are twice as many B-sites as A-sites, there is a net moment of spins yielding ferrimagnetic ordering for the crystal. Therefore, the choice of metal cation and the distribution of ions between the A and B-sites give a changeable magnetic system [100]. **Fig. 1.9** represents the crystal structure of spinel ferrite and the distribution of metal. In brief, there are the following kinds of spinel ferrites based on the distribution of cations.

(1) Normal spinel structure, where all M^{2+} ions occupy A-sites; structural formula of such ferrites is $M^{2+}\ [Fe_2^{3+}]\ O_4^{2-}$. Zinc ferrites are where this kind of distribution occurs. $Zn^{2+}[Fe^{2+}Fe^{3+}]O_4^{2-}$.

(2) Inversed spinel structure, where Fe^{3+} ions are equally distributed between A and B-sites and all M^{2+} ions are in B-positions: $Fe^{3+}[Mn^{2+}Fe^{3+}]\ O_4^{2-}$ is the structural formula of

these ferrites. The spinel structure of magnetite Fe_3O_4 and ferrites $NiFe_2O_4$ and $CoFe_2O_4$ is inverse.

(3) Mixed spinel structure, when the cations Me^{2+} and Fe^{3+} occupy both the A and B locations; the structural formula of this ferrite is $M_{1-\delta}^{2+}Fe_{\delta}^{3+}[M_{\delta}^{2+}Fe_{2-\delta}^{3+}]O_4^{2-}$, where δ denotes the inversion degree. $MnFe_2O_4$ which is a type of structure with an inversion degree of δ = 0.2 and structure $Mn_{0.8}^{2+}Fe_{0.2}^{3+}[Mn_{0.2}^{2+}Fe_{1.8}^{3+}]O_4^{2-}$. Additionally, Mn-Zn ferrites have a mixed spinel structure, with Zn^{2+} favoring A-site occupancy with structure $Zn_x^{2+}Mn_y^{2+}Fe_{1-x-y}^{3+}[Mn_{1-x-y}^{2+}Fe_{1+x+y}^{3+}]O_4^{2-}$. In this case, δ = 1 − x − y.

SFNP are widely used in many different applications, from biomedical to industrial. In the former scenario, SFNP main uses are in cancer diagnosis, cancer gene therapy, and drug delivery. In the latter scenario, on the other hand, they may be employed as a gas sensor, a catalyst and pollutant removal through adsorption or photodegradation, a high-frequency device, water splitting, and membrane modification. When SFNP are employed as catalysts, they help to speed up chemical reactions in a variety of inorganic and organic synthesis processes as well as the photodegradation of contaminants found in organic waste. An external magnetic field can be used to easily extract SFNPs from the solution mixture when treatment is completed. Another crucial characteristic is their ability to photodegrade organic contaminants, which is why their nanoparticles and nanocomposites are used to remediate wastewater [4].

1.2.2.1. Synthesis method of spinel ferrite nanoparticles

The synthesis of homogeneous nanoparticles is crucial because their dimensions heavily influence their electrical, optical, and magnetic properties [101]. Typically, the relative surface area of nanoparticles increases with their decreasing size. At the nanoscale, conductivity and electrical structure differ significantly from bulk size [102]. Nanomaterials synthesis methods fall into two categories: "bottom-up" and "top-down." Bottom-up synthesis involves chemically combining ions to make particles, whereas top-down synthesis involves crushing chemicals to form tiny particles. Several synthesis techniques exist for the "bottom-up" approach, including co-precipitation, hydrothermal, thermal decomposition, solvothermal, sol-gel, sonochemical, microwave-assisted, microemulsion, and polyol techniques. The first four are the most common. Mechanical milling and pulsed laser ablation are the only commonly used "top-down" synthesis techniques.

The properties of SFNPs are heavily influenced by the synthesis procedures utilized, which in turn has a substantial impact on their adsorption capacity when used to remove contaminants from wastewater. For example, in a study comparing brilliant green decolorization by $NiFe_2O_4$ NPs [41], 60% of brilliant green decolorization was achieved within 10 minutes of microwave irradiation in the presence of $NiFe_2O_4$ NPs synthesized by co-precipitation, whereas no significant change was observed when $NiFe_2O_4$ synthesized by sol-gel method was used. The difference between the two was attributed to alkali residual release by $NiFe_2O_4$ produced via the co-precipitation method. Similarly, the magnetite-hematite mixture generated by various methods was successfully used as an adsorbent material and extremely efficient for the removal of metal from water such as Pb(II), Cd(II) and Cr(III) [103].

1.2.2.2. Waste water treatment using graphene and spinel ferrite nanocomposites (GSF)

Research has clearly demonstrated the wide range of applications for GSF in water and wastewater treatment. Among the most well-known applications for GSF are adsorption and photocatalytic degradation of organic dye pollutants, which will be explored in the following sections. Several procedures have been used to treat water and wastewater, with varied degrees of success. Other treatment options could be utilized for eliminating effluent dyes from water; however, many issues impede their use, such as insufficient dye removal, difficulty with adsorbent recovery, lack of cost-effectiveness of the method, and, in some cases, waste sludge is voluminous and requires proper design, as well as a large amount of space for disposal [104] .

Because of the aforementioned constraints, current adsorbents for water and wastewater treatment are ineffective. As a result, there is a need for an adsorbent that is inexpensive, efficient, and easy to recover and reuse. Keeping this in mind, GSFs are the most appropriate materials for addressing water filtration and quality issues [105]. This is mostly owing to their remarkable physical and chemical qualities, along with magnetism which allow for the simultaneous removal of a wide range of contaminants while also being easy to recover and reuse. the simplicity of recovery and the ability to reuse recovered adsorbents for numerous cycles without losing removal capability make GSF one of the best options. Spinel ferrite nanoparticles and their equivalent GSF composites have significant advantages over their bulk counterparts, particularly in terms of increased adsorption capacity, cost-effectiveness, and pollutant removal efficiency [106].

Some of the benefits of spinel ferrite nano particles for water and wastewater treatment are as follows [107].

- Small amount required
- Simple preparation
- No filtration
- Fast adsorption
- Cost effective
- Efficient
- Easily recovered and reused.

Adsorption studies of inorganic contaminants [e.g., Cr(VI), U(VI), As(V), and Pb(II)] on different GSFs have demonstrated that the protonation/deprotonation of surface functional groups of GSFs over a wide pH range results in the electrostatic interactions, ion exchange, and formation of the inner-sphere surface complexes as the dominant adsorption mechanisms. The U(VI) ions, for instance, were firmly attached to rGO/$CoFe_2O_4$/polyaniline (rGO/CF/PANI) via hydrogen bonding and electrostatic interactions between the surface functional groups ($SeNH_2$, S]NH, and SeCOOH, where S denotes the surface) of the rGO/CF/PANI and U(VI) [108].

On a number of GSFs, the π-π stacking interaction was discovered to be the main adsorption mechanism for the removal of organic pollutants (such BPA and MB dye). Wang et al. reported that the π-π stacking interactions between rGO and MB molecules may be responsible for the increased adsorption efficiency of rGO/$ZnFe_2O4$ [109]. Hu et al. [110] further showed that the increased surface area and π-π stacking interactions between the hydrophobic BPA and rGO's skeletal structures improved the BPA adsorption when rGO (wt%) was added to $BFO_{249}/GO_{4.5}$. Prior to that, in $BFO_{249}/GO_{4.5}$, the overabundance of GO's functional groups restricted the π-π interaction, which in turn decreased the BPA adsorption.

On the other hand, with NPs of heterogeneous photocatalysts, different non-magnetic nanoparticles with high surface areas are crucial for catalytic processes in many industrial applications. However, these photocatalysts, such as semiconductors (TiO_2, ZnO, and ZnS), have some limitations because their recovery after waste treatment is a challenging process that is expensive and time-consuming due to their small sizes [111].

As a result, the issue of inadequate recovery not only results in the loss of the photocatalyst but also causes the leftover photocatalyst to contribute to additional environmental contaminants. The practical use of nonmagnetic photocatalytic semiconductors is limited by these issues. Recently, potential remedies for reducing the aforementioned restriction have developed, including the incorporation of magnetic SFNPs into semiconductors [112-114]. Additionally, the ferrites show improved photocatalytic effectiveness because of their additional catalytic sites and favorable optical absorption for lower energy photons (hν~2 eV) [115]. Graphene inhibits the leaching of hazardous nanoparticles and forms ferrites on graphene nanosheets that can prevent agglomeration, enhancing both adsorption and photocatalytic performance. These properties are due to graphene's large specific surface area, chemical durability, and reduced electronic band gap. It was reported by Liang et al., that MB molecules adsorbed on rGO/$NiFe_2O_4$ by π-π stacking and electrostatic contact were broken down by h^+, $^{\bullet}OH$ and $O_2^{\bullet-}$ produced by interaction with H_2O or OH^- ion under visible light irradiation was the predominant oxidative species in the photocatalytic breakdown of MB [116]. The reaction between photogenerated e and $O_2^{\bullet-}$ produced the minor species known as O_2. The graphene-based $CoFe_2O_4$/CdS (Gr-$CoFe_2O_4$/CdS) system, which was generated from $CoFe_2O_4$, showed better photocatalytic activity, according to Shi et al. [117]. This was because of the reduced electronic band gap (0.8 eV) of graphene. Using graphene as an electron mediator, the photo-excited *e* in $CoFe_2O_4$ moved to the CB of CdS. $^{\bullet}OH$ and $O_2^{\bullet-}$ which serve as the primary species for the breakdown of MB dye, are created during this process. Further research by Singh et al. revealed that nitrogen-doped graphene/ $NiFe_2O_4$ ($NiFe_2O_4$-NG) limited direct *h*-*e* recombination by trapping the delocalized electrons and improved the adsorption of MB dye through π-π interactions with the aromatic rings of hydrophobic MB molecules [118]. $CuFe_2O_4$@g-C_3N_4 core-shells were synthesized by a self-assembly technique under visible light irradiation in another study [119]. This combination performed exceptionally well in the degradation of Orange II dye when H_2O_2 was present as an oxidant. When compared to $CuFe_2O_4$ or g-C_3N_4, the composite exhibited higher activity. Complete degradation of Orange II dye (0.28 mM) at 65 °C was seen in 90 minutes at a catalyst dosage of 0.1 $g.l^{-1}$ and 0.01 M H_2O_2. This study also showed how crucial it is to raise the temperature to break down the activation energy barrier that prevents H_2O_2 from breaking down, which increases the production of hydroxide radicals.

1.2.2.3. Electrochemical properties of spinel ferrites and its composite with graphene:

The unique physico-chemical properties of metal oxide nanostructures, including high specific surfaces, exceptional electrical conductivity, low toxicity, and low production costs, make them an attractive class of materials for a wide range of applications. Transition metal spinel ferrites have been the subject of much research over the past century because of their important dielectric, magnetic, and electronic properties. These qualities are of utmost relevance to the electronic industry [120, 121]. Spinel ferrites have also been employed in electrochemistry (lithium-ion batteries, EC sensors, supercapacitors, etc.) and energy supply studies due to their chemical stability [122]. Spinel ferrites have long been regarded as an active electrode material for supercapacitors [123]. Several spinel ferrites in various shapes and sizes have been investigated as supercapacitor materials (electrodes). For example, the Fe-based spinel $NiFe_2O_4$ has been investigated as a supercapacitor electrode material. Crystallite size and distribution were discovered to influence $NiFe_2O_4$'s electrochemical performance [124]. Among other ferrites , $MnFe_2O_4$, $CoFe_2O_4$ have also gained huge attention in the field of supercapacitor [125, 126]. Despite all possible advantages of spinel ferrites, such as a wide potential window, excellent cycling stability, and high-power delivery capabilities, their poor electrical conductivity limits its actual applications in supercapacitors. Several composites of spinel ferrite nanoparticles with electrically conductive carbon-based materials, such as carbon nanotubes (CNT) and graphene, have been presented to improve the electrochemical performance [127], [128].

Graphene-based materials are widely used due to its superior electrical conductivity, increased chemical stability, and specific surface area when compared to other forms of carbon. Xiong et al. reported that the specific capacitance of $CoFe_2O_4$ can be increased with rGO doping from 52.5 to 254.5 F/g. The rate capability and stability of the material are also improved alongside the specific capacitance [129]. He et al. showed enhanced cycle stability and improvement in the specific capacitance of $CoFe_2O_4$ from 18.7 F/g to 123.2 F/g when there is composite formation with rGO [130]. In essence, the production of composite materials containing metal oxide and graphene materials offers advantages in terms of high surface area, porosity, and conductivity, leading to high specific capacitance of ferrite nanoparticles with long cycle life [131].

1.3. Motivation and objective of the Thesis

The removal of harmful contaminants from water resources is one of the main environmental concerns in pollution control. It has been a severe issue for both the environment and human health since industrial effluents carrying dangerous dyes like Congo red, Methyl orange, and Methyelene Blue which are contaminating the water resources. Due to their high toxicity and carcinogenicity and non-biodegradable aromatic structure, the majority of dyes are dangerous [132]. Among various waste water treatment, Photocatalytic water treatment is a well-known advanced oxidation process in which the photocatalyst material with the production of electron-hole pair upon the irradiation with light, mineralize complex organic compound to mainly CO_2, H_2O, and other non-harmful inorganic materials [133]. Adsorption is also the preferred method because to its low cost, ease of usage, and minimal sludge generation [134]. So, for treating huge amounts of wastewater, it is crucial to create innovative Photocatalyst as well as adsorbents with high removal efficiency for dye along with the quality of quick separation rates. On the other hand, due to the demands of contemporary civilization and growing ecological concerns, there has been an ever-increasing demand for the investigation of creative, inexpensive, ecologically friendly, and high-performance energy storage devices [135]. Due to their high-rate capability, pulse power supply, long cycle life, straightforward principles, high dynamic charge propagation, and low maintenance costs, supercapacitors-also known as electrochemical capacitors and ultracapacitors-are thought to be a promising candidate for alternative energy storage devices.

Due to their excellent catalytic and magnetic properties and ease of fabrication, spinel ferrite $MnFe_2O_4$ magnetic nanoparticles have recently become potential candidates for a variety of applications, including energy storage, waste water treatment, drug delivery, etc. But in case of photocatalysis, high recombination rate of the photo-induced charge carriers results in typically low photocatalytic efficiency. $MnFe_2O_4$ is also a great material for energy storage, but its performance as a pseudocapacitor has occasionally been hindered by its low electronic conductivity. This can lead to insufficient charge transport at the electrode/electrolyte interface and in electrodes, which inhibits the production of enough faradaic redox reactions [127].

Since it has strong conductivity and a sizable surface area of about 2600 m^2g^{-1}, graphene, a single atom thick sheet with a hexagonal honeycomb sp^2 -hybridized carbon atom network, has been

widely employed as an EDLC material. Theoretically, graphene-based supercapacitors can achieve capacitance of 550 Fg^{-1} when their entire surface area is used [136]. Given that graphene has structural and surface restrictions, its specific capacitance in practice ranges from 130 to 200 Fg^{-1}, which is significantly less than its theoretical value [137]. Graphene has a high surface area, strong chemical stability, and high electron mobility in its chemical structure, making it a promising material to remove significant quantities of organic pollutants from sludge [138-141]. Though Graphene is an effective adsorbent, but it is difficult to reuse, which could drive up costs and lead to secondary pollution.

Summing up all the challenges, and based on above discussions, the objectives of the present thesis work have been:

1. To develop $MnFe_2O_4$/rGO based photocatalyst for the removal towards the photodegradation of Methylene Blue (MB) dye in an aqueous solution under UV light irradiation. To identify the dominant active species during photocatalytic processes, to explore the kinetics, and to suggest photocatalytic mechanisms and to explore the link between the active species and photocatalytic activity.
2. To prepare N doped graphene, with the help of graphene oxide by a facile solvothermal method at, using DMF as a source of nitrogen as well as a reducing agent. Our intention was to achieve theoretical value capacitance of pristine graphene.
3. To prepare $MnFe_2O_4$ nanoparticles on the surface of reduced graphene oxide *via* a facile one-step solvothermal strategy which includes the reduction of graphene oxide (GO) to reduced graphene oxide as well as the formation of $MnFe_2O_4$ nanoparticles on a graphene sheet. To investigate the enhanced electrochemical properties with the introduction of graphene.
4. To prepare $CoFe_2O_4$/rGO-based adsorbent for the removal of Methylene Blue (MB) dye, to explore the kinetics, and to suggest adsorption mechanisms. To explore the reusability of the composite as adsorbent.

References

[1] M. A. Montgomery and M. Elimelech, "Water and sanitation in developing countries: including health in the equation," *Environmental science & technology*, vol. 41, no. 1, pp. 17-24, 2007.

[2] A. Sudhaik, P. Raizada, P. Shandilya, and P. Singh, "Magnetically recoverable graphitic carbon nitride and $NiFe_2O_4$ based magnetic photocatalyst for degradation of oxytetracycline antibiotic in simulated wastewater under solar light," *Journal of environmental chemical engineering*, vol. 6, no. 4, pp. 3874-3883, 2018.

[3] Y. Zhang *et al.*, "Nanomaterials-enabled water and wastewater treatment," *NanoImpact*, vol. 3, pp. 22-39, 2016.

[4] N. K. Gupta, Y. Ghaffari, S. Kim, J. Bae, K. S. Kim, and M. Saifuddin, "Photocatalytic Degradation of Organic Pollutants over MFe_2O_4 (M= Co, Ni, Cu, Zn) Nanoparticles at Neutral pH," *Scientific reports*, vol. 10, no. 1, pp. 1-11, 2020.

[5] T. Setiadi, Y. Andriani, and M. Erlania, "Treatment of textile wastewater by a combination of anaerobic and aerobic processes: A denim processing plant case," *Proceedings of the Southeast Asian Water Environment*, vol. 1, 2006.

[6] M. M. Hassan and C. M. Carr, "A critical review on recent advancements of the removal of reactive dyes from dyehouse effluent by ion-exchange adsorbents," *Chemosphere*, vol. 209, pp. 201-219, 2018.

[7] M. Imran, D. E. Crowley, A. Khalid, S. Hussain, M. W. Mumtaz, and M. Arshad, "Microbial biotechnology for decolorization of textile wastewaters," *Reviews in Environmental Science and Bio/Technology*, vol. 14, no. 1, pp. 73-92, 2015.

[8] J. M. Aquino, R. C. Rocha-Filho, L. A. Ruotolo, N. Bocchi, and S. R. Biaggio, "Electrochemical degradation of a real textile wastewater using β-PbO2 and DSA® anodes," *Chemical Engineering Journal*, vol. 251, pp. 138-145, 2014.

[9] M. C. Newman, *Fundamentals of ecotoxicology*. CRC press, 2009.

[10] Y. Zhang, Z. Yang, R. Li, H. Geng, and C. J. C. Dong, "Investigation of fine chalk dust particles' chemical compositions and toxicities on alveolar macrophages in vitro," vol. 120, pp. 500-506, 2015.

[11] R. Kishor *et al.*, "Ecotoxicological and health concerns of persistent coloring pollutants of textile industry wastewater and treatment approaches for environmental safety," *Journal of Environmental Chemical Engineering*, vol. 9, no. 2, p. 105012, 2021.

[12] J. Zhang, Y. Zhang, Y. Lei, C. J. C. S. Pan, and Technology, "Photocatalytic and degradation mechanisms of anatase TiO_2: a HRTEM study," vol. 1, no. 2, pp. 273-278, 2011.

[13] P. Raizada *et al.*, "Fabrication of Ag3VO4 decorated phosphorus and sulphur co-doped graphitic carbon nitride as a high-dispersed assisted photocatalyst for phenol mineralization and E. coli disinfection," *Separation and purification technology*, vol. 212, pp. 887-900, 2019.

[14] P. Raizada, A. Sudhaik, P. Singh, P. Shandilya, P. Thakur, and H. Jung, "Visible light photodegradation of 2, 4-dinitrophenol using Ag_2CO_3 loaded phosphorus and sulphur co-doped graphitic carbon nitride nanosheets in simulated wastewater," *Arabian Journal of Chemistry*, vol. 13, no. 1, pp. 3196-3209, 2020.

[15] M. A. Mir *et al.*, "Studies on the synthesis and characterization of polyaniline-zeolite nanostructures and their role in carbon monoxide sensing," *Journal of environmental chemical engineering*, vol. 6, no. 1, pp. 1137-1146, 2018.
[16] H.-H. Chun, J. Y. Lee, and W.-K. Jo, "Photocatalysis of low-concentration gaseous organic pollutants over electrospun iron-doped titanium dioxide nanofibers," *Solid state sciences*, vol. 25, pp. 103-109, 2013.
[17] B. J. C. Ohtani, "Titania photocatalysis beyond recombination: A critical review," vol. 3, no. 4, pp. 942-953, 2013.
[18] S. Irfan, L. Li, A. S. Saleemi, and C.-W. J. J. o. M. C. A. Nan, "Enhanced photocatalytic activity of La 3+ and Se 4+ co-doped bismuth ferrite nanostructures," vol. 5, no. 22, pp. 11143-11151, 2017.
[19] K. J. J. o. W. R. Rita and Protection, "Adsorption of dye eosin from an aqueous solution on two different samples of activated carbon by static batch method," vol. 2012, 2012.
[20] M. A. M. Salleh, D. K. Mahmoud, W. A. W. A. Karim, and A. J. D. Idris, "Cationic and anionic dye adsorption by agricultural solid wastes: a comprehensive review," vol. 280, no. 1-3, pp. 1-13, 2011.
[21] Y. Bulut and H. J. D. Aydın, "A kinetics and thermodynamics study of methylene blue adsorption on wheat shells," vol. 194, no. 1-3, pp. 259-267, 2006.
[22] J. Zhang, Q. Zhou, L. J. J. o. C. Ou, and E. Data, "Kinetic, isotherm, and thermodynamic studies of the adsorption of methyl orange from aqueous solution by chitosan/alumina composite," vol. 57, no. 2, pp. 412-419, 2012.
[23] M. T. Yagub, T. K. Sen, H. J. W. Ang, Air,, and S. Pollution, "Equilibrium, kinetics, and thermodynamics of methylene blue adsorption by pine tree leaves," vol. 223, pp. 5267-5282, 2012.
[24] M. E. Argun, S. Dursun, M. Karatas, and M. J. B. t. Gürü, "Activation of pine cone using Fenton oxidation for Cd (II) and Pb (II) removal," vol. 99, no. 18, pp. 8691-8698, 2008.
[25] B. Nandi, A. Goswami, and M. J. A. C. S. Purkait, "Removal of cationic dyes from aqueous solutions by kaolin: kinetic and equilibrium studies," vol. 42, no. 3-4, pp. 583-590, 2009.
[26] S. Chowdhury, S. Chakraborty, P. J. C. Saha, and s. B. Biointerfaces, "Biosorption of Basic Green 4 from aqueous solution by Ananas comosus (pineapple) leaf powder," vol. 84, no. 2, pp. 520-527, 2011.
[27] S. Dawood and T. K. J. W. r. Sen, "Removal of anionic dye Congo red from aqueous solution by raw pine and acid-treated pine cone powder as adsorbent: equilibrium, thermodynamic, kinetics, mechanism and process design," vol. 46, no. 6, pp. 1933-1946, 2012.
[28] S. Bilgen, "Structure and environmental impact of global energy consumption," *Renewable and Sustainable Energy Reviews*, vol. 38, pp. 890-902, 2014.
[29] S. Sorrell, "Reducing energy demand: A review of issues, challenges and approaches," *Renewable and Sustainable Energy Reviews*, vol. 47, pp. 74-82, 2015.
[30] S. Zeng, Y. Liu, C. Liu, and X. Nan, "A review of renewable energy investment in the BRICS countries: History, models, problems and solutions," *Renewable and Sustainable Energy Reviews*, vol. 74, pp. 860-872, 2017.
[31] H. Wang *et al.*, "Three dimensional graphene based materials: Synthesis and applications from energy storage and conversion to electrochemical sensor and environmental remediation," *Advances in colloid and interface science*, vol. 221, pp. 41-59, 2015.

[32] X. Hu, C. Zou, C. Zhang, and Y. Li, "Technological developments in batteries: a survey of principal roles, types, and management needs," *IEEE Power and Energy Magazine*, vol. 15, no. 5, pp. 20-31, 2017.
[33] V. G. Gude, "Energy storage for desalination processes powered by renewable energy and waste heat sources," *Applied Energy*, vol. 137, pp. 877-898, 2015.
[34] B. Dunn, H. Kamath, and J.-M. Tarascon, "Electrical energy storage for the grid: a battery of choices," *Science*, vol. 334, no. 6058, pp. 928-935, 2011.
[35] R. E. Smalley, "Future global energy prosperity: the terawatt challenge," *Mrs Bulletin*, vol. 30, no. 6, pp. 412-417, 2005.
[36] M. Winter and R. J. J. C. r. Brodd, "What are batteries, fuel cells, and supercapacitors?," vol. 104, no. 10, pp. 4245-4270, 2004.
[37] F. J. P. Walsh and a. chemistry, "Electrochemical technology for environmental treatment and clean energy conversion," vol. 73, no. 12, pp. 1819-1837, 2001.
[38] G. Wang, L. Zhang, and J. Zhang, "A review of electrode materials for electrochemical supercapacitors," *Chemical Society Reviews*, vol. 41, no. 2, pp. 797-828, 2012.
[39] H. Du, X. Lin, Z. Xu, and D. J. J. o. M. S. Chu, "Electric double-layer transistors: a review of recent progress," vol. 50, pp. 5641-5673, 2015.
[40] R. Burt, G. Birkett, and X. J. P. C. C. P. Zhao, "A review of molecular modelling of electric double layer capacitors," vol. 16, no. 14, pp. 6519-6538, 2014.
[41] L. L. Zhang and X. Zhao, "Carbon-based materials as supercapacitor electrodes," *Chemical Society Reviews*, vol. 38, no. 9, pp. 2520-2531, 2009.
[42] S.-M. Chen, R. Ramachandran, V. Mani, and R. Saraswathi, "Recent advancements in electrode materials for the high-performance electrochemical supercapacitors: a review," *Int. J. Electrochem. Sci*, vol. 9, no. 8, pp. 4072-4085, 2014.
[43] Z. Bo, Z. Wen, H. Kim, G. Lu, K. Yu, and J. Chen, "One-step fabrication and capacitive behavior of electrochemical double layer capacitor electrodes using vertically-oriented graphene directly grown on metal," *Carbon*, vol. 50, no. 12, pp. 4379-4387, 2012.
[44] A. P. Singh, N. K. Tiwari, P. Karandikar, and A. Dubey, "Effect of electrode shape on the parameters of supercapacitor," in *2015 International Conference on Industrial Instrumentation and Control (ICIC)*, 2015, pp. 669-673: IEEE.
[45] Y. Jiang, J. J. E. Liu, and E. Materials, "Definitions of pseudocapacitive materials: a brief review," vol. 2, no. 1, pp. 30-37, 2019.
[46] P. J. J. o. E. S. Bhojane, "Recent advances and fundamentals of Pseudocapacitors: Materials, mechanism, and its understanding," vol. 45, p. 103654, 2022.
[47] V. Sudha and M. J. T. J. o. P. C. B. Sangaranarayanan, "Underpotential deposition of metals: structural and thermodynamic considerations," vol. 106, no. 10, pp. 2699-2707, 2002.
[48] H. Xia, Y. S. Meng, G. Yuan, C. Cui, L. J. E. Lu, and S.-S. Letters, "A symmetric RuO2/RuO2 supercapacitor operating at 1.6 V by using a neutral aqueous electrolyte," vol. 15, no. 4, p. A60, 2012.
[49] S. P. Gupta, B. A. Kakade, B. R. Sathe, Q. Qiao, D. J. Late, and P. S. J. A. A. E. M. Walke, "Thermally driven high-rate intercalated pseudocapacitance of flower-like architecture of ultrathin few layered δ-MnO2 nanosheets on carbon nano-onions," vol. 3, no. 11, pp. 11398-11409, 2020.
[50] V. Augustyn, P. Simon, B. J. E. Dunn, and E. Science, "Pseudocapacitive oxide materials for high-rate electrochemical energy storage," vol. 7, no. 5, pp. 1597-1614, 2014.

[51] A. C. Neto, F. Guinea, N. M. Peres, K. S. Novoselov, and A. K. Geim, "The electronic properties of graphene," *Reviews of modern physics,* vol. 81, no. 1, p. 109, 2009.
[52] R. K. Layek and A. K. Nandi, "A review on synthesis and properties of polymer functionalized graphene," *Polymer,* vol. 54, no. 19, pp. 5087-5103, 2013.
[53] K. Novoselov, A. Geim, S. Morozov, S. Dubonos, Y. Zhang, and D. Jiang, "Room-temperature electric field effect and carrier-type inversion in graphene films," *arXiv preprint cond-mat/0410631,* 2004.
[54] S. Basu and P. Bhattacharyya, "Recent developments on graphene and graphene oxide based solid state gas sensors," *Sensors and Actuators B: Chemical,* vol. 173, pp. 1-21, 2012.
[55] M. Acik and Y. J. Chabal, "Nature of graphene edges: a review," *Japanese Journal of Applied Physics,* vol. 50, no. 7R, p. 070101, 2011.
[56] G. Yang, L. Li, W. B. Lee, and M. C. Ng, "Structure of graphene and its disorders: a review," *Science and technology of advanced materials,* vol. 19, no. 1, pp. 613-648, 2018.
[57] S. Bharech and R. Kumar, "A review on the properties and applications of graphene," *J Mater Sci Mech Eng,* vol. 2, no. 10, p. 70, 2015.
[58] S. Morozov *et al.,* "Giant intrinsic carrier mobilities in graphene and its bilayer," *Physical review letters,* vol. 100, no. 1, p. 016602, 2008.
[59] C. Lee, X. Wei, J. W. Kysar, and J. Hone, "Measurement of the elastic properties and intrinsic strength of monolayer graphene," *science,* vol. 321, no. 5887, pp. 385-388, 2008.
[60] S. S. Shams, R. Zhang, and J. Zhu, "Graphene synthesis: a Review," *Mater. Sci. Pol,* vol. 33, no. 3, pp. 566-578, 2015.
[61] I. E. Abbott's, "Graphene: exploring carbon flatland," *Phys. Today,* vol. 60, no. 8, p. 35, 2007.
[62] K. S. Novoselov *et al.,* "Electric field effect in atomically thin carbon films," *science,* vol. 306, no. 5696, pp. 666-669, 2004.
[63] O. Shenderova, V. Zhirnov, and D. Brenner, "Carbon nanostructures," *Critical reviews in solid state and material sciences,* vol. 27, no. 3-4, pp. 227-356, 2002.
[64] J. Sakamoto, J. van Heijst, O. Lukin, and A. D. Schlüter, "Two-dimensional polymers: just a dream of synthetic chemists?," *Angewandte Chemie International Edition,* vol. 48, no. 6, pp. 1030-1069, 2009.
[65] J. C. Meyer *et al.,* "On the roughness of single-and bi-layer graphene membranes," *Solid State Communications,* vol. 143, no. 1-2, pp. 101-109, 2007.
[66] P. Blake *et al.,* "Making graphene visible," *Applied physics letters,* vol. 91, no. 6, p. 063124, 2007.
[67] J. Campos-Delgado *et al.,* "CVD synthesis of mono-and few-layer graphene using alcohols at low hydrogen concentration and atmospheric pressure," *Chemical Physics Letters,* vol. 584, pp. 142-146, 2013.
[68] B. H. Min, D. W. Kim, K. H. Kim, H. O. Choi, S. W. Jang, and H.-T. Jung, "Bulk scale growth of CVD graphene on Ni nanowire foams for a highly dense and elastic 3D conducting electrode," *Carbon,* vol. 80, pp. 446-452, 2014.
[69] D. A. Brownson and C. E. Banks, "The electrochemistry of CVD graphene: progress and prospects," *Physical Chemistry Chemical Physics,* vol. 14, no. 23, pp. 8264-8281, 2012.
[70] X. Lee, L. Lee, L. Foo, K. Tan, and D. Hassell, "Evaluation of carbon-based nanosorbents synthesised by ethylene decomposition on stainless steel substrates as potential sequestrating materials for nickel ions in aqueous solution," *Journal of Environmental Sciences,* vol. 24, no. 9, pp. 1559-1568, 2012.

[71] X. Chen, B. Wu, and Y. Liu, "Direct preparation of high quality graphene on dielectric substrates," *Chemical Society Reviews*, vol. 45, no. 8, pp. 2057-2074, 2016.
[72] B. Gupta, M. Notarianni, N. Mishra, M. Shafiei, F. Iacopi, and N. Motta, "Evolution of epitaxial graphene layers on 3C SiC/Si (1 1 1) as a function of annealing temperature in UHV," *Carbon*, vol. 68, pp. 563-572, 2014.
[73] S. Hussain *et al.*, "Physical and electrical properties of graphene grown under different hydrogen flow in low pressure chemical vapor deposition," vol. 9, pp. 1-9, 2014.
[74] W. S. Hummers Jr and R. E. J. J. o. t. a. c. s. Offeman, "Preparation of graphitic oxide," vol. 80, no. 6, pp. 1339-1339, 1958.
[75] N. Zaaba, K. Foo, U. Hashim, S. Tan, W.-W. Liu, and C. J. P. e. Voon, "Synthesis of graphene oxide using modified hummers method: solvent influence," vol. 184, pp. 469-477, 2017.
[76] D. C. Marcano *et al.*, "Improved synthesis of graphene oxide," vol. 4, no. 8, pp. 4806-4814, 2010.
[77] E. J. C. Amieva, J. López-Barroso, A. L. Martínez-Hernández, and C. J. R. a. i. g. r. Velasco-Santos, "Graphene-based materials functionalization with natural polymeric biomolecules," vol. 1, pp. 257-298, 2016.
[78] Q. Xiang, J. Yu, and M. J. C. S. R. Jaroniec, "Graphene-based semiconductor photocatalysts," vol. 41, no. 2, pp. 782-796, 2012.
[79] S. Vadivel *et al.*, "Synthesis of yttrium doped BiOF/RGO composite for visible light: Photocatalytic applications," *Materials Science for Energy Technologies*, vol. 2, no. 1, pp. 112-116, 2019.
[80] A. Khan, A. A. P. Khan, A. M. Asiri, and B. M. Abu-Zied, "Green synthesis of thermally stable Ag-rGO-CNT nano composite with high sensing activity," *Composites Part B: Engineering*, vol. 86, pp. 27-35, 2016.
[81] M.-Q. Yang, N. Zhang, M. Pagliaro, and Y.-J. Xu, "Artificial photosynthesis over graphene–semiconductor composites. Are we getting better?," *Chemical Society Reviews*, vol. 43, no. 24, pp. 8240-8254, 2014.
[82] A. Kubacka, M. Fernández-García, and G. Colón, "Photocatalysis on TiO_2 Surfaces: Principles, Mechanisms, and Selected Results," *Chem. Rev*, vol. 112, pp. 1555-1614, 2012.
[83] H. Zhang, X. Lv, Y. Li, Y. Wang, and J. J. A. n. Li, "P25-graphene composite as a high performance photocatalyst," vol. 4, no. 1, pp. 380-386, 2010.
[84] J. Altmann, A. S. Ruhl, F. Zietzschmann, and M. J. W. r. Jekel, "Direct comparison of ozonation and adsorption onto powdered activated carbon for micropollutant removal in advanced wastewater treatment," vol. 55, pp. 185-193, 2014.
[85] F. Liu, S. Chung, G. Oh, T. S. J. A. a. m. Seo, and interfaces, "Three-dimensional graphene oxide nanostructure for fast and efficient water-soluble dye removal," vol. 4, no. 2, pp. 922-927, 2012.
[86] P. Sharma, B. K. Saikia, M. R. J. C. Das, S. A. Physicochemical, and E. Aspects, "Removal of methyl green dye molecule from aqueous system using reduced graphene oxide as an efficient adsorbent: Kinetics, isotherm and thermodynamic parameters," vol. 457, pp. 125-133, 2014.
[87] G. Ramesha, A. V. Kumara, H. Muralidhara, S. J. J. o. c. Sampath, and i. science, "Graphene and graphene oxide as effective adsorbents toward anionic and cationic dyes," vol. 361, no. 1, pp. 270-277, 2011.

[88] Z. Geng *et al.*, "Highly efficient dye adsorption and removal: a functional hybrid of reduced graphene oxide–Fe 3 O 4 nanoparticles as an easily regenerative adsorbent," vol. 22, no. 8, pp. 3527-3535, 2012.
[89] M. S. Fuhrer, C. N. Lau, and A. H. MacDonald, "Graphene: materially better carbon," *MRS bulletin*, vol. 35, no. 4, pp. 289-295, 2010.
[90] R. Prasher, "Graphene spreads the heat," *Science*, vol. 328, no. 5975, pp. 185-186, 2010.
[91] B. E. Conway, *Electrochemical supercapacitors: scientific fundamentals and technological applications*. Springer Science & Business Media, 2013.
[92] Y.-H. Hwang, S. M. Lee, Y. J. Kim, Y. H. Kahng, and K. Lee, "A new approach of structural and chemical modification on graphene electrodes for high-performance supercapacitors," *Carbon*, vol. 100, pp. 7-15, 2016.
[93] A. Yu, I. Roes, A. Davies, and Z. Chen, "Ultrathin, transparent, and flexible graphene films for supercapacitor application," *Applied physics letters*, vol. 96, no. 25, p. 253105, 2010.
[94] M. F. El-Kady, V. Strong, S. Dubin, and R. B. Kaner, "Laser scribing of high-performance and flexible graphene-based electrochemical capacitors," *Science*, vol. 335, no. 6074, pp. 1326-1330, 2012.
[95] Y.-Z. Zhang, Y. Wang, T. Cheng, W.-Y. Lai, H. Pang, and W. Huang, "Flexible supercapacitors based on paper substrates: a new paradigm for low-cost energy storage," *Chemical Society Reviews*, vol. 44, no. 15, pp. 5181-5199, 2015.
[96] K. Chen, S. Song, F. Liu, and D. Xue, "Structural design of graphene for use in electrochemical energy storage devices," *Chemical Society Reviews*, vol. 44, no. 17, pp. 6230-6257, 2015.
[97] N. Jung *et al.*, "Synthesis of chemically bonded graphene/carbon nanotube composites and their application in large volumetric capacitance supercapacitors," *Advanced Materials*, vol. 25, no. 47, pp. 6854-6858, 2013.
[98] L. Sun *et al.*, "Nitrogen-doped graphene with high nitrogen level via a one-step hydrothermal reaction of graphene oxide with urea for superior capacitive energy storage," *Rsc Advances*, vol. 2, no. 10, pp. 4498-4506, 2012.
[99] M. Kurian and S. J. O. C. Thankachan, "Structural diversity and applications of spinel ferrite core-Shell nanostructures-A review," vol. 8, p. 100179, 2021.
[100] C. R. Vestal and Z. J. J. I. j. o. n. Zhang, "Magnetic spinel ferrite nanoparticles from microemulsions," vol. 1, no. 1-2, pp. 240-263, 2004.
[101] A. Baykal, E. Karaoglu, H. Sözeri, E. Uysal, M. S. J. J. o. s. Toprak, and n. magnetism, "Synthesis and characterization of high catalytic activity magnetic Fe_3O_4 supported Pd nanocatalyst," vol. 26, pp. 165-171, 2013.
[102] A. G. Abraham *et al.*, "Enhanced magneto-optical and photo-catalytic properties of transition metal cobalt (Co2+ ions) doped spinel MgFe2O4 ferrite nanocomposites," vol. 452, pp. 380-388, 2018.
[103] M. Ahmed, S. Ali, S. El-Dek, A. J. M. S. Galal, and E. B, "Magnetite–hematite nanoparticles prepared by green methods for heavy metal ions removal from water," vol. 178, no. 10, pp. 744-751, 2013.
[104] M. M. El-Moselhy, A. K. Sengupta, and R. J. J. o. h. m. Smith, "Carminic acid modified anion exchanger for the removal and preconcentration of Mo (VI) from wastewater," vol. 185, no. 1, pp. 442-446, 2011.
[105] G. R. Chaudhary *et al.*, "Adsorption studies of cationic, anionic and azo-dyes via monodispersed Fe3O4 nanoparticles," vol. 13, no. 5, pp. 3240-3245, 2013.

[106] S. Giri, N. Das, G. J. C. Pradhan, S. A. Physicochemical, and E. Aspects, "Synthesis and characterization of magnetite nanoparticles using waste iron ore tailings for adsorptive removal of dyes from aqueous solution," vol. 389, no. 1-3, pp. 43-49, 2011.
[107] K. K. Kefeni, B. B. Mamba, T. A. J. S. Msagati, and P. Technology, "Application of spinel ferrite nanoparticles in water and wastewater treatment: a review," vol. 188, pp. 399-422, 2017.
[108] T. Q. Dat, N. T. Ha, P. Van Thin, and N. V. J. I. T. o. M. Tung, "Synthesis of RGO/CF/PANI magnetic composites for effective adsorption of uranium," vol. 54, no. 6, pp. 1-6, 2018.
[109] W. Wang, K. Cai, X. Wu, X. Shao, X. J. J. o. A. Yang, and Compounds, "A novel poly (m-phenylenediamine)/reduced graphene oxide/nickel ferrite magnetic adsorbent with excellent removal ability of dyes and Cr (VI)," vol. 722, pp. 532-543, 2017.
[110] Z.-T. Hu, J. Liu, X. Yan, W.-D. Oh, and T.-T. J. C. E. J. Lim, "Low-temperature synthesis of graphene/Bi2Fe4O9 composite for synergistic adsorption-photocatalytic degradation of hydrophobic pollutant under solar irradiation," vol. 262, pp. 1022-1032, 2015.
[111] G. Mamba and A. Mishra, "Advances in magnetically separable photocatalysts: smart, recyclable materials for water pollution mitigation," *Catalysts,* vol. 6, no. 6, p. 79, 2016.
[112] B. F. Johnson, "Nanoparticles in catalysis," *Topics in Catalysis,* vol. 24, no. 1, pp. 147-159, 2003.
[113] J. Govan and Y. K. Gun'ko, "Recent advances in the application of magnetic nanoparticles as a support for homogeneous catalysts," *Nanomaterials,* vol. 4, no. 2, pp. 222-241, 2014.
[114] M. B. Gawande, Y. Monga, R. Zboril, and R. Sharma, "Silica-decorated magnetic nanocomposites for catalytic applications," *Coordination Chemistry Reviews,* vol. 288, pp. 118-143, 2015.
[115] R. Dom, R. Subasri, K. Radha, and P. H. J. S. S. C. Borse, "Synthesis of solar active nanocrystalline ferrite, MFe2O4 (M: Ca, Zn, Mg) photocatalyst by microwave irradiation," vol. 151, no. 6, pp. 470-473, 2011.
[116] J. Liang *et al.*, "Scalable green method to fabricate magnetically separable $NiFe_2O_4$-reduced graphene oxide nanocomposites with enhanced photocatalytic performance driven by visible light," vol. 57, no. 12, pp. 4311-4319, 2018.
[117] Y. Shi *et al.*, "Ternary graphene– $CoFe_2O_4$/CdS nanohybrids: preparation and application as recyclable photocatalysts," vol. 2, no. 2, pp. 535-544, 2014.
[118] R. Singh, J. Ladol, H. Khajuria, and H. N. J. A. C. S. Sheikh, "Nitrogen Doped Graphene Nickel Ferrite Magnetic Photocatalyst for the Visible Light Degradation of Methylene Blue," vol. 64, no. 1, 2017.
[119] Y. Yao *et al.*, "Magnetic core–shell $CuFe_2O_4$@ C3N4 hybrids for visible light photocatalysis of Orange II," vol. 297, pp. 224-233, 2015.
[120] V. Tsurkan, H.-A. K. Von Nidda, J. Deisenhofer, P. Lunkenheimer, and A. J. P. R. Loidl, "On the complexity of spinels: Magnetic, electronic, and polar ground states," vol. 926, pp. 1-86, 2021.
[121] V. G. Harris *et al.*, "Recent advances in processing and applications of microwave ferrites," vol. 321, no. 14, pp. 2035-2047, 2009.
[122] K. Bindu, K. Sridharan, K. Ajith, H. Lim, and H. J. E. A. Nagaraja, "Microwave assisted growth of stannous ferrite microcubes as electrodes for potentiometric nonenzymatic H2O2 sensor and supercapacitor applications," vol. 217, pp. 139-149, 2016.

[123] A. Shanmugavani, D. Kalpana, and R. K. J. M. R. B. Selvan, "Electrochemical properties of CoFe2O4 nanoparticles as negative and Co (OH) $_2$ and Co_2Fe (CN) $_6$ as positive electrodes for supercapacitors," vol. 71, pp. 133-141, 2015.

[124] M. Sethi, U. S. Shenoy, S. Muthu, and D. K. J. F. o. M. S. Bhat, "Facile solvothermal synthesis of $NiFe_2O_4$ nanoparticles for high-performance supercapacitor applications," vol. 14, pp. 120-132, 2020.

[125] R. Wang *et al.*, "Electrochemical properties of manganese ferrite-based supercapacitors in aqueous electrolyte: the effect of ionic radius," vol. 457, pp. 94-99, 2014.

[126] V. Kumbhar, A. Jagadale, N. Shinde, and C. J. A. S. S. Lokhande, "Chemical synthesis of spinel cobalt ferrite ($CoFe_2O_4$) nano-flakes for supercapacitor application," vol. 259, pp. 39-43, 2012.

[127] W. Cai, T. Lai, W. Dai, and J. J. J. o. P. S. Ye, "A facile approach to fabricate flexible all-solid-state supercapacitors based on $MnFe_2O_4$/graphene hybrids," vol. 255, pp. 170-178, 2014.

[128] C. Xia *et al.*, "Spotlighting the boosted energy storage capacity of $CoFe_2O_4$/Graphene nanoribbons: A promising positive electrode material for high-energy-density asymmetric supercapacitor," vol. 270, p. 126914, 2023.

[129] P. Xiong, H. Huang, and X. J. J. o. p. s. Wang, "Design and synthesis of ternary cobalt ferrite/graphene/polyaniline hierarchical nanocomposites for high-performance supercapacitors," vol. 245, pp. 937-946, 2014.

[130] P. He, K. Yang, W. Wang, F. Dong, L. Du, and Y. J. R. J. o. E. Deng, "Reduced graphene oxide- $CoFe_2O_4$ composites for supercapacitor electrode," vol. 49, pp. 359-364, 2013.

[131] H. Chang, H. J. E. Wu, and E. Science, "Graphene-based nanocomposites: preparation, functionalization, and energy and environmental applications," vol. 6, no. 12, pp. 3483-3507, 2013.

[132] J. Hu, L. Liu, and Z. J. R. a. Xiao, "Adsorptions of Cd (II) and methylene blue from aqueous solution by silica hybrid hollow spheres," vol. 5, no. 83, pp. 68092-68098, 2015.

[133] M. A. Lazar, S. Varghese, and S. S. J. C. Nair, "Photocatalytic water treatment by titanium dioxide: recent updates," vol. 2, no. 4, pp. 572-601, 2012.

[134] W. Yin, S. Hao, and H. J. R. a. Cao, "Solvothermal synthesis of magnetic $CoFe_2O_4$/rGO nanocomposites for highly efficient dye removal in wastewater," vol. 7, no. 7, pp. 4062-4069, 2017.

[135] A. S. Arico, P. Bruce, B. Scrosati, J.-M. Tarascon, and W. J. N. m. Van Schalkwijk, "Nanostructured materials for advanced energy conversion and storage devices," vol. 4, no. 5, pp. 366-377, 2005.

[136] M. F. El-Kady, V. Strong, S. Dubin, and R. B. J. S. Kaner, "Laser scribing of high-performance and flexible graphene-based electrochemical capacitors," vol. 335, no. 6074, pp. 1326-1330, 2012.

[137] L. Kong *et al.*, "Three-dimensional graphene network deposited with mesoporous nitrogen-doped carbon from non-solvent induced phase inversion for high-performance supercapacitors," vol. 558, pp. 21-31, 2020.

[138] R. Nasiri and N. J. J. o. C. P. Arsalani, "Synthesis and application of 3D graphene nanocomposite for the removal of cationic dyes from aqueous solutions: response surface methodology design," vol. 190, pp. 63-71, 2018.

[139] T. H. Tu, P. T. N. Cam, M. T. Phong, H. M. Nam, and N. H. J. M. L. Hieu, "Synthesis and application of graphene oxide aerogel as an adsorbent for removal of dyes from water," vol. 238, pp. 134-137, 2019.

[140] M. Azarang, A. Shuhaimi, R. Yousefi, and S. P. J. R. A. Jahromi, "One-pot sol–gel synthesis of reduced graphene oxide uniformly decorated zinc oxide nanoparticles in starch environment for highly efficient photodegradation of Methylene Blue," vol. 5, no. 28, pp. 21888-21896, 2015.

[141] M. Adel, M. A. Ahmed, A. A. J. J. o. P. Mohamed, and C. o. Solids, "Synthesis and characterization of magnetically separable and recyclable crumbled $MgFe_2O_4$/reduced graphene oxide nanoparticles for removal of methylene blue dye from aqueous solutions," vol. 149, p. 109760, 2021.

CHAPTER 2

EXPERIMENTAL AND CHARACTERIZATION TECHNIQUES

In this chapter a comprehensive information regarding the instrumentation that are utilized for the study of the present work is presented. To fulfill the research aim, experimental work was performed in the laboratory, followed by the characterization of the synthesized graphene oxide and spinel ferrite nanoparticles. A brief description of various techniques for the determination of crystal structure, morphology, chemical composition, magnetic properties, optical properties, and electrochemical properties etc. are presented. This includes instrumental techniques, their theories, operational procedures and methods of analysis that are used for the study of the present thesis work.

2.1 Synthesis of spinel ferrite nanoparticles

The creation of homogeneous nanoparticles is crucial because their dimensions heavily influence their electrical, optical, and magnetic properties [1]. Typically, the relative surface area of nanoparticles increases with their decreasing size. At the nanoscale, conductivity and electrical structure differ significantly from bulk size [2]. Spinel ferrites can be made using two general methods: traditional synthesis and green synthetic pathways. The two most common methods of synthesis are physical and chemical. Spinel ferrites can typically be made by utilizing Fe(III) and M(II) (M=Mn, Co, Cu, Ni, Zn) salts as precursors, and the ratio and constituents of these salts can be changed to control the structural composition. In particular, biological methods can be recognized as green synthetic pathways when taking the environmental friendliness of the synthesis process and the biocompatibility of the produced products into account.

2.1.1 Co-precipitation

A quick and inexpensive method for making spinel ferrites is co-precipitation. By combining two or more different types of cations in a solution, one can produce a precursor through metal precipitation. After precipitation and calcination, the desired material can be created. This approach shows promise for large-scale preparation by utilizing moderate conditions and the potential for direct synthesis in water [3]. Many variables, such as salt precursors, precipitation medium, reaction temperature, pH, the ionic strength of the media, hybrid rate, surfactant addition, as well as mechanical and heating processes, may alter the size and shape of the particles [3]. For instance, it was looked into how the structure and magnetic properties of co-precipitated $CoFe_2O_4$ nanoparticles were affected by different calcination temperatures (500° C and 800° C) [4]. The findings showed that the crystallite size and magnetic characteristics were significantly influenced by the reaction temperature and the calcination temperature. The size of the crystallite grew larger as the calcination temperature rose. This was due to the fact that the activation energy needed by the crystal nucleus decreased with increasing calcination temperature [5].

2.1.2 Solvo(hydro)thermal method

The solvothermal method (or hydrothermal if water is the solvent) employs the use of aqueous or non-aqueous solvents for a better control of particle size distribution and morphology. It is one of the most environmentally friendly and promising synthesis methods currently accessible [6]. The production of a homogeneous solution of the metal salts is the first step in this process, which is followed by the addition of a base until a basic pH is obtained. The resulting mixture is then put into an Teflon lined stainless-steel autoclave **(Fig. 2.1)** and heated for a long time, between 140-220 °C [7]. Depending on the nature of the nanoparticles, the heating temperature and duration of heating are fixed. The solid products are collected, thoroughly cleaned multiple times in separate batches of distilled water and ethanol, and then dried. The dried powders are thereafter sintered once again [8]. The mechanism entails the initial creation of metal hydroxides, which are oxidized and transformed into the crystalline spinel ferrite as a result of the thermal treatment under high pressures. High crystallinity and a suitable narrow size distribution characterize the nanoparticles that are produced. By modifying the reaction temperature, duration, solvent, surfactant, and precursor types, it is possible to optimize the nanoparticles' size and shape [9].

Fig. 2.1. Teflon chamber and stainless-steel chamber where all the synthesis were carried out.

2.2 Characterization techniques

This section provides a brief description of the instrumental techniques used to characterize our synthesized samples. This includes experimental techniques, theories, operational procedures, and methods of analysis that are used for the study of the present thesis work. The structural, morphological and chemical composition of the sample were investigated by X-ray Diffraction (XRD), Field emission Scanning Electron Microscopy (FE-SEM), High-resolution Transmission Electron Microscopy (HR-TEM), Selected Area Electron Diffraction (SAED), Fourier Transformed Infra-Red (FTIR) spectroscopy, and Raman spectroscopy. The magnetic characterizations were investigated employing Vibrating Sample Magnetometer (VSM) and superconducting Quantum Interference Device (SQUID). The optical properties were studied by Ultraviolet-visible (UV-Vis) absorption spectroscopy and Fluorescence spectroscopy. The electrochemical properties of prepared samples were investigated by electrochemical station with conventional three electrode system.

2.2.1. X-ray Diffraction (XRD)

A sample's unknown crystal structure can be determined via X-ray diffraction (XRD). There is a one-to-one relationship between the positions and intensities of the peaks indicated in the XRD pattern and those indexed peaks in the candidate diffraction pattern. As a result, the XRD findings are regarded as the "fingerprint" of crystals in materials. The crystal structures of GO, rGO, $MnFe_2O_4$, $MnFe_2O_4$/rGO, $CoFe_2O$, and N-RGO were characterized in this work using XRD.

The cathode ray tube creates X-rays when a focused electron beam bombards a solid target that is either stationary or rotating while being driven across a high voltage field. The beams are then focused and collimated to produce monochromatic radiation before being directed at the substance [10].

Then, these diffracted X-rays are found, examined, and tallied. Due to the powdered sample's unpredictable orientation, the samples are scanned at a range of 2θ angles to obtain all potential lattice diffraction directions. The conversion of diffraction peaks to *d*-spacings follows. Due to the fact that each element in the sample has a specific set of *d*-spacings, the *d*-spacings enable the identification of the elements within the sample. There are three indices (*h*, *k*, and *l*) for each

crystallographic plane. The JCPDS database can then be used to index each plane with a unique set of *h*, *k*, and *l*.

There are two fundamental configurations for powder diffractometers: *θ-θ*, in which the detector and X-ray tube move simultaneously, and *θ-2θ*, in which the X-ray tube is fixed and the specimen travels half as fast as the detector to preserve the *θ-2θ* geometry. The system for our Bruker D8 Advanced Diffractometer is a *θ-2θ* system. A detector is used to electronically record the diffraction angles and intensities, and specialized software is used to visualize the sample's *2θ* (horizontal axis) vs. intensity (vertical axis) data [11].

Using the Debye-Scherrer formula, the sample's crystallite size (*D*) can be calculated as:

$$D = (0.9\,\lambda)/(\beta\cos\theta)$$

Where, D = Crystallite size,

λ = wavelength of light

β = Full-width half maximum (FWHM) of the peak in radians

θ = Bragg angle.

Our samples' PXRD patterns were generated using Cu K_α radiation (λ = 1.54184 Å at 35 kV, 35 mA) on a Bruker D8 Advanced Diffractometer. The diffraction patterns were recorded by using a scanning rate of 0.02° s^{-1} in the *2θ* range from 20° to 80°.

2.2.2. Field Emission Scanning Electron Microscopy (FE-SEM)

A scanning electron microscope (SEM) is a type of electron microscope that provides topography of a material by scanning its surface with a concentrated stream of electrons [12-14]. An electron column, a scanning system, a vacuum system, electrical controls, a detector or detectors, and a display are the main parts of a conventional SEM. The SEM's electron column is made up of an electron gun and two or more vacuum-operated electromagnetic lenses. In SEM, an electron gun with a tungsten filament cathode with an energy range of (0.2 keV to 40 keV) thermionically discharges an electron beam. The electron beam is then pin-pointed into a tiny probe and scanned across the sample's surface using scanning coils. The voltage range used by SEM is between 2 and 50 kV, and the beam diameter used to scan the sample is between 5-2 nm. Electromagnetic radiation is produced as a result of the interaction between the electron beam and electrons close to the specimen's surface. Secondary electron emission (SE) is caused by inelastic scattering, while

backscattered electron emission (BSE) is caused by elastic scattering and electromagnetic radiation is produced by the electronic transition from an excited atom.

The SE or BSE among them are detected by a detector, amplified, and shown on a computer screen. The image of the sample is captured as a 2D intensity distribution, and it is discovered that the density of SE corresponds exactly to this distribution. In our case, lyophilized samples were placed on carbon tape over a stub, vacuum-dried, and gold coated before being examined using FESEM (FEI, INSPECT F50).

2.2.3. High-Resolution Transmission Electron Microscopy (HR-TEM)

In comparison to SEM, TEM can image with a much better resolution. The HR-TEM is a flexible technique for the characterization of the nanostructured particles since it even enables the production of pictures below 0.5 Å and allows the exploration of shape, composition, and crystallographic information [15, 16]. In TEM, the electrons are emitted by a source and accelerated by an anode in the range of 40-400 keV with respect to the cathode. A condenser lens helps to focus this stream of electrons into a narrow, coherent beam. After that, the condenser aperture allows the electron beam, which is restricted by the two condenser lenses, to pass through and hit the specimen's surface. The electron beams that are transmitted and elastically dispersed travel via the objective lens. A portion of the specimen is transmitted when the beam strikes it. The objective lens concentrates the transmitted portion to create an image. The elastically dispersed electrons that will create the microscope's image are chosen using the objective lens and the area aperture. The three lenses that made up the magnifying system are finally reached by the beam. The resulting image is displayed on a monitor, a fluorescent screen, or both. When an image hits a phosphor image screen, light is produced that the user can see. because there will be fewer transmitted unscattered electrons in the thicker parts of the specimen, it will seem darker.

The specimen with smaller regions will, however, have more transmitted electrons and will therefore seem brighter. Bright-field imaging mode is the mode of operation used to obtain contrast in an image. For TEM operation, extremely high vacuum and high voltage are needed. In a TEM, several picture kinds are acquired by choosing the appropriate apertures and various electron types. Diffraction patterns are produced as a result of the dispersed electrons. However, the choice of the unscattered beam allows for the creation of bright field photographs. If the objective aperture picks

up diffracted beams, dark field images can be captured. Magnetic lenses can be used to gather the scattered electrons, forming a pattern of spots or rings as a result. The term "selected area diffraction" (SAED) pattern is used to describe each spot or ring that corresponds to a specific atomic spacing in this case. This SAED pattern offers a special ability to show the crystal structure of the individual as well as several components of the nanomaterials or nanocomposites. In our case, the sample was made by drop-casting on a copper grid coated in lacey carbon from a solution of the sample dispersed in a nonpolar solvent typically chloroform, and then drying it. A JEOL JEM 2012 electron microscope was used to observe the grid after that. It was operated at 200 kV accelerating voltage.

2.2.4. Fourier Transform Infrared Spectroscopy

A characterization technique called infrared (IR) spectroscopy can be used to determine the IR frequencies that correlate to the stretching, bending, and vibrational motion of atoms in a molecule [17]. A fingerprint is often used to describe an infrared spectrum because it shows important details about the atoms' vibrational bonds using the sample's absorption peaks. Because no two compounds have an identical infrared spectrum, every material has a unique atom arrangement. The He-Ne gas laser, an infrared source, emits a wide spectrum of infrared radiation with various wavelengths. An interferometer modifies the infrared light as it passes through it. The incoming IR radiation is then subjected to an optical inverse Fourier transform via the interferometer. The modulated IR beam passes through the sample and is partially transmitted (passing through) after being absorbed to varying degrees at various wavelengths by the various types of molecules present in the sample.

In order to get the sample's IR spectrum, a detector measures the intensity of the IR beam. The detected signal is then digitalized and Fourier transformed by a computer on a Perkin Elmer FTIR spectrum RXI spectrometer. IR spectrum in the range of 4000-400 cm^{-1} were recorded for this thesis work at room temperature. Powdered samples were combined with KBr powder for all measurements before being pelletized for the test. Using a KBr pellet reference blank, the background correction was made.

2.2.5. Raman Spectroscopy

A useful spectroscopic method for identifying rotational, vibrational, and other low-frequency modes in a chemical system is Raman spectroscopy. This particular sort of spectroscopy is linked to molecular vibrations that correspond to an overall change in electrical polarizability (α). Raman spectroscopy is frequently employed as a fingerprint to identify compounds because it provides important information about the symmetry and chemical interactions in the system [18, 19]. As some modes of vibration are not visible in IR spectra but can be recognized with Raman spectra, hence Raman spectra are frequently analyzed alongside IR spectra in studies. When photons and molecules interact via Raman scattering, energy is transferred between them. This is a sort of inelastic scattering. Raman spectroscopy involves exposing the sample to monochromatic light and detecting the scattered light. Rayleigh scattering or elastic scattering is the name of this method. Because of interactions between the incident photon and the vibrational energy levels of the molecules of a material, a tiny portion of the incident light is scattered at optical frequencies that are distinct from the frequency excitation source in this case.

When light interacts with an excited molecule's electron cloud, it moves the molecule from its ground state to a virtual energy state. After that, a photon is released before returning to the original rotational or vibrational state. The energy difference between the original state and this new state causes a change in the frequency of the photons that are released as a result. The emitted photon will be shifted to the lower energy level if the molecule's final vibrational state has higher energy than its beginning state; this change in frequency is known as the Stokes shift. The emitted photon is moved to a higher frequency level and called an Anti-Stokes shift if the final vibrational energy is lower than that of their initial state. When a molecule's electric dipole interacts with the electric field of incident light, the Raman Effect occurs. Here, a laser source illuminates a sample, while a lens collects electromagnetic radiation from the illuminated spot. After that, a monochromator is used to pass the electromagnetic radiation. The laser line's associated elastically scattered radiation (Rayleigh scattering) is removed using a filter, and the remaining light is spread onto a detector using various filters. The spectrometer's optics focus the scattered light, which a charge-coupled device (CCD) uses to detect it. A commercial Raman Spectrometer (HORIBA, Lab RAM, HR800) apparatus with a diode laser as a photon source and a 532 nm wavelength was used in our work to record Raman spectra.

2.2.6. Ultraviolet-Visible (UV-Vis) Spectroscopy

Ultraviolet-visible (UV-vis) spectroscopy is frequently used to determine how optical radiation interacts with a sample and absorbs as a function of wavelength [20, 21]. It is frequently employed to describe the type of electronic excitation that occurs in a variety of organic, inorganic, or biological materials. In particular, it is helpful to determine the band-gap property from the absorption spectra of these materials. The electrical distribution of the materials as well as the surroundings they are in generally affect how much light they absorb.

The components of a fundamental spectrophotometer are a light source (a deuterium arc lamp for the UV region and a tungsten filament for the visible region), a sample holder, a diffraction grating in a monochromator to separate the various light wavelengths, and a detector-typically a photomultiplier tube. In a typical apparatus, a monochromator such a prism or diffraction grating is used to separate a beam of light from a visible and/or ultraviolet light source into its many component wavelengths.

The spectrophotometer has a half mirror device that divides each monochromatic beam of light into two beams of equal intensity. A light beam travels through the sample, which is often contained in a quartz cuvette or maybe a solid substrate retained in the spectrophotometer's sample chamber. While the other beam, which is used as the reference, travels through the exact same container as the first one, passing solely through the solvent to cancel out background noise. Then, using silicon photodiode or photomultiplier tube-based electronic detectors and the accompanying software, the intensities of these light beams are measured. The chemical composition and particle size have a significant impact on the absorption peaks width in the spectrum of nanoparticles. Here, a Shimadzu, UV-1800 spectrophotometer was used to characterize our samples **(Fig. 2.2).**

Fig. 2.2: The Shimadzu, UV-1800 spectrophotometer

2.2.7. Vibrating Sample Magnetometer

The vibrating sample magnetometer (VSM) is an adaptive instrument that detects a material's magnetic moment when it is vibrated perpendicular to a homogeneous magnetizing field. A physical property measurement system (PPMS) VSM was used to study magnetic properties of ferrite-based materials. The basic idea of this measurement is based on Faraday's law of induction.

An electromotive force is created in the loop when the number of magnetic field lines passing through it changes. The magnetic moment is determined by VSM by subjecting the sample to sinusoidal motion and inducing the associated voltage near stationary pickup coils. Its intensity is proportional to the sample's magnetic moment, vibration amplitude, and frequency (ν). The simplest PPMS setup consists of a liquid He dewar into which the PPMS probe is put. The probe is equipped with an electromagnet, a sample chamber, and a temperature controller (1.8 K to 400 K) in this configuration. A superconducting solenoid made of niobium-titanium alloy embedded in copper serves as the magnet. Because it is on the probe's exterior, it is always submerged in liquid helium. A closed superconducting circuit is formed by the magnet coil. The sample chamber includes a universal 12-pin platform, and each experimental option has its own insert. The PPMS

sample chamber requires the regular VSM detection (pick up) coil to be inserted. To oscillate the sample in the PPMS-VSM option, a linear motor is installed on top of the sample chamber. The oscillation has a frequency of 40 Hz and an amplitude of 2 mm (which can vary between 0.5 and 5 mm). This setup measures the DC magnetization of the sample very quickly and with high sensitivity down to 10^{-6} emu. The magnetic measurements were carried out by vibrating sample magnetometer (Lake Shore Cryotonics, USA).

2.2.8. Superconducting Quantum Interference Device (SQUID)

One of the best and most accurate methods for analyzing a specimen's magnetic characteristics is SQUID magnetometry. It is the sole method that enables direct measurement of a sample's magnetic moment in absolute units. Two core ideas of superconductivity serve as the foundation for the SQUID's operation [22-24]. One is the quantization of magnetic flux in a superconducting ring, while the other is the Josephson effect. Cooper pairs, which are superconducting electron pairs, can tunnel through an extremely thin layer of insulator and into another superconductor. The propagation of electron waves can be used to understand the Josephson effect. The electron wave in one superconductor can cross over with the electron wave in the other superconductor if the insulating layer separating the two superconductors is thin enough. The cooper pairs subsequently tunnel through the insulating junction. Let us consider a SQUID made up of two identical Josephson junctions. The whole supercurrent is split into I_a and I_b, which tunnel through junctions a and b. Hence

$$I = I_a + I_b$$

When a magnetic field is provided, a magnetic flux flows through the superconducting loop, causing a persistent current J to be generated. Induced current contributes to I_a while subtracting from I_b. When current waves pass through the junctions, their phases shift by δ_a and δ_b. That is

$$I_a = I_0 \, Sin \, \delta_a$$

$$I_b = I_0 \, Sin \, \delta_b$$

Where I_0 denotes the maximum permissible current via the junction. Magnetic flux is quantized as it passes through a superconducting loop. As a result, after traveling through the junctions, there is interference between I_a and I_b. When a magnetic moment is maintained in a loop containing a Josephson junction, an emf is induced in the loop, causing a current to be induced at a frequency

determined by the Josephson equations. To calculate the magnetic moment of a sample, the SQUID monitors changes in currents or frequency. For our measurement, we employed a Quantum Design made magnetic property measurement system (MPMS) XL-7 SQUID magnetometer.

2.2.9. Electrochemical characterizations

Different electrochemical characterizations are used to evaluate an electrode material's electrochemical charge storage performance. Among them, Cyclic Voltammetry (CV), Galvanostatic Charge Discharge (GCD), and Electrochemical Impedance Spectroscopy (EIS) are principal. These three characterizations can be carried out in both three-electrode and two-electrode modes. The 3-electrode mode is used to assess the efficiency of electrochemical charge storage. The 2-electrode mode, on the other hand, is used to characterize the performance of a two-electrode supercapacitor device. An electrochemical workstation equipped with hardware to precisely control and measure potential and current can be used to perform both 3-electrode and 2-electrode characterizations. Furthermore, in order to perform EIS, the workstation must be equipped with hardware capable of controlling the frequency of an AC signal across a large range (0.01 Hz to 105 Hz).

As the name implies, there are three electrodes in 3-electrode mode. The working electrode (WE) is the electrode to which the voltage is supplied with respect to the reference electrode (RE) and the current is measured with respect to the the counter electrode (CE). The WE is formed of inert material that does not participate in the electrochemical reaction, such as gold, platinum, or glassy carbon. The material (active material) whose electrochemical performance must be assessed is coated on the surface of WE. In these circumstances, the WE's covered surface acts as an active area for the electrochemical reaction.

The WE in the majority of our tests has been represented by glassy carbon rods. The circular flat end of the rod is polished with fine emery paper and repeatedly rinsed before being coated with the active substance. The rods are then vacuum-dried after that. The round flat end of the dried rods is kept open by wrapping them with Teflon tape. The sidewall of the rod is encapsulated by teflon tape. The active substance is then dropped onto the flat circular end. This is accomplished by mixing 85 weight percent active substance, 10 weight percent carbon black, and 5 weight percent polyvinylidene fluoride (PVDF) in a solvent called N-Methyl-2-pyrrolidone (NMP). Drop

casting involves using this slurry. Here, PVDF is utilised as a binder while carbon black is utilized as a conductive addition [25]. The coated slurry is dried on the rods after drop-casting by keeping them in a vacuum at 65 ºC for three hours. On the flat end of the rod, the active material forms a thin coating as a result. After and before deposition, the rods were weighed. The mass of the deposition material can be calculated from the difference in masses. The counter electrode (CE) is an inert conductor that is often constructed of platinum. Between CE and WE, a current is present. **Fig. 2.3a** depicts the platinum counter electrode we utilised in our investigation, which was 1 cm by 1 cm in size. The third and final electrode used for measuring the potential of the WE is the reference electrode (RE).

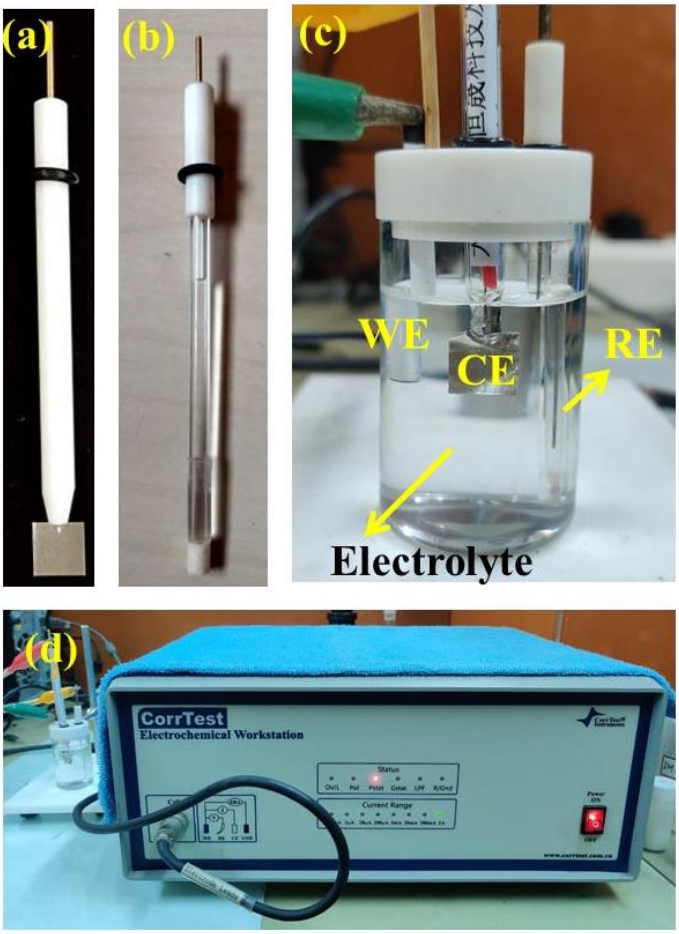

Fig. 2.3 Photo of the (a) CE (b) RE (c) electrochemical cell and (d) Corrtest CSC-313 electrochemical work station.

During the electrochemical process, RE should be able to maintain a steady voltage and chemically stable. Saturated Calomel Electrode (SCE), Standard Hydrogen Electrode (SHE), and other REs

are examples of different REs. All of the electrochemical measurements were performed using Ag/AgCl electrodes in saturated KCl (**Fig. 2.3b**). With regard to SHE, it keeps a steady potential of 0.197 V.

Equation states that a redox reaction in the RE produces high stability in the potential value.

$$AgCl(s) + e^- \leftrightarrow Ag(s) + Cl^-$$

As seen in **Fig. 2.3c** [26], these three electrodes are each connected to the appropriate terminals of the electrochemical workstation before being kept submerged in an electrolyte solution to conduct the tests. For all electrochemical measurements, we employed the Corrtest CS313 electrochemical workstation. **Fig. 2.3d** displays a photograph of the workstation. The WE is linked to the device's positive terminal while the CE and RE are connected to the negative terminal to complete the 2-electrode measurement.

References

[1] A. Baykal, E. Karaoglu, H. Sözeri, E. Uysal, M. S. J. J. o. s. Toprak, and n. magnetism, "Synthesis and characterization of high catalytic activity magnetic Fe 3 O 4 supported Pd nanocatalyst," vol. 26, pp. 165-171, 2013.

[2] A. G. Abraham *et al.*, "Enhanced magneto-optical and photo-catalytic properties of transition metal cobalt (Co2+ ions) doped spinel MgFe2O4 ferrite nanocomposites," vol. 452, pp. 380-388, 2018.

[3] Y.-j. Sun, Y.-f. Diao, H.-g. Wang, G. Chen, M. Zhang, and M. J. C. I. Guo, "Synthesis, structure and magnetic properties of spinel ferrite (Ni, Cu, Co) Fe2O4 from low nickel matte," vol. 43, no. 18, pp. 16474-16481, 2017.

[4] T. Prabhakaran, R. Mangalaraja, J. C. Denardin, J. A. J. J. o. A. Jiménez, and Compounds, "The effect of calcination temperature on the structural and magnetic properties of co-precipitated CoFe2O4 nanoparticles," vol. 716, pp. 171-183, 2017.

[5] T. Prabhakaran and J. J. C. I. Hemalatha, "Chemical control on the size and properties of nano NiFe2O4 synthesized by sol–gel autocombustion method," vol. 40, no. 2, pp. 3315-3324, 2014.

[6] T. Tatarchuk, M. Bououdina, J. Judith Vijaya, and L. John Kennedy, "Spinel ferrite nanoparticles: synthesis, crystal structure, properties, and perspective applications," in *Nanophysics, Nanomaterials, Interface Studies, and Applications: Selected Proceedings of the 4th International Conference Nanotechnology and Nanomaterials (NANO2016), August 24-27, 2016, Lviv, Ukraine*, 2017, pp. 305-325: Springer.

[7] X. Zhang, Z. Chen, C. Wu, J. Zhang, and F. J. C. P. L. Wang, "Solvothermal synthesis of spinel ZnFe2O4 nanoparticles with enhanced infrared radiation property," vol. 732, p. 136647, 2019.

[8] M. P. Reddy, A. J. M. Mohamed, and M. Materials, "One-pot solvothermal synthesis and performance of mesoporous magnetic ferrite MFe2O4 nanospheres," vol. 215, pp. 37-45, 2015.
[9] O. F. Odio, E. J. M. s.-s. Reguera, properties, and applications, "Nanostructured spinel ferrites: Synthesis, functionalization, nanomagnetism and environmental applications," pp. 185-216, 2017.
[10] C. Kittel, *Introduction to solid state physics*. John Wiley & sons, inc, 2005.
[11] B. Cullity and S. J. P. H. Stock, "Elements of X-ray diffraction third edition prentice hall upper saddle river," 2001.
[12] M. J. A. t. o. f. Kannan and a. o. nanotechnology, "Scanning electron microscopy: Principle, components and applications," pp. 81-92, 2018.
[13] T. Groves, H. Pfeiffer, T. Newman, F. J. J. o. V. S. Hohn, T. B. M. Processing, and Phenomena, "EL3 system for quarter-micron electron beam lithography," vol. 6, no. 6, pp. 2028-2032, 1988.
[14] C. A. Evans, *Encyclopedia of materials characterization: Surfaces, interfaces, thin films*. Butterworth-Heinemann, 1992.
[15] D. B. W. C. B. Carter, *Transmission Electron Microscopy A Textbook for Materials Science*. springer publication, 2009.
[16] D. B. Williams, C. B. Carter, D. B. Williams, and C. B. Carter, *The transmission electron microscope*. Springer, 1996.
[17] A. A. Ismail, F. R. van de Voort, and J. Sedman, "Fourier transform infrared spectroscopy: principles and applications," in *Techniques and instrumentation in analytical chemistry*, vol. 18: Elsevier, 1997, pp. 93-139.
[18] J. R. Ferraro, *Introductory raman spectroscopy*. Elsevier, 2003.
[19] J. J. S. N. Javier, "An Introduction to Raman Spectroscopy: introduction and basic principles," vol. 1, 2014.
[20] H.-H. Perkampus, *UV-VIS Spectroscopy and its Applications*. Springer Science & Business Media, 2013.
[21] H. J. C. I.-.-. Förster, "UV/vis spectroscopy," pp. 337-426, 2004.
[22] J. J. P. o. t. I. Clarke, "Principles and applications of SQUIDs," vol. 77, no. 8, pp. 1208-1223, 1989.
[23] J. J. s. d. Clarke, "SQUIDs: Principles, noise, and applications," pp. 51-99, 1990.
[24] D. Drung, M. J. T. S. H. F. Mück, T. o. SQUIDs, and S. Systems, "SQUID electronics," vol. 1, pp. 127-170, 2004.
[25] M. Arunkumar and A. J. A. o. Paul, "Importance of electrode preparation methodologies in supercapacitor applications," vol. 2, no. 11, p. 8039, 2017.
[26] N. Elgrishi, K. J. Rountree, B. D. McCarthy, E. S. Rountree, T. T. Eisenhart, and J. L. J. J. o. c. e. Dempsey, "A practical beginner's guide to cyclic voltammetry," vol. 95, no. 2, pp. 197-206, 2018.

CHAPTER 3

$MnFe_2O_4$ DECORATED REDUCED GRAPHENE OXIDE HETEROSTRUCTURES: NANOPHOTOCATALYST FOR METHYLENE BLUE DYE DEGRADATION

In this chapter, the photocatalytic degradation of methylene blue dye (MB) has been investigated using bare manganese ferrite ($MnFe_2O_4$) nanoparticles and $MnFe_2O_4$ nanoparticles-decorated reduced graphene oxide heterostructures ($MnFe_2O_4$/rGO) under ultra-violet irradiation. MB degraded by 84% in the presence of $MnFe_2O_4$ after UV irradiation of 290 minutes, while 97% of it degraded in merely 60 minutes in the case of $MnFe_2O_4$/rGO heterostructures. This is further confirmed by the well-fitted Langmuir-Hinshelwood Kinetics equation. A possible mechanism of enhanced photocatalytic activity is also proposed.

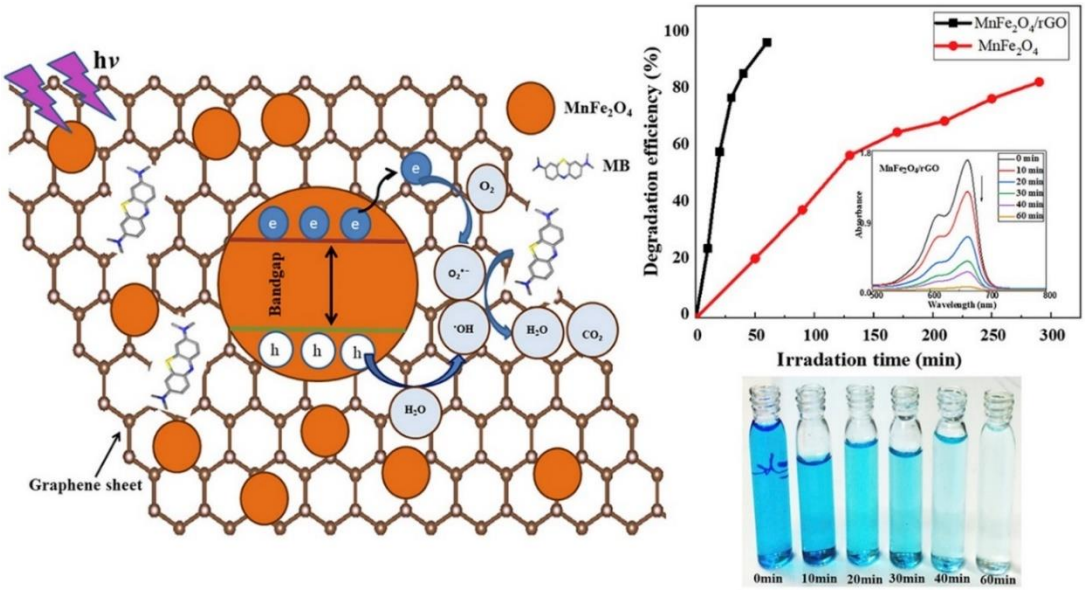

Work published in ***Vacuum*****, *173 (2020), p.109150*.** *https://doi.org/10.1016/j.vacuum.2019.109150*

3.1. Introduction

One of the major environmental concerns in pollution control is the removal of hazardous materials from water resources. The pollution of water resources by industrial effluents containing toxic dyes like, Congo red, Methyl orange, Methyele Blue etc. have been a serious problem to the human health and environment. Most of the dyes are harmful due to the high toxicity and carcinogenicity from their non-biodegradable aromatic structure [1]. Therefore, to control the pollution of water, elimination of these dyes from water is of utmost importance. Several methods and technologies have been developed to remove such organic dyes which include membrane treatment [2], adsorption [3], electrochemical [4], biological method [5], ion-exchange method [6], photocatalysis [7], etc. Among all these methods, photocatalysis has gained a huge interest in last few decades due to its low cost and simple execution [8]. Photocatalytic water treatment is a well-known advanced oxidation process in which the photocatalyst material with the production of electron-hole pair upon the irradiation with light, mineralize complex organic compound to mainly CO_2, H_2O, and other non-harmful inorganic materials [9].

Nowadays, spinel ferrite magnetic nanoparticles (with formula MFe_2O_4: M =Zn, Co, Mn, Ni, etc.) have emerged as potential candidates for various applications such as energy storage, pollution control, drug delivery etc. [10-12], due to their excellent catalytic and magnetic properties and ease of fabrication [13-14]. Several different types of magnetic ferrites such as copper ferrite ($CuFe_2O_4$) [15], cobalt ferrite ($CoFe_2O_4$) [16] and manganese ferrite ($MnFe_2O_4$) [17] have been reported to exhibit excellent catalytic and photocatalytic activity. The spinel ferrites have a relatively narrow band gap (~2.0 eV) which makes them suitable photocatalyst candidates for degradation processes [18]. In addition, they can be easily separated from the polluted aqueous solution or reaction system with the application of an external magnetic field which has the added advantage of its repetitive use which is of great interest in wastewater management.

Among all spinel ferrites, $MnFe_2O_4$ has attracted huge attention for application in pollution control because of its low cost, nontoxicity, and high chemical stability [19]. In the case of photocatalytic degradation, $MnFe_2O_4$ faces a major drawback as it agglomerates during synthesis due to the magnetic interaction which can result in a decrease of the active surface area and hence the degradation efficiency [20]. To address this problem, surface alteration of these nanomaterials with planar sheet-like structures such as graphene which hinders their agglomeration, has become a

popular method for achieving better photocatalytic performance [21]. In the field of material science, sp^2 hybridized two-dimensional carbon material: Graphene has opened up much promising application because of its high specific surface area, excellent conductivity, high chemical, and thermal stability and structural flexibility [22-23]. Also, the rapid recombination rate of photogenerated carriers in photocatalyst material is one of the main reasons for poor photocatalytic performance [24]. But it is possible to reduce this rate of recombination in $MnFe_2O_4$ by coupling it with metal like graphene as it has the excellent ability as an electron acceptor. Many reports have shown that Graphene has been extensively used as a support material for catalysts for achieving improved efficiency [23,25].

In this present study, we address the synthesis of $MnFe_2O_4$ nanoparticle and its composite heterostructure with reduced graphene oxide (rGO) for the efficient removal of cationic pollutant dye Methylene blue (MB) from the aqueous medium. $MnFe_2O_4$ was synthesized by simple co-precipitation method and GO was synthesized by Hummer's method which was further reduced by hydrazine hydrate. The results showed that rGO plays an important role to enhance the photocatalytic activity of $MnFe_2O_4$ by suppressing the agglomeration of nanoparticles and electron-hole recombination. Photodegradation efficiency of the experimentally synthesized materials was evaluated by pseudo-first-order kinetics, which showed impressively higher reaction rate of the composite heterostructure than that of bare $MnFe_2O_4$ nanoparticles. The possible mechanism of improved catalytic efficiency due to the incorporation of rGO is also explored.

3.2. Experimental

3.2.1. Materials

Chemicals used for this experiment are Natural Graphite flakes, Sodium Nitrate ($NaNO_3$), Manganese chloride tetrahydrate ($MnCl_2.4H_2O$, ≥99%), ferric chloride hexahydrate ($FeCl_3.6H_2O$, ≥99%), sodium hydroxide (NaOH), potassium permanganate ($KMnO_4$, 99.9%), hydrogen peroxide (H_2O_2, 30%), sulfuric acid (H_2SO_4, 98%), hydrochloric acid (HCl, 37%), and nitric acid (HNO_3,63%). Methylene blue (MB, $C_{16}H_{18}ClN_3S.3H_2O$) was used as model dye substance for photocatalytic degradation. All the chemicals were purchased from Sigma-Aldrich, India.

Throughout the experiment, every material was used without any further purification. Deionized water was used throughout the study.

3.2.2. Synthesis of Graphene oxide (GO)

Graphene oxide (GO) was synthesized by the Hummer's method with slight modification [26]. In brief 2g of Graphite powder and 2g of $NaNO_3$ were mixed in 90 ml H_2SO_4. The mixture was stirred in a beaker keeping in an ice bath under a controlled temperature between 5-15 ^oC. After three hours of continuous stirring 10gm of $KMnO_4$ was added to oxidize the graphite powder to graphitic oxide in a controlled way so that the temperature remained under 15^oC. After one hour of stirring with added $KMnO_4$, 90 ml water was added to the solution and as a result, huge amount of heat energy was developed which helped to separate graphitic oxide layers into Graphene Oxide. At last, the reaction was terminated by adding Hydrogen Peroxide (H_2O_2). Graphene Oxide solution was washed several times with water and ethanol and finally dried at 60 ^oC.

3.2.3. Synthesis of $MnFe_2O_4$/rGO heterostructure

Graphite oxide (GO), synthesized by the modified Hummer's method was used for the synthesis of reduced graphene oxide (rGO). Dark brown colored GO (100mg) was dispersed with deionized water (200 ml) in a beaker. The suspension was subjected to ultrasonication for about 1 h. As a result of ultrasonication, a light brown colored, homogeneous dispersion of GO was obtained. For the reduction of graphite oxide to graphene (rGO), 90 ml of hydrazine solution and 50 ml of ammonia solution were added to the homogeneous dispersion of GO and the beaker containing reaction mixture was placed again for sonication for another 10 h. The reaction mixture was then stirred and heated (at 90 ^oC) for 1 h. Finally, a black colored stable reduced graphene oxide solution was obtained. A part of that reduced graphene oxide solution was further used for the synthesis of nanocomposites with $MnFe_2O_4$ and remaining part was separated, washed and dried for further characterizations.

For the preparation of $MnFe_2O_4$/rGO heterostructure, $MnFe_2O_4$ was prepared by a modified co-precipitation method according to the previous report with slight modification [27]. Firstly $MnCl_2.4H_2O$ and $FeCl_3.6H_2O$ were dissolved in prepared rGO solution with a molar ratio of 1:2

(Mn: Fe). The mixed solution was then constantly stirred using a magnetic stirrer and heated to 80 ^{o}C. Next, 20 ml of 0.5 M NaOH solution was added dropwise to the mixture solution. When the pH of the solution reached to 10.5, the colour changed immediately from orange to dark brown, which indicated the formation of composite nanoparticles. The reaction mixture was then kept at a constant temperature of about 80^{o}C for 1 h. After that, reaction was terminated and cooled to room temperature. The product, namely, the $MnFe_2O_4$/rGO nanocomposite, was separated from the solution by an external magnetic field and washed several times with deionized water and acetone. The separated material was finally dried at 60 ^{o}C and was used for characterization and application. For the purpose of comparison, bare particles of $MnFe_2O_4$ were also synthesized using the same procedure as above using deionized water without adding the rGO solution.

3.2.4. Characterization

For the establishment of the crystal phase, prepared samples were characterized by XRD. The XRD patterns of the as-prepared samples were obtained by Bruker D8 advanced Diffractometer, using CuKα (λ=1.54059 Å) radiation with a step size of 0.0199 in the range between 10 and 75 degrees. The external surface morphologies of the as-prepared samples were analyzed by Field emission SEM (FEI INSPECT F50) at an operating voltage 20 kV. Prior to SEM characterization samples were platinum coated in vacuum. TEM images were obtained using Transmission Electron Microscope (JEOL ER) with operating voltage 20 kV.

Raman spectroscopic measurements were done using a Raman Microscope (HORIBA, Lab RAM, HR800) at room temperature over a range of 500-3000 cm^{-1}. FTIR spectra were recorded at room temperature by a Perkin-Elmer FTIR spectrum RXI spectrometer in the range 500-4000 cm^{-1} in transmittance mode. For FTIR measurement, pallets were prepared by mixing the samples with KBr powder homogeneously. The background was corrected by a reference of KBr pellets. Magnetic studies were performed in a SQUID. For the study of photocatalysis, we used a UV lamp as the UV light source, the aqueous solution of MB as the pollutant substance, and the synthesized $MnFe_2O_4$ nanoparticles and $MnFe_2O$/rGO composites as the photocatalyst materials. For measuring the concentration of MB solution, UV-Vis absorption spectra were recorded with a Shimadzu, UV-1800 spectrophotometer. Photoluminescence (PL) spectra were recorded on a Perkin Elmer

Spectrofluoimeter with model LS55 using a quartz cuvette of 1 cm path length. For PL measurements samples were dispersed in water.

3.2.5. Photocatalysis Experiment:

The photocatalytic activity of the prepared samples was investigated by the degradation of 10 mg/l (10 ppm) Methylene blue (MB) aqueous solution. MB shows blue colour in water and absorbs in the visible region at 612 and 664 nm. All the experiments were performed under the same atmospheric condition. The photocatalytic activities of the catalysts were tested using UV-Vis spectroscopy under the irradiation of UV lamp (λ =365 nm, intensity = 40 W) as a light source. In each photocatalytic degradation experiment, 0.03 g of the photocatalyst was added to a 100 ml solution of MB (10 mg/l). Before starting the UV irradiation, the reaction mixture was stirred for 60 min in the dark in order to reach the adsorption equilibrium between MB and the catalyst. After that, each time at a predefined time interval of irradiation, 5 ml aliquots were withdrawn and centrifuged to remove the catalyst.

After removing the catalyst, the concentrations of the solutions were analyzed using quartz cuvettes on a UV-Vis spectrophotometer in the absorption band (664 nm) with distilled water as the reference medium. The schematic representation of the whole photocatalytic test process has been presented in **Fig. 3.1**.

The percentage of degradation was calculated by the following equation (1) [4,17,18]

$$\text{Percentage of degradation } (\%) = \frac{C_0 - C_t}{C_0} \times 100 \qquad (1)$$

where C_0 stands for the initial concentration after the equilibrium and C_t stands for the changed concentration at any desired time interval t.

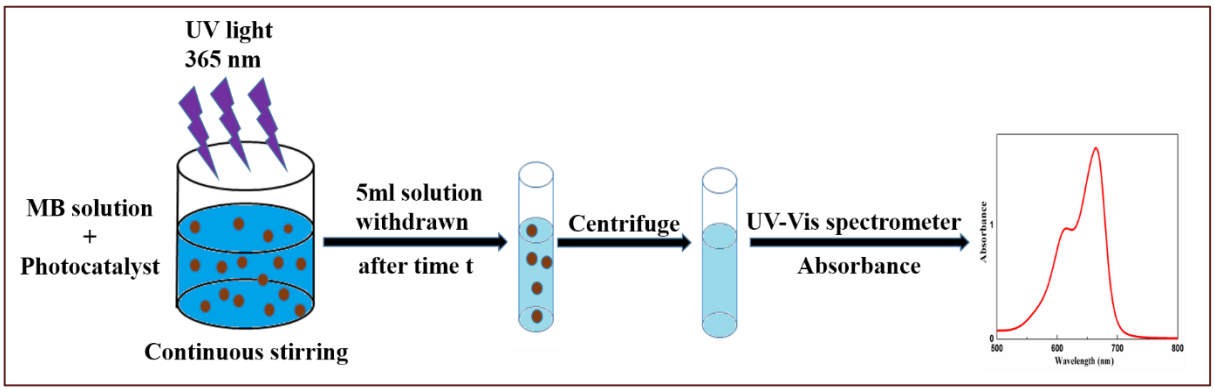

Fig. 3.1. Schematic representation of the process of photocatalysis experiment.

3.3. Results and discussion:

3.3.1. XRD

The XRD patterns recorded for as prepared rGO, $MnFe_2O_4$ and $MnFe_2O_4$/rGO composite particles are shown in **Fig. 3.2a**. In case of rGO, two characteristic peaks of rGO can be seen at 2θ =25.2 ^{o} and 42.3^o corresponding to the crystal planes (002) and (100) respectively, which is consistent with the reported values [28].

All major diffraction peaks of $MnFe_2O_4$ are found to be related to the single-phase cubic spinel structure (JCPDS data no-74-2403). The peaks corresponding to the 2θ values of 30.2^o, 35.5^o, 43.1^o, 57.2^o, 62.7^o matches with diffractions planes of (220), (311), (400), (511) and (440) respectively [29, 30]. The $MnFe_2O_4$/rGO composite sample displays similar XRD pattern but with peaks of broader width which indicates the decrease in crystallite size of $MnFe_2O_4$ particles with the introduction of rGO. No characteristic peak of rGO was observed in the XRD pattern of the composite particles. This may be due to the permeation of $MnFe_2O_4$ particles into the reduced graphene oxide layers consequently separating them [12, 30]. The comparatively higher peak intensities indicate that both $MnFe_2O_4$, as well as composite particles, are crystalline in nature. The mean crystallite size of the nanoparticles was calculated from the XRD pattern corresponding to the (311) plane using the Debye-Scherrer equation (2) [8]:

$$D = \frac{K\lambda}{\beta cos\theta} \qquad (2)$$

where D is the average crystallite size of the nanoparticles, K is a dimensionless shape factor (~0.9), λ is the wavelength of the incident X-ray and β is the full width half maximum (FWHM) of the (311) diffraction peak corresponding to the Bragg angle θ. The average crystallite size of $MnFe_2O_4$ and composite particles were calculated to be 21.32 and 17.61 nm respectively. This decreased size can be attributed to the functional groups of graphene sheets which effectively restrict the size of the nanoparticle [31].

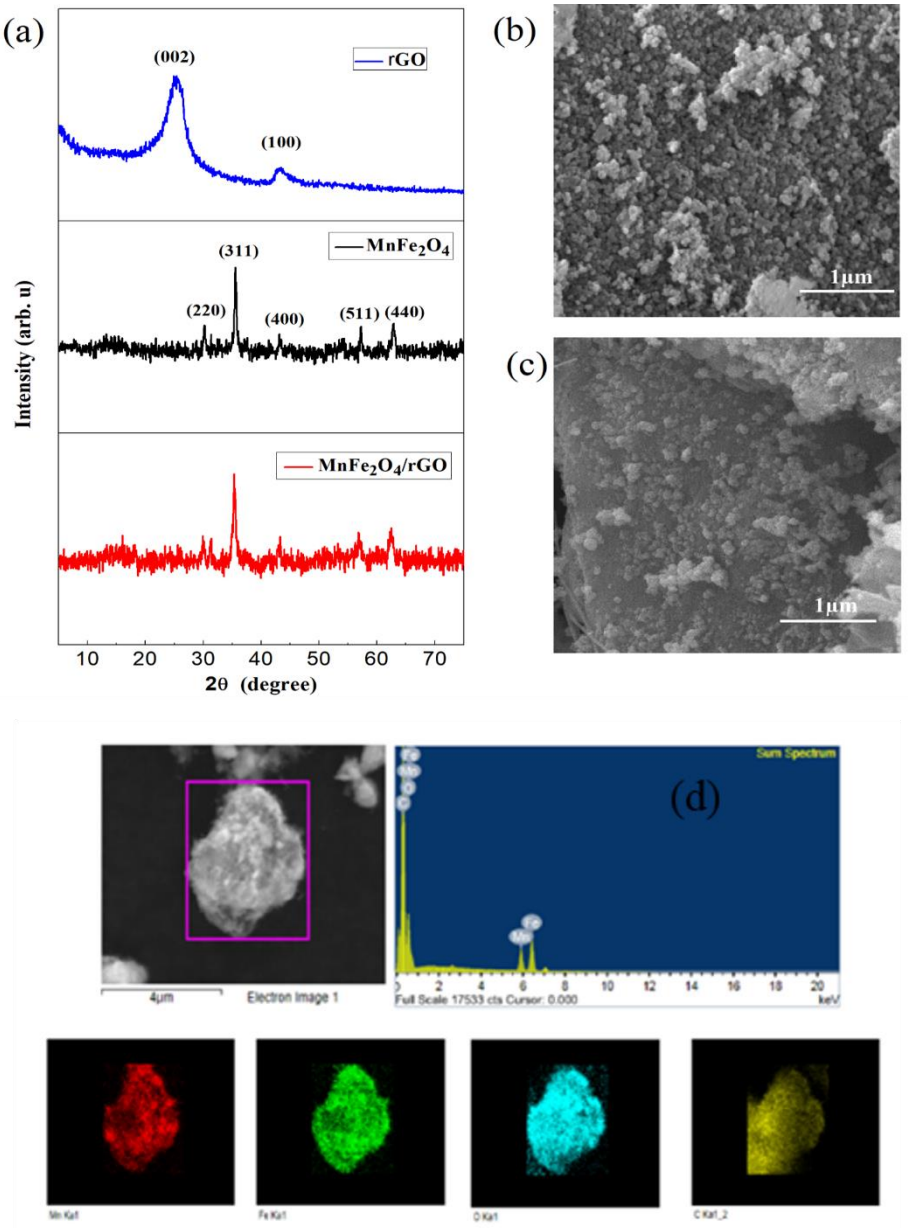

Fig. 3.2. (a) XRD pattern of rGO, $MnFe_2O_4$, and $MnFe_2O_4$/rGO. SEM image of (b) $MnFe_2O_4$ nanoparticles and (c) of $MnFe_2O_4$/rGO heterostructure. (d)EDAX spectrum and element mapping of $MnFe_2O_4$/rGO composite (Please note: carbon contrast region has gone to outer SEM region as sample was mounted on carbon tape).

3.3.2. Morphological and Elemental composition study:

The surface morphology and structure of the prepared samples were further analyzed by FE-SEM and TEM. The FE-SEM image of $MnFe_2O_4$ nanoparticles as shown in **Fig. 3.2b** clearly depicts serious agglomeration of bare nanoparticles. The agglomeration may have been produced due to the method of preparation and possible magnetic interaction between the particles. **Fig. 3.2c** shows the FE-SEM image of the nanocomposite, which shows sphere-like $MnFe_2O_4$ particles with the formation of clusters well attached on reduced graphene oxide sheets. It can be also inferred that the rGO sheet reduces agglomeration of nanoparticles effectively which is also confirmed from the TEM image of the composite as shown in **Fig. 3.3a,b**. The inset of **Fig. 3.3b** shows the corresponding high-resolution TEM image of the $MnFe_2O_4$/rGO composite depicting lattice fringes with interlayer distances of 0.25 nm and 0.30 nm which can be attributed to the (311) and (220) planes respectively of $MnFe_2O_4$ cubic spinel structure. In addition, the EDS spectrum and elemental mapping of $MnFe_2O_4$/rGO composite confirms the presence of Mn along with Fe, C and O (**Fig. 3.2d).** All these studies justify the successful incorporation of $MnFe_2O_4$ nanoparticles into rGO layers and hence the formation of $MnFe_2O_4$/rGO heterostructure.

3.3.3. Spectroscopic study:

Raman spectroscopy is one of the most important techniques to study the irregularity in sp^2 carbon material and to investigate the structural property of the nanomaterials. This spectroscopy is a vibrational technique which is intenesely sensitive to the geomtric structure molucular bonding. **Fig. 3.3c** shows the Raman spectra of bare rGO and $MnFe_2O_4$/rGO composite. The positions of the D and G bands of rGO are found at 1331 cm^{-1} and 1584 cm^{-1} respectively. The peak intensities of D and G band are symbolized by I_D and I_G respectively. It is well known that D band is associated with the existence of defects and disorderliness in graphene lattice structure and that defects are associated with sp^3 defects, grain boundary, vacancy sites etc. G bands are ascribed to the vibration of the sp^2-hybridized carbon atoms in the graphitic structure and this band is the characteristic of all sp^2 carbon system [30,32,33]. The degree of graphitization i.e. the order of graphene structuring is defined by the ratio of the intensity (I_D/I_G), which is found approximately as 1.22 and 1.26 for rGO and $MnFe_2O_4$/rGO respectively. The increased I_D/I_G ratio of the composite material compared to bare rGO may be due to the introduction of structural defects during the formation of the

composite. These defects can help to inhibit the aggregation of the magnetic $MnFe_2O_4$ nanoparticles and act as active sites during the photocatalytic degradation of the dye. In the Raman spectrum of $MnFe_2O_4$/rGO, an additional peak near 623 cm^{-1} indicates the formation of $MnFe_2O_4$ [34].

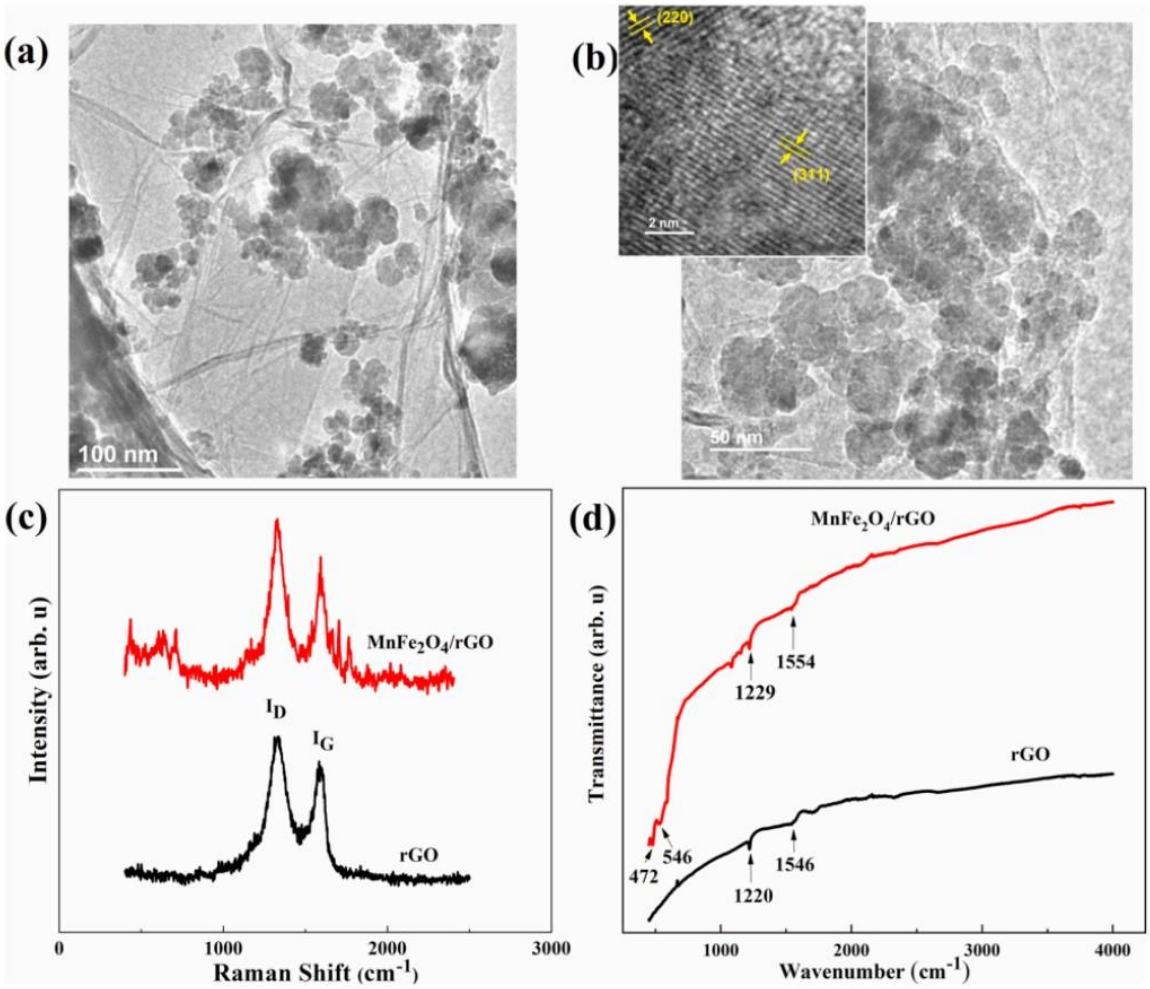

Fig. 3.3(a). TEM image of $MnFe_2O_4$/rGO composite, (b) corresponding higher magnification TEM image. The inset is a high-resolution image showing lattice fringes, (c) Raman spectra of rGO and $MnFe_2O_4$/rGO, and (d) FTIR spectra of rGO and $MnFe_2O_4$/rGO composite.

The FTIR spectra of the as-synthesized samples were carried out to investigate the functional groups of rGO and $MnFe_2O_4$/rGO. **Fig. 3.3d** shows the FTIR spectra of rGO and the $MnFe_2O_4$/rGO nanocomposite. The spectrum of rGO showed the absorption peak at 1570 cm^{-1} which can be attributed to the C=C of the graphene sheets and the absorption peak at 1223 cm^{-1} is due to the C-

OH stretching [35]. After the introduction of $MnFe_2O_4$ in rGO sheets, two peak appeared at 472 and 546 cm^{-1} which are related to intrinsic stretching vibration of the metal oxygen at the octahedral and tetrahedral sites respectively of spinel $MnFe_2O_4$ [36]. This gives the confirmation of successful formation of $MnFe_2O_4$/rGO nanocomposite.

3.3.4. Magnetic property study:

Magnetic measurements were carried out for the as-synthesized bare $MnFe_2O_4$ and $MnFe_2O_4$/rGO using a superconducting quantum interference device (SQUID). **Fig. 3.4a** shows the plot of magnetization versus applied magnetic field (*M-H*) corresponding to the $MnFe_2O_4$ nanoparticles and the heterostructure at 300 K measured in the field range of –50 to +50 kOe. Both *M-H* curves show negligible remanence (M_r) and coercivity (H_c) which confirms the superparamagnetic nature of both the $MnFe_2O_4$ nanoparticles and the $MnFe_2O_4$/rGO heterostructures at room temperature [37]. The saturation magnetization (M_s) values of $MnFe_2O_4$ and $MnFe_2O_4$/rGO heterostructures are found to be 41.0 and 37.19 emu/g respectively at 300 K.

The reduced M_s value of $MnFe_2O_4$/rGO is due to the introduction of the non-magnetic rGO into the $MnFe_2O_4$. Also, the M_s value of $MnFe_2O_4$/rGO heterostructure increases with decreasing temperature (inset of Fig 3a) which can be ascribed to the thermal effects and hence blocking of the spins of single domain particles at low temperatures [19]. **Fig. 3.4b** shows the magnetization versus temperature (*M-T*) plot of the $MnFe_2O_4$/rGO heterostructure under zero field-cooled (ZFC) and field-cooled (FC) conditions measured at 300 Oe field. The ZFC curve has its maximum vaue at 98.5 K, which is an indicative of the blocking temperature. In addition, both the FC and ZFC curves merge at 255 K, much below the room temperature confirming the superparamagnetic nature of the heterostructure at room temperature. Inset of **Fig. 3.4b** shows the separation of the $MnFe_2O_4$/rGO particles from the solution phase using an external magnetic field. Thus, the obtained information about the magnetic behavior of $MnFe_2O_4$ and its rGO heterostructure is indeed useful in the magnetical separation of these photocatalysts after the dye degradation process for its further re-use.

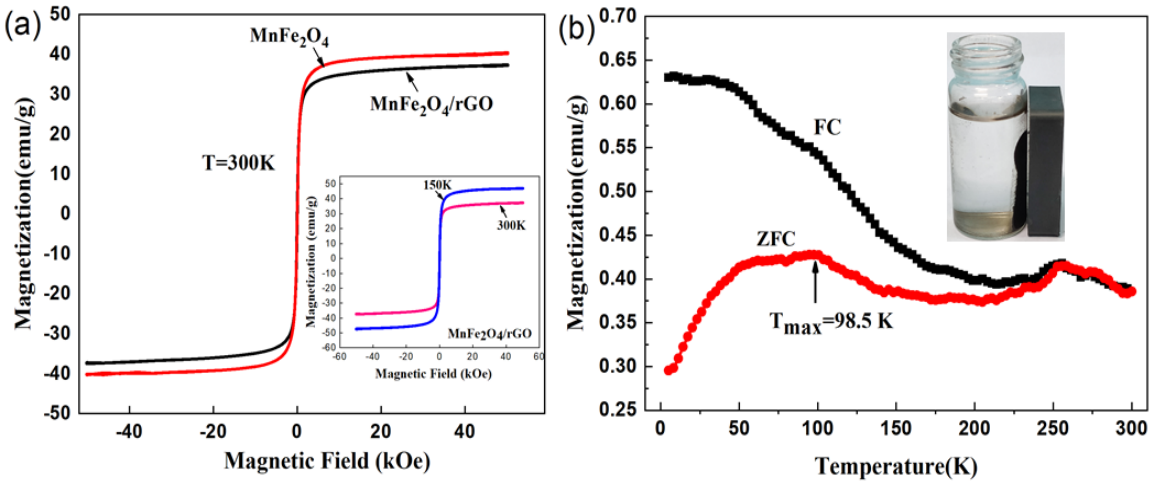

Fig. 3.4. (a) *M-H* curves of $MnFe_2O_4$ nanoparticles and $MnFe_2O_4$/ rGO heterostructures measured at 300 K using a SQUID magnetometer. Inset shows the M-H curves of $MnFe_2O_4$/ rGO measured at 150K and 300K. (b) The zero field-cooled (ZFC) and field cooled (FC) curves of $MnFe_2O_4$/ rGO measured at an applied field of 300 Oe. Inset shows the magnetic separation of the $MnFe_2O_4$/ rGO particles from the solution phase using an external magnet.

3.4. Study of photocatalytic degradation:

The photocatalytic degradation of methylene blue (MB) dye as a model pollutant was investigated under UV light in the presence of $MnFe_2O_4$ and $MnFe_2O_4$/rGO heterostructure as photocatalysts. As the concentration of MB solution is proportional to its absorption of light, the degradation process was evaluated by monitoring the change in the absorption spectrum of MB in aqueous solution with the help of a UV-Vis spectrophotometer. In a typical absorption spectrum of MB, there is a high monomeric absorption band corresponding to the wavelength at ~ 662 nm which corresponds to π-π* transition, and a broadened peak appears around 610 nm which is attributed to the 0-1 vibronic transition of methylene blue monomer [38]. In order to analyze the photocatalytic performance, highest intensity of the band at 662 nm has been considered. On addition of the photocatalysts in the MB solution, the absorbance intensity at 662 nm starts to decrease with time when the mixed solution was exposed to UV light irradiation. The UV-Vis absorption spectra of the MB dye solution in the presence of $MnFe_2O_4$ and $MnFe_2O_4$/rGO photocatalysts are shown in **Fig. 3.5a**,**b** respectively. In the case of bare $MnFe_2O_4$ nanoparticles, it took 290 min to decrease

the absorbance of MB from 1.67 to 0.285. After the addition of $MnFe_2O_4$/rGO to the MB ye under UV-light irradiation, the absorbance intensity

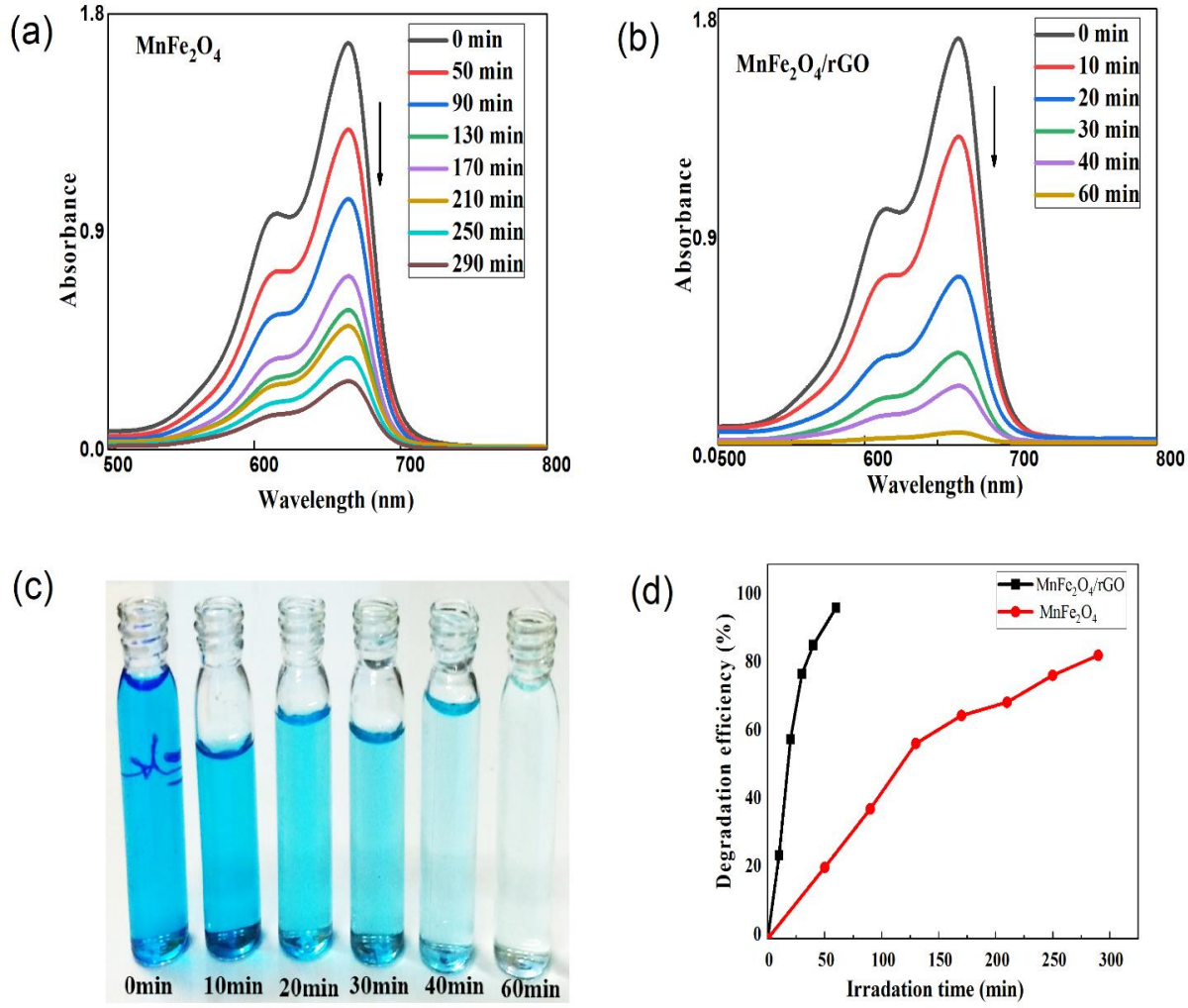

Fig. 3.5. Time-dependent absorption spectra of methylene blue solution in presence of the photocatalyst (a) $MnFe_2O_4$ nanoparticles and (b) $MnFe_2O_4$/rGO heterostructures, (c) Photograph showing the change in colour of the methylene blue solution in presence of $MnFe_2O_4$/rGO (d) The photocatalytic dye degradation efficiency of $MnFe_2O_4$ and $MnFe_2O_4$/rGO photocatalysts at different irradiation time.

gradually decreased from 1.67 to 0.05 within just 60 min and the final solution became almost colourless. **Fig. 3.5c** shows the photograph of the colour change of the MB solution in the presence of $MnFe_2O_4$/rGO for easy visualization of the decolourization. The dye degradation efficiency was calculated from equation (1). A comparison of the photocatalytic efficiency of $MnFe_2O_4$ and

$MnFe_2O_4$/rGO with respect to irradiation time is presented in **Fig. 3.5d**. In case of bare $MnFe_2O_4$ nanoparticles, the MB dye degradation efficiency is found to be ~84% in 290 minutes time, whereas for $MnFe_2O_4$/rGO heterostructure, the degradation efficiency is found to be 97% in 60 minutes time. This result reveals that the $MnFe_2O_4$/rGO heterostructure shows excellent photocatalytic activity towards the degradation of MB compared to bare $MnFe_2O_4$. This improved photocatalytic performance with the introduction of rGO in $MnFe_2O_4$ mainly due to the decelerated recombination rate of photogenerated carriers which has been explained in details in the mechanism part (section 3.3). Also, there is an increase in the effective surface area of the nanoparticles due to the decrease in crystallite size of $MnFe_2O_4$ on the introduction of rGO [39]. Thus, the reduced agglomeration of bare nanoparticles within the nanocomposite and at the same time increase in surface area of the nanocomposite which provides more active sites for the reaction is also responsible for this improved photocatalytic activity.

3.4.1. Mechanism of the enhanced photocatalytic degradation of MnFe2O4/rGO photocatalyst

Compared to bare $MnFe_2O_4$ nanoparticles, the $MnFe_2O_4$/rGO composite showed enhanced photocatalytic performance. This is mainly ascribed to the reduction of the recombination rate due to the presence of rGO. In case of bare $MnFe_2O_4$ nanoparticles, the photocatalytic reaction is initiated when a photoelectron is promoted from the valence band to the conduction band as a result of the UV light excitation. The excitation process creates a hole in the valence band. As a result, electron and hole pair (e^-/h^+) is generated [40]. The photogenerated holes at the valence band then react with the water molecules to produce $^{\bullet}OH$ radicals which are extremely powerful oxidizing agents. On the other hand, electrons in the conduction band are captured by the oxygen in order to generate anionic superoxide radical $O_2^{\bullet -}$ which also takes part in the further oxidation process [41]. However, these electron-hole pairs created under UV light irradiation recombine rapidly, leaving a very small part of it available for the photocatalytic reaction and hence preventing the photocatalysis process [24].

The remarkable improvement in the photocatalytic activity of $MnFe_2O_4$/rGO heterostructure under UV light irradiation occurs mainly due to the presence of reduced graphene oxide as the photoinduced electrons from the conduction band of $MnFe_2O_4$ can move easily to the rGO since graphene has excellent electron accepting ability and unique electron transport properties [21, 23, 42]. This process thus effectively prevents the direct recombination of electrons and holes and

consequently improve photodegradation [43,44]. The above-mentioned explanation can be understood from the following possible reaction mechanism [45]:

$MnFe_2O_4$+ hν (UV)→ $MnFe_2O_4$ (e+h) (3)

$MnFe_2O_4$ (e) + graphene → $MnFe_2O_4$ + graphene (e) (4)

graphene (e) + O_2 → $O_2^{\bullet -}$ + graphene (5)

$MnFe_2O_4$ (h) + H_2O → $^{\bullet}OH$ + $MnFe_2O_4$ (6)

$MnFe_2O_4$ (h) +$O_2^{\bullet -}$ + $^{\bullet}OH$ + MB dye → H_2O + CO_2 + Other intermediates (7)

Thus, the active radicals ($O_2^{\bullet -}$, •OH) and the holes finally oxidize the molecules of the MB dye leading to MB degradation. The basic mechanism of the photocatalytic degradation of the MB dye by the $MnFe_2O_4$/rGO particles is illustrated in **Fig. 3.6**.

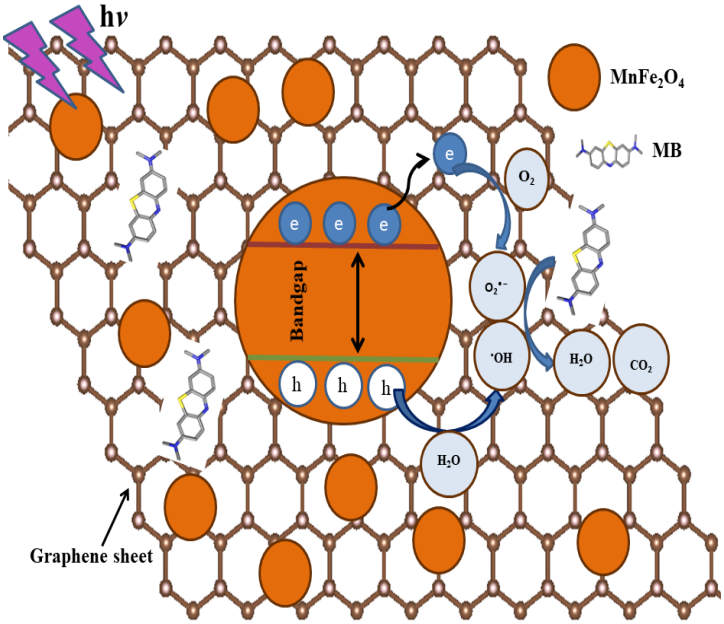

Fig. 3.6. Schematic representation of the photocatalytic degradation mechanism of MB dye with $MnFe_2O_4$/rGO heterostructure**.**

To figure out the most active species and their role in the enhanced photodegradation process, a series of experiments with traditional scavengers were carried out [46]. Ethylenediaminetetracetic acid (EDTA), Isopropyl alcohol (IPA), Benzoquinone (BQ) were mixed separately with the dye solution as hole, hydroxyl radical and superoxide radical scavenger respectively. For each experiment, initial concentration of MB dye, dosage of the photocatalyst ($MnFe_2O_4$/rGO) and reaction time was kept fixed at 10 $mg.l^{-1}$(100 ml), 0.03 g, and 60 min, respectively. A scavenger

partially suppresses the photocatalytic oxidation reaction and consequently lowers the photodegradation process. The amount of reduced photodegradation efficiency due to scavenger, defines the contribution of the corresponding reactive oxidant species [47]. **Fig. 7a** depicts the effect of three scavengers on the photocatalytic degradation which shows degradation efficiency is 97% with no scavenger. It can be observed that with isopropyl alcohol, degradation efficiency decreased to 48%. With addition of EDTA and BQ degradation efficiency was 85% and 89% respectively. Therefore, the result shows most of the holes reacts with water and produces •OH radical only few of them directly take part in the oxidation process of dye [43]. $O_2^{\bullet -}$ has also very little contribution in direct oxidation process and it may further produce •OH via chain reaction [48]. So it is evident that •OH is the major active species which plays key role in the degradation process of MB dye rather than h^+ and $O_2^{\bullet -}$.

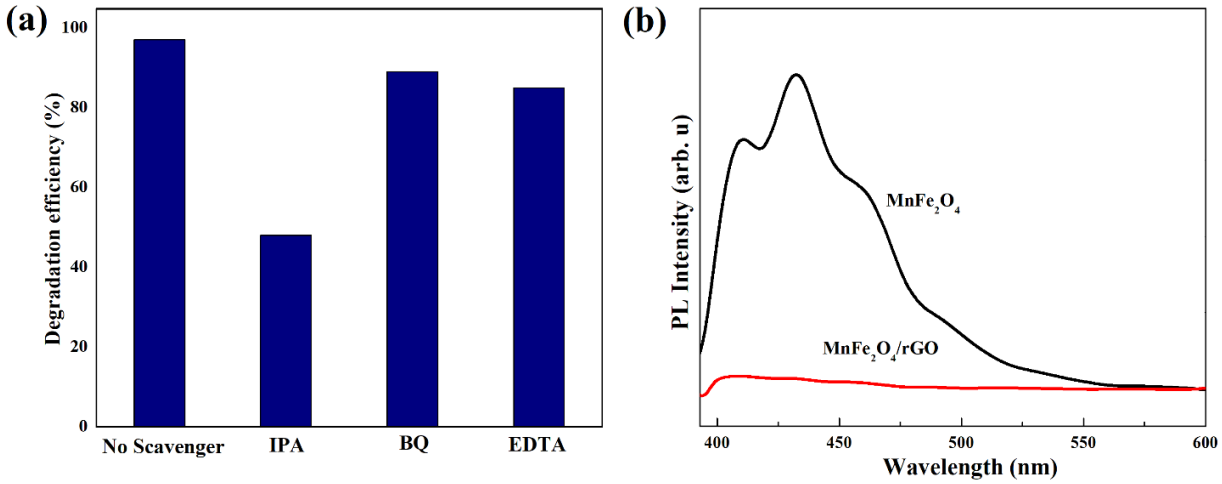

Fig. 3.7. (a) Effect of scavengers on the photocatalytic degradation of MB over $MnFe_2O_4$/rGO under UV irradiation, (b)Photoluminescence (PL) spectra of pure $MnFe_2O_4$ and $MnFe_2O_4$/rGO (ex = 365 nm).

Photoluminescence spectroscopy method was carried out to explore the transfer of electron and the recombination process of photogrnarated electron–hole pair in our prepared photocatalysts. **Fig. 7.b** depicts PL emission spectra of $MnFe_2O_4$/rGO and $MnFe_2O_4$ at an excitation wavelength of 365 nm. It can be observed that emission intensity of $MnFe_2O_4$ nanoparticle has been much lowered with the introduction of graphene which can be attributed to the inhibition of photogenerated electron and hole in the composite particle. Being a great electron acceptor graphene sheets can dramatically quench the fluorescence intensity $MnFe_2O_4$. Photogenerated electrons from

conduction band of exited $MnFe_2O_4$ were shifted to graphene sheet giving rise to enhanced charge separation and eventually accelerated photocatalytic activity [49].

3.4.2. Kinetics of photodegradation:

To understand the dye degradation better, we investigated degradation rates by fitting the experimentally obtained result with the pseudo-first-order kinetic equation which is derived from the Langmuir-Hinshelwood (L-H) kinetics model. According to this model, it is assumed that the adsorption of dye molecules on the surface of the catalyst particles takes place before the starting of the photocatalytic process [50].

The rate of reaction can be expressed as

$$r = \frac{dc}{dt} = \frac{\kappa K C}{1 + K C} \qquad (8)$$

where r (mg/min) is the rate of photodegradation of the dye material, C (mg/l) is the concentration of the dye, t is the photo-irradiation time, κ (mg/min) is the rate constant of reaction and K (mg^{-1}) is the adsorption coefficient of the reactant [50, 51]. If the initial concentration is very small, the above equation can be simplified to the following apparent pseudo first order equation.

$$ln\frac{C_0}{C_t} = \kappa K t = k_1 t \qquad (9)$$

where k_1 is the pseudo-first-order rate constant, C_0 and C_t are the concentrations of the dye at the time 't' and 't = 0' respectively. The plot of ln (C_0/C_t) vs irradiation time (t) as obtained from equation (9) for the MB dye degradation in presence of $MnFe_2O_4$ and $MnFe_2O_4$/rGO composite material is presented in **Fig. 3.8**a and **3.8**b respectively, which depicts a linear relationship. The rate constant values were calculated from the slope of the straight line. The parameters of the dye degradation kinetics such as correlation coefficient (R^2), the first-order rate constant (k_1) and best fit linear equation, etc. corresponding to $MnFe_2O_4$ and $MnFe_2O_4$/rGO photocatalyst as obtained from the pseudo-first-order kinetic model is presented in Table 3.1.

Table 3.1. Fitting Parameters calculated from pseudo-first-order kinetics model [50].

Catalyst	**k_1 (min^{-1})**	**R^2**	**Linear equation**
$MnFe_2O_4$	0.006	0.989	Y= 0.006X - 0.021
$MnFe_2O_4$/rGO	0.0586	0.983	Y= 0.586X - 0.213

From Table 3.1, it is observed that the obtained R^2 value is very close to 1 (>0.98) for both $MnFe_2O_4$and $MnFe_2O_4$/rGO photocatalyst. So, it can be concluded that the experimental data is well fitted with the modified expression of the Langmuir-Hinshelwood equation. The Pseudo-first-order kinetics rate constant of the $MnFe_2O_4$/rGO composite material is 0.0586 min^{-1}, which is almost 10 times faster than that of the bare $MnFe_2O_4$ nanoparticles which also confirms the higher photocatalytic efficiency of the $MnFe_2O_4$/rGO heterostructure [52].

3.4.3. Reusability:

The consecutive usage of the photocatalyst has a determining role for the extended use of the photocatalyst in real time applications [53]. To investigate the reusability of the photocatalyst $MnFe_2O_4$/rGO nanocomposite, a four-run cyclic experiment was done for the photodegradation of MB (**Fig. 3.9**). During each run the photocatayst material was separated from the aqueous dye solution with the help of external magnet and was washed properly with distilled water and was further dried to use for the next cycle. After each run the degradation efficiency reduced slightly and finally reached from 97% to 88% after fourth run. The result clearly exhibits that magnetically separable $MnFe_2O_4$/rGO nanocomposite have high stability in the degradation of MB dye in aqueous solutions.

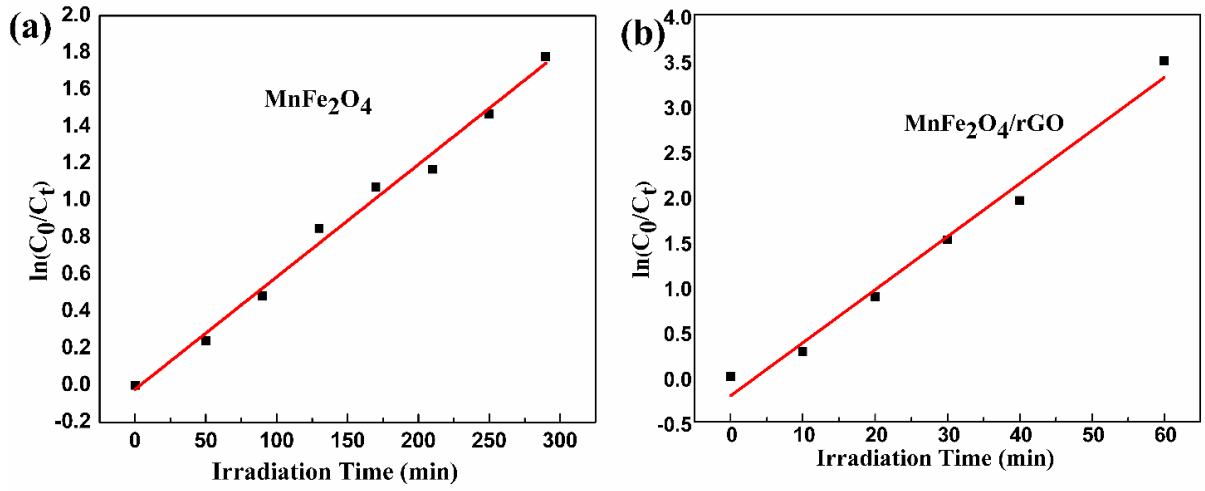

Fig. 3.8. Pseudo first order kinetics plot showing $\ln(C_0/C_t)$ versus irradiation time for photocatalytic degradation of methylene blue with (a) $MnFe_2O_4$ and (b) $MnFe_2O_4$/rGO.

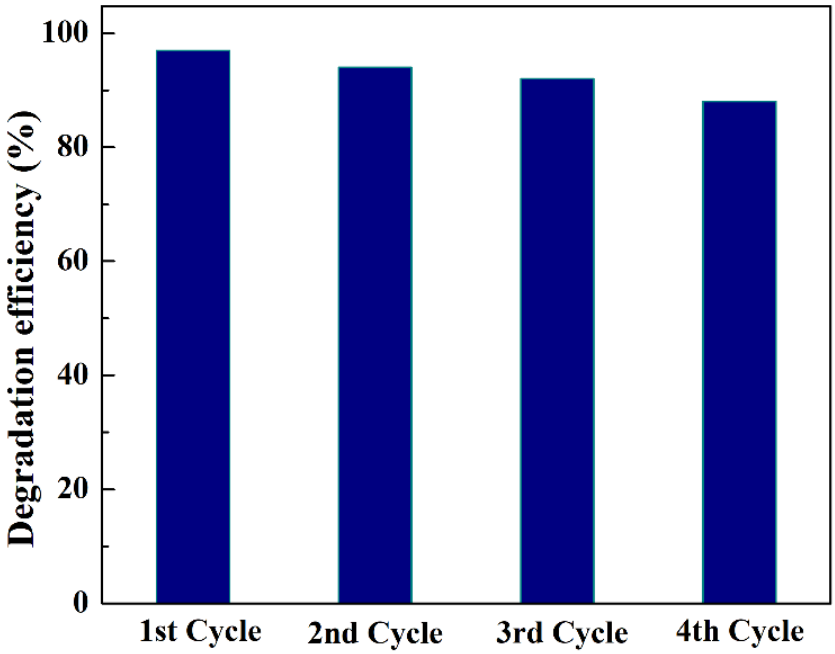

Fig. 3.9. Recycling test run for the photodegradation of MB under UV irradiation over $MnFe_2O_4$/rGO.

3.5. Conclusion:

In this study, the photocatalytic performances of $MnFe_2O_4$ nanoparticles and $MnFe_2O_4$/rGO heterostructure synthesized using chemical co-precipitation method were investigated for methylene blue (MB) dye degradation. The XRD, FTIR, and Raman results confirmed the formation of cubic spinel $MnFe_2O_4$ and $MnFe_2O_4$/rGO composite particles. The SEM and HR-TEM images showed the formation of sphere-like $MnFe_2O_4$ nanoparticles well attached on the rGO nanosheets with reduced agglomeration compared to bare nanoparticles. The dye degraded by 84% in the presence of $MnFe_2O_4$ after UV light irradiation of 290 minutes, while 97% of it degraded in merely 60 minutes in case of $MnFe_2O_4$/rGO heterostructure. Also, the rate constant corresponding to the pseudo-first-order kinetics equation in case of the composite particles/heterostruture was 10 times higher than that of the bare $MnFe_2O_4$ particles. To conclude, the cubic spinel $MnFe_2O_4$/rGO heterostrucures showed enhanced photocatalytic efficiency than the bare $MnFe_2O_4$ nanoparticles which can be used as an effective photocatalyst for MB dye degradation. Hydroxyl radical played the key role in the MB dye photodegradation process by $MnFe_2O_4$/rGO heterostructure.In addition, the superparamagnetic nature of this photocatalyst gives it an added advantage which makes it re-

usable further by magnetically separating it from the dye solution after the purification process. Further studies should be done for investigating its photocatalytic potential for degradation of other toxic industrial dyes.

References:

[1] J. Hu, L. Liua , Z. Xiao, Adsorptions of Cd(II) and methylene blue from aqueous solution by silica hybrid hollow spheres, RSC Adv. 5 (2015) 68092. https://doi: 10.1039/c5ra13413g.

[2] Y. Pan, T. Zhu, Z. He, Enhanced removal of Azo Dye by a electrochemical System Integrated with a membrane Biofilm reactor, Ind. Eng. Chem. Res. 57 (2018) 16433−16441. https://doi: 10.1021/acs.iecr.8b04725.

[3] M. T. Yagub , T. K. Sen , S. Afroze , H.M. Ang , Dye and its removal from aqueous solution by adsorption: A review, Adv. Colloid Interface Sci. 209 (2014) 172–184. https://dx.doi.org/10.1016/j.cis.2014.04.002

[4] P. Kariyajjanavar, N. Jogttappa, Y.A. Nayaka, Studies on degradation of reactive textile dyes solution by electrochemical method, J. Hazard. Mater. 190 (2011) 952–961. https:// doi:10.016/j.jhazmat.2011.04.032.

[5] C.A. Hsu, T.N. Wen, Y.C. Su, Z.B. Jiang, C.W. Chen, L.F. Shyur, Biological Degradation of Anthroquinone and Azo Dyes by a Novel Laccase from Lentinus sp., Environ. Sci. Technol. 46 (2012) 5109−5117. https://dx.doi.org/10.1021/es2047014.

[6] Saruchi, V. Kumar, B. S. Kaith, R. Jindal, Synthesis of Hybrid Ion Exchanger for Rhodamine B Dye Removal:Equilibrium, Kinetic and Thermodynamic Studies, Ind. Eng. Chem. Res. 55 (2016) 10492−10499. https://doi: 10.1021/acs.iecr.6b01690.

[7] E.Casbeer, V.K. Sharma, X.-Z. Li, Synthesis and photocatalytic activity of ferrites under visible light: a review, Sep. Purif. Technol. 87 (2012) 1–14. https://doi.org/10.1016/j.seppur.2011.11.034.

[8] K.N. Harish, H.S. Bhojya Naik, P.N. Prashanth kumar and R. Viswanath, Synthesis, enhanced optical and photocatalytic study of Cd–Zn ferrites under sunlight, Catal. Sci. Technol. 2 **(**2012**)** 1033–1039. https://doi: 10.1039/c2cy00503d.

[9] M.A. Lazar, S. Varghese, S.S. Nair, Photocatalytic Water Treatment by Titanium Dioxide: Recent Updates Photocatalytic Water Treatment by Titanium Dioxide: Recent Updates, Catalysts. 2 (2012) 572-601. https://doi:10.3390/catal2040572.

[10] H. Younes, F. Ravaux , N. E. Hadri , L. Zou, Nanostructuring of pseudocapacitive $MnFe_2O_4$/Porous rGO electrodes in capacitive deionization, Electrochim Acta. 306 (2019) 1-8. https://doi.org/10.1016/j.electacta.2019.03.097.

[11] Y. Yang, J. Liu, B. Zhang, F. Liu, Mechanistic studies of mercury adsorption and oxidation by oxygen over spinel type $MnFe_2O_4$, J. Hazard. Mater. 321 (2017) 154–16. https://dx.doi.org/10.1016/j.jhazmat.2016.09.007.

[12] G. Wang, Y. Ma, Z. Wei, M. Qi,. Development of multifunctional cobalt ferrite/graphene oxide nanocomposites for magnetic resonance imaging and controlled drug delivery.Chem. Eng. J., 289 (2016) 150-160.
https://doi.org/10.1016/j.cej.2015.12.072

[13] S. Chandrasekaran, C. Bowen, P. Zhang, Z. Li, Q. Yuan,X. Ren and L. Deng , Spinel photocatalysts for environmental remediation, hydrogen generation, CO_2 reduction and photoelectrochemical water splitting, J. Mater. Chem. A. 6 (2018) 11078–11104. https://doi: 10.1039/c8ta03669a.

[14] L. Zheng, K. Fang, M. Zhang, Z. Nan, L. Zhao, D.Zhou, M. Zhub ,W. Li, Tuning of spinel magnesium ferrite nanoparticles with enhanced magnetic properties, RSC Adv. 8 (2018) 39177–39181. https://doi: 10.1039/c8ra07487a.

[15] Y.H. Guan, J. Ma, Y.M. Ren, Y.L.Liu, J.Y. Xiao, L. Lin, C.Zhang, Efficient degradation of atrazine by magnetic porous copper ferrite catalyzed peroxymonosulfate oxidation via the formation of hydroxyl and sulfate radicals, Water Res. 47 (2013) 5431-5438. https://dx.doi.org/10.1016/j.watres.2013.06.023.

[16] Y. Ren, L. Lin, J. Ma, J. Yang, J. Feng, Z. Fan, Sulfate radicals induced from peroxymonosulfate by magnetic ferrospinel MFe_2O_4 (M=Co, Cu, Mn, and Zn) as heterogeneous catalysts in the water, Applied Cat. B: Env. 165 (2015) 572-578. https://doi.org/10.1016/j.apcatb.2014.10.051.

[17] M. Stoia, C. Muntean, B. Militaru, $MnFe_2O_4$ nanoparticles as new catalyst for oxidative degradation of phenol by peroxydisulfate, J. Environ. Sci . 53 (2017) 269-277. https://doi.org/10.1016/j.jes.2015.10.035.

[18] R. Ciocarlan, E.M. Seftel, M. Mertens, A. Pui, M. Mazaj, N.N.Tusar, P.Cool, Novel magnetic nanocomposites containing quaternary ferrites systems Co0.5Zn0.25M0.25Fe2O4 (M = Ni, Cu,

Mn, Mg) and TiO2-anatase phase as photocatalysts for wastewater remediation under solar light irradiation, Mater. Sci. Eng. B. 230 (2018) 1-7. https://doi.org/10.1016/j.mseb.2017.12.030.

[19] E.H.M. Sakho, S. Thomas, N. Kalarikkal, O.S. Oluwafemi, Dielectric and dye adsorption properties of luminescent-superparamagnetic MFe_2O_4 (M = Mn, Mg)/reduced graphene oxide composites, Ceram. Int. 44 (2018) 3904-3914. https://doi.org/10.1016/j.ceramint.2017.11.181.

[20] X. Wua,, W. Wanga, F. Lia, S. Khaimanova, N. Tsidaeva, M. Lahoubi, PEG-assisted hydrothermal synthesis of $CoFe_2O_4$ nanoparticles with enhanced selective adsorption properties for different dyes, Appl. Surf. Sci. 389 (2016) 1003–1011, https://dx.doi.org/10.1016/j.apsusc.2016.08.053

[21] L. Wang, L. Zhuo, C. Zhang , F. Zhao, Carbon dioxide-induced homogeneous deposition of nanometer-sized cobalt ferrite ($CoFe_2O_4$) on graphene as high-rate and cycle-stable anode materials for lithium-ion batteries, J. Power Sources. 275 (2015) 650-659. https://dx.doi.org/10.1016/j.jpowsour.2014.11.051.

[22] Z. Wu, W. Ren, L. Wen, L. Gao, J. Zhao, Z. Chen, G. Zhou, F. Li, H.M. Cheng, Graphene anchored with Co_3O_4 nanoparticles as anode of lithium ion batteries with enhanced reversible capacity and cyclic performance. ACS Nano. 4 (2010) 3187−3194.
https://doi:10.1021/nn100740x.

[23] D. Wang ,X. Li, J. Chen , X. Tao, Enhanced photoelectrocatalytic activity of reduced graphene oxide/TiO_2 composite films for dye degradation, Chem. Eng. J. 198-199 (2012) 547–554. https://dx.doi.org/10.1016/j.cej.2012.04.062.

[24] R.M. Asmussen, M. Tian, and A. Chen, A new approach to wastewater remediation based on bifunctional electrodes, Environ. Sci. Technol. 43 (2009) 5100–5105.
https:// doi:10.1021/es900582m.

[25] S.V. Nipane, P.V. Korake, G.S. Gokavi, Graphene-zinc oxide nanorod nanocomposite as photocatalyst for enhanced degradation of dyes under UV light irradiation, Ceram. Int. 41 (2015) 4549–4557. https://dx.doi.org/10.1016/j.ceramint.2014.11.151.

[26] W.S. Hummers, R.E. Offeman, Preparation of Graphitic oxide, J. Am. Chem. Soc. 80 (1958) 1339-1339. https://doi.org/10.1021/ja01539a017.

[27] S. Kumar, R.R. Nair, P. B. Pillai, S. N. Gupta, M. A. R. Iyengar, and A. K. Sood, Graphene Oxide−$MnFe_2O_4$ Magnetic Nanohybrids for Efficient Removal of Lead and Arsenic from Water ACS Appl. Mater. Interfaces. 6(2014)17426−17436. https://dx.doi.org/10.1021/am504826q.

[28] Y. Zhang, H. Tang, X. Ji, C. Li, L. Chen, D. Zhang, X. Yang, H. Zhang, Synthesis of reduced graphene oxide/Cu nanoparticle composites and their tribological properties, RSC Adv. 3(2013) 26086–26093.http:// DOI: 10.1039/c3ra42478b.

[29] W. Cai, T. Lai, W. Dai, J. Ye, A facile approach to fabricate flexible all-solid-state supercapacitors based on MnFe2O4/graphene hybrids, J. Power Sources. 255 (2014) 170-178. https://doi.org/10.1016/j.jpowsour.2014.01.027.

[30] A.G.Tabrizi, N.Arsalani, A. Mohammadi, H.Namazi, L.S.Ghadimi, I. Ahadzadeh, Facile synthesis of $MnFe_2O_4$/rGO nanocomposite for an ultra-symmetric supercapacitor, New J. Chem. 41 (2017) 4974-4984. https://doi.org/10.1039/C6NJ04093D.

[31] J. Wang, Q. Deng, M. Li, K. Jiang, J. Zhang, Z. Hu, J. Chu, Copper ferrites@reduced graphene oxide anode materials for advanced lithium storage applications, Scientific Reports, Volume **7**, Article number: 8903 (2017). DOI:10.1038/s41598-017-09214-0.

[32] R. Beams, L. G. Cancado, L. Novotny, Raman characterization of defects and dopants in graphene, J. Phys.: Condens. Matter. 27 (2015) 083002-083028. http://doi:10.1088/0953-8984/27/8/083002.

[33] S .Yu, R .Tang, K. Zhang, S .Wu, X .Yang, W .Wu, Y .Chen, Y. Shen, X .Zhang, J. Qian, Y .Song, Z .Sun, One-step synthesis of tunable nitrogen-doped graphene from graphene oxide and its high performance field emission properties, Vacuum 168 (2019) 108817. doi: https://doi.org/10.1016/
j.vacuum.2019.108817.

[34] Y.L. Xiao, J.T. Zai, L.Q. Tao, B. Li, Q.Y. Han, C. Yu, X.F. Qian, $MnFe_2O_4$–graphene nanocomposites with enhanced performances as anode materials for Li-ion batteries, Phys. Chem. Chem. Phys. 15 (2013) 3939–3945. https://doi.org/10.1039/C3CP50220A.

[35] Y. Gong, D. Li, Q. Fu, C. Pan, Influence of graphene microstructures on electrochemical performancefor supercapacitors, Prog Nat Sci-Mater. 25 (2015) 379-385. https://doi.org/10.1016/j.pnsc.2015.10.004.

[36] K. Zipare, J. Dhumal, S. Bandgar, V. Mathe, G. Shahane, Superparamagnetic Manganese Ferrite Nanoparticles: Synthesis and Magnetic Properties, Journal of Nanoscience and Nanoengineering. 1 (2015) 178-182. http://creativecommons.org/licenses/by-nc/4.0/.

[37] G. Wang, Y. Ma, L. Zhang, J. Mu, Z. Zhang, X. Zhang, H. Che, Y. Bai, J. Hou, Facile synthesis of manganese ferrite/graphene oxide nanocomposites for controlled targeted drug delivery, J. Magn. Magn. Mater. 401 (2016) 647650. https://doi.org/10.1016/j.jmmm.2015.10.096.

[38] U. Chakraborty , T. Singha , R.l R. Chianelli , C. Hansda ,P. K. Paul, Organic-inorganic hybrid layer-by-layer electrostatic self-assembled film of cationic dye Methylene Blue and a clay mineral: Spectroscopic and Atomic Force microscopic investigations, J. Lumin. 187 (2017) 322–332. https://dx.doi.org/10.1016/j.jlumin.2017.03.039.

[39] K.J.A. Raj, B. Viswanathan, Effect of surface area, pore volume and particle size of P25 titania on the phase transformation of antanese to rutile, Indian J. Chem. 48 (2009)1378-1382. https://hdl.handle.net/123456789/6124.

[40] A.R. Khataee, M.B. Kasiri, Photocatalytic degradation oforganic dyes in the presence of nanostructured titanium dioxide:Influence of the chemical structure of dyes, J. Mol. Catal. A. 328 (2010) 8–26. https://doi.org/10.1016/j.molcata.2010.05.023.

[41] J.H. Zeng, B.B. Jin, and Y. F. Wang, Facet enhanced photocatalytic effect with uniform single-crystalline zinc oxide nanodisks, Chem. Phys. Lett. 472 (2009) 90–95. https://doi.org/10.1016/j.cplett.2009.02.082.

[42] X.F. Zhang , Q. Xi, A graphene sheet as an efficient electron acceptor and conductor for photoinduced charge separation, Carbon. 49 (2011) 3842 –3850. https://doi:10.1016/jcarbon.2011.05.019.

[43] Y. Fu, P. Xiong, H. Chen, X. Sun, X. Wang, High Photocatalytic Activity of Magnetically Separable Manganese Ferrite Graphene Heteroarchitectures, Ind. Eng. Chem. Res. 51 (2012) 725–731. https://doi.org/10.1021/ie2026212.

[44] X. Gaoa, T. T. Nguyen, X. Gong, X. Chen, Z. Song, W. Du, R. Chai, M. Guo, A composite material of vacuum heat-treated CQDs/$Ce_{0.7}Zr_{0.3}O_2$ with enhanced charge separation for efficient photocatalytic degradation, Vacuum 169 (2019) 108912. https://doi.org/10.1016/j.vacuum.2019.108912.

[45] Y. Fu, Q. Chen, M. He, Y. Wan, X.Sun, H. Xia, X. Wang, Copper Ferrite-Graphene Hybrid: A Multifunctional Heteroarchitecture for Photocatalysis and Energy Storage, Ind. Eng. Chem. Res. 51 (2012) 11700−11709. https://dx.doi.org/10.1021/ie301347j.

[46] E. Regulska , J. Breczko, A. Basa, Pristine and Graphene-Quantum Dots-Decorated Spinel Nickel Aluminate for Water Remediation from Dyes and Toxic Pollutants,
Water. 11 (2019) 953.http://doi:10.3390/w11050953.

[47] A. Hassani, P. Eghbali, A. Ekicibil, Ö. Metin, Monodisperse cobalt ferrite nanoparticles assembled on mesoporous graphitic carbon nitride ($CoFe_2O_4$/mpg-C3N4): A magnetically recoverable nanocomposite for the photocatalytic degradation of organic dyes, J. Magn. Magn. Mater. 456 (2018) 400–412. https://doi.org/10.1016/j.jmmm.2018.02.067.

[48] M. M. Mohamed, I. Ibrahim, T. M. Salama, Rational design of manganese ferrite-graphene hybrid photocatalysts: Efficient water splitting and effective elimination of organic pollutant, Appl Catal A-Gen. 524 (2016)182-191. https://doi.org/10.1016/j.apcata.2016.06.031.

[49] Y. Fua, H. Chenb, X. Sunb, X. Wang, Combination of cobalt ferrite and graphene: High-performance and recyclable visible-light photocatalysis, Appl Catal B: Env. 112 (2012) 280– 287. doi:10.1016/j.apcatb.2011.10.009

[50] B.B. Çırak, B. Caglar, T. Kılınç, S.M. Karadeniz, Y.Erdoğan, S. Kılıç, E. Kahveci, A. E. Ekinci, Ç. Çırak, Synthesis and characterization of ZnO nanorice decorated TiO_2 nanotubes for enhanced photocatalytic activity, Mater. Res. Bull. 109 (2019) 160–167. https://doi.org/10.1016/j.materresbull.2018.09.039

[51] I.K. Konstantinou, T.A. Albanis, TiO_2-assisted photocatalytic degradation of azo dyes in aqueous solution: kinetic and mechanistic investigations A review, Appl. Catal. B Environ. 49 (2004) 1–14. https:// doi:10.1016/j.apcatb.2003.11.010.

[52] M. Sundararajan, V. Sailaja, L. J. Kennedy, J. J. Vijaya, Photocatalytic degradation of rhodamine B under visible light using nanostructured zinc doped cobalt ferrite: Kinetics and mechanism, Ceram. Int. 43 (2017) 540–548. http://dx.doi.org/10.1016/j.ceramint.2016.09.191

[53] A. Khataee, R. D. C. Soltani, Y. Hanifehpour, M. Safarpour, H. G. Ranjbar, S. W. Joo, Synthesis and Characterization of Dysprosium-Doped ZnO Nanoparticles for Photocatalysis of a Textile Dye under Visible Light Irradiation, Ind. Eng. Chem. Res. 53 (2014) 924−1932. http://dx.doi.org/10.1021/ie402743u.

CHAPTER 4

SUPERCAPACITOR PERFORMANCE OF NITROGEN DOPED GRAPHENE SYNTHESIZED VIA DMF ASSISTED SINGLE-STEP SOLVOTHERMAL METHOD

In this chapter, a single-step dimethylformamide (DMF) assisted solvothermally synthesized nitrogen-doped reduced graphene oxide (N-rGO) was prepared as a novel electrode material The highest specific capacitance of N-rGO was found to be 516 Fg^{-1} at a scan rate of 2 mVs^{-1} along with good cyclic stability and stable coulombic efficiency. The electrochemical impedance spectroscopy study showed a typical capacitive behavior of the N-rGO and a faster frequency response with a relaxation time constant of 0.4 s. Thus, the synthesized N-rGO using this simple, cost-effective, environment-friendly method could be a potential candidate for high performance energy-storage applications

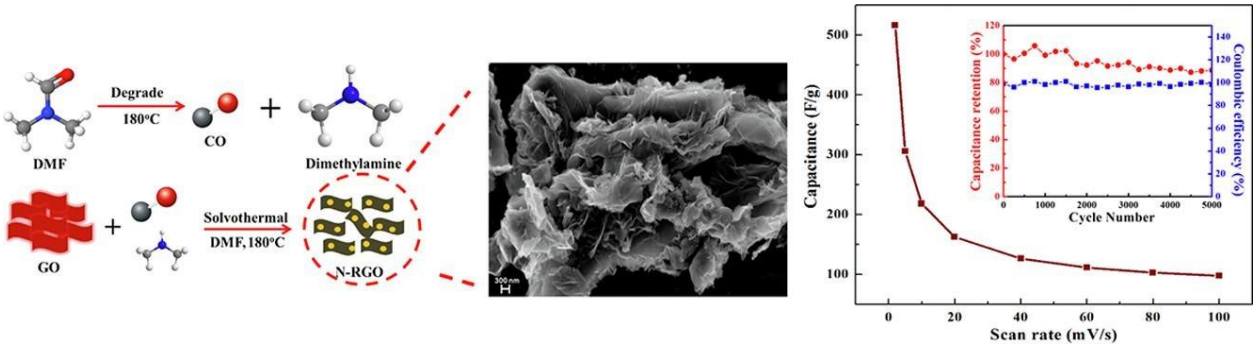

*Work published in **FlatChem** 34 (2022), p 100400. https://doi.org/10.1016/j.flatc.2022.100400*

4.1. Introduction

Today, the demand for a very fundamental requirement of mankind, energy is expected to increase significantly. The world energy assessment report estimates that consumption of global energy is going to reach about 27.6 terawatts by 2050 due to the population explosion and change in present lifestyle [1]. To achieve ever-increasing desired energy due to the fast gradual decrement of fossil fuel, global warming and pollution, researchers are forced to explore sustainable energy and efficient energy storage devices [2, 3]. One of the different energy storage systems, supercapacitors are drawing huge attention because of their high power density, environmental friendliness, long operating life and product safety [2, 4-6]. With respect to the process of charge storage and usage of the material for electrodes, supercapacitors are categorized mainly into two parts: electrical double-layer capacitors (EDLC) and pseudo-capacitor. Generally, carbonaceous materials having excellent conductivity and large specific surface area are utilized as EDLC material in which the charge storage process occurs through the physical accumulation of charges electrostatically via non Faradaic process at the interfaces of electrode and electrolyte where there is no transfer of electrons. As this category is a surface process, it strongly depends on the electrode surface area which can be accessible to the electrolyte. On the contrary, redox operative metal oxides/sulfides/hydroxides including conductive polymer composite materials have been employed as electrode material for Pseudo capacitors in which charge storage arises due to rapid electrochemical Faradaic reactions [7-11].

Graphene, a single atom thick sheet having a hexagonal honeycomb sp^2-hybridized carbon atom network has been extensively used as EDLC material as it possesses good conductivity and a large surface area of approximately 2600 m^2/g [12, 13]. By and large, graphene-based supercapacitors are effective to attain capacitance of 550 Fg^{-1} theoretically when the complete surface area is employed [14, 15]. In a practical situation, graphene electrode exhibits a specific capacitance of 130-200 Fg^{-1} which is considerably lower than that of the theoretical value as graphene have limitations in structure and surface properties [16, 17]. Particularly, due to π- π interactions, in chemically synthesized graphene, the adjacent sheets are likely to be restacked in the synthesis process associated with vigorous consequences like the extensive loss of effective surface area to be exposed to electrolyte ions thereby resulting in low specific capacitance [15, 18].

Also, that reduced capacitance arises from the hydrophobic nature of the pristine graphene, which limits the interaction of aqueous electrolyte ions with the electrode material surface [19].

One of the most effective ways to minimize the restacking is to incorporate heteroatoms on the graphene sheets by producing defects and further changing its electronic structure. Among various dopants, nitrogen has been extensively studied because it has an almost similar covalent radius as carbon and available valence electrons which can be used to form stable covalent bonds with carbon atoms and also due to the availability of abundant precursors [20, 21]. Incorporating N atoms successfully upgrade the electronic properties of graphene, particularly the supercapacitor performance as electrodes. Moreover, the doping of nitrogen with graphene can enhance the wettability which in turn can improve its accessibility of the electroactive surface area within electrolyte solution which may give rise to electrochemical performance [22].

To date, several techniques have been grown for the synthesis of nitrogen-doped graphene. Among them, some are direct synthesis methods like chemical vapour deposition (CVD) [23, 24], segregation growth method [25], arc-discharge method [26], and post-treatment synthesis procedures like hydrazine hydrate, plasma treatments [27] and heat treatment [28]. Most of these methods comprise the incorporation of nitrogen-containing precursors (polypyrrole, urea, ammonia, N_2H_4) during the doping process. In these cases, the toxicity of the corrosive, explosive, or hazardous nitrogen source (N_2H_4, NH_3) and essential involvement of special sophisticated instruments along with required rigorous conditions such as high vacuum and high temperature have to be considered. Also, the involvement of several steps limits their application for large scale production. Therefore, it remains an important challenge for developing a simple, non-toxic, low-cost, large-scale production of heteroatom-doped graphene. However, to the best of our knowledge, only a little research has been done on this aspect. Recently some works have reported that a solvothermal method using N, N-dimethylmethanamide (DMF) can be used to effectively reduce Graphene Oxide (GO) as well as to dope nitrogen into the Graphene network [29, 30].

In this work, N doped graphene, with the help of graphene oxide has been prepared by a facile solvothermal method at a reaction temperature of 180 ºC, using DMF as a source of nitrogen as well as a reducing agent. Our preparation method for nitrogen-doped graphene is more advantageous than other existing methods as the usage of harmful chemicals has been removed by using DMF and it avoids the necessity of any kind of special instrument in the reduction process and doping. The electrochemical properties of prepared N-rGO have been carried out

using cyclic voltammetry (CV), Galvanostatic charge-discharge (GCD) and electrochemical impedance spectroscopy (EIS) using a conventional three-electrode system in an aqueous 1 M Na_2SO_4 electrolyte solution. The obtained EIS data of N-rGO was furthermore investigated with respect to complex capacitance and then the relaxation time constant was calculated. Relaxation time constant defines the charge discharge rate performance of the electrode material. The N-rGO material eliminates the trend of pristine graphene sheets to be restacked, consequently creating a porous network composed of graphene sheets that is capable to provide an adequate channel for transport of charges and abundant active sites for effective ion adsorption/desorption.

4.2. Experimental details

4.2.1 Materials

For this experiment, chemicals used are Natural Graphite flakes, sulfuric acid (H_2SO_4, 98%), Sodium Nitrate ($NaNO_3$), potassium permanganate ($KMnO_4$, 99.9%), hydrogen peroxide (H_2O_2, 30%), and N, N-Dimethylformamide (DMF). All the chemicals were purchased from Sigma-Aldrich, India and have been used with no additional refinement purification.

4.2.2 Synthesis of Graphene Oxide

Graphene oxide was prepared by the modified Hummer's method with minor modifications [31]. In a typical synthesis procedure, 2g of $NaNO_3$ and 2g of graphite powder were mixed in 100 ml of concentrated H_2SO_4. Then this solution in a beaker was kept under continuous stirring after placing it on an ice bath to control the temperature between 5-15^oC. Then after 3 h of uninterrupted stirring, 10g of powdered $KMnO_4$ was added to the mixture for oxidizing the graphite powder to graphitic oxide in a very controlled manner to make sure that the temperature remains under 15^oC throughout the addition. For this step, adequate amount of ice was provided while monitoring temperature of the system continuously. Then after 1 h of reaction, the ice bath was removed and 100 ml of double-distilled water was added very slowly to the brown coloured solution in stirring condition. Consequently, due to an exothermic reaction, a large amount of heat energy was developed which helped in separating the layers of graphitic oxide to create graphene oxide (GO). At last, 10 ml of Hydrogen peroxide (H_2O_2) was added to the solution to terminate the reaction process. After that, the collected graphene oxide solution was washed several times with distilled water and ethanol, until the pH became

neutral. At last, GO was obtained through centrifugation of the suspension with an rpm of 4,000 and was dried at 60 ^{o}C.

4.2.3 Synthesis of Nitrogen doped Graphene (N-rGO)

Graphene Oxide was reduced and doped by nitrogen simultaneously in a single step solvothermal method with DMF. This is broadly used in the chemical industry as it is inexpensive and has high solvent power also can be used as the source of nitrogen. In this process, 150 mg of prepared GO was mixed with 60 ml of DMF and the solution was further sonicated. After 1 h of sonication, GO/DMF dispersion was shifted within the Teflon coated hydrothermal autoclave unit. The autoclave was then kept at the temperature of 180°C for 12 h. Afterwards, the autoclave unit was kept to come down to the ambient temperature in a natural way. Finally, black coloured nitrogen-doped reduced graphene oxide (N-rGO) was dried after getting collected and purified a number of times with distilled water and ethanol.

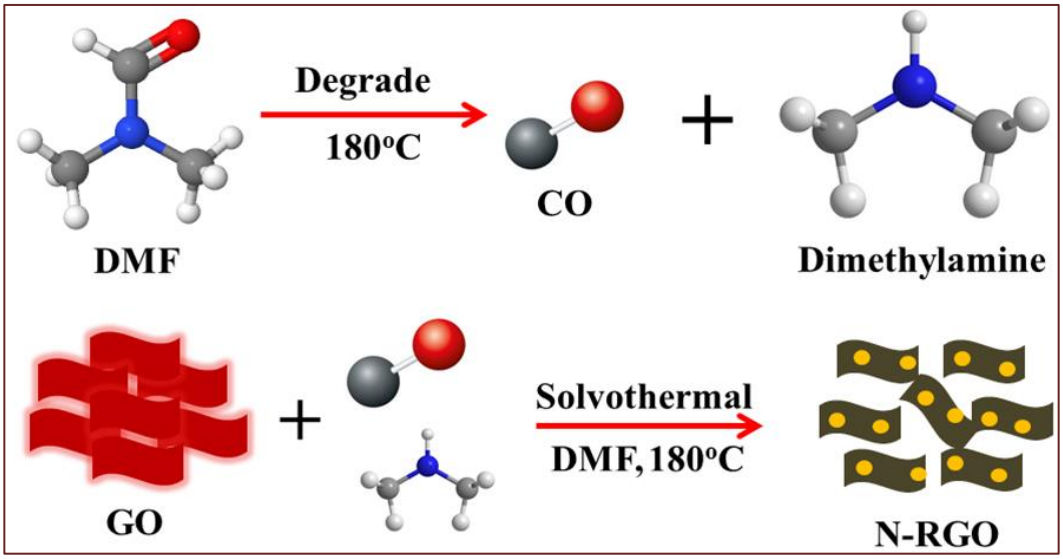

Fig. 4.1. Schematic diagram of the synthesis of nitrogen doped graphene (N-RGO).

During the synthesis process when the DMF gets heated higher than its boiling point (153 ^{o}C), it can decompose into intermediate carbon monoxide (CO) and dimethylamine [$NH(CH_3)_2$] [32, 33]. It is well known that carbon monoxide is a strong reducing agent, which can effectively remove the oxygen from graphene oxide. Therefore, it is expected that graphene oxides can be reduced by the reducing agent (CO) from DMF to produce rGO sheets in large

quantities. Additionally, simultaneous bonding of dimethyleamine with rGO gives rise to N-rGO. A schematic diagram of the synthesis process of N-rGO has been represented in **Fig. 4.1**.

4.2.4. Material Characterization

The X-ray powder diffraction (XRD) patterns for the samples were carried out by a Bruker D8 advanced Diffractometer, equipped with Cu K_α (λ=1.54059Å) radiation in the range between 5 and 75 degrees with a step size of 0.0199. The external surface morphologies of the as-prepared samples were analyzed by Field emission Scanning Electron Microscope (FEI INSPECT F50) operated at 10 kV. The Raman spectroscopy data were recorded using Raman Microscope (HORIBA, Lab RAM, HR800) at room temperature over a range of 500-2500cm^{-1}. Fourier Transformed Infrared (FTIR) spectroscopy was performed at ambient temperature by a Perkin-Elmer FTIR spectrum RXI spectrometer in transmittance mode in the range 500-4000cm^{-1}. For FTIR measurement, samples were mixed with KBr powder and pressed into pallet form by applying hydraulic pressure. The background correction was done with respect to KBr pallets. The elemental composition of as prepared N-rGO was investigated by X-ray photoelectron spectroscopy (XPS; Omicron, serial no:0571). For XPS measurement, an aqueous dispersion solution of N-rGO was prepared and spin-coated onto silicon substrate followed by air drying.

4.2.5. Electrochemical characterization

The energy storage performance of N-rGO was investigated in a traditional three-electrode system. The investigation was carried out through cyclic voltammetry (CV), Galvanostatic charge-discharge (GCD) and electrochemical impedance spectroscopy (EIS) techniques on a multichannel electrochemical station (CS313 CorrTest, China). Three electrode system is composed of a working electrode, counter electrode and reference electrode. For the preparation of the working electrode, 85% active material N-rGO, 10% conducting additive acetylene black and 5% binder PVDF-HFP were mixed in N-Methyl Pyrrolidine (NMP) solvent to form a slurry. After that, the slurry was layered onto Teflon-coated graphite rod. This was then dried keeping at 60 ºC (in a vacuum oven). The value of the loaded mass of the active material was 0.8 mg. Platinum (Pt) electrode (1cm × 1cm) was used as the counter electrode and for the reference electrode, Ag/AgCl in saturated KCl solution was employed. As an electrolyte, a 1 M Na_2SO_4 aqueous solution was used.

Calculation of the specific capacitance (C_m) is performed from CV curves using the following formula

$$C_m = \frac{i}{2mv} \quad (1)$$

Where m stands for the mass of the active material and v is the scan rate. The value of i is attained by calculating the bound surface area of the CV curve by applying the following equation

$$i = \frac{\int_{v_a}^{v_c} i(v)dv}{v_c - v_a} \quad (2)$$

Where, v_c and v_a indicate the lowest and highest end value respectively of the potential range. The value specific capacitance can also be obtained from GCD curves using the following formula:

$$C_m = \frac{i}{(-\frac{dv}{dt})} \quad (3)$$

Here i stands for the applied current density in Ag^{-1} and, $\frac{dv}{dt}$ is the average slope of the discharge curve.

4.3. Results and discussions:

4.3.1 XRD

The structural characterization of graphite powder, as prepared graphene oxide (GO) and N-rGO were investigated by powder X-ray diffraction (XRD) method and presented in **Fig. 4.2**.

The XRD spectrum of Pristine graphite (Inset **Fig. 4.2**) exhibits a strong intense peak at around 26.33° ascribed to (002) plane having an interlayer spacing of 0.34 nm. After the process of chemical oxidation with $KMnO_4$, exfoliated GO exhibits a prominent peak at 11.63° associated with the (002) plane having an interlayer spacing of 0.76 nm.

In the XRD spectrum of GO, the appearance of the peak at 11.63° and the vanishing of the peak at 26.33° show the successful transformation of graphite to graphene oxide [19]. The greater interlayer spacing for GO is associated with the introduction of different oxygenated functional groups like carboxylic, carbonyl, hydroxyl, epoxy etc. at the time of oxidation. Finally, for N- rGO, two diffraction peaks are observed at 25.16° and 43.12° which arise due to the (002) and (100) planes respectively. The peak at 25.16° also indicates effective exfoliation and hence formation of multiple layers of graphene [19,20].

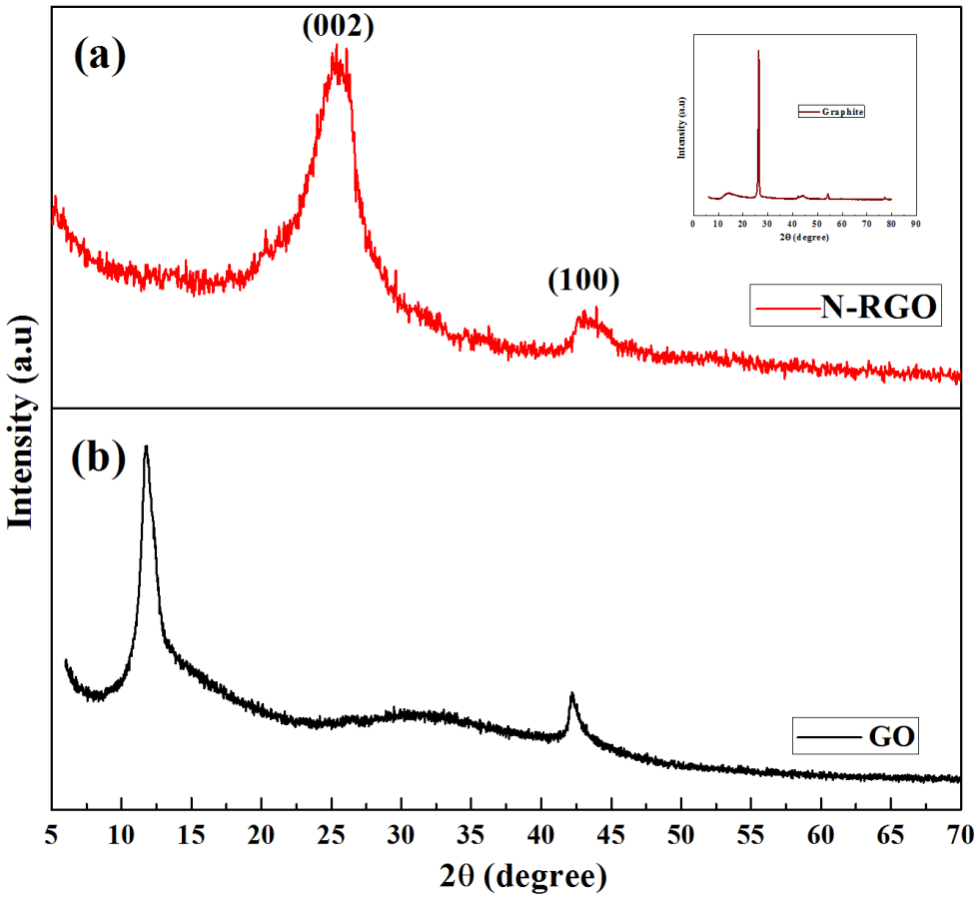

Fig. 4.2. XRD pattern of GO, N-rGO and Graphite powder (inset).

In N-rGO, the small-angle peak at 11.63° got disappeared which indicates that graphene oxide is reduced effectively by the solvothermal process.

4.3.2. SEM analysis

The structural and morphological analysis of GO and the N-rGO was carried out by the high-resolution scanning electron microscopy (SEM). **Fig. 4.3a** and **4.3b** depict the representative SEM image of the GO which reveals classic exfoliated nanosheets with almost flat and smooth morphology with a number of stacked layers which happened due to the exfoliation followed by restacking during the synthesis process. Functionalization with nitrogen eliminated the restacking tendency of graphene sheets effectively as shown in **Fig 4.3c,d.** Furthermore, in the case of N-rGO, the sheets after exfoliation were arranged randomly and as a result, numerous crumpled layers were created which are connected. This change in morphology can be attributed to the doping of nitrogen which introduced high-density defects in the N-rGO surface leading to a fluffy structure in the solvothermal process. This kind of graphene structure having

highly open porous surfaces tangled with each other is effective to construct electrode materials that can be highly accessible to the electrolyte solution which in turn provides adequate space to form EDLC [34, 35]. In addition, the corresponding energy dispersive X-ray (EDX) spectrum study performed on N-rGO as presented in **Fig. 4.3e** depicts the presence of C, N and O and gives confirmation about the successful incorporation of Nitrogen in graphene sheets. The presence of a very small amount of oxygen may be developed either from the oxygen incorporated with nitrogen or from an oxygen-containing functional group in graphene that could not be reduced fully by the solvothermal treatment [15].

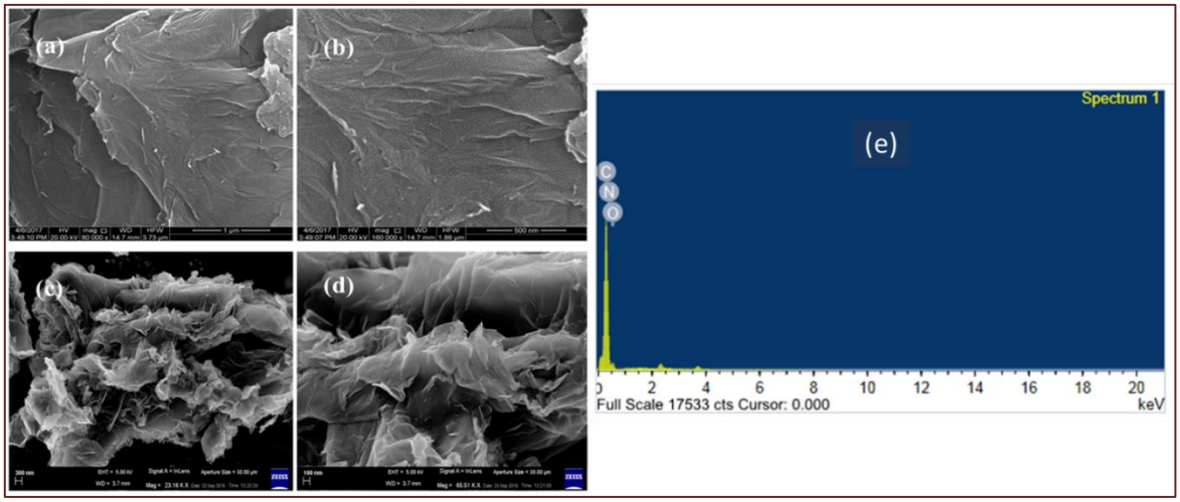

Fig. 4.3. (a), (b) SEM image of GO and (c), (d) of N-rGO sheets at different magnification. (e) EDX spectrum of N-rGO.

4.3.3 Raman analysis

Fig. 4.4a represents Raman spectra of as-prepared GO and N-rGO. Raman spectroscopy comes up with very useful information for graphene as this is very sensitive to carbonaceous material to investigate the structural property. In the Raman spectra, the characteristic D band is observed at 1337 cm^{-1} and 1329 cm^{-1} whereas the G band is noticed at 1591 cm^{-1} and 1585 cm^{-1} for GO and N-rGO respectively. Usually, the D band is originated from the presence of disorderliness of carbon or defected mode of the carbonaceous materials, whereas the G band arises from the vibration related to the sp^2-hybridized carbon atoms in the graphitic materials and is common to all sp^2 carbon materials [21,31]. Compared to the Raman spectra of GO, N-rGO exhibits a red shift of the G-band (6 cm^{-1}) indicating restoration of sp^2 graphitic domains in N-rGO during the process of solvothermal reduction [36].

The intensities for the peak of the D and G band are represented as I_D and I_G respectively. The order for the graphene structuring which is determined by the relative ratio of I_D and I_G (I_D /I_G) is associated with structural defects like boundaries, vacancies, disorders and the presence of heteroatoms. The (I_D/I_G) value is approximately 1.200 and 1.263 for GO and N-rGO respectively. The ratio of intensity in the case of the N-rGO compared to GO has slightly increased which may be due to thermally derived defects during the reduction process and introduction of the nitrogen atom in the graphene network [21, 22].

4.3.4. FTIR analysis

The FTIR spectra of GO, and N-rGO have been represented in **Fig. 4.4b.** In the spectrum of GO, a broad band situated at around 3234 cm^{-1} is observed, which can be related to the O-H stretching vibration of water. Another two absorption peaks can be observed at 1740 and 1632 cm^{-1} which are associated with C=O group stretching vibration and the skeletal vibrations from the un-oxidized graphitic network respectively. And the rest two absorption peaks at 1226 and 1056 cm^{-1} appeared due to C-OH and C-O stretching vibrations respectively. All the mentioned peaks are characteristic peaks of GO which confirms the successful synthesis of GO [37, 38]. Contrarily, in the FTIR spectrum of N-rGO, the absorption peak at 3234 cm^{-1} got disappeared, which may be associated with the elimination of the OH group in the reduction process. Moreover, for the N-rGO, the disappearance of other absorption peaks due to oxygeneous groups confirms the successful reduction of GO in solvothermal treatment. Additionally, two absorption peaks can be observed at 1595 and 1210 cm^{-1}, which may arise because of the bands of C=C and C–N respectively confirms the effective doping of Nitrogen into graphene [2,39].

4.3.5. XPS analysis

The elemental composition and detailed configuration of nitrogen bonding of the synthesized N-rGO were additionally investigated by X-ray photoemission spectroscopy (XPS). As can be observed in **Fig. 4.5a,** the wide scanning spectra of the prepared N-rGO depicts the peak at 284 eV which is associated with the binding energy related to C *1s* electron orbit. Another peak at 534 eV indicates the binding energy related to O *1s* electron orbit. Also, it can be observed additional distinct existence of a peak in the region of 400 eV, which is correlated with the binding energy linked with N *1s* electron orbit, establishing the successful incorporation of Nitrogen in the graphene network [25, 26].

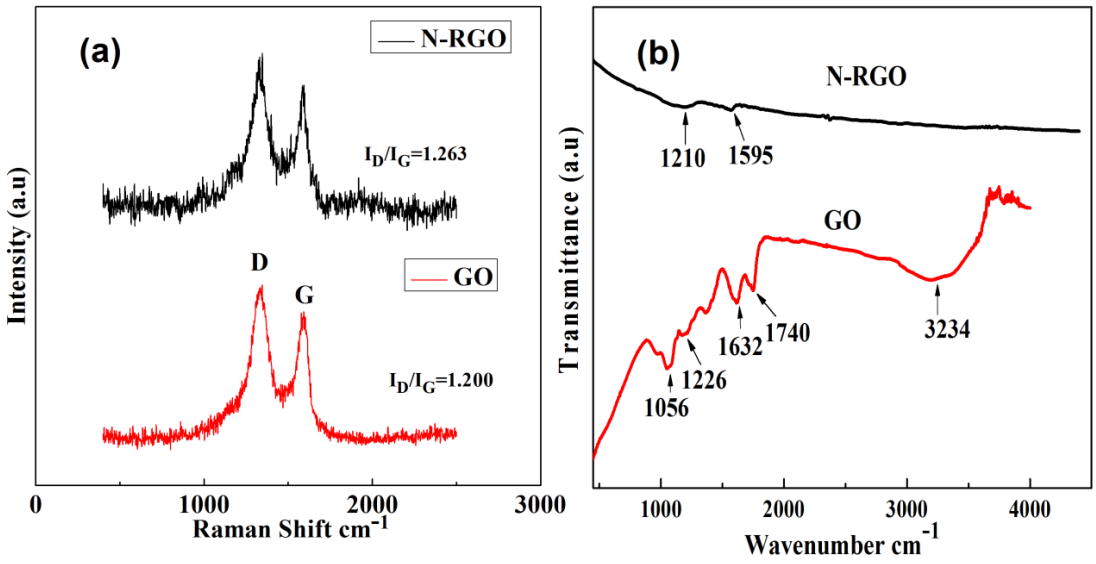

Fig. 4.4. (a) Raman spectra of GO and N-rGO (b) FTIR spectra of GO and N-rGO.

Furthermore, to rigorously investigate the specific configurations of bonding in N-rGO, the high-resolution spectra for N *1s* and C *1s* are obtained and represented in **Fig 4.5b**,**c** sequentially. The N *1s* spectrum (**Fig. 4.5b)** was de-convoluted into three peaks centered at 398.17, 399.77 and 400.45 eV are associated with the N-6 (pyridinic N), N-5 (pyrrolic N), and N-Q (graphitic N) respectively [22, 25, 40].

The schematic diagram **Fig. 4.5d** depicts the probable arrangements for N atoms bonding in N-rGO. The N-Q bonding indicates the N atom as a replacement of a Carbon atom in the honeycomb lattice. The N-6 bonding is related to the bond between two C atoms and one N at the border of the graphene lattice. Whereas, the N-5 indicates the N atom bonding situated in a five-membered ring structure [41]. Previous reports have shown pyrrolic N can produce a large number of active sites and extrinsic defects on the graphitic basal plane, which can increase the wettability of N-rGO in the electrolyte solution consequently improving mass-transfer efficiency [22, 42]. While the N-6 and N-Q bonds are able to supply two electrons to the conductive π-system as they are connected with two and three sp^2 Carbon atoms, respectively [43]. Both of those N atoms can provide one extra electron to the π-system, which is supposed to significantly improve the conductivity of graphene [15, 44, 45]. Additionally, the N-Q group of atoms can enhance its interactivity with the negatively charged ions in the electrolyte solution for the development of the electrical double layer, which is helpful for the enhancement of the capacitance [45]. Hence, this N-rGO material can be a good candidate to be an electrode for high-performance supercapacitor applications.

Similarly, the C *1s* spectrum **(Fig. 4.5c)** can be convoluted into three peaks, which are detected at 284.43, 285.20, and 287.19 eV respectively. The main peak at around 284.43 eV is associated with graphite-like sp^2 C atoms constituting a graphitic lattice, from which it can be inferred that maximum carbon atoms are distributed in a honeycomb lattice. Another two weak peaks are detected at 285.20 and 287.19 eV corresponding to sp^3 C atoms and the C-N group respectively [46]. In addition, the O *1s* spectrum was fitted into two subpeaks situated at 531.03, and 533.14 eV **(Fig. 4.5e),** which correspond to different oxygeneous functionalities such as C=O, and O=C-O, respectively [47]. It is to be considered that the presence of oxygen-containing functional groups in N-rGO can reduce its conductivity and prevent ions from penetrating deep into its pore [48]. But they are advantageous for the capacitance value as it can enhance the hydrophilic nature facilitating the diffusion of ions on the electrode surface [49]; eventually making it smooth for ions for developing an electrochemical double layer which in turn increases the capacitance [48-50].

4.3.6. Electrochemical property analysis

As discussed earlier in section 2.5, an investigation for the electrochemical performances of N-rGO has been executed in a typical three-electrode system applying cyclic voltammetry (CV), galvanostatic charge-discharge (GCD) and electrochemical impedance spectroscopy (EIS) method in 1M Na_2SO_4 aqueous electrolyte at room temperature. **Fig. 4.6a** displays all the CV curves for N- RGO at different scan rates varying from 2 to 100 mVs^{-1} in the potential window from – 0.2 to + 0.9 V. Shapes of all the CV curves of the N-rGO sheets-based electrode clearly depicts approximately ideal rectangular shape without any prominent visible redox peak indicating the characteristic of ideal electrical double layer capacitors (EDLC).

It is worth noting that each of the CV curves persisted rectangular in shape without any significant change even for high scan rates of 100 mVs^{-1}, which suggests that the electrode is highly stable in nature [22, 51]. The value of the specific capacitance at different scan rate of the synthesized material was calculated using equation (1) and its variation with scan rate has been presented in **Fig. 4.6c.** It can be noted that when the scanning rate increases, specific capacitance decreases which is associated with the movement of electrolyte ions through the electrode.

In case of a low scan rate, ions can have sufficient time for reaching both inner as well as the outer surface of the electrode and it results in more accumulation of charges enhancing the specific capacitance. Whereas in the case of a high scan rate, for the ions, mobility is higher

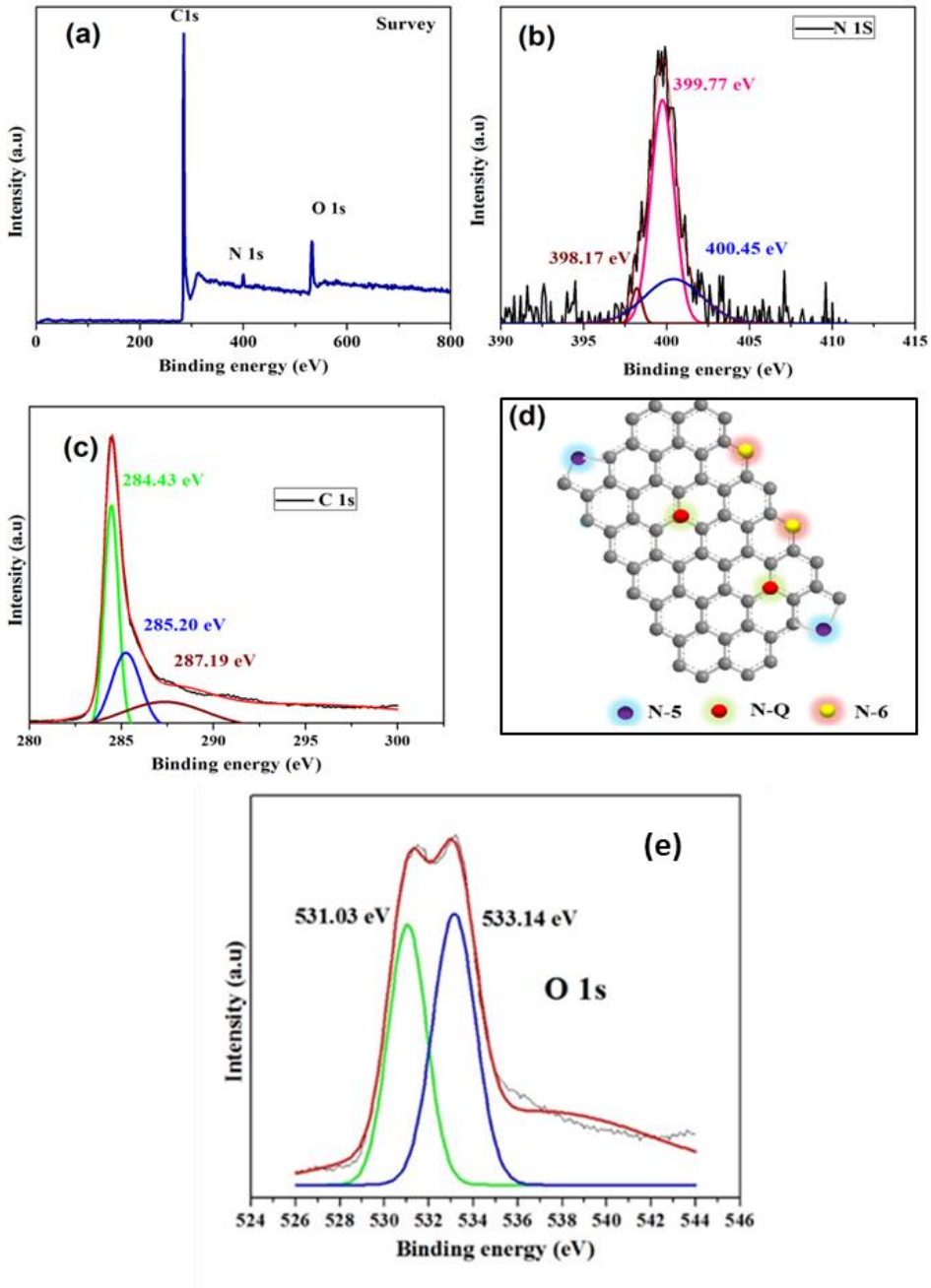

Fig. 4.5. XPS spectra of N-rGO sample showing the (a) whole spectra, (b) high-resolution N*1s* spectrum and (c) C*1s* spectrum of the N-rGO; (d) Schematic showing the possible locations for nitrogen incorporation into the carbon network.(e) O1s XPS spectra of N-rGO

and as a consequence, they don't get adequate time to access the inner surface area of the electrode which eventually decreases the amount of charge accumulation as well as capacitance. From the calculated value, the highest specific capacitance of N-rGO is 516 Fg^{-1} at 2 mVs^{-1}. Our electrode material exhibited superior electrochemical performance to other reported results for Nitrogen doped graphene and almost reached the theoretical value of specific capacitance of pristine graphene. **Table 4.1.** has been presented to compare the value

of specific capacitance of our N-rGO material with other Nitrogen doped reduced graphene oxides in various electrolyte solutions which already have been reported in different literatures. **Fig. 4.6b** represents Galvanometric charge discharge (GCD) curves of N-rGO within the potential window from – 0.2V to + 0.9V for various current densities (3, 5, 7.5, and 10 Ag^{-1}) with respect to the reference electrode, which is same as the CV measurement. The curves exhibit almost linear and symmetrical shapes in 1 M Na_2SO_4 electrolyte, and no prominent IR drop is visible in any curve which indicates good electrochemical reversibility and excellent transport of carrier inside the electrodes for the EDLCs. The highest calculated specific capacitance from GCD curves of N-rGO is 494.31 Fg^{-1} at $3Ag^{-1}$, as calculated from equation (3). It can also be observed that GCD curves have some trail, particularly at 3 Ag^{-1}. This possibly happens as at very low current density, the ions can penetrate deep into active material and thus discharge mechanism becomes very sluggish which results in a trail in the GCD plot. In order to explore the long term cyclic stability of the prepared N-rGO for practical application, the cyclic charging discharging test was assessed within the potential window from – 0.2 to + 0.9V for 5000 cycle at a constant current density 10 Ag^{-1}. **Fig. 4.7** displays the capacitance retention rate and coulombic efficiency of the N-rGO electrode as a function of the cycle numbers. Initially, the specific capacitance decreases to 97% of the starting value then

Table 4.1. Electrochemical supercapacitor performances of the N-doped reduced graphene oxide electrodes prepared by different methods.

Materials	Synthesis process	Electrolyte	Specific capacitance Fg^{-1}	Scan rate/ Current density	Ref.
NRGO	Microwave assisted hydrothermal method	1 M H_2SO_4	233	25 mV/s	[52]
N-rGO	Thermal expansion-exfoliation	0.5 M H_2SO_4 1 M $TEABF_4$	234.3 187.8	5 mV/s 5 mV/s	[53]
NRGO	Hydrothermal	1 M H_2SO_4 6 M KOH	199 179	0.1 Ag^{-1} 0.1 Ag^{-1}	[54]
NG	Aerogel via vacuum filtration and freeze drying	0.5 M H_2SO_4	455.4	1 Ag^{-1}	[55]
3D-Porous nitrogen doped graphene	Thermal decomposition method	6 M KOH	405	1 Ag^{-1}	[50]
N-rGO	Solvothermal method	1.0 M Na_2SO_4	516	2 mV/s	This work

starts to increase upto 750th cycle to the value of 105% of the starting value. After that specific capacitance started to decrease and then reached a value of 89% of the initial value after 5000 GCD cycles which shows long time stability. The coulombic efficiency, η (%) is represented as [t_d /t_c)×100] where, t_d (s) stands for the discharge time, and t_c (s) is the charge time. In case of coulombic efficiency, it was found to be quite stable and almost 100% efficiency was observed through all the cycles with slight deviation.

Such an outstanding electrochemical behavior of the as-prepared N-rGO electrode may be assigned to the introduction of nitrogen doping in graphene which provides the high specific area and active sites to allow efficient ion adsorption/desorption. In addition, Nitrogen doping in N-rGO, minimizes the level of agglomeration in graphene sheets and generates fluffy structure along with interconnected open pores consequently enhancing the wettability, which is advantageous for efficient charge transportation.

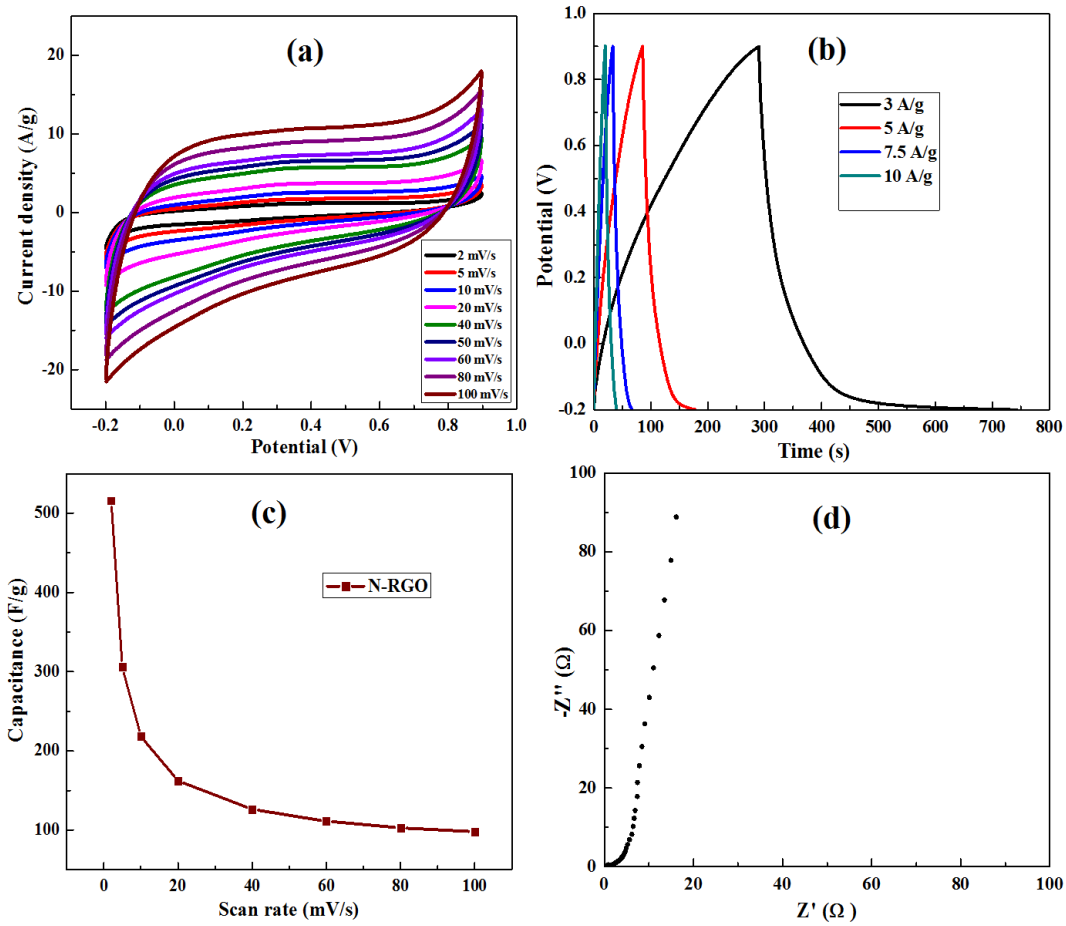

Fig. 4.6. Electrochemical performance of the prepared N-rGO in 1M Na_2SO_4 electrolyte (a) CV curves at different scan rates (b) Galvanostatic charge discharge curves at different current densities (c) the effect of increasing the scan rate on the specific capacitance. (d) Nyquist plot.

The electrochemical behavior of the N-rGO electrode and the function of the electrolyte was investigated by the EIS technique within the frequency span from 0.01 to 100 kHz with the perturbation voltage of 10 mV. **Fig. 4.6d** exhibits the Nyquist plot of the N-rGO. Based on the value of frequency, the observed Nyquist plot can be split up into three distinct parts, which are low, mid and high.

In the case of low frequency, EIS data exhibit a steep rise of the imaginary impedance approaching 90° suggesting a good capacitive behavior with electrode stability [50, 56]. This can be ascribed to the good exposure between electrode and the electrolyte. In high-frequency domain, where the EIS curve intersects the Z' axis, gives the value of electrolyte resistance (R_s) which is close to 0.48 Ω.

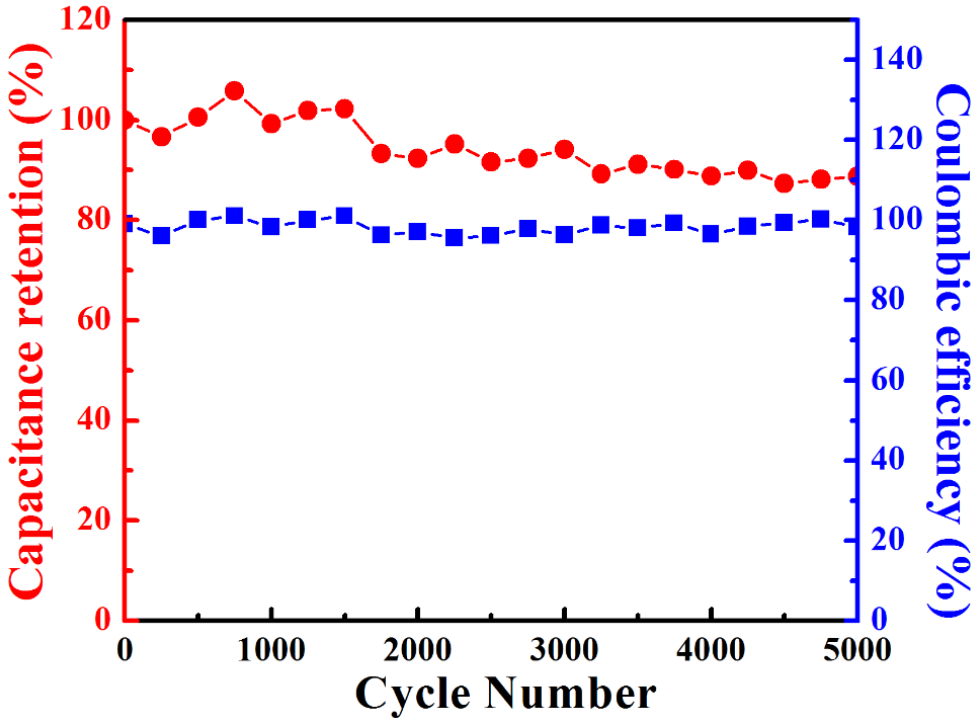

Fig. 4.7. Cyclic stability and Coulombic efficiency of N-rGO for 5000 cycles.

Moreover, a small distorted semicircle with a diameter of 0.71 Ω in the high-frequency region can be observed and that can be associated with the charge transfer resistance (R_{ct}). The R_{ct} is ascribed to the total value of the electrode resistance, the electrolyte resistance, and the contact resistance between the electrode and the current collector [57].

Furthermore, complex capacitance calculations were conducted for better comprehension. The variation of the electrode capacitance with respect to frequency was carried out from EIS data,

making use of the complex capacitance model [58] in which, the capacitance is represented as follows:

$$C(\omega) = C'(\omega) - j\,C''(\omega)$$

where, $C'(\omega)$ and $C''(\omega)$ are the real and imaginary parts of the capacitance respectively and are stated as:

$$C'(\omega) = \frac{-Z''(\omega)}{\omega|Z(\omega)|^2}$$

$$C''(\omega) = \frac{Z'(\omega)}{\omega|Z(\omega)|^2}$$

Where ω indicates the angular frequency, $Z'(\omega)$ and $Z''(\omega)$ stand for the real part and the imaginary part of the impedance respectively, and the term $|Z(\omega)|$ represents to the modulus of impedance. This model is effective to investigate the qualitative study of the variation of capacitance in regard to frequency.

Fig. 4.8a depicts the variation of the real part of capacitance [$C'(\omega)$] with respect to frequency. The change of capacitance with the frequency represents the electrolyte ion penetration pattern inside the pores of active material at a specific frequency.

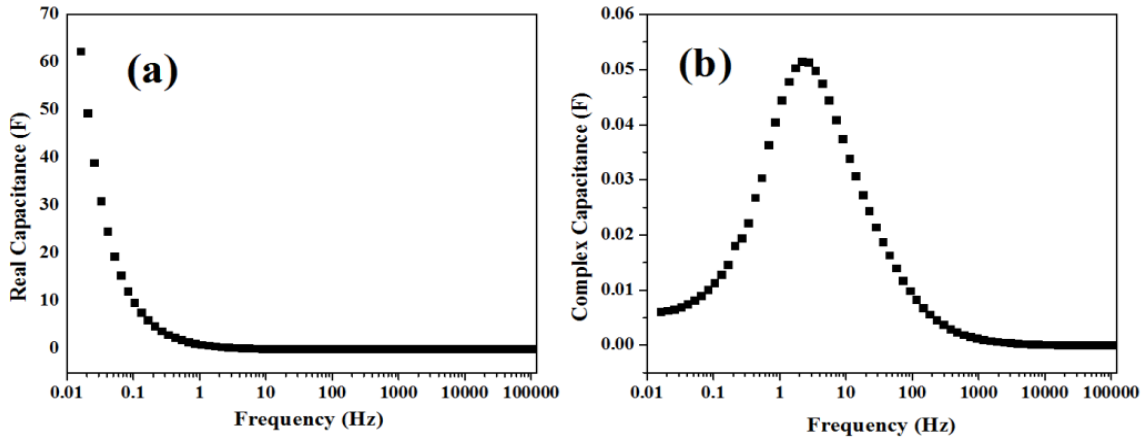

Fig. 4.8. (a) Behavior of the real specific capacitance of N-rGO as a function of frequency at 1M Na_2SO_4 solution. (b) The imaginary part of the complex capacitance C" as a function of frequency.

In the lower frequency range, the electrolyte ions get enough time to reach deep down the inside surfaces of N-rGO and hence more charge storage occurs which results in an increment of $C'(\omega)$. On the contrary, in the higher frequency range, only outer surface of the electrode is accessible to the electrolyte ions within a short time interval which results in inadequate charge accumulation leading to a significant reduction in capacitance. Also, it can be observed that at excessively high frequencies, $C'(\omega)$ does not depend on the frequency and it acts like a resistor

[58]. Variation of $C''(\omega)$ with frequency has been represented in **Fig. 4.8b** which gives an additional information about the relaxation time constant (τ_o) as it passes through a maximum value at a frequency, f_0. The values of the relaxation time constants are calculated by taking the inverse of f_0 [59, 60]. τ_o is also associated with the time which is needed for the discharge of all the stored energy with an efficiency greater than 50% [61]. Materials having small relaxation are capable of delivering power rapidly and possess high power density [62]. The calculated value of τ_o in the case of our N-rGO electrode is about 0.4 s. Considering the fact, that τ_o essentially represents the minimum time needed for effectively delivering the stored energy, the calculated value for N-rGO indicates a satisfactory ability for quick delivery of high power.

4.4. Conclusion

In conclusion, we have used a facile single-step approach for the preparation of nitrogen-doped graphene using DMF which acts as a nitrogen source and reducing material at the same time. This method is advantageous over other conventional methods as it does not involve highly corrosive and toxic elements such as NH_3 and is free from multiple complicated steps. EDX spectrum, FTIR and XPS confirmed the incorporation of nitrogen in graphene sheets. The electrode prepared from N-rGO exhibits excellent charge storing property with a specific capacitance of 516 Fg^{-1} at a scan rate of 2 mVs^{-1} in 1.0 M Na_2SO_4 aqueous electrolyte solution. Such remarkable electrochemical performance of our synthesized N-rGO can be ascribed to the interconnected, porous nanosheets with reduced restacking and hence highly available surface area, good conductivity and wettability. The EIS data for N-rGO depicted good capacitive behavior and corresponding relaxation time constant of 0.4 s signifying its faster response time. In addition, our electrode material was found to have good cyclic performance (89%) capacitance retention after 5000 cycles) and almost stable Coulombic efficiency. Thus, the N-doped graphene prepared using this single step method has the potential for its use in advanced energy storage applications.

References

[1] N. S. Lewis and D. G. Nocera, "Powering the planet: Chemical challenges in solar energy utilization," *Proceedings of the National Academy of Sciences*, vol. 103, pp. 15729-15735, 2006.

[2] Y. Miao, Y. Ma, and Q. Wang, "Plasma-assisted simultaneous reduction and nitrogen/sulfur codoping of graphene oxide for high-performance supercapacitors," *ACS Sustainable Chemistry & Engineering*, vol. 7, pp. 7597-7608, 2019.

[3] X. Li, S. Ding, X. Xiao, J. Shao, J. Wei, H. Pang, *et al.*, "N, S co-doped 3D mesoporous carbon–Co 3 Si 2 O 5 (OH) 4 architectures for high-performance flexible pseudo-solid-state supercapacitors," *Journal of Materials Chemistry A*, vol. 5, pp. 12774-12781, 2017.

[4] Y. Zhu, S. Murali, M. D. Stoller, K. Ganesh, W. Cai, P. J. Ferreira, *et al.*, "Carbon-based supercapacitors produced by activation of graphene," *science*, vol. 332, pp. 1537-1541, 2011.

[5] G. Wang, L. Zhang, and J. Zhang, "A review of electrode materials for electrochemical supercapacitors," *Chemical Society Reviews*, vol. 41, pp. 797-828, 2012.

[6] M. Liu, M. Shi, W. Lu, D. Zhu, L. Li, and L. Gan, "Core–shell reduced graphene oxide/MnOx@ carbon hollow nanospheres for high performance supercapacitor electrodes," *Chemical Engineering Journal*, vol. 313, pp. 518-526, 2017.

[7] S. S. Balaji, M. Sandhiya, and M. Sathish, "Enhanced electrochemical performance of supercritical fluid aided P-doped graphene nanoflakes by I3−/I− redox couple," *Journal of Energy Storage*, p. 102085, 2020.

[8] Y. Zhu, S. Cheng, W. Zhou, J. Jia, L. Yang, M. Yao, *et al.*, "Construction and performance characterization of α-Fe2O3/rGO composite for long-cycling-life supercapacitor anode," *ACS Sustainable Chemistry & Engineering*, vol. 5, pp. 5067-5074, 2017.

[9] S. Saha, A. Roy, A. Ray, T. Das, M. Nandi, B. Ghosh, *et al.*, "Effect of particle morphology on the electrochemical performance of hydrothermally synthesized NiMn2O4," *Electrochimica Acta*, p. 136515, 2020.

[10] L.-H. Tseng, C.-H. Hsiao, D. D. Nguyen, P.-Y. Hsieh, C.-Y. Lee, and N.-H. Tai, "Activated carbon sandwiched manganese dioxide/graphene ternary composites for supercapacitor electrodes," *Electrochimica Acta*, vol. 266, pp. 284-292, 2018.

[11] J. Li, D. Xiong, L. Wang, M. K. S. Hirbod, and X. Li, "High-performance self-assembly MnCo2O4 nanosheets for asymmetric supercapacitors," *Journal of Energy Chemistry*, vol. 37, pp. 66-72, 2019.

[12] K. Xia, Q. Li, L. Zheng, K. You, X. Tian, B. Han, *et al.*, "Controllable fabrication of 2D and 3D porous graphene architectures using identical thermally exfoliated graphene oxides as precursors and their application as supercapacitor electrodes," *Microporous and Mesoporous Materials*, vol. 237, pp. 228-236, 2017.

[13] Y. Sun, Q. Wu, and G. Shi, "Graphene based new energy materials," *Energy & Environmental Science*, vol. 4, pp. 1113-1132, 2011.

[14] M. F. El-Kady, V. Strong, S. Dubin, and R. B. Kaner, "Laser scribing of high-performance and flexible graphene-based electrochemical capacitors," *Science*, vol. 335, pp. 1326-1330, 2012.

[15] S. Dai, Z. Liu, B. Zhao, J. Zeng, H. Hu, Q. Zhang, *et al.*, "A high-performance supercapacitor electrode based on N-doped porous graphene," *Journal of Power Sources*, vol. 387, pp. 43-48, 2018.

[16] L. Kong, Q. Ma, Z. Xu, X. Shen, J. Wang, and J. Zhu, "Three-dimensional graphene network deposited with mesoporous nitrogen-doped carbon from non-solvent induced phase inversion for high-performance supercapacitors," *Journal of Colloid and Interface Science,* vol. 558, pp. 21-31, 2020.
[17] L. Xu, J. Wu, W. Zhou, F. Jiang, H. Zhang, R. Wang, *et al.*, "Using nitroaromatic fused-heterocycle molecules as nitrogen source to hugely boost the capacitance performance of graphene," *Electrochimica Acta,* vol. 354, p. 136703, 2020.
[18] X. Zhou, Z. Bai, M. Wu, J. Qiao, and Z. Chen, "3-Dimensional porous N-doped graphene foam as a non-precious catalyst for the oxygen reduction reaction," *Journal of Materials Chemistry A,* vol. 3, pp. 3343-3350, 2015.
[19] H. Zhang, T. Kuila, N. H. Kim, D. S. Yu, and J. H. Lee, "Simultaneous reduction, exfoliation, and nitrogen doping of graphene oxide via a hydrothermal reaction for energy storage electrode materials," *Carbon,* vol. 69, pp. 66-78, 2014.
[20] K. H. Lee, J. Oh, J. G. Son, H. Kim, and S.-S. Lee, "Nitrogen-doped graphene nanosheets from bulk graphite using microwave irradiation," *ACS applied materials & interfaces,* vol. 6, pp. 6361-6368, 2014.
[21] S. S. Balaji, A. Elavarasan, and M. Sathish, "High performance supercapacitor using N-doped graphene prepared via supercritical fluid processing with an oxime nitrogen source," *Electrochimica Acta,* vol. 200, pp. 37-45, 2016.
[22] Y. Yang, W. Shi, R. Zhang, C. Luan, Q. Zeng, C. Wang, *et al.*, "Electrochemical exfoliation of graphite into nitrogen-doped graphene in glycine solution and its energy storage properties," *Electrochimica Acta,* vol. 204, pp. 100-107, 2016.
[23] D. Wei, Y. Liu, Y. Wang, H. Zhang, L. Huang, and G. Yu, "Synthesis of N-doped graphene by chemical vapor deposition and its electrical properties," *Nano letters,* vol. 9, pp. 1752-1758, 2009.
[24] L. Qu, Y. Liu, J.-B. Baek, and L. Dai, "Nitrogen-doped graphene as efficient metal-free electrocatalyst for oxygen reduction in fuel cells," *ACS nano,* vol. 4, pp. 1321-1326, 2010.
[25] C. Zhang, L. Fu, N. Liu, M. Liu, Y. Wang, and Z. Liu, "Synthesis of nitrogen-doped graphene using embedded carbon and nitrogen sources," *Advanced materials,* vol. 23, pp. 1020-1024, 2011.
[26] N. Li, Z. Wang, K. Zhao, Z. Shi, Z. Gu, and S. Xu, "Large scale synthesis of N-doped multi-layered graphene sheets by simple arc-discharge method," *Carbon,* vol. 48, pp. 255-259, 2010.
[27] M. Rybin, A. Pereyaslavtsev, T. Vasilieva, V. Myasnikov, I. Sokolov, A. Pavlova, *et al.*, "Efficient nitrogen doping of graphene by plasma treatment," *Carbon,* vol. 96, pp. 196-202, 2016.
[28] Z.-S. Wu, W. Ren, L. Xu, F. Li, and H.-M. Cheng, "Doped graphene sheets as anode materials with superhigh rate and large capacity for lithium ion batteries," *ACS nano,* vol. 5, pp. 5463-5471, 2011.
[29] R. Wang, C. Xu, J. Sun, L. Gao, and H. Yao, "Solvothermal-induced 3D macroscopic SnO2/nitrogen-doped graphene aerogels for high capacity and long-life lithium storage," *ACS applied materials & interfaces,* vol. 6, pp. 3427-3436, 2014.
[30] R. Wang, C. Xu, J. Sun, and L. Gao, "Three-dimensional Fe 2 O 3 nanocubes/nitrogen-doped graphene aerogels: Nucleation mechanism and lithium storage properties," *Scientific reports,* vol. 4, pp. 1-7, 2014.
[31] B. Mandal, J. Panda, P. K. Paul, R. Sarkar, and B. Tudu, "MnFe2O4 decorated reduced graphene oxide heterostructures: Nanophotocatalyst for methylene blue dye degradation," *Vacuum,* vol. 173, p. 109150, 2020

[32] J. Muzart, "N, N-Dimethylformamide: much more than a solvent," *Tetrahedron*, vol. 65, pp. 8313-8323, 2009.
[33] Kao, W. Y., Chen, W. Q., Chiu, Y. H., Ho, Y. H., & Chen, C. H. (2016). General solvent-dependent strategy toward enhanced oxygen reduction reaction in graphene/metal oxide nanohybrids: effects of nitrogen-containing solvent. Scientific reports, 6(1), 1-11, 2016.
[34] Sethi, M., Shenoy, U. S., & Bhat, D. K. (2020). Porous graphene–NiCo 2 O 4 nanorod hybrid composite as a high performance supercapacitor electrode material. New Journal of Chemistry, 44(10), 4033-4041.
[35] Aldalbahi, A., Rahaman, M. & Almoiqli, M. Performance Enhancement of Modified 3D SWCNT/RVC Electrodes Using Microwave-Irradiated Graphene Oxide. Nanoscale Res Lett 14, 351 (2019). https://doi.org/10.1186/s11671-019-3174-9..
[36] J. Lee, H. Kim, A. Kim, and H. Jung, "Nitrogen-doped mesoporous graphene with fine-tuned pore size in a few nanometer-scale for supercapacitor applications," *Microporous and Mesoporous Materials*, vol. 293, p. 109794, 2020.
[37] D. Konios, M. M. Stylianakis, E. Stratakis, and E. Kymakis, "Dispersion behaviour of graphene oxide and reduced graphene oxide," *Journal of colloid and interface science*, vol. 430, pp. 108-112, 2014.
[38] Y. Gong, D. Li, Q. Fu, and C. Pan, "Influence of graphene microstructures on electrochemical performance for supercapacitors," *Progress in Natural Science: Materials International*, vol. 25, pp. 379-385, 2015.
[39] J. Porwal, N. Karanwal, S. Kaul, and S. L. Jain, "Carbocatalysis: N-doped reduced graphene oxide catalyzed esterification of fatty acids with long chain alcohols," *New Journal of Chemistry*, vol. 40, pp. 1547-1553, 2016.
[40] Z. Li, W. He, X. Wang, X. Wang, M. Song, and J. Zhao, "N/S dual-doped graphene with high defect density for enhanced supercapacitor properties," *International Journal of Hydrogen Energy*, vol. 45, pp. 112-122, 2020.
[41] H. Wang, T. Maiyalagan, and X. Wang, "Review on recent progress in nitrogen-doped graphene: synthesis, characterization, and its potential applications," *Acs Catalysis*, vol. 2, pp. 781-794, 2012.
[42] L.-F. Chen, X.-D. Zhang, H.-W. Liang, M. Kong, Q.-F. Guan, P. Chen, *et al.*, "Synthesis of nitrogen-doped porous carbon nanofibers as an efficient electrode material for supercapacitors," *ACS nano*, vol. 6, pp. 7092-7102, 2012.
[43] W. Zhang, C. Xu, C. Ma, G. Li, Y. Wang, K. Zhang, *et al.*, "Nitrogen-superdoped 3D graphene networks for high-performance supercapacitors," *Advanced Materials*, vol. 29, p. 1701677, 2017.
[44] Y. Liu, Y. Shen, L. Sun, J. Li, C. Liu, W. Ren, *et al.*, "Elemental superdoping of graphene and carbon nanotubes," *Nature communications*, vol. 7, pp. 1-9, 2016.
[45] Y. Deng, Y. Xie, K. Zou, and X. Ji, "Review on recent advances in nitrogen-doped carbons: preparations and applications in supercapacitors," *Journal of Materials Chemistry A*, vol. 4, pp. 1144-1173, 2016.
[46] J. Li, X. Li, P. Zhao, D. Y. Lei, W. Li, J. Bai, *et al.*, "Searching for magnetism in pyrrolic N-doped graphene synthesized via hydrothermal reaction," *Carbon*, vol. 84, pp. 460-468, 2015.
[47] Z. Xing, Z. Ju, Y. Zhao, J. Wan, Y. Zhu, Y. Qiang, *et al.*, "One-pot hydrothermal synthesis of Nitrogen-doped graphene as high-performance anode materials for lithium ion batteries," *Scientific reports*, vol. 6, pp. 1-10, 2016.
[48] W. Hooch Antink, Y. Choi, K. d. Seong, J. M. Kim, and Y. Piao, "Recent progress in porous graphene and reduced graphene oxide-based nanomaterials for electrochemical energy storage devices," *Advanced Materials Interfaces*, vol. 5, p. 1701212, 2018.

[49] Y. He, Y. Zhang, X. Li, Z. Lv, X. Wang, Z. Liu, *et al.*, "Capacitive mechanism of oxygen functional groups on carbon surface in supercapacitors," *Electrochimica Acta*, vol. 282, pp. 618-625, 2018.
[50] N. A. Elessawy, J. El Nady, W. Wazeer, and A. Kashyout, "Development of high-performance supercapacitor based on a novel controllable green synthesis for 3D nitrogen doped graphene," *Scientific reports*, vol. 9, pp. 1-10, 2019.
[51] W. Zhao, T. Chen, W. Wang, B. Jin, J. Peng, S. Bi, *et al.*, "Conductive Ni3 (HITP) 2 MOFs thin films for flexible transparent supercapacitors with high rate capability," *Science Bulletin*, vol. 65, pp. 1803-1811, 2020.
[52] Y.-H. Lee, K.-H. Chang, and C.-C. Hu, "Differentiate the pseudocapacitance and double-layer capacitance contributions for nitrogen-doped reduced graphene oxide in acidic and alkaline electrolytes," *Journal of Power Sources*, vol. 227, pp. 300-308, 2013.
[53] S.-M. Li, S.-Y. Yang, Y.-S. Wang, H.-P. Tsai, H.-W. Tien, S.-T. Hsiao, *et al.*, "N-doped structures and surface functional groups of reduced graphene oxide and their effect on the electrochemical performance of supercapacitor with organic electrolyte," *Journal of Power Sources*, vol. 278, pp. 218-229, 2015.
[54] T. K. Das, S. Banerjee, A. Kumar, A. Debnath, and V. Sudarsan, "Electrochemical performance of hydrothermally synthesized N-Doped reduced graphene oxide electrodes for supercapacitor application," *Solid State Sciences*, vol. 96, p. 105952, 2019.
[55] Y. Jin, Y. Meng, W. Fan, H. Lu, T. Liu, and S. Wu, "Free-standing macro-porous nitrogen doped graphene film for high energy density supercapacitor," *Electrochimica Acta*, vol. 318, pp. 865-874, 2019.
[56] X.-Q. Lin, W.-D. Wang, Q.-F. Lü, Y.-Q. Jin, Q. Lin, and R. Liu, "Nitrogen-doped graphene/carbon nanohorns composite as a high-performance supercapacitor electrode," *Journal of materials science & technology*, vol. 33, pp. 1339-1345, 2017.
[57] B.-A. Mei, O. Munteshari, J. Lau, B. Dunn, and L. Pilon, "Physical interpretations of Nyquist plots for EDLC electrodes and devices," *The Journal of Physical Chemistry C*, vol. 122, pp. 194-206, 2018.
[58] P. Taberna, P. Simon, and J.-F. Fauvarque, "Electrochemical characteristics and impedance spectroscopy studies of carbon-carbon supercapacitors," *Journal of the Electrochemical Society*, vol. 150, p. A292, 2003.
[59] H. Randriamahazaka and K. Asaka, "Electromechanical analysis by means of complex capacitance of bucky-gel actuators based on single-walled carbon nanotubes and an ionic liquid," *The Journal of Physical Chemistry C*, vol. 114, pp. 17982-17988, 2010.
[60] J. Wu, Y. Lin, X. Xia, J. Xu, and Q. Shi, "Pseudocapacitive properties of electrodeposited porous nanowall Co3O4 film," *Electrochimica Acta*, vol. 56, pp. 7163-7170, 2011.
[61] Z. Wu, L. Li, Z. Lin, B. Song, Z. Li, K.-S. Moon, *et al.*, "Alternating current line-filter based on electrochemical capacitor utilizing template-patterned graphene," *Scientific reports*, vol. 5, pp. 1-7, 2015.
[62] V. Ganesh, S. Pitchumani, and V. Lakshminarayanan, "New symmetric and asymmetric supercapacitors based on high surface area porous nickel and activated carbon," *Journal of Power Sources*, vol. 158, pp. 1523-1532, 2006.

CHAPTER 5

ENHANCED ELECTROCHEMICAL PROPERTIES OF $MnFe_2O_4$/REDUCED GRAPHENE OXIDE NANOCOMPOSITE WITH A POTENTIAL FOR SUPERCAPACITOR APPLICATION

In this chapter, a single-step solvothermal method has been employed to synthesize $MnFe_2O_4$ composite nanoparticles where graphene sheets have been incorporated into spherical, ultra-small $MnFe_2O_4$ nanoparticles of size ~57 nm. When used as an electrochemical electrode, the $MnFe_2O_4$/rGO composite nanoparticles showed an enhanced specific capacitance of 253 Fg^{-1} compared to 133 Fg^{-1} corresponding to the bare nanoparticles, at a current density of 10 Ag^{-1} within the potential range of -0.3 to 1.2V. The unification of 2D graphene structure and $MnFe_2O_4$ nanoparticles leads to enhanced electrochemical performance and excellent cyclic stability of 96% (after 5000 cycles), providing a good strategy for improving future supercapacitor electrode materials.

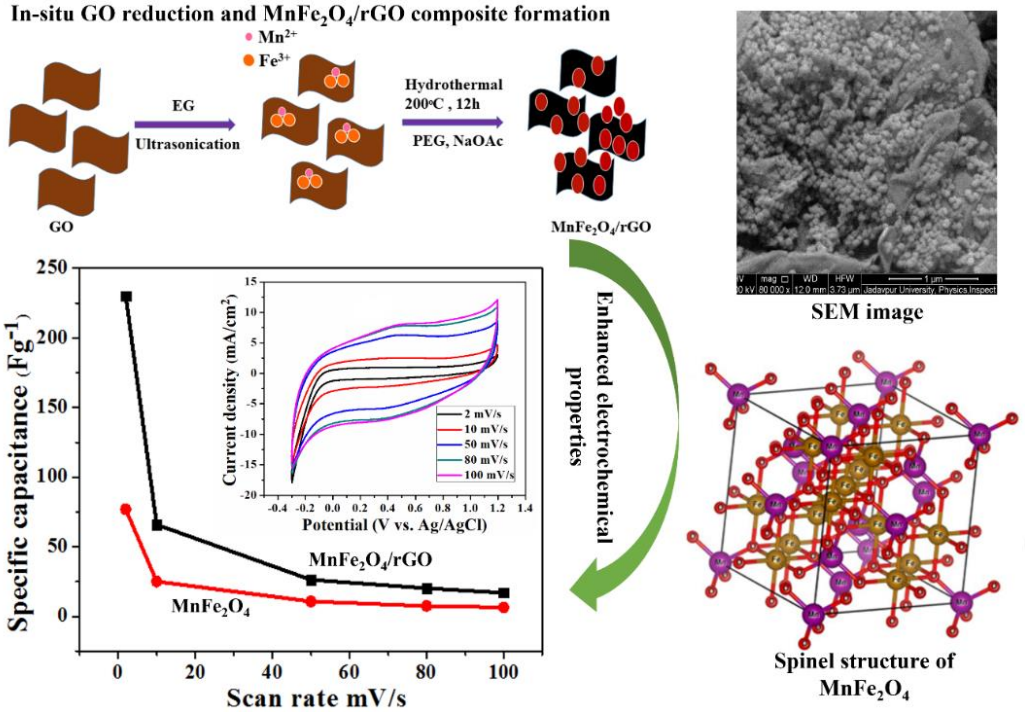

5.1. Introduction

With the severe problem of rapid urbanization and the increasing unavailability of fossil fuels, the development of sustainable energy storage systems to fulfill ever-increasing energy demands has become one of the highest concerns at present. Among various energy storage systems, supercapacitors have gained huge popularity as they have higher power density than the battery and higher energy density than conventional dielectric capacitors due to high power density, low cost, low equivalent series resistance, cyclic stability and environment adaptability [1-3]. Depending on the charge-storing process, supercapacitors can be categorized mainly into two groups namely electric double-layer capacitors (EDLC) and pseudo-capacitors [4]. The specific capacitance of EDLC depends on the surface area of conductive electrode materials such as carbon, accessible to the electrolyte. In this case, the electrical energy is stored at the electrode-electrolyte interface as a result of the physical accumulation of electrolyte ions. Whereas in pseudo-capacitors storage of energy takes place as a consequence of redox (Faradaic) reactions on the surface of electrodes [5-7]. Various kinds of metal oxides, including transition metal oxides [8-10], and conducting polymers [11, 12] have been explored as pseudocapacitive material in recent years. Spinel ferrites with general formula AB_2O_4 possess a crystal structure which is very effective in the electrochemical capacitor application as it can offer superior three-dimensional architectures for providing electronic pathways for diffusion. These days, several spinel ferrites including $CuFe_2O_4$ [3], $NiFe_2O_4$ [13], $CoFe_2O_4$ [14] are being reported as supercapacitor electrode materials because of their multiple oxidation states, environment-friendly nature, and low-cost.

As a significant member of the spinel ferrite family, $MnFe_2O_4$ nanoparticles have drawn much attention in the field of supercapacitors owing to their low cost, high electrochemical activity, environment friendliness and abundant resources [15, 16]. Nevertheless, the performance of $MnFe_2O_4$ as a pseudocapacitor has many times been limited by lower-electronic conductivity which in turn can result in inadequate transportation of charges at the electrode/electrolyte interface and in electrodes, resulting in insufficient Faradaic redox reactions [17, 18]. Also the morphology and exposed surface area ratio of the electrode-electrolyte interface to the electrolyte plays an important role in accumulating charges, consequently increasing the supercapacitance [19-21]. In this regard, $MnFe_2O_4$ has a disadvantage as it suffers agglomeration during the synthesis process owing to the magnetic interaction that results in a reduction of the active surface area and hereby limits the charge accumulation process. Therefore, introducing highly conductive support material like graphene is a feasible solution

for the aforementioned problems by providing adequate electroactive species in the electrode-electrolyte interface.

Graphene is one of the highly conductive carbonaceous materials which can be used as an attractive additive material to the metal oxide for providing a good electron transfer pathway and also can improve the stability of the whole heterostructure, as it has porous 2-D structure, large specific surface area and high conductivity [22-25]. Owing to these properties, graphene can serve as a support for preventing the added nanomaterials from agglomeration by balancing their high interface energy and hence such nanomaterials can be utilized in a better way [26-28]. A wide range of electrode materials incorporating pseudocapacitive spinel ferrites along with graphene has been effectively developed to achieve high-performance energy storage devices [21, 29]. The hybrid materials can enhance the electrochemical performance due to the synergistic effect with graphene which provides not only a conductive backbone to promote the transportation of electrons but also a mechanical strength which offers the integrity of the electrode through the electrochemical processes. In addition, preparing composite with graphene and spinel ferrite for supercapacitor electrode material can be economical and easy.

Recently, a group used the $MnFe_2O_4$/rGO nanocomposite to construct a hybrid supercapacitor using a two electrode setup. The results showed a specific capacitance of 271 Fg^{-1} at a current density of 0.5 Ag^{-1} with a cycling durability of 104% after 5000 cycles [30]. Another group in 2019, prepared a ternary composite graphene/metal doped iron oxide/polypyrrole (rGO/ $MnFe_2O_4$/Ppy) electrode which showed capacitance 232 Fg^{-1} at the scan rate of 5 mVs^{-1} [31].

Here, we present the synthesis of spherical $MnFe_2O_4$ nanoparticles on the surface of reduced graphene oxide (denoted as $MnFe_2O_4$/rGO) via a facile one-step solvothermal strategy which includes the reduction of graphene oxide (GO) to reduced graphene oxide as well as the formation of $MnFe_2O_4$ nanoparticles on the graphene sheets. The formation of $MnFe_2O_4$/rGO heterostructures was confirmed by XRD, SEM, FTIR, Raman spectroscopy and XPS method. The combination of graphene and $MnFe_2O_4$ nanoparticles develop a synergistic effect. $MnFe_2O_4$ nanoparticles are effective to provide a large number of electrochemically active sites for redox reactions and sheet-like graphene serves as a conductive network and provides a large surface area suitable for EDLC. In addition, the $MnFe_2O_4$/rGO composites exhibit good electrochemical properties with huge potential for supercapacitor application. The obtained EIS data of the composite was furthermore investigated with the help of a complex capacitance model and then the relaxation time constant was calculated.

5.2. Experimental details

5.2.1 Materials

Natural graphite flakes, sulfuric acid (H_2SO_4, 98%), sodium nitrate ($NaNO_3$), potassium permanganate ($KMnO_4$, 99.9%), hydrogen peroxide (H_2O_2, 30%), sodium acetate (NaOAc), ferric chloride ($FeCl_3$), manganese chloride ($MnCl_2$, $4H_2O$), polyethylene glycol (PEG; M.W.=6000), ethanol etc. were obtained from Sigma-Aldrich Co. (Bangalore, India). All the chemicals obtained were of scientific grade and used without any further cleaning.

5.2.2 Synthesis

Synthesis of GO

Graphene oxide (GO) was prepared using the Hummers method with a small moderation. In short, 2 g of graphite powder and 2 g of $NaNO_3$ were mixed in 90 ml H_2SO_4. The mixture was then kept in continuous stirring condition in a beaker after placing it in an ice bath so that the temperature remained controlled between 5-15˚C. After three hours of continuous stirring 10 g of $KMnO_4$ was slowly added in a controlled manner to the solution for oxidizing the graphite powder into graphitic oxide. After adding $KMnO_4$, again the solution was kept in stirring condition for another one hour. Then 90 ml water was added to the solution so that a large amount of heat energy could evolve to help in the separation of the graphitic oxide layers into graphene oxide. At last, the reaction was ceased by adding hydrogen peroxide (H_2O_2). The graphene oxide solution was then separated and washed many times with distilled water and ethanol and lastly dried at 70˚C.

Synthesis of $MnFe_2O_4$/rGO

In a typical procedure, graphene oxide was used as a precursor for the preparation of $MnFe_2O_4$/rGO. Firstly, 100 mg of GO was dissolved in 40 ml of ethylene glycol. In that graphene oxide solution, 4 mmol of $FeCl_3$ and 2 mmol of $MnCl_2.4H_2O$ were added. After that, the mixed solution was kept under ultrasonication for 3h. Subsequently, 1 g of PEG and 3 g of NaOAc were added followed by vigorous stirring for 1h. The whole mixed solution was then transferred to stainless steel autoclave and heated at 200˚C for 12h. After reaching room temperature, the precipitated blackish product was collected from the autoclave and was separated using centrifugation for several times with de-ionized water and ethanol. The final

product, i.e. $MnFe_2O_4$/rGO was then centrifuged and dried at 60 ˚C. A schematic illustration for the synthesis procedure of $MnFe_2O_4$/rGO is presented in **Fig. 5.1**. The likely process for the formation of $MnFe_2O_4$ can be broken down into two phases: the first is nucleation from atoms created by metal salt reduction, and the second is atomic growth, which is the process by which nuclei expand into nanospheres. Due to its unique physical and chemical characteristics, ethylene glycol is known to be a successful reaction medium in the solvothermal technique. It is also an excellent solvent to obtain monodisperse nanoparticles. The Mn^{2+} and Fe^{3+} ions were nucleated under solvothermal conditions in the current system under study with the water produced from metal precursors to create nanosized crystalline $MnFe_2O_4$.

PEG is a structure-directing agent because it forms spherical grains by easy self-assembly. For all systems, the Ostwald ripening process is crucial to the development of nanocrystals. Crystalline particles evolve into crystalline nuclei, which assemble isotropically to form spherical grains in ethylene glycol solution, and then further to nanospherical crystallites, according to the Ostwald ripening mechanism. At the end of the process, $MnFe_2O_4$ nanospheres were formed on the surface of rGO. In order to prevent particle agglomeration, NaOAc was added for electrostatic stabilization. Minimization of the total surface energy of $MnFe_2O_4$ occurs under thermodynamic control [32]. For comparison purposes, pure $MnFe_2O_4$ was also synthesized under the same condition without adding GO.

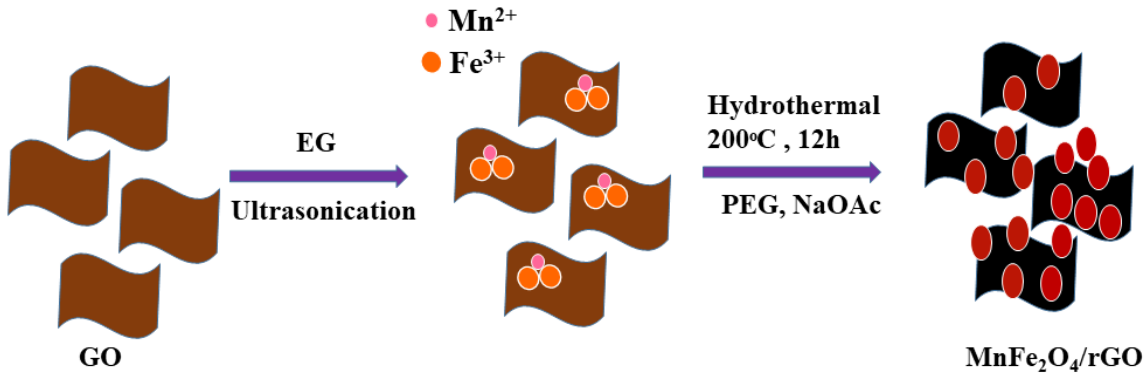

Fig. 5.1. Schematic illustration for the synthesis of $MnFe_2O_4$/rGO.

5.2.3 Material Characterization

The powder X-ray diffraction (XRD) spectra for the as-prepared samples were investigated by a Bruker D8 advanced diffractometer in Bragg Brentano geometry, using Cu K_α (λ=1.54059Å) radiation between 20˚ to 80˚. The step size and scan speed were 0.0188˚ and 0.035˚/s

respectively. The surface morphology of the products was obtained by Field emission scanning electron microscope (FEI INSPECT F50) operated at 10 kV. The Raman spectroscopy was conducted with the help of a Raman Microscope (HORIBA, Lab RAM, HR800) within 500-2500 cm^{-1} at room temperature. The chemical groups present in the sample were investigated by Fourier transform infrared (FTIR) spectroscopy at ambient temperature with a Perkin-Elmer FTIR spectrum RXI spectrometer in transmission mode within 500-4000 cm^{-1}. For FTIR measurement, pallets were prepared by applying hydraulic pressure on samples mixed with KBr powder. The background correction was performed with reference to KBr pallets. The elemental binding energy of the as-prepared $MnFe_2O_4$/rGO composite was obtained by X-ray photoelectron spectroscopy (XPS; Omicron, serial no:0571). To perform XPS measurement, an aqueous solution of $MnFe_2O_4$/rGO was made and dropcasted onto a glass substrate followed by air drying.

5.2.4 Electrochemical characterization

The electrochemical study of the bare $MnFe_2O_4$ and its composite was performed in a conventional three-electrode system. The experiment was done by cyclic voltammetry (CV), galvanostatic charge-discharge (GCD) and electrochemical impedance spectroscopy (EIS) techniques on a multichannel electrochemical workstation (CS313 CorrTest, China). In a typical procedure, working electrodes were prepared with definite masses of prepared electro-active materials, acetylene black and polyvinylidene fluoride (PVDF) with a mass ratio of 85:10:5 respectively. The mixtures were dispersed in a very small amount of N-methyl pyrrolidone (NMP) solution to form a homogeneous slurry that was pasted onto a teflon-coated graphite rod. The prepared working electrode (WE) was then dried overnight at 60°C in an electric oven and hence NMP was completely evaporated. Platinum (Pt) (1cm × 1cm) and Ag/AgCl in saturated KCl solution were considered as the counter and reference electrodes respectively. 1 M Na_2SO_4 aqueous solution was used as the electrolyte. The reference electrode potential was monitored carefully and the measurement protocol was maintained throughout. Mass loading of 0.5 mg and 0.6 mg respectively was used for the $MnFe_2O_4$ and $MnFe_2O_4$/rGO active materials.

The specific capacitance (C_m) of the samples can be calculated using CV curves using following formula

$$C_m = \frac{i}{2mv} \qquad (1)$$

where m is the mass of the active material and v stands for the scan rate. The value of i can be calculated by integrating the surface area bounded by the CV curves using the following formula

$$i = \frac{\int_{v_a}^{v_c} i(v)dv}{\Delta v} \qquad (2)$$

Here, v_c and v_a respectively stands for the lowest and highest end values of the potential window. The value of specific capacitance can also be calculated from GCD curves using the following equation:

$$C_m = \frac{i \times \Delta t}{\Delta v} \qquad (3)$$

where i is the applied current density in Ag^{-1}, Δt (s) is discharge time and Δv (V) is the potential window during the discharge process.

5.3. Results and discussion

5.3.1 XRD

The crystalline nature and phase characteristics of the as-prepared samples were investigated by powder X-ray diffraction studies. The XRD pattern recorded for $MnFe_2O_4$ and $MnFe_2O_4$/rGO composite particles have been presented in **Fig. 5.2b**. Eight distinct diffraction peaks were detected for pristine $MnFe_2O_4$ as well as in $MnFe_2O_4$/rGO composite. The characteristics peaks for bare $MnFe_2O_4$ were detected approximately at 2θ values of 30.2°, 35.5°, 43.1°, 53.4°, 57.2°, 62.7°, 71.1° and 73.8° which were respectively assigned to the crystallographic peaks 220, 311, 400, 422, 333, 440, 620 and 533. All these major diffraction peaks of $MnFe_2O_4$ are related to single-phase cubic spinel structure (JCPDS data no-74-2403) [33]. The nanoparticles having intense sharp peak indicates that the particles are highly crystalline. Also, the absence of any extra peak confirms the purity of the nanoparticles. From the Scherrer formula, the average crystallite sizes of $MnFe_2O_4$ and $MnFe_2O_4$/rGO were found to be ~14 nm and 12 nm respectively, considering the highest intense peak 311. In addition, the Rietveld refinement analysis of the XRD data has been carried out using the FullProf software to learn more about the structural details of the $MnFe_2O_4$ nanoparticles. All the peaks of the powder XRD pattern were well-matched with those of the pure phase of $MnFe_2O_4$ nanoparticles with a GOF (Goodness of fit) value of 1.32 and it belongs to the *Fd-3m* space group [34-37]. In a normal spinel ferrite structure, the X^{2+} ions occupy the tetrahedral sites, while the octahedral sites contain the ferrite (i.e. Fe^{3+}) ions, yielding the experimental

formula $[X^{2+}]^{tetrahedral}[Fe^{3+}]^{octahedral}{}_2O_4$ [35]. The space group and crystal planes of these nanoparticles were determined from the fitted curve (**Fig. 5.2c)** and are in good agreement with previously published results [35, 36]. The peak profiles were modelled using the Pseudo-Voigt function. The Rietveld refined data suggest that the experimental and simulated patterns are well matched and the difference between them is negligible.

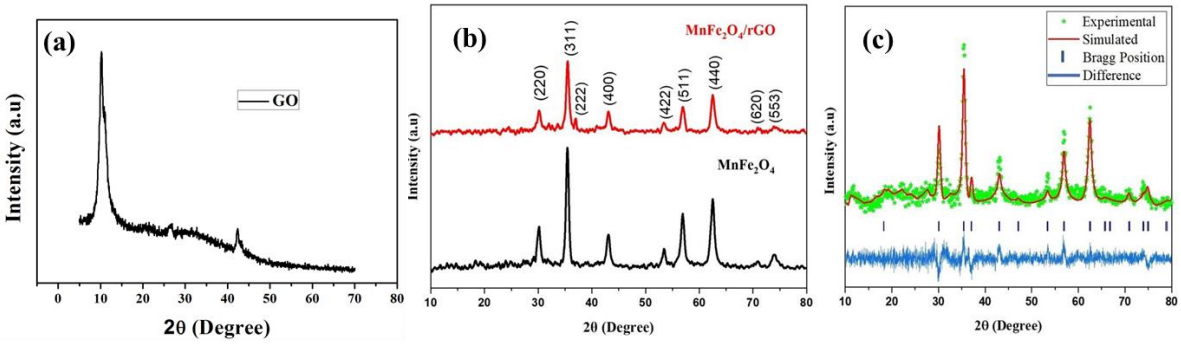

Fig. 5.2. X-ray diffraction spectrum of **(a)** GO **(b)** $MnFe_2O_4$ (black) and $MnFe_2O_4$/rGO (red) **(c)** XRD pattern of $MnFe_2O_4$ nanoparticles (green) along with the Rietveld refinement plot showing the simulated curve (red), Bragg's position and the corresponding difference of experimental and simulated data.

Table 5.1. Crystal data along with the Metal-Oxygen bond lengths and bond angles of the $MnFe_2O_4$ nanoparticles obtained from Rietveld refinement of XRD data

Parameters	**Values**
Formula weight	230.63
Crystal system	Cubic
Space group	Fd-3m
Lattice parameter	8.415 Å
Volume of unit cell	595.855 $Å^3$
GOF	1.32
Metal-oxygen bond length (Å)	Mn-O = 1.822
	Fe-O = 2.104
Metal-oxygen bond angle	Mn-O bond angle = 109.5º
	Fe-O bond angle = 90º

In addition, certain additional structural parameters were determined from the Rietveld refinement output data, such as the lattice parameter (a~ 8.415Å) and unit cell volume (a^3 ~ 595.855 $Å^3$). The bond length between the iron-oxygen (Fe-O) atoms is ~2.1Å and manganese-oxygen (Mn-O) atoms is ~ 1.8Å, whereas the angle between two Fe-O bonds is 90º and two Mn-O bonds is ~109.5º. These parameters are listed in **Table 5.1**. A schematic of the 3D unit

cell of $MnFe_2O_4$ nanoparticles with metal and oxygen bonds, bond length and angle was also obtained from the refined data using VESTA structure visualization software which is shown in **Fig. 5.3.**

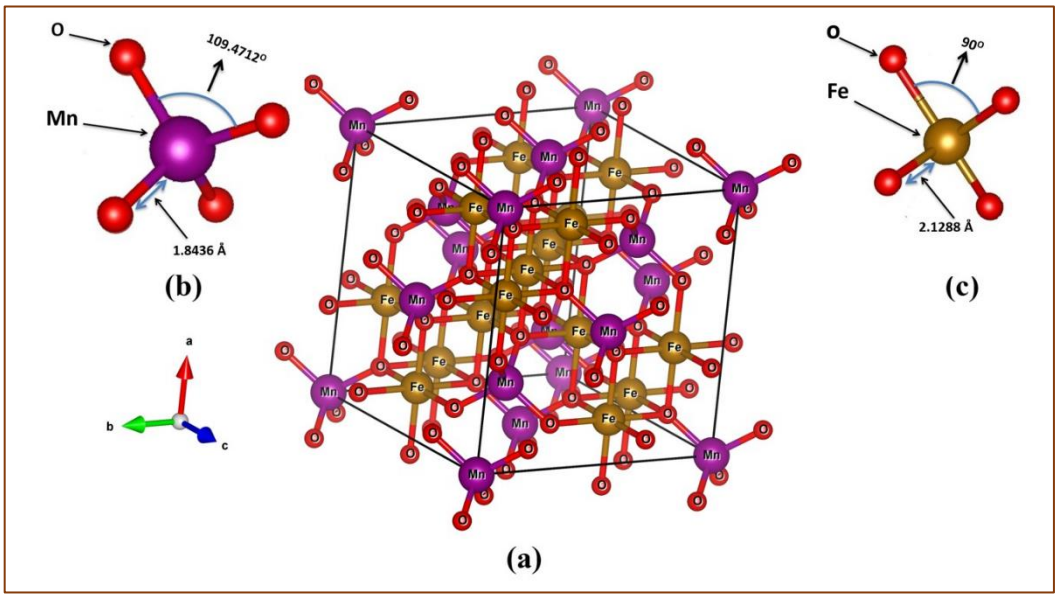

Fig. 5.3 (a) The schematic (Ball and Stick) diagram of 3D unit cell structure of cubic spinel crystal (fcc) of the $MnFe_2O_4$ nanoparticles (space group *Fd-3m*). The oxygen, manganese and iron positions are marked in red, violet and brown colours respectively. Bond length and bond angle of **(b)** Mn-O and of **(c)** Fe-O as obtained using the VESTA software.

The XRD spectrum of GO shows a characteristic 001 peak at 10.3° (**Fig. 5.2a).** It is very evident that in the case of composite, there is no extra significant graphene-related peak other than the main peaks of $MnFe_2O_4$. The non-appearance of the diffraction peaks corresponding to rGO can be attributed to the complete exfoliated state of rGO in the composite material. It can also be inferred that restacking has been prevented effectively because if the regular stacking of rGO gets impaired, the diffraction peak is not visible or becomes weaker [38]. Moreover, the absence of any graphene peak also indicates that the crystallinity of $MnFe_2O_4$ was not affected by the introduction of graphene. This exfoliation of rGO in the composite material is beneficial for superior electrochemical performance.

5.3.2 SEM:

The external surface morphology and structure of the synthesized materials were additionally investigated by scanning electron microscope (SEM). The representative SEM image of $MnFe_2O_4$ as shown in **Fig. 5.4a,** reveals its morphological appearance to be almost spherical. It was further investigated from the histogram analysis (**Fig. 5.4d)** that the average particle size

of the synthesized $MnFe_2O_4$ was about ~57 nm. These types of low-dimension $MnFe_2O_4$ nanoparticles can have high active surface area and hence can facilitate electrochemical performances with better exposure to the electrolyte ions.

Fig. 5.4b demonstrates that the $MnFe_2O_4$ nanoparticles are distributed on the randomly arranged graphene planar sheet simultaneously creating an abundant porous structure with a high active surface area. This kind of porous hybrid structure is favorable to achieve a better ion diffusion process and larger charge accumulation resulting in enhanced electrochemical

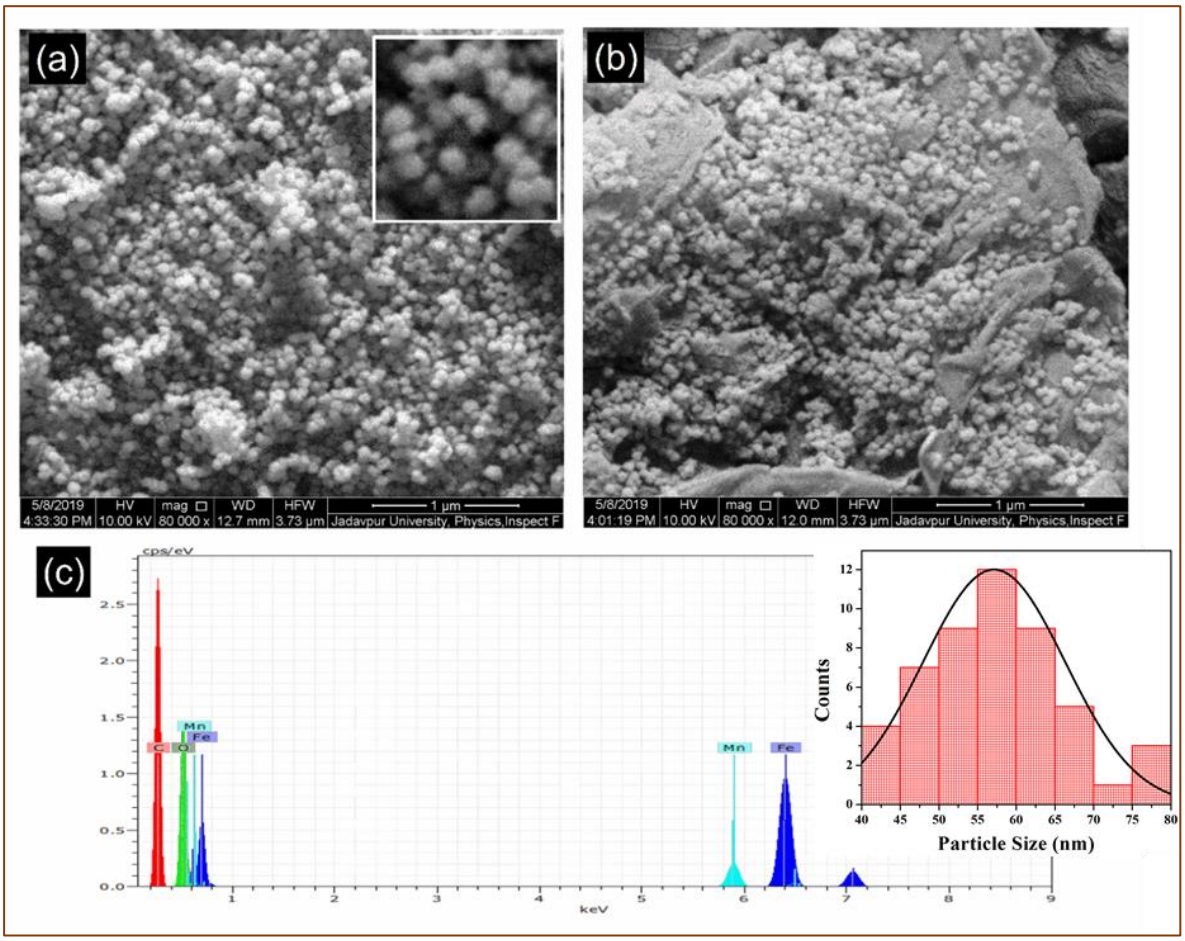

Fig. 5.4. SEM image of (a) $MnFe_2O_4$ and (b) of $MnFe_2O_4$/rGO and (c) EDX spectrum of $MnFe_2O_4$/rGO. Inset shows the histogram of particle size distribution for $MnFe_2O_4$ nanoparticles.

performance. Furthermore, the graphene sheets may prevent the agglomeration of the $MnFe_2O_4$ nanoparticles as well, which in turn, increases the probability of the active sites on the electrode getting exposed to the electrolyte ions. Additionally, the nanocomposite may provide a highly conductive path for accelerating ion adsorption and extraction. The elemental analysis was also executed on the $MnFe_2O_4$/rGO nanocomposite. **Fig. 5.4c** represents the EDX spectra of the

composite which confirms the presence of Mn, Fe, O and C. The EDX result clearly depicts that the nanocomposite is composed of $MnFe_2O_4$ and graphene.

5.3.3 Raman

Raman spectroscopy was employed to study irregularity in sp^2 carbon material and for exploring the structural property of the materials. **Fig. 5.5(a)** illustrates Raman spectra of prepared GO and $MnFe_2O_4$/rGO. The Raman spectrum of GO exhibits two characteristic prominent peaks at 1333 cm^{-1} and 1591 cm^{-1} which can be assigned to D and G bands, respectively. The D band is related to the imperfection and disorder within the lattice structure of the graphitic network, whereas the G band is associated with the vibration of sp^2- bonded **c**arbon [39, 40]. For gaining further information on defects and the order of graphitization, the ratio of I_D and I_G was calculated using peak intensities of the D and G bands. In the case of GO, the I_D/I_G ratio was 1.22. After the solvothermal reduction of GO and with the incorporation of $MnFe_2O_4$ nanoparticles into the rGO sheets, I_D/I_G value decreased to 1.09. Theoretically, when GO is reduced, the oxygeneous functional groups are removed which in turn increases the degree of ordering of the sp^2 carbon network structure. This makes the sp^2 region larger, and hence the I_D/I_G ratio decreases. Additionally, the vibrational modes associated with $MnFe_2O_4$ can be noticed with a broad hump centered at 623 cm^{-1}.

5.3.4 FTIR:

Fourier transform infrared spectroscopy was carried out for investigating the functional groups in the prepared samples. **Fig. 5.5b** depicts the FTIR spectra recorded for the prepared samples between 500-4000 cm^{-1}. It can be observed that the GO spectrum contains different oxygen-containing functional groups attached to the graphite lattice. Stretching vibrations of the epoxy (C-O) functional group can be noticed at 1045 cm^{-1}. Emergence of the peak at 1365 cm^{-1} might be because of the presence of tertiary C-OH group. Another characteristic peak at 1609 cm^{-1} is associated with the skeletal vibrations from the unoxidized (C=C) graphitic network. The C=O stretching vibrations related to sp^3 carbon associated with carboxyl COOH groups which are placed at the edges of graphene oxide sheets can be noticed at 1723 cm^{-1}. The band at 3335 cm^{-1} is ascribed to the stretching vibrations of hydroxyl groups. FTIR spectrum of GO is found to be in good agreement with reported work [41, 42]. In both $MnFe_2O_4$ and the composite, the broad bands at ~ 3000-3500 cm^{-1}

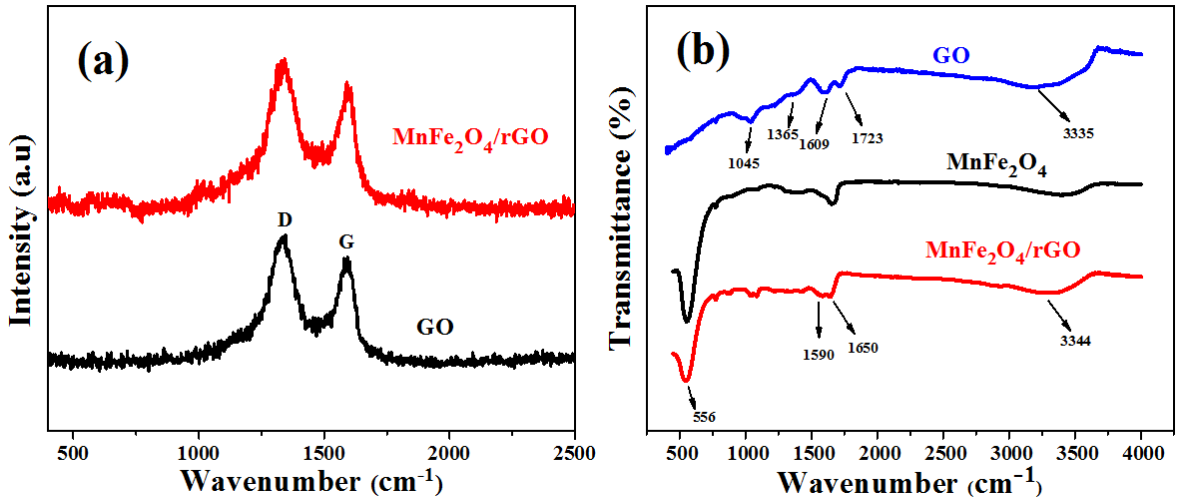

Fig. 5.5. (a) Raman spectra and **(b)** FTIR spectra of GO, $MnFe_2O_4$ and $MnFe_2O_4$/rGO composite

are associated with the O-H stretching vibration and 1650 cm^{-1} corresponds to the bending vibration. Also, in both cases, a strong band at 556 cm^{-1} is related to the metal-oxygen bond [43]. Moreover, for the nanocomposite, the disappearance of absorption peak (C=O) and declination of (C-O and C-OH) corresponding to oxygen-containing groups confirm the effective reduction of GO in solvothermal treatment. The peak at 1609 cm^{-1} for GO indicating C=C skeletal vibration for the unoxidized graphitic network is red-shifted to 1590 cm^{-1}, suggesting non-violation of the aromatic structure of rGO within the composite [41].

5.3.5 X-ray photoelectron spectroscopy (XPS)

To explore the elemental composition of $MnFe_2O_4$/rGO composite, XPS was adopted. The complete XPS spectrum of $MnFe_2O_4$/rGO composite is presented in **Fig. 5.6e**, which ensures the existence of Mn, Fe, C and O elements. The high-resolution XPS spectra along with the fitted ones corresponding to Mn *2p*, Fe *2p*, C *1s* and O *1s* are presented in **Fig. 5.6a-d**. As displayed in **Fig. 5.6a,** the spectrum of Mn *2p* can be fitted into three peaks with two characteristic principal peaks at binding energies of 641.11 eV (Mn $2p_{3/2}$) and 652.77 eV (Mn $2p_{1/2}$). The difference in the binding energies of these two peaks is nearly 11.66 eV, which is close to the numerical value for Mn_3O_4, suggesting the existence of both Mn^{2+} and Mn^{3+} ions [44, 45]. The other peak at binding energy 642.8 eV is associated with the satellite peak.

Likewise, the XPS spectrum related to Fe *2p* can be fitted into four peaks (Fig. **5.6b).** In addition to the satellite peak at 716.73 eV, the binding energy at two sub-peaks at 710.11 eV

and 712.05 eV are associated with Fe $2p_{3/2}$ whereas the peak at 724.24 eV is assigned to Fe $2p_{1/2}$ and it validates the presence of Fe^{3+} species in $MnFe_2O_4$/rGO composite. Specifically,

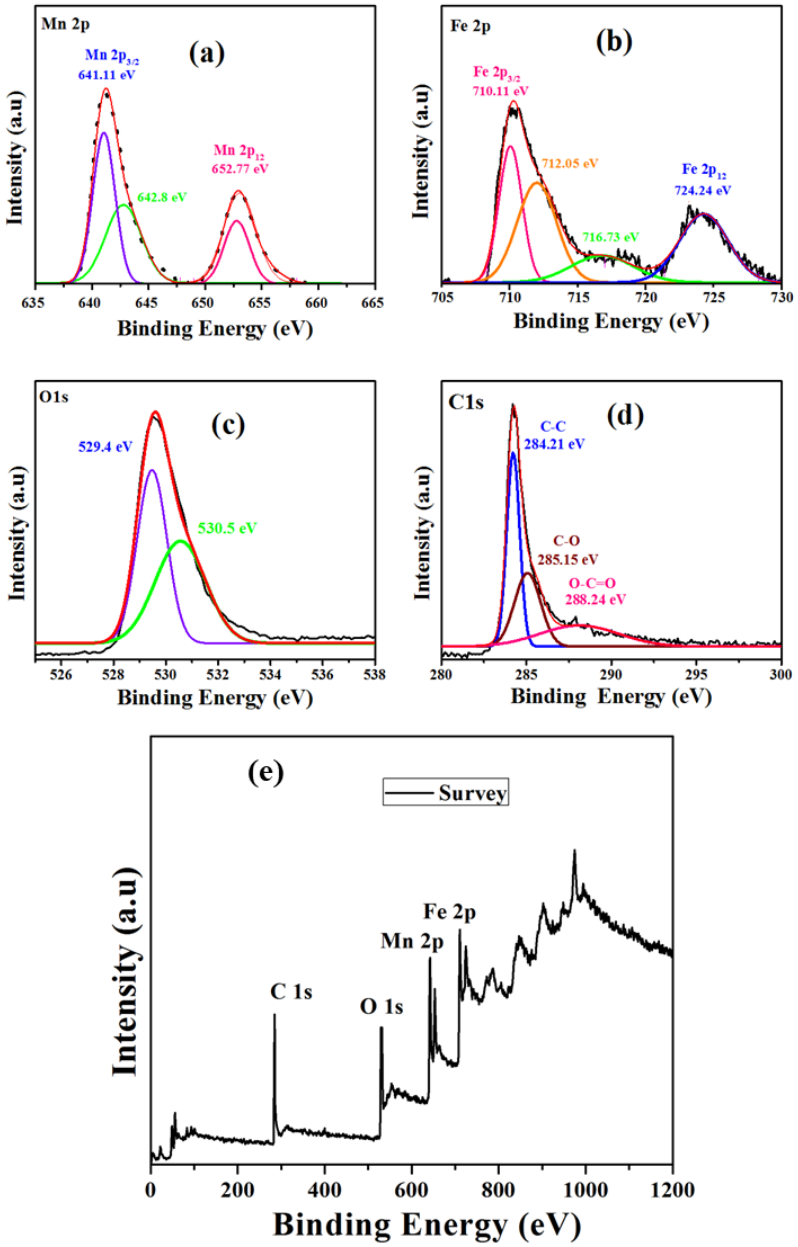

Fig. 5.6. The XPS spectra of $MnFe_2O_4$/rGO **(a)** Mn *2p*, **(b)** Fe 2p, **(c)** O *1s*, **(d)** C *1s*. (e) XPS Survey spectrum of $MnFe_2O_4$/rGO composite.

the binding energy at 712.05 eV for Fe $2p_{3/2}$ arises due to the Fe^{3+} ions in tetrahedral sites. On the other hand, the binding energy at 710.11 eV for Fe $2p_{3/2}$ and binding energy at 724.24 eV for Fe $2p_{1/2}$ comes from Fe^{3+} ions in octahedral sites. Moreover, the satellite peak confirms the existence of Fe^{2+} ions [43, 46, 47].

Fig. 5.6c depicts the O *1s* spectrum with two peaks at 529.4 eV and 530.5 eV. The O *1s* peak associated with the binding energy of 529.4 eV is representative of the metal-oxygen bond of $MnFe_2O_4$, while the peak related to binding energy around 530.5 eV determines the oxygen-containing functional group [43].

In **Fig. 5.6d,** it can be observed that the XPS spectrum of C *1s* is fitted with three peaks at the binding energy values of 284.21, 285.15 and 288.24 eV and they are generally associated with C=C, C-O and O-C=O bond respectively [42]. The two observably weaker peaks in **Fig. 5.6d** can be associated with the oxygen-containing carbons, suggesting the reduction process of GO. This observation confirmed that GO was efficiently reduced to rGO with a small amount of remaining oxygenated groups and for this reduction, ethylene glycol was utilized as a reducing material in the solvothermal process [3].These obtained results firmly suggest the successful formation of $MnFe_2O_4$/rGO composite and the confirmation of the presence of functional groups which are beneficial for the process of adsorption and motion of charges.

5.3.6 Electrochemical Studies:

For its feasible application as a supercapacitor electrode, the electrochemical performance of bare $MnFe_2O_4$ nanoparticles and $MnFe_2O_4$/rGO composite were investigated with the assistance of a traditional three-electrode system in a 1M Na_2SO_4 aqueous electrolyte as described earlier in section 5.2.4. The CV curves of $MnFe_2O_4$ and $MnFe_2O_4$/rGO recorded at various scan rates within the range 2 to100 mV/s, in a 1 M Na_2SO_4 aqueous electrolyte in the potential window from -0.3 to 1.2 V have been shown in **Fig. 5.7a** and **5.7b** respectively. It can be seen that the CV curves of $MnFe_2O_4$ consist of prominent redox peaks which differ from the usual rectangular shape of an ideal electric double-layer capacitor. These peaks arise due to the reversible redox processes involving Mn and Fe ions occurring at the electrode's surface. The nature of CV curves suggests the pseudocapacitive behaviour of $MnFe_2O_4$ nanoparticles. This implies that the maximum charge-storing process in the $MnFe_2O_4$ nanoparticle electrode takes place through the Faradaic process. The Na^+ ions from the electrolyte interact with the $MnFe_2O_4$ nanoparticles by a reversible redox couple reaction as given in eqn (4) [48, 49]

$$Na^+ + e^- + MnFe_2O_4 \leftrightarrow NaMnFe_2O_4 \qquad (4)$$

As the specific capacitance of a sample is equivalent to the area under the CV curve, it is perceptible that $MnFe_2O_4$/rGO nanocomposite exhibits a notably larger integrated area than that of bare $MnFe_2O_4$ nanoparticles, suggesting a higher electrochemical performance. The

specific capacitance of the electrode was calculated with the help of CV curves using eqn (1) and (2) at various scan rates and have been presented in **Fig. 5.7c.** The highest specific capacitance of $MnFe_2O_4$ and $MnFe_2O_4$/rGO composite are 92 and 192 Fg^{-1} respectively at 2 mV/s, clearly indicating that the composite possesses higher capacitance than that of bare

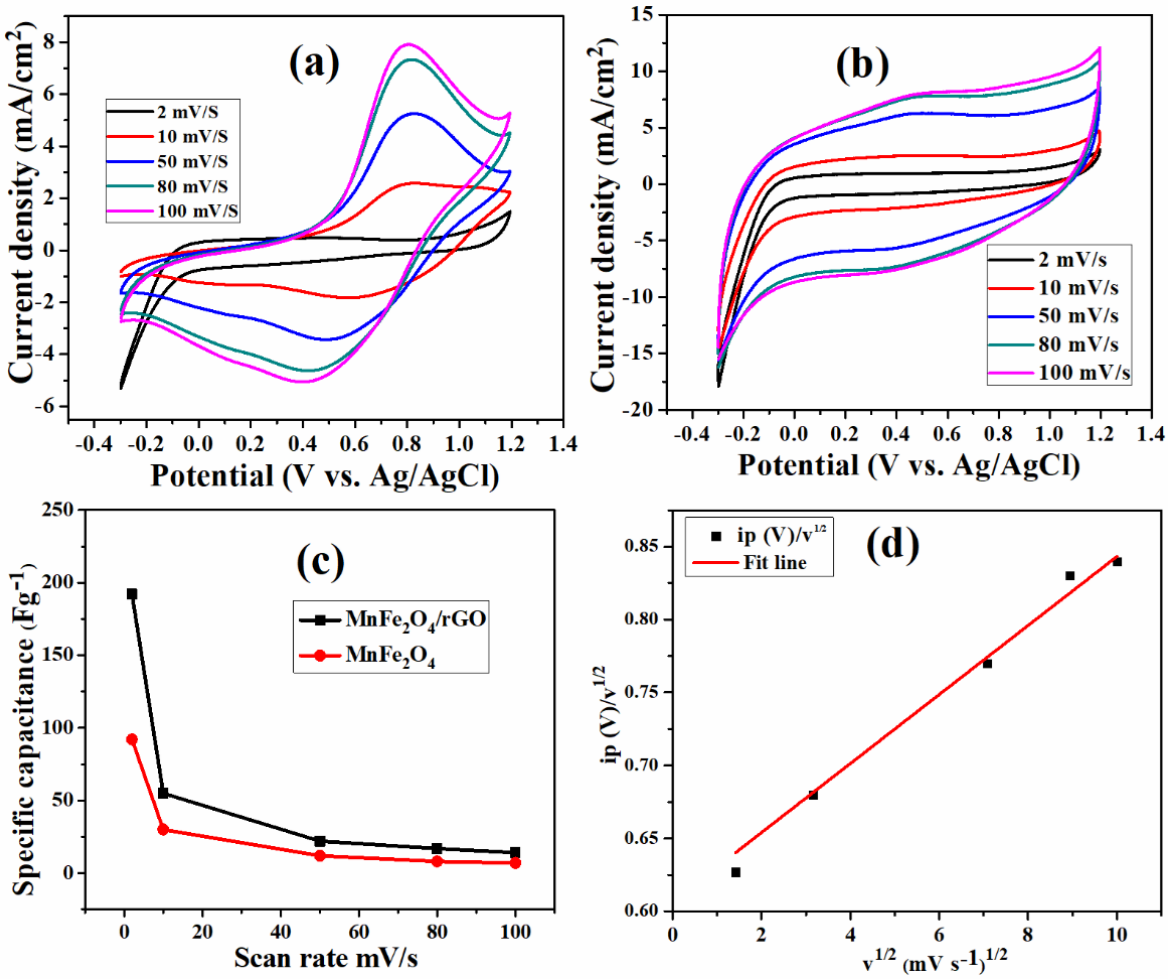

Fig. 5.7. CV curves of **(a)** $MnFe_2O_4$ and **(b)** $MnFe_2O_4$/rGO composite at different scan rates within the potential window range of -0.3 to 1.2 V vs. Ag/AgCl. **(c)** Scan rate-dependent specific capacitance of $MnFe_2O_4$ and $MnFe_2O_4$/rGO. (**d)** Plot of $i_p/v^{1/2}$ versus $v^{1/2}$ for $MnFe_2O_4$/rGO.

nanoparticles. It can also be observed that the specific capacitance decreases as the scan rate increases from 2 to 100 mV/s. At a lower scan rate, electrolyte ions in the Na_2SO_4 aqueous solution get a higher time to access the inner and external surface of the electrode which results in the accumulation of a large number of charges as well as enhanced capacitance. Inversely, at a higher scan rate, the ions in the electrolyte with higher mobility obtain inadequate time to

interact with the inner surface of the electrode. Accordingly, a very small amount of charges get accumulated on the outer surface resulting in decreased specific capacitance.

The $MnFe_2O_4$/rGO composite is constituted of materials which individually contribute to the charge-storing mechanisms: one through an electric double layer and the other through the redox reaction mechanism. Specifically, the mechanism of charge accumulation comprises a Faradaic electron transfer process between the two or more redox states of the metal (Mn) centres in the spinel crystals and non-Faradaic electric double layer formation from the carbonaceous graphene materials. In such case, the peak current of active electrode material is made up of both capacitive current and adsorption/desorption current which can be represented in terms of sweep rate as: [8]

$$i_p\,(V) = k_1 v + k_2 v^{1/2} \qquad (5)$$

where $k_1 v$ and $k_2 v^{1/2}$ represent capacitive current and charge adsorption/desorption current, respectively. Now dividing the equation on both sides by $v^{1/2}$, one obtains

$$i_p/v^{1/2} = k_1 v^{1/2} + k_2 \qquad (6)$$

The values of k_1 and k_2 can be obtained from the slope and intercept respectively of the linear fit corresponding to eqn (6). **Fig. 5.7(d)** shows the plot of $i_p/v^{1/2}$ with $v^{1/2}$. The k_1 and k_2 values as obtained from the linear fit of the graph are 0.02367 and 0.60669 respectively. The significantly low value corresponding to the capacitive current reflects the fact that the Faradaic redox charge transfer process is dominant over the capacitive mechanism in case of the composite. Such an enhanced electrochemical property of the composite particle was further confirmed by Galvanostatic charge-discharge (GCD) measurements which were done in addition to cyclic voltammetry in the same 1M Na_2SO_4 electrolyte and within the potential window range of -0.3 to 1.2V**. Fig. 5.8a** shows the GCD curves for the bare nanoparticles and composite at 10 Ag^{-1}. As shown in these curves, the discharge time for the $MnFe_2O_4$/rGO composite is significantly longer than for bare nanoparticles. This data undoubtedly confirmed that $MnFe_2O_4$/rGO possess a larger charge capacity than the pristine $MnFe_2O_4$, which is consistent with the CV results. **Fig. 5.8b** represents GCD curves for the composite and it can be seen that the shapes of charge/discharge curves at different current densities are almost the same without any prominent change and a trivial IR drop, suggesting small internal resistance, good reversibility and rate capability [48]. The specific capacitances of active material electrodes based on GCD curves can be calculated using equation (3) which are found to be ~ 253, 224, 195, 180 and 166 Fg^{-1} at current densities of 10, 11.16, 13.33, 15 and 16.6 Ag^{-1}

respectively for the composite, neglecting the very small IR drop present. The highest specific capacitance, as well as the longest discharge time of the $MnFe_2O_4$/rGO electrode was for a current density of 10 Ag^{-1}. A comparison of the highest specific capacitance values reported for other $MnFe_2O_4$/graphene based materials is summarized in **Table 5.2**. The higher specific capacitance at lower current density can be due to the adequate transfer time for ions between electrode and electrolyte. For the bare nanoparticles, the specific capacitance calculated from GCD curve **(Fig. 5.8a)** is found to be 133 Fg^{-1} at a current density of 10 Ag^{-1}.

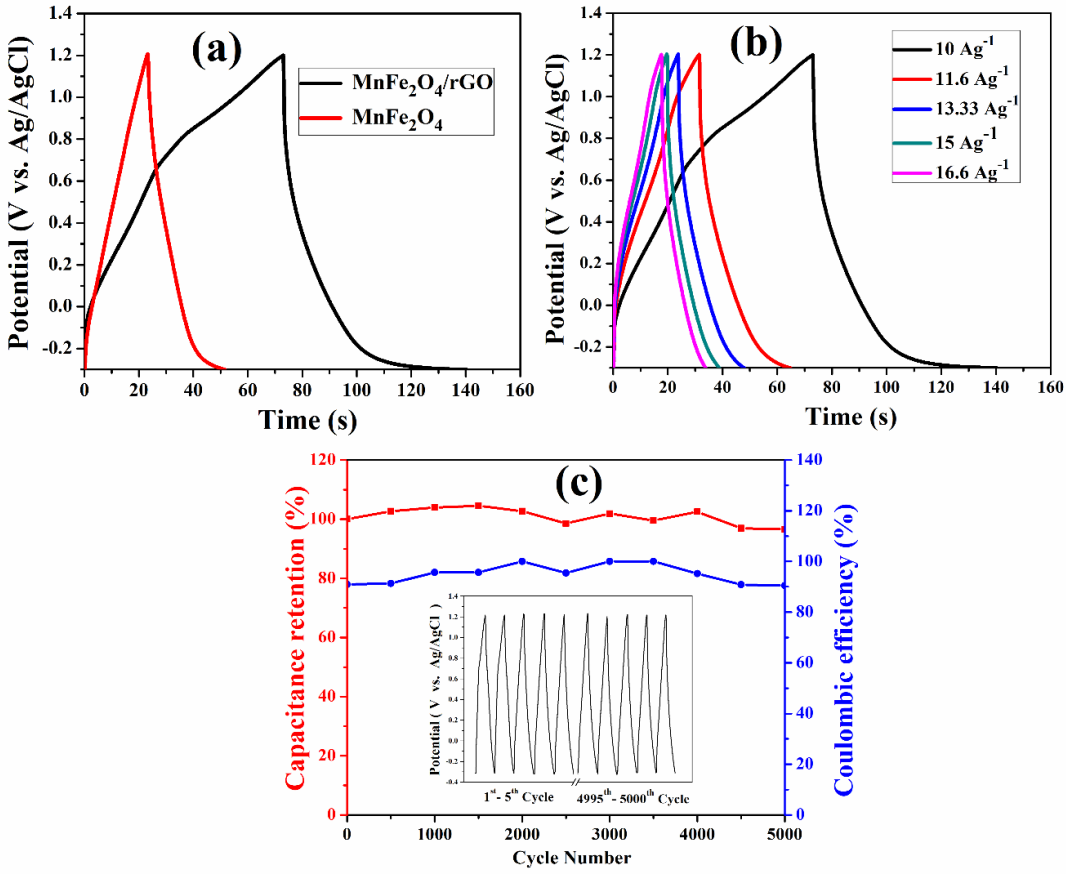

Fig. 5.8. GCD curves of **(a)** $MnFe_2O_4$ and $MnFe_2O_4$/rGO at current density 10 Ag^{-1} **(b)** $MnFe_2O_4$/rGO at different current densities within the potential window range of -0.3 to 1.2V. **(c)** Cyclic stability and Coulombic efficiency of $MnFe_2O_4$/rGO for 5000 cycles. Inset shows first and last five consecutive GCD curves out of 5000 cycles.

This improved capacitance can be ascribed to the incorporation of graphene. With the introduction of graphene within the composite heterostructure, the accessible specific surface area increased which in turn increased the electrode-electrolyte contact area providing more usable space for electrolyte diffusion on the $MnFe_2O_4$/rGO electrodes which give rise to a larger number of ion accumulation enhancing charge storage capacity. Also, due to less agglomeration, nanomaterials become more accessible on the surface and increase the specific

capacitance due to the increase of the Faradaic process. On the other hand, $MnFe_2O_4$ nanoparticles provide Faradaic process to enhance the total capacitance by penetrating the rGO layers and preventing the restacking of the graphene sheets.

Table 5.2. A comparison of the synthesis method, electrolyte used, specific capacitance and capacitance retention (%) obtained in this study with existing literature on other $MnFe_2O_4$ based materials.

Sample	Synthesis method	Electrolyte	Specific Capacitance (Fg^{-1})	Capability Retention (%)	Ref
$MnFe_2O_4$ NPs	Thermal decomposition	2 M KOH	25.21 (at 50 mV s^{-1})	-	[50]
$MnFe_2O_4$ microsphere	solvothermal	2 M KOH	88.4 (at 0.01 Ag^{-1})	69.2% after 2000 cyclces	[51]
rGO/$MnFe_2O_4$/Ppy	Co-precipitation	1 M H_2SO_4	232 (at 5 mV s^{-1})	-	[31]
$MnFe_2O_4$/graphene	Solvothermal	1 M H_2SO_4	120 (at 0.1 Ag^{-1})	105 % after 5000 cycles	[17]
$MnFe_2O_4$/GO	Co-precipitation	1 M H_2SO_4	298 (at 1 Ag^{-1})	92 % after 500 cycles	[52]
$MnFe_2O_4$/rGO	Solvothermal	1 M Na_2SO_4	253 (at 10 Ag^{-1})	96 % after 5000 cycles	This work

To investigate the long-term cyclic stability of prepared $MnFe_2O_4$/rGO for practical use as electrode material, a 5000 cycle charging and discharging cyclic test was conducted with a constant current density of 15 Ag^{-1} within a potential window of -0.2 to + 1.3 V. **Fig. 5.8c** depicts capacitance retention rate and coulombic efficiency as a function of cycle number. Initially, the specific capacitance increases over to 104% of the starting value then starts to decrease and reaches the value of 98% of the starting value at 2500th cycle. Ultimately, capacitance retention becomes 96% after 5000th cycle. The first five and last five consecutive GCD curves (inset of **Fig. 5.8c**) with a current density of 15 Ag^{-1} showed an almost linear and typical triangular shape which could be attributed to the good electrochemical capacitive characteristic with high degree of reversibility. The formula for the coulombic efficiency, η, is (t_d/t_c), where t_d (s) is the discharge time and t_c (s) is the charge time. It was discovered that the coulombic efficiency was rather consistent, exhibiting good efficiency with a minimum value of 90 % throughout the cycles. This is due to easy insertion-desertion of electrolyte ions through the electrode material. The results of capacitance retention and coulombic efficiency verify the long life and high efficiency of $MnFe_2O_4$/rGO.

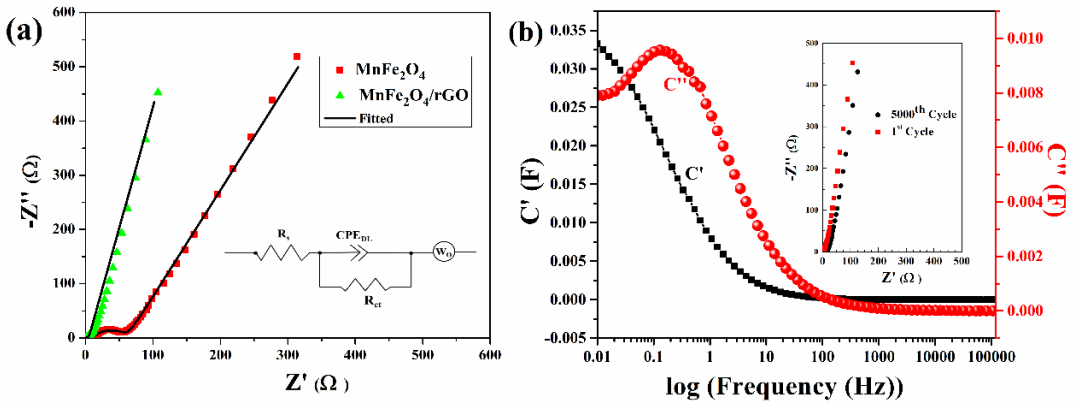

Fig. 5.9. **(a)** Nyquist plots of $MnFe_2O_4$, the $MnFe_2O_4$/rGO composite. **(b)** The behaviour of real and imaginary capacitance values of $MnFe_2O_4$/rGO composite as a function of frequency. Inset shows the EIS spectra of $MnFe_2O_4$/rGO composite before cycling and after 5000 cycles.

Electrical impedance spectroscopy (EIS) was performed to understand the conductive and capacitive nature of the electrodes with the three-electrode system within the frequency range from 0.01 to 100 kHz with the perturbation voltage of 10 mV. The Nyquist plots of the composite and bare particles have been shown in **Fig. 5.9a**. In the high-frequency region of the Nyquist plot, the semi-circular part describes the interfacial charge transfer resistance (R_{ct}) between the electrode and electrolyte whereas the straight line in the low-frequency region signifies a capacitive nature [53, 54]. A larger diameter of the semi-circle indicates higher resistance provided to the mobility of ions and conversely, a smaller diameter means enhanced electrochemical properties.

It can be observed that as compared to pure $MnFe_2O_4$, the $MnFe_2O_4$/rGO nanocomposite exhibits a much shorter diameter suggesting lower charge transfer resistance. Moreover, at the low-frequency region, the slope corresponding to the composite is closer to 90° than the bare $MnFe_2O_4$ nanoparticles, indicating a better capacitive behaviour. The Nyquist plot has been fitted with Z-view software using the equivalent circuit shown in the inset of **Fig. 5.9a**. Here constant phase element (CPE_{DL}) is used in parallel with R_{ct} to model the imperfect capacitor in high-frequency region. On the other side, Warburg impedance (W_O) indicates the straight line in low-frequency region. It is well known that the intersection of the semicircle on the real axis at a high-frequency region signifies the electrolyte solution resistance (R_s). The R_s and R_{ct} values of $MnFe_2O_4$ are found to be 9.31Ω and 45.6Ω whereas for $MnFe_2O_4$/rGO they are only 0.25 Ω and 1.25 Ω respectively. This drastic improvement in the charge transfer region can be

related to the incorporation of conductive graphene which improved the conductivity of the composite particle which also in turn increased the specific capacitance.

Additionally, EIS measurement was also done after the 5000 cycle charging discharging test. Inset of **Fig. 5.9b** shows the EIS spectra of $MnFe_2O_4$/rGO before and after cycling, where only a slight increase of resistances can be observed without affecting the pattern remarkably, which can be attributed to the repeated long-term cycling effect. The EIS results along with good capacitance retention and coulombic efficiency thus ensures high cyclic durability with a very slight possible reduction of electrochemical activities of the $MnFe_2O_4$/rGO electrode material after 5000 cycles.

To obtain further comprehension, complex capacitance calculations for the composite were conducted. To further explore the electrode capacitance dependency on the frequency, the complex capacitance model was used [55], in which the capacitance can be written as:

$$C(\omega) = C'(\omega) - j\,C''(\omega) \qquad (7)$$

where $C'(\omega)$ and $C''(\omega)$ stand for the real and imaginary parts of the capacitance respectively and are represented as:

$$C'(\omega) = \frac{-Z''(\omega)}{\omega |Z(\omega)|^2} \qquad (8)$$

$$C''(\omega) = \frac{Z'(\omega)}{\omega |Z(\omega)|^2} \qquad (9)$$

where ω is the angular frequency, $Z'(\omega)$ and $Z''(\omega)$ indicate respectively the real and imaginary parts of the impedance, and the term $|\,Z(\omega)\,|$ shows the modulus of the impedance. This model is potent to explore the qualitative study of the variation of capacitance with respect to frequency.

Variations of $C'(\omega)$, and $C''(\omega)$ with frequency in case $MnFe_2O_4$/rGO have been displayed in **Fig. 5.9b**. The frequency dependence of real capacitance describes how electrolyte ions penetrate within the pores of electrodes at a specific frequency. In case of low frequencies, the pores deep inside the electrode become easily accessible for the electrolyte ions and consequently $C'(\omega)$ increases. But, in the case of high frequencies, the electrolyte ions merely access the surface of the pores which results in decreased $C'(\omega)$. At very high frequencies, it can be observed that $C'(\omega)$ does not depend on frequency. The imaginary capacitance $C''(\omega)$ indicates the dissipation of energy in the time of the charging process [48]. Here the $C'(\omega)$ and $C''(\omega)$ values are not comparable with the calculated specific capacitance which was previously calculated from CV and GCD curves since in EIS measurements, immobility takes place as the ions get confined within the electrolyte solution [56]. Furthermore, for the determination of the

charge-discharge rate performance of $MnFe_2O_4$/rGO, the relaxation time τ_o (s) is derived from the imaginary part of the capacitance [$C''(\omega)$] with the help of the inverse of the maximum value of frequency f_0. In addition, τ_o is also related to the time which is required to discharge all the stored energy with an efficiency greater than 50% [57]. A relaxation time of 7s suggests that only a short time is needed for discharging all the energy from the electrode.

5.4 Conclusion:

In summary, manganese ferrite nanoparticles and its nanocomposite with graphene have been prepared by a facile single-step solvothermal method for its possible application as electrode material for supercapacitors. The experimental results showed that $MnFe_2O_4$/rGO composites have highly improved electrochemical performance in comparison to the bare $MnFe_2O_4$ nanoparticles. Reduced graphene oxide executes an important role in providing better conductivity as well as structure for improving the electrochemical properties of $MnFe_2O_4$/rGO nanocomposite. The specific capacitance of $MnFe_2O_4$/rGO composite electrode greatly increased to a value of 253 Fg^{-1} from 133 Fg^{-1} obtained for $MnFe_2O_4$ electrode corresponding to a current density of 10 Ag^{-1}. Furthermore, the $MnFe_2O_4$/rGO composite exhibited significantly reduced charge transfer resistance. Additionally, even after 5000 cycles, the charge/discharge stability of $MnFe_2O_4$/rGO electrode dropped by only 4%, indicating reduced 'cycle fatigue'. Thus, the $MnFe_2O_4$/rGO nanocomposite synthesized using our single step solvothermal method can be a potential electrode material with good specific capacitance, high stability, and low impedance, indicating its promising practical functioning in future supercapacitor devices.

References:

[1] K. Sharma, A. Arora, and S. K. Tripathi, "Review of supercapacitors: Materials and devices," *Journal of Energy Storage,* vol. 21, pp. 801-825, 2019.

[2] H. Gao, Y. Li, H. Zhao, J. Xiang, and Y. Cao, "A general fabrication approach on spinel MCo2O4 (M= Co, Mn, Fe, Mg and Zn) submicron prisms as advanced positive materials for supercapacitor," *Electrochimica Acta,* vol. 262, pp. 241-251, 2018.

[3] W. Zhang *et al.*, "One-step facile solvothermal synthesis of copper ferrite–graphene composite as a high-performance supercapacitor material," *ACS applied materials & interfaces,* vol. 7, no. 4, pp. 2404-2414, 2015.

[4] X. Sun *et al.*, "Facile synthesis of Co3O4 with different morphologies loaded on amine modified graphene and their application in supercapacitors," *Journal of Alloys and Compounds,* vol. 685, pp. 507-517, 2016.

[5] M. Arunkumar and A. Paul, "Importance of electrode preparation methodologies in supercapacitor applications," *ACS omega,* vol. 2, no. 11, p. 8039, 2017.
[6] S. Suresh, A. Prakash, and D. Bahadur, "The role of reduced graphene oxide on the electrochemical activity of MFe2O4 (M= Fe, Co, Ni and Zn) nanohybrids," *Journal of Magnetism and Magnetic Materials,* vol. 448, pp. 43-51, 2018.
[7] T. Purkait, G. Singh, D. Kumar, M. Singh, and R. S. Dey, "High-performance flexible supercapacitors based on electrochemically tailored three-dimensional reduced graphene oxide networks," *Scientific reports,* vol. 8, no. 1, pp. 1-13, 2018.
[8] V. Augustyn, P. Simon, and B. Dunn, "Pseudocapacitive oxide materials for high-rate electrochemical energy storage," *Energy & Environmental Science,* vol. 7, no. 5, pp. 1597-1614, 2014.
[9] N. Parveen *et al.*, "Renewable biopolymer-derived carbon–nickel oxide nanocomposite as an emerging electrode material for energy storage applications," p. 100591, 2023.
[10] F. Arshad, N. Parveen, S. A. Ansari, J. A. Khan, M. P. J. E. S. Sk, and P. Research, "Microwave-mediated synthesis of tetragonal Mn3O4 nanostructure for supercapacitor application," vol. 30, no. 28, pp. 71464-71471, 2023.
[11] H. Souri and D. Bhattacharyya, "Highly stretchable multifunctional wearable devices based on conductive cotton and wool fabrics," *ACS applied materials & interfaces,* vol. 10, no. 24, pp. 20845-20853, 2018.
[12] Y. Wang, Y. Ding, X. Guo, and G. Yu, "Conductive polymers for stretchable supercapacitors," *Nano Research,* vol. 12, no. 9, pp. 1978-1987, 2019.
[13] T. Arun *et al.*, "NiFe2O4 nanospheres with size-tunable magnetic and electrochemical properties for superior supercapacitor electrode performance," *Electrochimica Acta,* vol. 399, p. 139346, 2021.
[14] B. Rani and N. K. Sahu, "Electrochemical properties of CoFe2O4 nanoparticles and its rGO composite for supercapacitor," *Diamond and Related Materials,* vol. 108, p. 107978, 2020.
[15] S. Nilmoung, P. Kidkhunthod, and S. Maensiri, "The structural and electrochemical properties of CNF/MnFe2O4 composite nanostructures for supercapacitors," *Materials Chemistry and Physics,* vol. 220, pp. 190-200, 2018.
[16] L. S. Ghadimi, N. Arsalani, A. G. Tabrizi, A. Mohammadi, and I. Ahadzadeh, "Novel nanocomposite of MnFe2O4 and nitrogen-doped carbon from polyaniline carbonization as electrode material for symmetric ultra-stable supercapacitor," *Electrochimica Acta,* vol. 282, pp. 116-127, 2018.
[17] W. Cai, T. Lai, W. Dai, and J. Ye, "A facile approach to fabricate flexible all-solid-state supercapacitors based on MnFe2O4/graphene hybrids," *Journal of Power Sources,* vol. 255, pp. 170-178, 2014.
[18] Y. Wang *et al.*, "Electropolymerized polyaniline/manganese iron oxide hybrids with an enhanced color switching response and electrochemical energy storage," *Journal of Materials Chemistry A,* vol. 3, no. 41, pp. 20778-20790, 2015.
[19] L. Niu *et al.*, "Simple synthesis of amorphous NiWO4 nanostructure and its application as a novel cathode material for asymmetric supercapacitors," *ACS applied materials & interfaces,* vol. 5, no. 16, pp. 8044-8052, 2013.
[20] Y. Liu, R. Wang, and X. Yan, "Synergistic effect between ultra-small nickel hydroxide nanoparticles and reduced graphene oxide sheets for the application in high-performance asymmetric supercapacitor," *Scientific reports,* vol. 5, no. 1, pp. 1-12, 2015.
[21] L. Li *et al.*, "Uniformly dispersed ZnFe2O4 nanoparticles on nitrogen-modified graphene for high-performance supercapacitor as electrode," *Scientific reports,* vol. 7, no. 1, pp. 1-12, 2017.

[22] Y. Huang, J. Liang, and Y. Chen, "An overview of the applications of graphene-based materials in supercapacitors," *small,* vol. 8, no. 12, pp. 1805-1834, 2012.
[23] C. X. Guo and C. M. Li, "A self-assembled hierarchical nanostructure comprising carbon spheres and graphene nanosheets for enhanced supercapacitor performance," *Energy & Environmental Science,* vol. 4, no. 11, pp. 4504-4507, 2011.
[24] B. Wang, J. Park, C. Wang, H. Ahn, and G. Wang, "Mn3O4 nanoparticles embedded into graphene nanosheets: preparation, characterization, and electrochemical properties for supercapacitors," *Electrochimica Acta,* vol. 55, no. 22, pp. 6812-6817, 2010.
[25] S. A. J. N. Ansari, "Graphene quantum dots: novel properties and their applications for energy storage devices," vol. 12, no. 21, p. 3814, 2022.
[26] W. Fu *et al.*, "β-Ni (OH) 2 nanosheets grown on graphene as advanced electrochemical pseudocapacitor materials with improved rate capability and cycle performance," *Materials Letters,* vol. 134, pp. 107-110, 2014.
[27] E. Umeshbabu, G. Rajeshkhanna, and G. Ranga Rao, "Effect of solvents on the morphology of NiCo2O4/graphene nanostructures for electrochemical pseudocapacitor application," *Journal of Solid State Electrochemistry,* vol. 20, no. 7, pp. 1837-1844, 2016.
[28] A. R. Ansari, S. A. Ansari, N. Parveen, M. O. Ansari, and Z. J. I. C. C. Osman, "Ag nanoparticles anchored reduced graphene oxide sheets@ nickel oxide nanoflakes nanocomposites for enhanced capacitive performance of supercapacitors," p. 110519, 2023.
[29] B. Bashir *et al.*, "Copper substituted nickel ferrite nanoparticles anchored onto the graphene sheets as electrode materials for supercapacitors fabrication," *Ceramics International,* vol. 45, no. 6, pp. 6759-6766, 2019.
[30] A. G. Tabrizi, N. Arsalani, A. Mohammadi, H. Namazi, L. S. Ghadimi, and I. J. N. J. o. C. Ahadzadeh, "Facile synthesis of a MnFe 2 O 4/rGO nanocomposite for an ultra-stable symmetric supercapacitor," vol. 41, no. 12, pp. 4974-4984, 2017.
[31] S. Ishaq *et al.*, "Facile synthesis of ternary graphene nanocomposites with doped metal oxide and conductive polymers as electrode materials for high performance supercapacitors," vol. 9, no. 1, p. 5974, 2019.
[32] M. P. Reddy, A. J. M. Mohamed, and M. Materials, "One-pot solvothermal synthesis and performance of mesoporous magnetic ferrite MFe2O4 nanospheres," vol. 215, pp. 37-45, 2015.
[33] M. Ahmed, N. Okasha, and S. El-Dek, "Preparation and characterization of nanometric Mn ferrite via different methods," *Nanotechnology,* vol. 19, no. 6, p. 065603, 2008.
[34] J. Panda, K. Ghorui, R. Sarkar, and B. Tudu, "Fabrication and characterization of self-assembled zinc ferrite nanospheres for biomedical applications," *Applied Physics A,* vol. 128, no. 4, pp. 1-9, 2022.
[35] H. L. Andersen, M. Saura-Múzquiz, C. Granados-Miralles, E. Canévet, N. Lock, and M. Christensen, "Crystalline and magnetic structure–property relationship in spinel ferrite nanoparticles," *Nanoscale,* vol. 10, no. 31, pp. 14902-14914, 2018.
[36] R. Pązik *et al.*, "Facile non-hydrolytic synthesis of highly water dispersible, surfactant free nanoparticles of synthetic MFe 2 O 4 (M–Mn 2+, Fe 2+, Co 2+, Ni 2+) ferrite spinel by a modified Bradley reaction," *RSC advances,* vol. 3, no. 30, pp. 12230-12243, 2013.
[37] H. Nikmanesh, E. Jaberolansar, P. Kameli, A. G. Varzaneh, M. Mehrabi, and M. Rostami, "Structural and magnetic properties of CoFe2O4 ferrite nanoparticles doped by gadolinium," *Nanotechnology,* vol. 33, no. 4, p. 045704, 2021.

[38] L. Wang, X. Wang, X. Xiao, F. Xu, Y. Sun, and Z. Li, "Reduced graphene oxide/nickel cobaltite nanoflake composites for high specific capacitance supercapacitors," *Electrochimica Acta,* vol. 111, pp. 937-945, 2013.

[39] C. Casiraghi, S. Pisana, K. Novoselov, A. K. Geim, and A. Ferrari, "Raman fingerprint of charged impurities in graphene," *Applied physics letters,* vol. 91, no. 23, p. 233108, 2007.

[40] G. Eda and M. Chhowalla, "Chemically derived graphene oxide: towards large-area thin-film electronics and optoelectronics," *Advanced materials,* vol. 22, no. 22, pp. 2392-2415, 2010.

[41] S. Ishaq *et al.*, "Facile synthesis of ternary graphene nanocomposites with doped metal oxide and conductive polymers as electrode materials for high performance supercapacitors," *Scientific reports,* vol. 9, no. 1, pp. 1-11, 2019.

[42] H. Pan, M. Xu, Q. Qi, and X. Liu, "Facile preparation and excellent microwave absorption properties of an RGO/Co 0.33 Ni 0.67 lightweight absorber," *RSC Advances,* vol. 7, no. 69, pp. 43831-43838, 2017.

[43] L. Yue *et al.*, "One-pot synthesis CoFe2O4/CNTs composite for asymmetric supercapacitor electrode," *Solid State Ionics,* vol. 329, pp. 15-24, 2019.

[44] S. Kogularasu *et al.*, "A comparative study on conventionally prepared MnFe2O4 nanospheres and template-synthesized novel MnFe2O4 nano-agglomerates as the electrodes for biosensing of mercury contaminations and supercapacitor applications," *Electrochimica Acta,* vol. 290, pp. 533-543, 2018.

[45] L. Geng, F. Yan, C. Dong, and C. An, "Design and regulation of novel MnFe2O4@ C nanowires as high performance electrode for supercapacitor," *Nanomaterials,* vol. 9, no. 5, p. 777, 2019.

[46] Z. Zhou *et al.*, "Electronic structure studies of the spinel CoFe2O4 by X-ray photoelectron spectroscopy," *Applied Surface Science,* vol. 254, no. 21, pp. 6972-6975, 2008.

[47] H. Gao, J. Xiang, and Y. Cao, "Hierarchically porous CoFe2O4 nanosheets supported on Ni foam with excellent electrochemical properties for asymmetric supercapacitors," *Applied Surface Science,* vol. 413, pp. 351-359, 2017.

[48] R. Rajalakshmi, K. Remya, C. Viswanathan, and N. Ponpandian, "Enhanced electrochemical activities of morphologically tuned MnFe 2 O 4 nanoneedles and nanoparticles integrated on reduced graphene oxide for highly efficient supercapacitor electrodes," *Nanoscale Advances,* vol. 3, no. 10, pp. 2887-2901, 2021.

[49] H. Xia, Y. Wang, J. Lin, and L. Lu, "Hydrothermal synthesis of MnO2/CNT nanocomposite with a CNT core/porous MnO2 sheath hierarchy architecture for supercapacitors," *Nanoscale research letters,* vol. 7, no. 1, pp. 1-10, 2012.

[50] G. Singh and S. J. i. j. o. h. e. Chandra, "Electrochemical performance of MnFe2O4 nano-ferrites synthesized using thermal decomposition method," vol. 43, no. 8, pp. 4058-4066, 2018.

[51] P. Guo *et al.*, "Electrochemical properties of colloidal nanocrystal assemblies of manganese ferrite as the electrode materials for supercapacitors," vol. 52, pp. 5359-5365, 2017.

[52] N. Foroutan, M. S. Lashkenari, E. Alizadeh, and M. J. I. J. o. H. E. Sedighi, "Synthesis of manganese ferrite/graphene oxide nanocomposite and investigation of its supercapacitor behaviors," Int. J. Hydrog. Energy, Vol. 48, no. 66, pp. 25859-2586, 2023.

[53] A. Soam, P. Kavle, A. Kumbhar, and R. O. Dusane, "Performance enhancement of micro-supercapacitor by coating of graphene on silicon nanowires at room temperature," *Current Applied Physics,* vol. 17, no. 2, pp. 314-320, 2017.

CHAPTER 6

TIME-DEPENDENT ADSORPTIVE REMOVAL OF METHYLENE BLUE DYE BY $CoFe_2O_4$/rGO NANOCOMPOSITE

In this chapter, the solvothermal method was employed to prepare spinel cobalt ferrite with graphene adsorbents (CF-rGO). By using X-ray diffraction, scanning electron microscopy (SEM), FTIR, XPS, and VSM, the properties of the produced samples were investigated. The high saturation magnetization value of the sample may be used by the external magnetic field, which is advantageous for the recycling procedure in the adsorption application. The analyses show that CF-rGO with adsorption capacity of 15.5 mg.g^{-1} has successfully removed 93% of MB from water. The produced composite of graphene and ferrite is promising since it is simple to separate, has a high adsorption capacity, and is inexpensive. As a result, it may be employed as a reusable adsorbent for very effective MB adsorption from aqueous solutions.

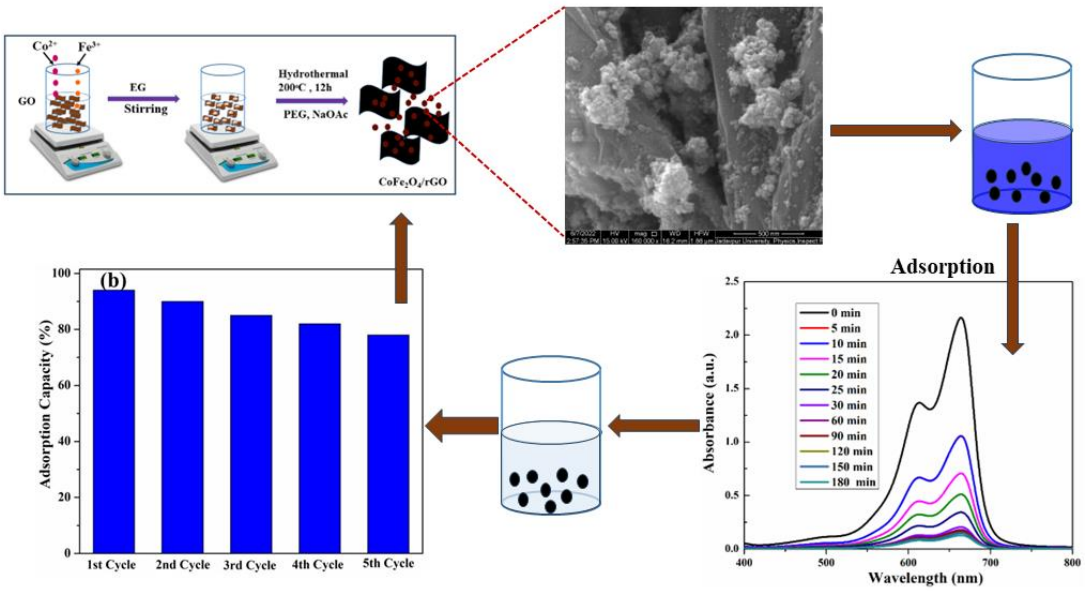

6.1. Introduction

Pollutants of several types can be found in the effluents produced by the textile industry. Organic dyes are widely used in the textile industry because they produce vibrant colors and exhibit beneficial qualities such as being easily water-soluble, less expensive to make, and simpler to apply to cloth. Maximum dyes are considered to be toxic and have a complex and stable aromatic structure, they are difficult to degrade [1, 2]. Hence, eliminating these dyes from industrial effluents has become one of the major environmental concerns in recent times [3]. Different techniques, such as adsorption, biological treatment, photocatalytic degradation, chemical oxidation, and coagulation, have been widely used to remove dyes from dye-containing wastewater [4-9]. Due to its low cost, straightforward design, simple operation, and chemical inertness to harmful compounds, adsorption is regarded as one of the most successful approaches for advanced wastewater treatment that removes organic dyes [10-12].

Many kinds of research have been performed for eliminating pollutant dyes using various materials. For treating huge amounts of wastewater, it is crucial to create new adsorbents with high adsorption capacity and quick separation rates [9, 13]. Graphene is a promising material for reducing large amounts of organic contaminants from industrial wastewater because of its high surface area, excellent chemical stability, and high electron mobility in its chemical structure [14-17]. Although efficient as an adsorbent, graphene is difficult to reuse, which could drive up costs and lead to secondary contamination. Many researchers have combined graphene with magnetic materials to overcome the aforementioned problems, where the resulting adsorbent can be easily removed from the treated water and used repeatedly without losing its properties.

In recent years, a lot of interest has been seen in using magnetic nanoparticles to solve environmental issues [18, 19]. Due to their outstanding qualities, including high saturation magnetization; and shape- and size-dependent magnetic behavior, cobalt ferrite ($CoFe_2O_4$) nanocrystals with spinel structure have received a lot of attention for environmental remediation [20]. The well-known inverse spinel cobalt ferrite has Fe^{3+} ions impartially distributed throughout the A and B sites and Co^{2+} ions on the B sites [21].

In the present work, $CoFe_2O_4$ (CF) nanoparticles and their composite with graphene (CF-rGO) were synthesized using a one-pot solvothermal method. An investigation was done on the samples' magnetic and structural characteristics. The samples were engaged as adsorbents for

the removal of Methylene Blue (MB) dye from an aqueous solution. For purifying water, the impact of contact time on the adsorption process was investigated. The findings demonstrated that rGO has a significant role in improving the adsorption capacity of $CoFe_2O_4$ by decreasing nanoparticle aggregation and enhancing the active surface area for adsorption. The adsorptive efficiency of the CF-rGO composite was analyzed and verified by pseudo-second-order kinetics. The possible mechanism of enhanced efficiency due to the incorporation of rGO has also been suggested.

6.2. Experimental section

6.2.1. Materials

Natural graphite flakes, sulfuric acid (H_2SO_4, 98%), sodium nitrate ($NaNO_3$), potassium permanganate ($KMnO_4$, 99.9%), hydrogen peroxide (H_2O_2, 30%), sodium acetate (NaOAc), Ferric chloride ($FeCl_3$), manganese chloride ($CoCl_2$, $4H_2O$), polyethylene glycol (PEG; M.W.=6000), ethanol etc. were obtained from Sigma-Aldrich Co. (Bangalore, India). All the chemicals purchased were of scientific grade and used directly without any purification.

6.2.2. Synthesis of GO

Graphene oxide (GO) was synthesized by the Hummer's method with slight modification [1]. In brief 2 g of Graphite powder and 2 g of $NaNO_3$ were mixed in 90 ml H_2SO_4. The mixture was stirred in a beaker and kept in an ice bath under a controlled temperature between 5-15^oC. This solution was kept under a continuous stirring process for three hours. After that, in this stirring condition, 10 g of $KMnO_4$ was added to oxidize the graphite powder to graphitic oxide in such a way that the temperature remained under 15 ^oC. After one hour of stirring with added $KMnO_4$, 90 ml water was added to the solution and as a result, a huge amount of heat energy was developed which helped to separate graphitic oxide layers into graphene oxide. At last, the reaction was terminated by adding hydrogen peroxide (H_2O_2). The obtained graphene oxide solution was washed several times with DI water and ethanol and finally dried at 60 ^oC.

6.2.3. Synthesis of $CoFe_2O_4$/rGO

CF-rGO nanocomposites were prepared via a solvothermal method in which GO was used as a precursor material (**Fig. 6.1**). Typically, 90 mg of GO was dispersed in 40 ml of ethylene

glycol with ultrasonication for 2 h. After that, 4 mmol of $FeCl_3$ and 2 mmol of $CoCl_2.4H_2O$ were poured into it and the mixed solution was kept under ultrasonication again for 3h. Subsequently, 1 g of polyethylene glycol (PEG) and 3 g of Sodium Acetate (NaOAc) were added followed by vigorous stirring for 1 h. The whole mixed solution was then transferred to a stainless-steel autoclave and heated at 200 °C for 12 h. After reaching room temperature, the precipitated blackish product was collected from the autoclave and was separated with centrifugation several times with de-ionized water and ethanol. The final product, namely $CoFe_2O_4$/rGO (CF-rGO) was then centrifuged and dried at 60 °C. For comparison purposes, pure $CoFe_2O_4$ (CF) was also synthesized under the same condition without adding GO.

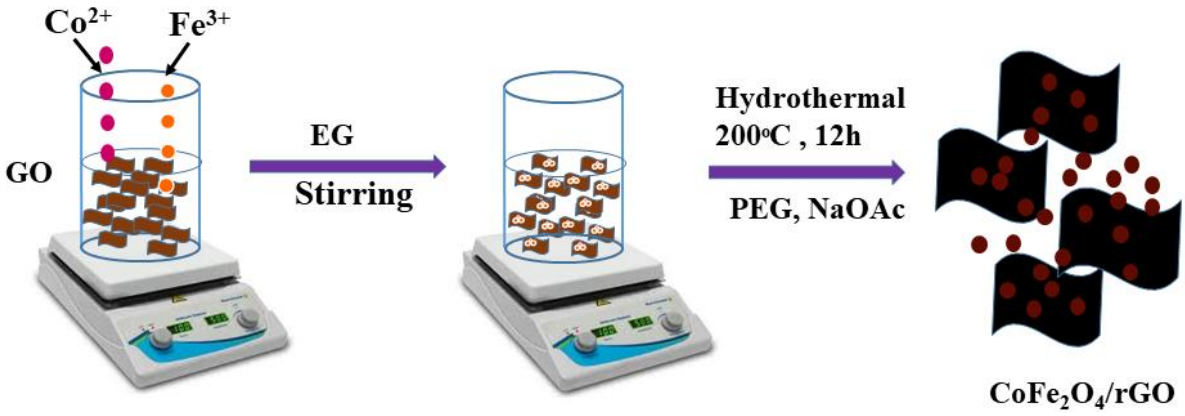

Fig. 6.1. Schematic of the in situ synthetic route for the CF-rGO nanocomposites.

6.2.4 Material Characterization

The X-ray powder diffraction (XRD) patterns for the samples were carried out by a Bruker D8 advanced diffractometer, equipped with Cu K_α (λ=1.54059Å) radiation with 2θ in the range of 20- 80^o with a step size of 0.0199°. The external surface morphologies of the as-prepared samples were analyzed by a field emission scanning electron microscope (FEI INSPECT F50) operated at 10 kV. The Raman spectroscopy data were recorded using a Raman microscope (HORIBA, Lab RAM, HR800) at room temperature over a range of 500-2500 cm^{-1}. Fourier-transformed infrared (FTIR) spectroscopy was performed at ambient temperature by a Perkin–Elmer FTIR spectrum RXI spectrometer in transmittance mode in the range 500-4000 cm^{-1}. For FTIR measurement, samples were mixed with KBr powder and pressed into pallets applying hydraulic pressure. The background correction was done with respect to KBr pallets.

The elemental composition of as-prepared CF-rGO was investigated by X-ray photoelectron spectroscopy (XPS; Omicron, serial no:0571). For XPS measurement, an aqueous dispersion solution of CF-rGO was prepared and spin-coated onto a silicon substrate followed by air drying. The magnetic measurement was carried out by a vibrating sample magnetometer (Lake Shore Cryotronics, USA) at room temperature in the range ±2 Tesla.

6.2.5. Adsorption studies

The adsorption experiments were carried out in a batch. 30 mg of the as-synthesized adsorbent was added into 50 ml MB solution (10 mg/l) and stirred under dark condition. At a pre-decided time, the concentration (C_t) of MB solution, from which the adsorbent was taken out by magnetic separation was studied through the measurement of the absorbance at 664 nm (λ_{max} of MB solution) using a Shimadzu UV-2550 UV-vis spectrophotometer.

The adsorption amount q_t (mg.g^{-1}) is calculated based on the following equation:

$$q_t = [(C_0 - C_t) \times V] / m \qquad (1)$$

in which q_t is the amount of adsorbed MB molecules on the adsorbent per gram, C_0 and C_t (mg/l) are the concentrations of the MB solution at the initial time t=0 and adsorption time t, respectively. V (l) is the initial volume of the MB solution and m (g) is the mass of the adsorbent.

The percentage removal efficiency, RE was calculated using:

$$\% RE = (C_0 - C_t) / C_0 \times 100 \qquad (2)$$

6.3. Results and Discussions

6.3.1. XRD

Powder XRD measurements were carried out to examine the structure of the synthesized nanomaterials. The XRD spectra of CF and CF-rGO composite particles have been shown in **Fig. 6.2a**. Both pure CF and the CF-rGO composite showed five distinct diffraction peaks. The characteristics peaks at 2θ values of 30.2°, 35.5°, 43.1°, 57.2°, and 62.7° were assigned to the

220, 311, 400, 511, and 440 crystallographic planes of $CoFe_2O_4$. All primary diffraction peaks of $CoFe_2O_4$ are linked together by a single-phase cubic spinel structure. The presence of an intense sharp peaks in XRD data indicates that the material is very crystalline in nature. Additionally, no extra peak is seen, which supports the nanoparticle's purity.

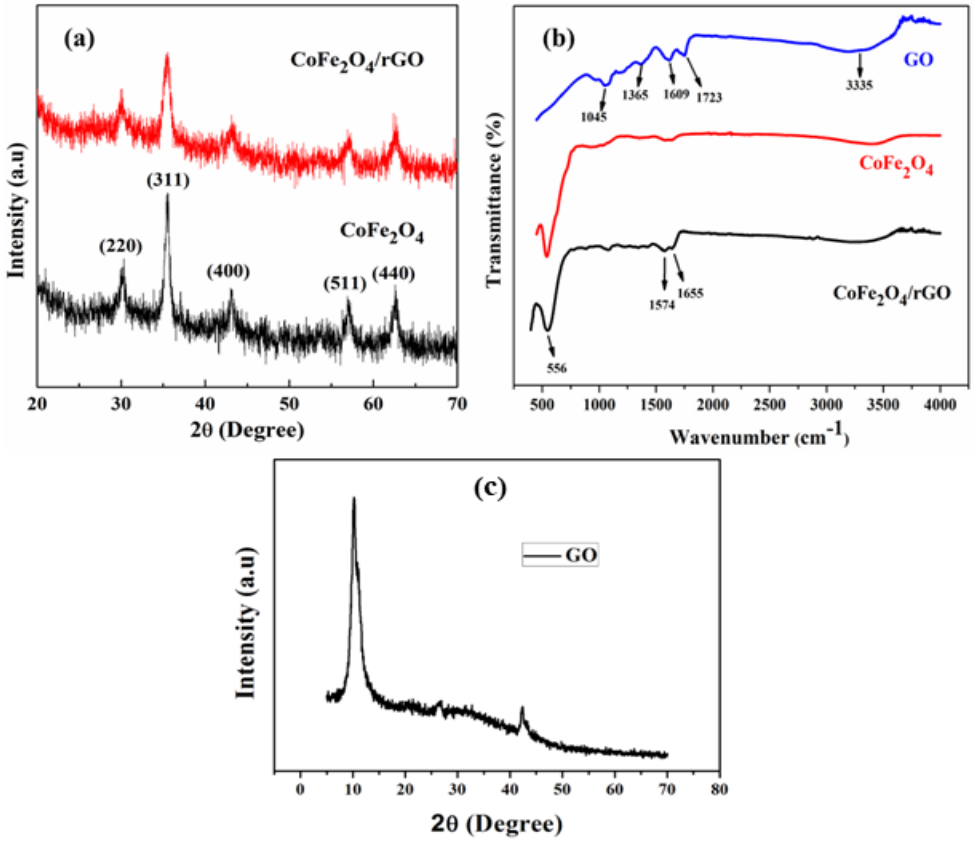

Fig. 6.2. (a) XRD patterns of $CoFe_2O_4$, and $CoFe_2O_4$-rGO (b) FTIR spectra of GO and CF and CF-rGO composite. (c) XRD spectrum of graphene oxide.

The XRD spectrum of GO (**Fig. 6.2c**) shows the distinctive GO peak near 11.5°, which represents the 001 crystallographic plane. A weak peak near ~ 42° may have arised due to defects in the GO sheets. **Fig. 6.2a** makes it evident that in the case of the composite, there are no other notable graphene-related peaks other than the primary peaks of $CoFe_2O_4$ as indicated above. The absence of the rGO-related diffraction peaks may also indicate that the rGO in the composite material has completely exfoliated, from which it may be deduced that restacking has been successfully avoided. A diffraction peak disappears or weakens if the regular stacking of rGO is reduced. The crystallinity of $CoFe_2O_4$ was not harmed by the addition of graphene as evidenced by the absence of any graphene peak. The performance of the adsorptive process is favoured by this exfoliation of rGO in the composite material.

6.3.2. FTIR

Fourier transform Infrared spectroscopy was carried out to investigate the functional groups within the prepared samples. **Fig. 6.2b** depicts the FTIR spectra recorded for the prepared samples between 500-4000 cm^{-1}. It can be noted that the GO spectrum contains various exogenous functional groups connected to the graphite lattice. Stretching vibrations of the epoxy (C-O) functional group were noticed at 1045 cm^{-1}. The appearance of a peak at 1365 cm^{-1} may be due to the presence of a tertiary C-OH group. One more characteristic peak at 1609 cm^{-1} is related to skeletal vibrations which come from the primitive (C=C) graphitic network. C=O stretching vibration of sp^3 carbon ascribed to carboxyl COOH groups located at the edges of graphite oxide sheets was noticed at 1723 cm^{-1}. The band at 3335 cm^{-1} was associated with the stretching vibrations of hydroxyl groups, respectively. FTIR spectrum of GO is very much matched with the previous literature [22, 23]. In the case of both CF and composite, the broad bands around 3000-3500 cm^{-1} are linked with the O-H stretching vibration and the one at 1650 cm^{-1} is connected with the corresponding bending vibration. Moreover, in each case, a strong band at 556 cm^{-1} is ascribed to the metal-oxygen bond. Also, for the nanocomposite, the absence of absorption peak (C=O) and declination of (C-O and C-OH) due to oxygen groups confirms the successful reduction of GO in the synthesis process. A peak noted at 1609 cm^{-1} for GO specifying C=C skeletal vibration of the un-oxidized graphitic lattice was red-shifted to 1590 cm^{-1} confirming upholding the aromatic structure in rGO.

6.3.3. SEM

By using a scanning electron microscope (SEM), the exterior surface morphology and structure of the synthesized samples were further investigated. The representative SEM image of $CoFe_2O_4$ as observed in **Fig. 6.3a,b** in different magnifications depicts morphological appearance to be almost spherical.

Fig. 6.3d,e demonstrate how the $CoFe_2O_4$ nanoparticles are dispersed across the randomly arranged graphene planar sheet, simultaneously producing a large number of pores with a high active surface area. This type of hybrid construction with a high porosity is useful for enhancing dye adsorption. Additionally, the $CoFe_2O_4$ nanoparticles may not aggregate as a result of the

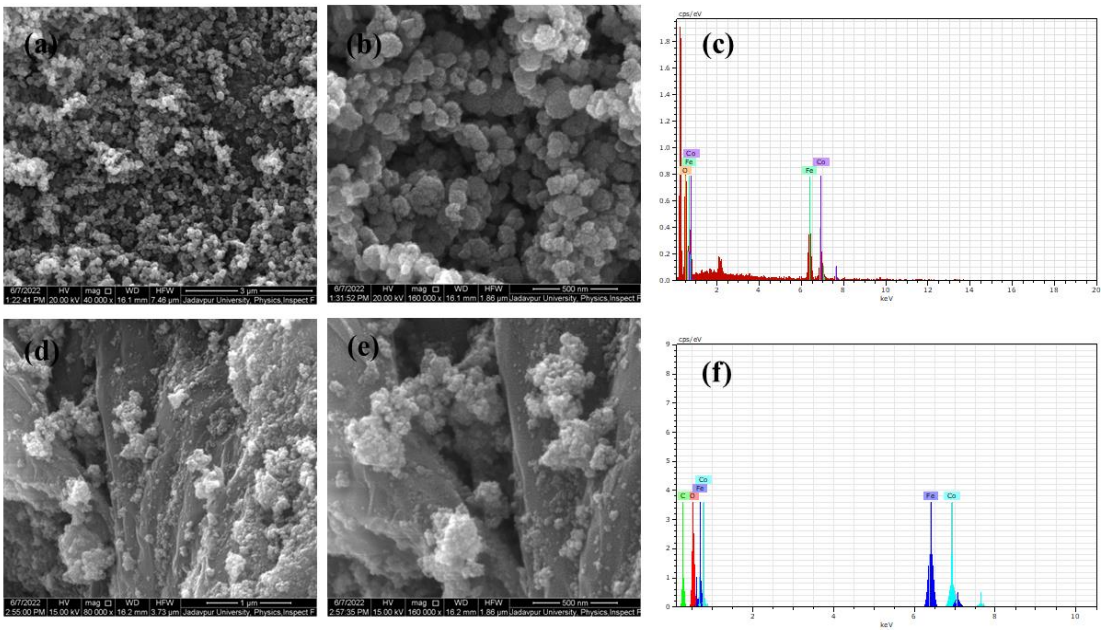

Fig. 6.3. SEM image of $CoFe_2O_4$ (CF) nanoparticles with scalebar 3 μm (a), and scalebar 500 nm (b) SEM image of CF-rGO nanocomposite with scalebar 1 μm (d) and 500 nm (e) EDS spectrum of CF nanoparticles (c) and CF-rGO nanocomposite(f).

graphene sheets, leaving more active sites available for additional adsorption. The graphene sheets also show considerable wrinkling, which strengthened the contact region with cobalt ferrite phases. An elemental analysis of the CF-rGO nanocomposite was also done. **Fig. 6.3c,f** depicts the EDS of the $CoFe_2O_4$ nanoparticles and $CoFe_2O_4$/rGO composite respectively. The presence of Co, Fe, O in $CoFe_2O_4$ and Co, Fe, O and C in the composite is clearly visible. The above observation validates that the nanocomposite is a combination of $CoFe_2O_4$ and graphene.

6.3.4. XPS

The elemental composition and functional groups of the CF-rGO composite were studied using XPS measurement. **Fig. 6.4a** exhibits the characteristic peaks of the as-prepared CF-rGO where no extra peaks were observed other than the peaks associated with the binding energy of O, C, Fe, and Co. For the sake of investigation of surface functionalities, the high-resolution spectrum of the C *1s* regions are fitted into four component peaks as depicted in

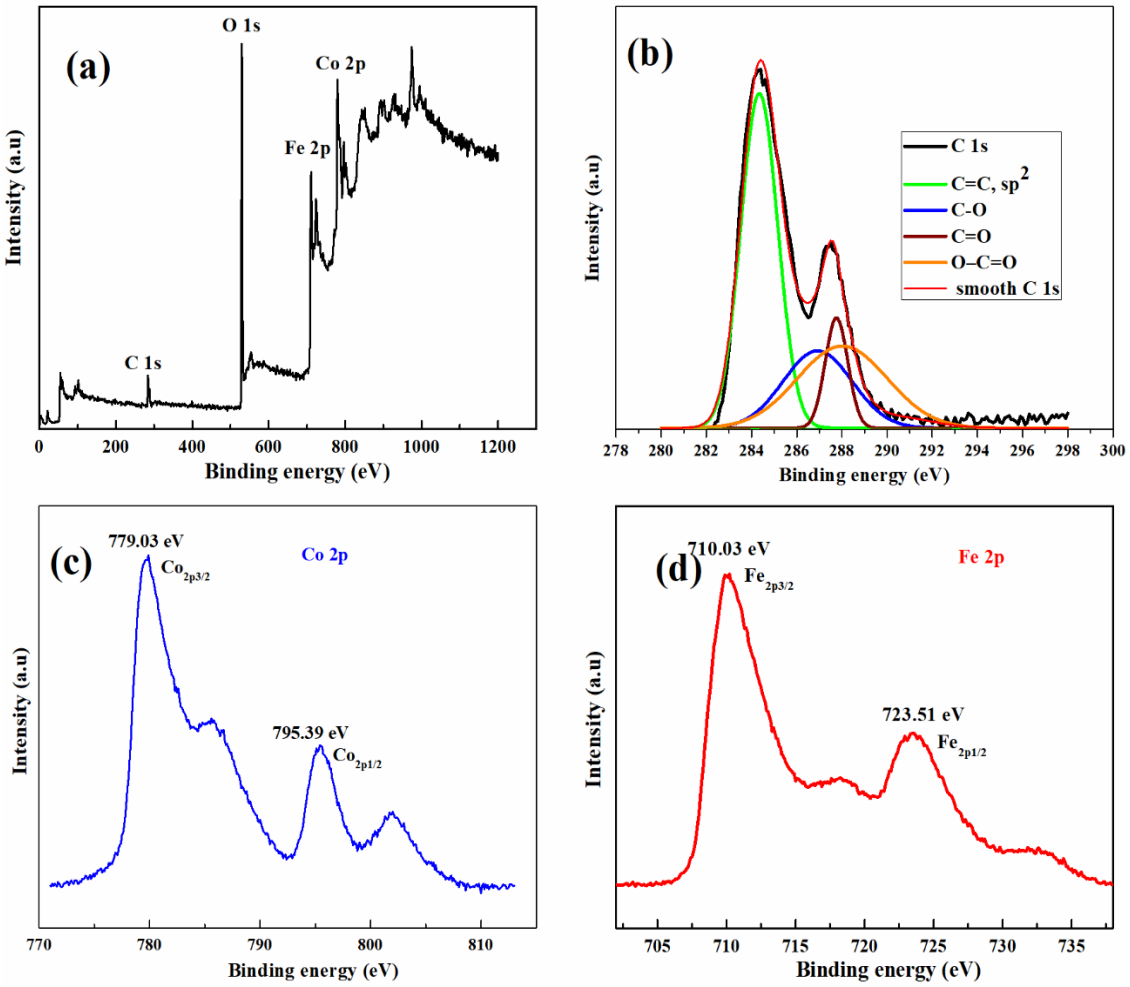

Fig. 6.4. XPS spectra of the CF-rGO nanocomposites showing (a) wide-scan survey (b) C *1s* (c) Co *2p* and (d) Fe *2p* spectra.

Fig. 6.4b, which are associated with sp^2 carbons (C=C, 284.35 eV), epoxy groups (C–O, 286.77 eV), carbonyl groups (C=O, 287.76 eV) and carboxyl groups (O–C=O, 288.13 eV). It can be observed that contributions from the functional group related to the oxygen-containing carbon in the CF-rGO were much reduced and the relatively higher percentage of graphitic carbon established the graphitic nature of the CF-rGO nanocomposites [24]. In the spectrum for Co 2*p* (**Fig. 6.4c**), it was observed that the first two peaks associated with the binding energies at around 779.03 and 785.77 eV are related to Co $2p_{3/2}$ and its shake-up satellites, respectively, on the other hand, the peaks with higher binding energy around 795.39 and 802.02 eV were associated with Co $2p_{1/2}$ and its shake-up satellites, respectively. The presence of a large number of Co^{2+} ions in the sample was confirmed by the sharp Co $2p_{3/2}$ shake-up satellite

because the low-spin Co^{3+} cation only produces significantly weaker satellite features than the high-spin Co^{2+} associated with unpaired valence 3*d* electron orbitals [25]. Finally, in Fig. **Fig. 6.4d**, two peaks of a Fe 2*p* level with binding energies of 710.03 and 723.51 eV were associated with Fe $2p_{3/2}$ and Fe $2p_{1/2}$, respectively. This result confirms the presence of Fe^{3+}. All the findings subsequently approved the presence of CF nanoparticles on the surface of graphene sheets without any extra element [4].

6.3.5. Magnetic property

Using a Vibrating Sample Magnetometer (VSM) with an applied magnetic field in the range of ±2 Tesla (20 kOe), the magnetic characteristics of as-prepared CF nanoparticles and CF-rGO nanocomposite were investigated at room temperature (300K). **Fig. 6.5** depicts the *M-H* curves of these synthesized CF and CF-rGO samples showing ferrimagnetic behaviour. The saturation magnetizations (M_s), retentivity (M_r) and coercivity (H_c) values of CF nanoparticles are 48 emu g^{-1}, 21 emu g^{-1} and 1.9 kOe respectively. Whereas the M_s, M_r and H_c values of CF-rGO nanocomposite are 27 emu g^{-1}, 7 emu g^{-1} and 0.6 kOe respectively. These values are also listed in **Table 1**.

Generally, the exchange interaction between tetrahedral and octahedral sub-lattices and site occupation can be employed to illustrate the reduction in saturation magnetization [26]. In spinel ferrite systems, net magnetization arises due to three types of magnetic interactions between tetrahedral and octahedral site ions, viz. A-A, B-B and A-B interaction. Compared to the other two interactions, the A-B interaction is dominant [26,27]. Additionally, certain Fe^{3+} ions are replaced by rGO in the octahedral B sites of the nanocomposite material. As a result, the incorporation of rGO in cobalt ferrite reduces the saturation magnetization value. The nanocomposite's magnetic properties suggest that it can be easily isolated from the solution phase as an adsorbent within a few minutes by applying an external magnetic field as depicted in the inset of **Fig. 6.5**.

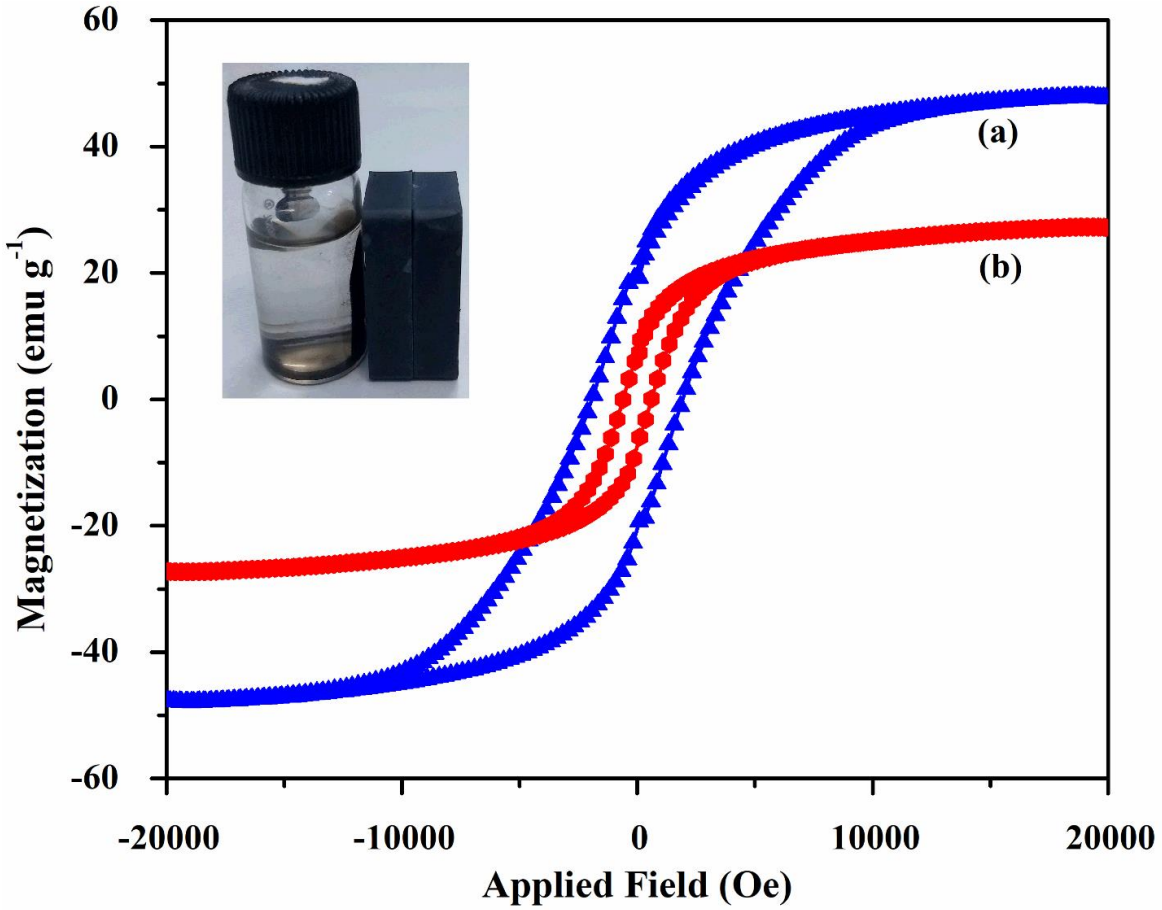

Fig. 6.5. *M-H* Curve of (a) CF nanoparticles and (b) CF-rGO nanocomposite at temperature 300 K with an applied magnetic field between ±2 Tesla. The inset shows a magnetic separation of the CF-rGO nanocomposite particles using a magnet.

The study of the magnetic property thus shows that the obtained CF-rGO heterostructure adsorbent has the advantage of being magnetically separable after the dye removal procedure, making its subsequent reuse possible.

Table 6.1. The Saturation Magnetization (M_s), Retentivity (M_r), coercivity (H_c) and Remanence ratio (M_r/M_s) values of CF nanoparticle and CF-rGO nanocomposite.

Sample	Saturation Magnetization (M_s) ($emu.g^{-1}$)	Retentivity (M_r) ($emu.g^{-1}$)	Coercivity (H_c) (kOe)	Remanence ratio (M_r/M_s)
CF	48	21	1.9	0.44
CF-rGO	27	7	0.6	0.26

6.3.6. Adsorption Property

The adsorptive removal of MB dye as a model pollutant was studied in the presence of CF and CF-rGO as adsorbents. As the concentration of MB solution is proportional to its absorption of light, the adsorption process was carried out by investigating the change in the absorption spectrum of MB in aqueous solution with the help of a UV-Vis spectrophotometer. The time-dependent absorption spectra of methylene blue solution in the presence both adsorbents is shown in **Fig. 6.6a,b**. A typical MB absorption spectrum shows a high monomeric absorption band associated with the wavelength around 662 nm, which refers to the π-π* transition, and a broadened peak at about 610 nm, which corresponds to the 0-1 vibronic transition of methylene blue monomer [28]. The maximum intensity of the band at 662 nm was used to analyze adsorption capability. The absorbance intensity at 662 nm began to diminish with time after the adsorbents were added to the MB solution. It can be observed that the concentration of MB (the initial concentration being 10 mg/l) decreased in an ordered way with the addition of CF and CF-rGO composite.

In the case of bare CF nanoparticles, the percentage of MB dye removal efficiency was found to be 24% in 180 min time, whereas for the CF-rGO composite, the efficiency was found to be 93% in the same amount of time. From the time-dependent adsorption capacity plot (**Fig. 6.6c**), it can be seen that pure CF exhibits meagrely adsorption performance compared to CF-rGO which shows enhanced adsorption activities with the introduction of rGO. Methylene blue with negatively charged groups was used in this study. In an MB solution, the adsorption amount of MB on CF-rGO was 15.5 $mg.g^{-1}$ within 30 min time. Thus showing better adsorption activity than bare CF nanoparticles where the adsorption amount of MB on CF was less than 4 $mg.g^{-1}$ in 180 min time. It is noteworthy that the adsorption properties of MB molecule on the composites are faster in the first 30 min. Afterwards, the increase is slow with time.

The pseudo-second-order kinetic model is used to investigate the kinetics behavior of MB adsorption on the nanocomposites, which is defined as follows [29] [30]:

$$t / q_t = t / q_e + 1 / k_2 q_e^{\,2} \qquad (3)$$

where q_e ($mg.g^{-1}$) is the adsorption amount at equilibrium, the parameter k_2 ($g.mg^{-1}.min^{-1}$) represents the pseudo-second-order rate constant of the kinetic model.

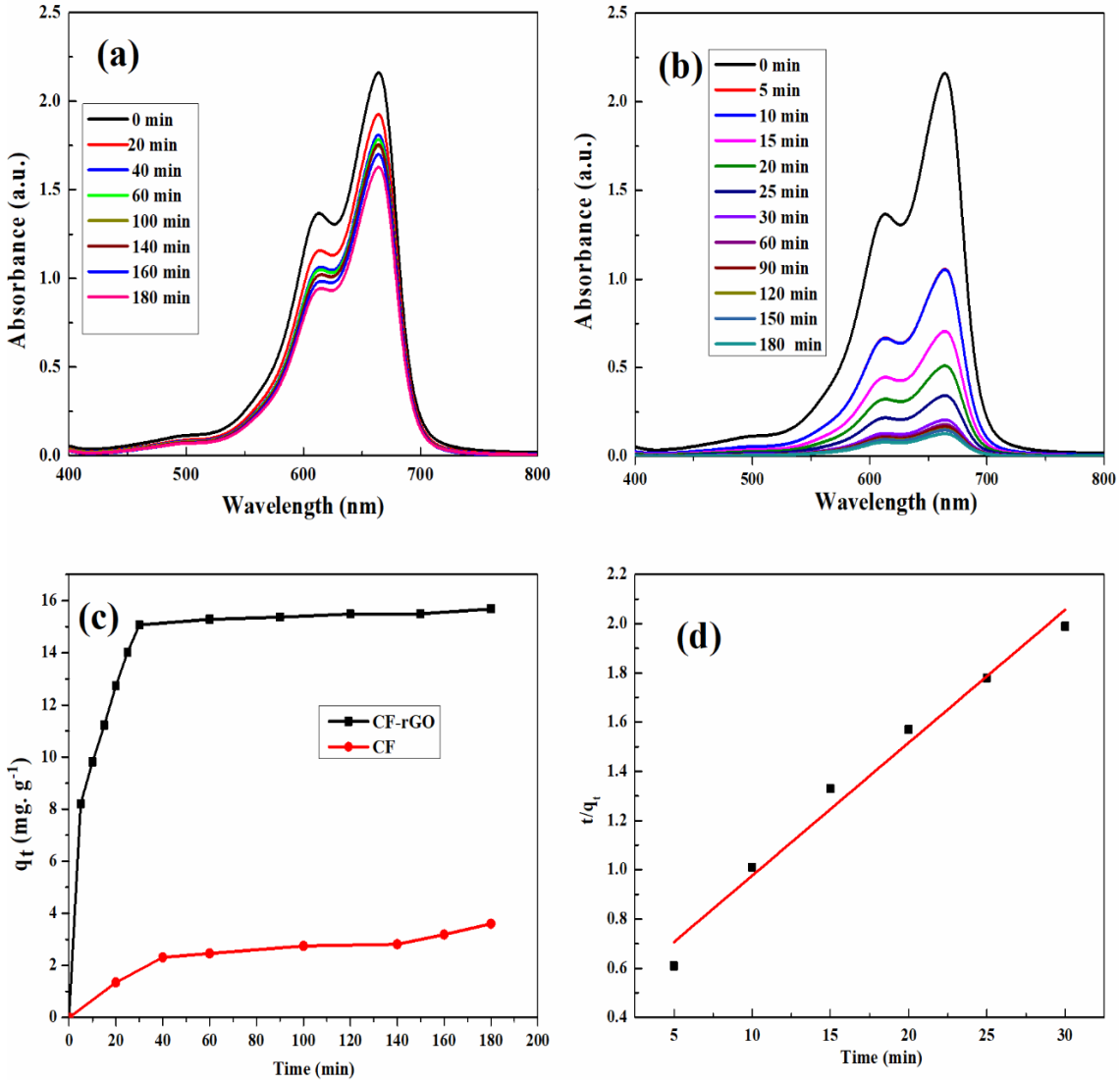

Fig. 6.6. Time-dependent absorption spectra of methylene blue solution in the presence of the adsorbents: (a) CF nanoparticles and (b) CF-rGO heterostructures. (c) The time-dependent adsorption capacity of both the adsorbents. (d) Plot of pseudo-second-order kinetics in case of CF-rGO for the adsorption process of MB.

The q_e and k_2 can be calculated from the slope and intercept of the linear plot of t/q_t vs. t. The plot of t/q_t versus t for the CF-rGO sample showing excellent adsorption properties is shown in **Fig. 6.6d.** The calculated values of q_e and k_2 from the plot are respectively 18.5 mg.g^{-1} and 0.436 g.mg^{-1}.min^{-1}.

The possible adsorption mechanism of MB on CF-rGO nanocomposites is illustrated in **Fig. 6.7a**. The high adsorption performance of the nanocomposites comes from the rGO. The enhanced performance of the CF-rGO is mainly related to the π-π stacking between dye

molecules and π-conjugation regions of the rGO. Furthermore, the adsorption of MB molecules over the adsorbent takes place via electrostatic interaction at the carboxyl and hydroxyl groups present on the CF-rGO, with reported interaction preference towards the carboxyl group as it has stronger electronegativity. The incorporation of CF nanoparticles benefits by enhancing the adsorption activity of the nanocomposite material since it assists in the exfoliation and unfolding of rGO wrinkled sheets and prevents the agglomeration of rGO sheets [30], which in turn increases the active surface area as well as surface adsorption.

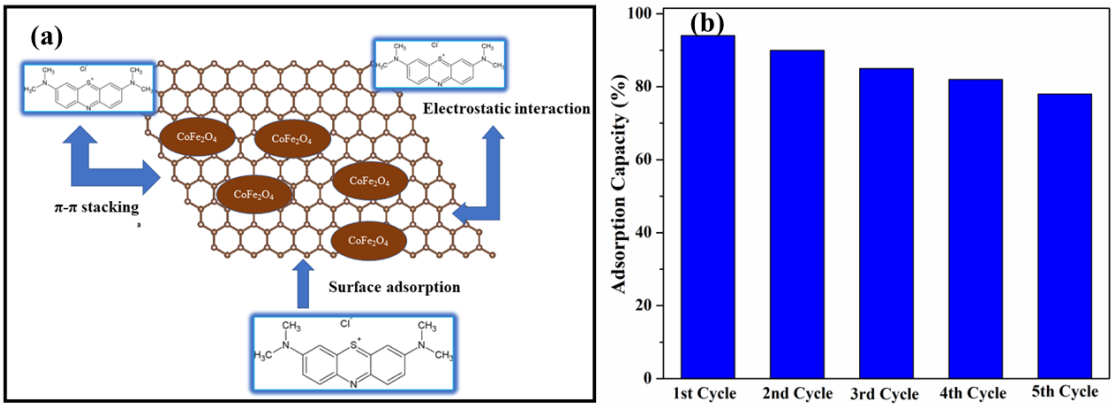

Fig. 6.7. (a) Schematic diagram of the possible mechanism of adsorption of MB on CF-rGO. (b) Recyclability test of CF-rGO for MB dye adsorption.

6.3.7. Recyclability of CF-rGO for dye adsorption

Recyclability is a major parameter for an adsorbent material for practical applications. The reason for that is adsorbents are costly and it can turn into a secondary pollutant to the environment if not reused. Therefore, it is important to investigate the reusability of adsorbent. In this study, the used CF-rGO adsorbent can be eliminated with the help of the external magnetic field, and then cleaned with ethanol for 30 min. under magnetic stirring and reused for MB adsorption. The aforementioned procedure was repeated five times. The adsorption capacity after each cycle is shown in **Fig. 6.7b**. It can be noted that the removal efficiency for MB at the end of the first cycle is close to 93%. Even after 4^{th} cycle of regeneration, the removal efficiency for MB was 82%. At the end of 5^{th} cycle, it reached 78%. Within this recycling process of the adsorbents, the adsorption properties get reduced because of the π-π stacking interaction between MB molecules and rGO. Therefore, it is tough to completely liberate MB molecules from the surface of the adsorbent in the washing process which in turn eliminates

active sites on the surface that hinders further adsorption of MB molecules. The performance of the CF-rGO in the first four cycles revealed that the nanocomposite has excellent recyclability and stability. Additionally, the easy segregation of CF-rGO adsorbents from water by an external magnet is beneficial for industrial applications by avoiding secondary pollution at the time of wastewater treatment.

6.4. Conclusions

In summary, the magnetic CF-rGO nanocomposite adsorbents for MB adsorption were successfully prepared via a simple solvothermal process. The results of adsorption experiments demonstrated that the CF-rGO showed improved performance for the removal of MB dye from water compared to bare nanoparticles. The maximum adsorption capacity for the composite was found to be 15.5 $mg.g^{-1}$ which can also be easily segregated under an external magnetic field due to its high saturation magnetization. The adsorption data for the CF-rGO were well-fitted with the pseudo-second-order kinetics model. The regeneration of magnetic CF-rGO adsorbent was done and was further used for five consecutive cycles to remove MB dye. Thus, the magnetically separable CF-rGO nanocomposite can behave as an excellent adsorbent material in the area of wastewater treatment techniques without creating secondary pollutants.

References

[1] Gan, P. P.; Li, S. F. Y. Potential of Plant as a Biological Factory to Synthesize Gold and Silver Nanoparticles and Their Applications. *Rev Environ Sci Biotechnol* **2012**, *11* (2), 169–206. https://doi.org/10.1007/s11157-012-9278-7.

[2] Gamoudi, S.; Srasra, E. Adsorption of Organic Dyes by HDPy+-Modified Clay: Effect of Molecular Structure on the Adsorption. *Journal of Molecular Structure* **2019**, *1193*, 522–531. https://doi.org/10.1016/j.molstruc.2019.05.055.

[3] Ventura-Camargo, B. de C.; Marin-Morales, M. A. Azo Dyes: Characterization and Toxicity- A Review; 2013.

[4] Yin, W.; Hao, S.; Cao, H. Solvothermal Synthesis of Magnetic CoFe 2 O 4 /RGO Nanocomposites for Highly Efficient Dye Removal in Wastewater. *RSC Advances* **2017**, *7* (7), 4062–4069. https://doi.org/10.1039/C6RA26948F.

[5] Han, X.; Dong, S.; Yu, C.; Wang, Y.; Yang, K.; Sun, J. Controllable Synthesis of Sn-Doped BiOCl for Efficient Photocatalytic Degradation of Mixed-Dye Wastewater under Natural Sunlight Irradiation. *Journal of Alloys and Compounds* **2016**, *685*, 997–1007. https://doi.org/10.1016/j.jallcom.2016.06.298.

[6] Shukla, S.; Oturan, M. A. Dye Removal Using Electrochemistry and Semiconductor Oxide Nanotubes. *Environ Chem Lett* **2015**, *13* (2), 157–172. https://doi.org/10.1007/s10311-015-0501-y.

[7] Zangeneh, H.; Zinatizadeh, A. A. L.; Habibi, M.; Akia, M.; Hasnain Isa, M. Photocatalytic Oxidation of Organic Dyes and Pollutants in Wastewater Using Different Modified Titanium Dioxides: A Comparative Review. *Journal of Industrial and Engineering Chemistry* **2015**, *26*, 1–36. https://doi.org/10.1016/j.jiec.2014.10.043.

[8] Ahmad, A.; Mohd-Setapar, S. H.; Chuong, C. S.; Khatoon, A.; Wani, W. A.; Kumar, R.; Rafatullah, M. Recent Advances in New Generation Dye Removal Technologies: Novel Search for Approaches to Reprocess Wastewater. *RSC Adv.* **2015**, *5* (39), 30801–30818. https://doi.org/10.1039/C4RA16959J.

[9] Gao, C.; Li, B.; Chen, N.; Ding, J.; Cai, Q.; Zhang, J.; Liu, Y. Novel Fe3O4/HNT@rGO Composite via a Facile Co-Precipitation Method for the Removal of Contaminants from Aqueous System. *RSC Adv.* **2016**, *6* (54), 49228–49235. https://doi.org/10.1039/C6RA01279E.

[10] Sharma, P.; Das, M. R. Removal of a Cationic Dye from Aqueous Solution Using Graphene Oxide Nanosheets: Investigation of Adsorption Parameters. *J. Chem. Eng. Data* **2013**, *58* (1), 151–158. https://doi.org/10.1021/je301020n.

[11] Song, S.; Ma, Y.; Shen, H.; Zhang, M.; Zhang, Z. Removal and Recycling of Ppm Levels of Methylene Blue from an Aqueous Solution with Graphene Oxide. *RSC Adv.* **2015**, *5* (35), 27922–27932. https://doi.org/10.1039/C4RA16982D.

[12] Tang, S.; Xia, D.; Yao, Y.; Chen, T.; Sun, J.; Yin, Y.; Shen, W.; Peng, Y. Dye Adsorption by Self-Recoverable, Adjustable Amphiphilic Graphene Aerogel. *Journal of Colloid and Interface Science* **2019**, *554*, 682–691. https://doi.org/10.1016/j.jcis.2019.07.041.

[13] Yang, H.; Zhang, J.; Liu, Y.; Wang, L.; Bai, L.; Yang, L.; Wei, D.; Wang, W.; Niu, Y.; Chen, H. Rapid Removal of Anionic Dye from Water by Poly(Ionic Liquid)-Modified Magnetic Nanoparticles. *Journal of Molecular Liquids* **2019**, *284*, 383–392. https://doi.org/10.1016/j.molliq.2019.04.029.

[14] Nasiri, R.; Arsalani, N. Synthesis and Application of 3D Graphene Nanocomposite for the Removal of Cationic Dyes from Aqueous Solutions: Response Surface Methodology Design. *Journal of Cleaner Production* **2018**, *190*, 63–71. https://doi.org/10.1016/j.jclepro.2018.04.143.

[15] Tu, T. H.; Cam, P. T. N.; Huy, L. V. T.; Phong, M. T.; Nam, H. M.; Hieu, N. H. Synthesis and Application of Graphene Oxide Aerogel as an Adsorbent for Removal of Dyes from Water. *Materials Letters* **2019**, *238*, 134–137. https://doi.org/10.1016/j.matlet.2018.11.164.

[16] One-Pot Sol–Gel Synthesis of Reduced Graphene Oxide Uniformly Decorated Zinc Oxide Nanoparticles in Starch Environment for Highly Efficient Photodegradation of Methylene Blue - RSC Advances (RSC Publishing). https://pubs.rsc.org/en/content/articlelanding/2015/ra/c4ra16767h.

[17] Synthesis and Characterization of Magnetically Separable and Recyclable Crumbled MgFe2O4/Reduced Graphene Oxide Nanoparticles for Removal of Methylene Blue Dye from Aqueous Solutions - ScienceDirect. https://www.sciencedirect.com/science/article/pii/S0022369720313032.

[18] Coal Based Magnetic Activated Carbon as a High Performance Adsorbent for Methylene Blue \textbar SpringerLink. https://link.springer.com/article/10.1007/s10934-016-0144-9.

[19] Hu, L.; Li, M.; Cheng, L.; Jiang, B.; Ai, J. Solvothermal Synthesis of Octahedral and Magnetic CoFe2O4–Reduced Graphene Oxide Hybrids and Their Photo-Fenton-like Behavior under Visible-Light Irradiation. *RSC Adv.* **2021**, *11* (36), 22250–22263. https://doi.org/10.1039/D1RA03103A.

[20] Li, N.; Zheng, M.; Chang, X.; Ji, G.; Lu, H.; Xue, L.; Pan, L.; Cao, J. Preparation of Magnetic CoFe2O4-Functionalized Graphene Sheets via a Facile Hydrothermal Method and Their Adsorption Properties. *Journal of Solid State Chemistry* **2011**, *184* (4), 953–958. https://doi.org/10.1016/j.jssc.2011.01.014.

[21] Chambers, S. A.; Farrow, R. F. C.; Maat, S.; Toney, M. F.; Folks, L.; Catalano, J. G.; Trainor, T. P.; Brown, G. E. Molecular Beam Epitaxial Growth and Properties of CoFe2O4 on MgO(001). *Journal of Magnetism and Magnetic Materials* **2002**, *246* (1), 124–139. https://doi.org/10.1016/S0304-8853(02)00039-2.

[22] Facile Synthesis of Ternary Graphene Nanocomposites with Doped Metal Oxide and Conductive Polymers as Electrode Materials for High Performance Supercapacitors \textbar Scientific Reports. https://www.nature.com/articles/s41598-019-41939-y (accessed 2023-07-10).

[23] Pan, H.; Xu, M.; Qi, Q.; Liu, X. Facile Preparation and Excellent Microwave Absorption Properties of an RGO/Co0.33Ni0.67 Lightweight Absorber. *RSC Adv.* **2017**, *7* (69), 43831–43838. https://doi.org/10.1039/C7RA06849B.

[24] Paredes, J. I.; Villar-Rodil, S.; Solís-Fernández, P.; Martínez-Alonso, A.; Tascón, J. M. D. Atomic Force and Scanning Tunneling Microscopy Imaging of Graphene Nanosheets Derived from Graphite Oxide. *Langmuir* **2009**, *25* (10), 5957–5968. https://doi.org/10.1021/la804216z.

[25] Zong, M.; Huang, Y.; Zhang, N. Reduced Graphene Oxide-CoFe2O4 Composite: Synthesis and Electromagnetic Absorption Properties. *Applied Surface Science* **2015**, *345*, 272–278. https://doi.org/10.1016/j.apsusc.2015.03.203.

[26] Vadivel, M.; Ramesh Babu, R.; Sethuraman, K.; Ramamurthi, K.; Arivanandhan, M. Synthesis, Structural, Dielectric, Magnetic and Optical Properties of Cr Substituted CoFe2O4 Nanoparticles by Co-Precipitation Method. *Journal of Magnetism and Magnetic Materials* **2014**, *362*, 122–129. https://doi.org/10.1016/j.jmmm.2014.03.016.

[27] More, S.; Kadam, R.; Kadam, A.; Mane, D.; Bichile, G. Structural Properties and Magnetic Interactions in Al3+ and Cr3+ Co-Substituted CoFe2O4 Ferrite. *Open Chemistry* **2010**, *8* (2), 419–425. https://doi.org/10.2478/s11532-009-0145-5.

[28] Chakraborty, U.; Singha, T.; Chianelli, R. R.; Hansda, C.; Kumar Paul, P. Organic-Inorganic Hybrid Layer-by-Layer Electrostatic Self-Assembled Film of Cationic Dye Methylene Blue and a Clay Mineral: Spectroscopic and Atomic Force Microscopic Investigations. *Journal of Luminescence* **2017**, *187*, 322–332. https://doi.org/10.1016/j.jlumin.2017.03.039.

[29] Ho, Y. S.; McKay, G. Sorption of Dye from Aqueous Solution by Peat. *Chemical Engineering Journal* **1998**, *70* (2), 115–124. https://doi.org/10.1016/S0923-0467(98)00076-1.

[30] Ai, L.; Zhang, C.; Chen, Z. Removal of Methylene Blue from Aqueous Solution by a Solvothermal-Synthesized Graphene/Magnetite Composite. *Journal of Hazardous Materials* **2011**, *192* (3), 1515–1524. https://doi.org/10.1016/j.jhazmat.2011.06.068.

CHAPTER 7

CONCLUSION AND FUTURE PERSPECTIVE

In this chapter, the summary of all the different work of this thesis is presented. The concluding remarks and future directions of the present work have been discussed.

7.1 Conclusion

This thesis presents a detailed work on the development and characterization of graphene-based spinel ferrite nanocomposite materials and doped graphene material for application in the field of waste water treatment and energy storage. The photocatalytic and adsorptive removal of methylene blue (MB) dye by $MnFe_2O_4$/rGO and $CoFe_2O_4$/rGO have been presented. On the other side, for energy storage applications, electrochemical properties of solvothermaly prepared $MnFe_2O_4$/rGO and N-doped rGO have been investigated and presented. The samples were thoroughly characterized by various techniques such as XRD, SEM, TEM, FTIR, RAMAN, spectroscopy, VSM, SQUID, XPS etc. For $MnFe_2O_4$/rGO and nitrogen-doped rGO, electrochemical performances were investigated in the conventional three-electrode system. The crucial findings drawn from the present work can be represented as follows.

In our first work, the photocatalytic performances of $MnFe_2O_4$ nanoparticles and $MnFe_2O_4$ /rGO heterostructures synthesized using chemical co-precipitation method were investigated for methylene blue dye degradation. The XRD, FTIR, and Raman results confirmed the formation of cubic spinel $MnFe_2O_4$ and $MnFe_2O_4$ /rGO heterostructure. The SEM and HR-TEM images showed the formation of sphere-like $MnFe_2O_4$ nanoparticles well attached on the rGO nanosheets with reduced agglomeration compared to bare $MnFe_2O_4$ nanoparticles. The dye degraded by 84% in the presence of $MnFe_2O_4$ after UV light irradiation of 290 min, while 97% of it degraded in merely 60 min time in case of $MnFe_2O_4$ /rGO heterostructure. Also, the rate constant corresponding to the pseudo-first-order kinetics equation in case of the heterostructure was 10 times higher than that of the bare $MnFe_2O_4$ particles. To conclude, the cubic spinel $MnFe_2O_4$ /rGO heterostructures showed enhanced photocatalytic efficiency than the bare $MnFe_2O_4$ nano-particles which can be used as an effective photocatalyst for MB dye degradation. Hydroxyl radicals played a key role in the MB dye photodegradation process in case of $MnFe_2O_4$ /rGO. In addition, the superparamagnetic nature of this photocatalyst gives it an added advantage which makes it re-useable further by magnetically separating it from the dye solution after the purification process.

In our second work, nitrogen-doped graphene (N-rGO) was prepared by a facile single-step solvothermal approach using DMF which acts as a nitrogen source and reducing material simultaneously. This method is advantageous over other conventional methods as it does not require highly corrosive and toxic elements such as NH_3 and is free from any kind multiple

complex steps for nitrogen doping. EDX spectrum, FTIR and XPS characterization gave the confirmation about the incorporation of nitrogen in graphene sheets. The electrochemical properties of the N-rGO were analysed using cyclic voltammetry (CV), Galvanostatic charge discharge (GCD) and electrochemical impedance spectroscopy (EIS). The electrode prepared from N-rGO exhibits excellent charge storing property with a specific capacitance of 516 Fg^{-1} at a scan rate of 2 mVs^{-1} in 1.0 M Na_2SO_4 aqueous electrolyte solution. Such remarkable electrochemical performance of our synthesized N-rGO can be ascribed to the interconnected, porous nanosheets with reduced restacking and hence highly available surface area, good conductivity and wettability. The EIS data for N-rGO depicted good capacitive behaviours and corresponding relaxation time constant of 0.4 s signifying its faster response time. In addition, our electrode material was found to have good cyclic performance (89% capacitance retention after 5000 cycles) and almost stable Coulombic efficiency. Thus, the N-doped graphene prepared using this single step method has the potential for its use in advanced energy storage applications.

In our third work, manganese ferrite nanoparticles and its nanocomposite with graphene ($MnFe_2O_4$/rGO) have been prepared by simple facile single step solvothermal method and have been explored as a high-performance electrode material for supercapacitors. XRD spectra confirmed, the prepared materials were crystallized with cubic spinel structure. FTIR ad XPS revealed the reduction of functional groups of GO i.e formation of rGO and development of the $MnFe_2O_4$/rGO composite. Raman analysis once again proved the formation of GO and $MnFe_2O_4$/rGO composite. FESEM images depicts the morphology of the prepared products, $MnFe_2O_4$ nanoparticles loaded over graphene sheets were observable from the images.

The electrochemical properties of $MnFe_2O_4$/rGO nanocomposite were also analysed using CV, GCD and EIS. The experimental results showed that $MnFe_2O_4$/rGO nanocomposites have better electrochemical performance in comparison with the bare component $MnFe_2O_4$ nanoparticles. Graphene in the composites took an important role in providing better conductivity as well as heterostructure and improving the electrochemical property of $MnFe_2O_4$/rGO nanocomposites. The specific capacitance of $MnFe_2O_4$/rGO composite electrode reached to 253 Fg^{-1} at current density of 10 Ag^{-1}. Furthermore, the $MnFe_2O_4$/rGO composite exhibited significantly reduced charge transfer resistance compared to bare nanoparticle. Additionally, even after 5000 cycles, the charge/discharge stability of $MnFe_2O_4$/rGO electrode dropped by only 4%, indicating reduced ‘cycle fatigue’. Due to the

superior electrochemical performance of $MnFe_2O_4$/rGO nanocomposite, it can be considered as a favourable material for supercapacitors applications.

In the next work, a facile solvothermal method was utilized to effectively prepare the magnetic cobalt ferrite nanoparticles and its nanocomposite with graphene (CF-rGO) adsorbents for MB adsorption. When it came to extracting MB dye from water, CF-rGO performed better than bare nanoparticles, according to the outcomes of adsorption tests. It was found that the composite has a maximum adsorption capacity of 15.5 $mg.g^{-1}$. Because of its high saturation magnetization, it can also be readily separated by an external magnetic field. For the CF-rGO adsorbents, the pseudo-second-order kinetics model provided a good fit to the adsorption data. The regeneration of magnetic CF-rGO adsorbent was done and was further used for five consecutive cycles to remove MB dye. Thus, the magnetically separable CF-rGO nanocomposite can behave as an excellent adsorbent material in the area of wastewater treatment techniques without creating secondary pollutants.

7.2 Future prospects of the work.

For prepared samples, some more characterization can be done to further analyse these materials. Brunauer-Emmett-Teller (BET) method can be used to analyse the surface, as it is one of the most important parts of wastewater treatment as well as in electrochemical performance. To further explain the specific capacity decrease in cycling performance, SEM and TEM of the samples after the cycling test can be done to study the morphology changes. XPS, FTIR and Raman spectroscopy of the samples after cycling performance can be tested and used to analyze the chemical and functional group change. For all the graphene-based composite, different graphene and iron compound ratios can be used to synthesize the composite materials and study the optimum graphene spinel ferrite composite ratio for both applications. Further two electrode based electrochemical performances of the sample can also be done for evaluating practical applications. With the large surface area of graphene and good photocatalyst properties of spinel ferrite, these nanocomposite materials have the potential for applications in the degradation of synthetic dyes in solutions. In this work, removal/degradation of MB was only studied for wastewater treatment. The adsorption or photocatalytic removal of other dyes could also be studied using the composite materials we reported.

APPENDIX I

Synthesis and Characterization of the nanocomposite GO@α-Fe_2O_3: Efficient Material for Dye Removal

In this work a composite of Graphene Oxide (GO) supported α-Fe_2O_3 nanoparticles (GF) has been synthesized via a simple co-precipitation method. Structural, and morphological study of nanocomposite (GF) are examined by powder X-ray diffraction (PXRD), field emission scanning electron microscopy (FESEM) and Transmission electron microscopy (TEM). The XRD study indicates that Graphene oxide is implanted with well crystalline α-Fe_2O_3 which has a pure rhombohedral phase. Surface morphological study of SEM depicts sphere-like shaped α-Fe_2O_3 particles with the formation of clusters embedded on graphene oxide nanosheet. TEM image reveals that GO sheet acts as a good supporting material for anchoring nano sized α-Fe_2O_3 particles. The efficiency of dye removal of the prepared GF composite has been measured by the degradation of methylene blue (MB) in an aqueous solution under visible light irradiation. The degradation of the dye has been evaluated by UV-visible spectroscopy, by a decrease in the intensity of absorbance and concentration. The degradation efficiency of GF is found to be 90% towards MB.

Work published in *AIP Conference Proceedings*. 1953 (1) (2018), p.030173
https://doi.org/10.1063/1.5032508

1.Introduction

In recent years, textile dyes have been found as one of the most hazardous pollutants of water. Generally, these dyes contribute to pollution as they are normally present in the effluents from the textile, leather, food processing, cosmetics and paper industries. The photocatalysis technique, which is a capable, efficient, easily available and green environmental method, has received worldwide attraction for degradation of dyes from wastewaters. Therefore, tremendous efforts have been focused on photocatalysts. The α-Fe_2O_3 nanomaterial has been identified as such a photocatalyst due to its excellent properties, such as high chemical stability, high catalytic activity and low cost. The electrons of α-Fe_2O_3 get excited from valance band to conduction band when they absorb visible light. These excited electrons and the corresponding holes activate the chemical process and enhance the reaction [1]. To get improved photocatalytic activity of α-Fe_2O_3, it's expected to achieve higher surface area. A 2-D material like graphene with higher specific surface area, when decorated with α-Fe_2O_3 can increase the photoactive surface; hence, improve the photocatalytic activity. Graphene, a monolayer of carbon atoms with a tight packing of honeycomb lattice, has attracted immense research interest in nanotechnology in recent years [2]. Graphene exhibits outstanding properties such as very low resistivity, high mobility of charge carriers, very good optical, and electrical properties [3,4]; which has been found to be very useful in a variety of technological applications, including photocatalysis [5]. GO was proven to be an effective and reliable precursor to produce graphene nanosheets owing to its low cost and massive scalability [6]. Moreover, functionalized graphene based materials can be prepared via chemical modification, which show unique electronic as well as optical properties. Many studies have claimed that Graphene based composites have improved the rate of light absorptivity. This work deals with the synthesis of GF nanocomposite for demineralization of MB under visible light irradiation.

2. Experimental

The α-Fe_2O_3 nanoparticles were prepared using iron chloride hexahydrate ($FeCl_3.6H_2O$) as precursor and NaOH solution as precipitator. For the synthesis of the nano composite all chemicals were of analytical grade and were used as received without further purification. Sample GF was synthesized by a simple co-precipitation method according to the following manner. For the implantation of GO sheets with α-Fe_2O_3 nano particles, first GO was

synthesized by the established Hummers' method [7]. Then GO (200 mg) was dispersed in distilled water and kept under ultrasonication for 2h, and then a homogeneous aqueous solution of ($FeCl_3.6H_2O$) was added and kept under ultrasonication for another 1h. Then the whole system was placed on the hot plate of magnetic stirrer and kept under vigorous stirring for 2h. A solution of NaOH was added to the solution drop wise. The obtained solution was washed with water and ethanol several times for purification and followed by separation by centrifugation (4000rpm). Finally, the solid was dried at 80 °C for 24 h to get the sample. Sample was characterized by powder X-ray diffraction (PXRD), field emission scanning electron microscopy (FESEM), Transmission electron microscope (TEM) and UV-VIS spectroscopy. Efficiency of dye (Methylene blue) degradation of the GF nanocomposite was investigated based on the photocatalytic activity under visible light irradiation. The photocatalytic experiments were carried out at room temperature. Of the sample, 5 mg of photocatalyst was added to 50 ml of 10 $mg.l^{-1}$ dye aqueous solution. Before visible light irradiation, the mixed solution was magnetically stirred for 30 min in the dark to attain equilibrium and then kept in the photocatalytic chamber with continuous stirring. After that the light was turned on for irradiation. At certain time intervals and after some light irradiation processes, about 3 ml of solution were taken from the reaction solution, and centrifuged at 4000 rpm for 5 min to remove the photocatalyst for analysis. For the duration of the photo catalytic process, the dye was decolorized, due to the photocatalytic activity. The percentage of removal was calculated using the following formula

$$\% \text{ Removal} = \frac{C_0 - C_t}{C_0} \times 100 \qquad (1)$$

Where C_0 is Initial concentration and C_t is Concentration at time t.

3. Result and discussion

The X-ray diffraction patterns (XRD) in the range 6°-80° of 2θ for GF is illustrated in **Fig.A1**. XRD analysis showed a series of diffraction peaks at 2θ of 24.12°, 33.09°, 35.60°, 40.79°, 49.36°, 53.98°, 57.40° ,62.29°, 63.90°, 71.78° and 75.44° can be assigned to (012), (104), (110), (113), (024), (116), (122), (214), (300), (1010) and (220) planes, respectively corresponding to α-Fe_2O_3. All the diffraction peaks were unambiguously indexed to a pure rhombohedral phase of α-Fe_2O_3 (JSPDS Card no. 24-0072). The diffraction patterns are very well matched with the earlier work [8]. Moreover, the strong and sharp diffraction peaks

confirm the high crystallinity of the product. Appearance of a narrow hump around 13.40° of GO, confirms the implantation of GO with α-Fe_2O_3.

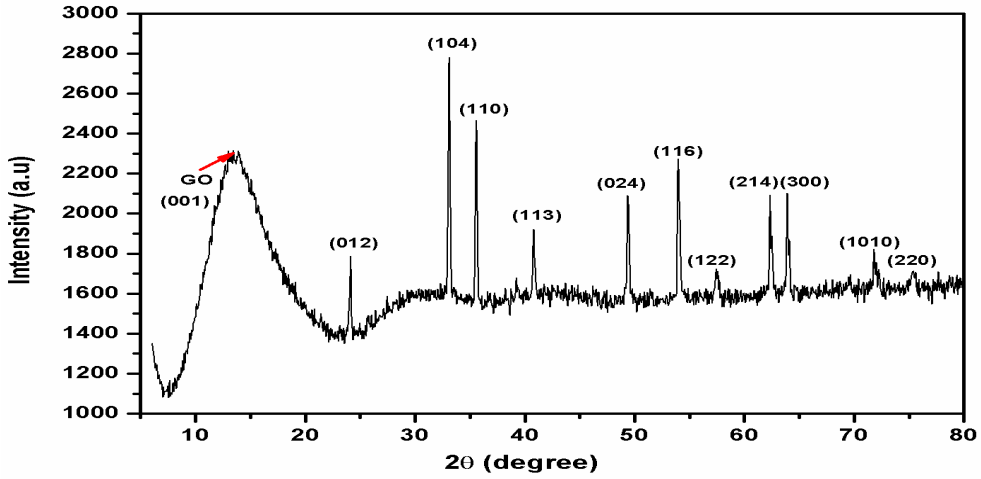

Fig.A1. X ray diffraction pattern of GO@ α-Fe_2O_3

Morphology and size of the nanoparticles are investigated by FESEM and TEM. The FESEM image demonstrates the α-Fe_2O_3 nanoparticles having spherical shape embedded on the graphene oxide sheets, as shown in **Fig.A2a**. SEM result shows that nanoparticles have been uniformly distributed on GO nanosheet which can produce a good electronic pathway for the photo-catalysis. The TEM image of α-Fe_2O_3 implanted on GO sheet infers the anchoring of α-Fe_2O_3 particles on GO sheets, as shown in **Fig.A2b**. This image reveals that α-Fe_2O_3 particles are not loosely bound on GO sheet rather the GO sheet acts as a supporting material for anchoring α-Fe_2O_3 particles.

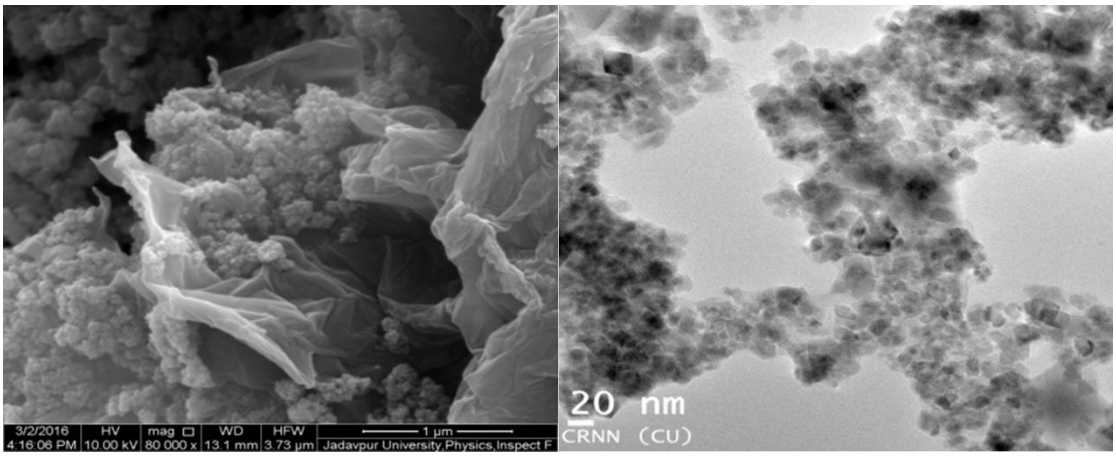

Fig. A2. (a)FESEM image of GO@α-Fe_2O_3 (b) TEM image of GO@α-Fe_2O_3

The UV-VIS spectroscopy was used to analyse the optical properties and absorption wavelength of α-Fe_2O_3 and GF nanocomposite. Absorption arises from electronic transitions associated within the samples. The UV-VIS absorption spectra of the α-Fe_2O_3 and GF samples are shown in **Fig.A3a**. This shows an increase in the absorption spectra intensity in the visible light region for the composite compared to pure α-Fe_2O_3, which indicates that the carbon sheets could help to absorb much more UV-visible light. Thus the introduction of GO into the α-Fe_2O_3 leads to a better utilization of UV-visible light almost without changing the spectral pattern of α-Fe_2O_3. Thus, the incorporation of GO could extend the light absorption rate, which facilitates higher degradation of the dyes faster than pure α-Fe_2O_3 [9]. **Fig. A3b**. Confirms that the removal rate of MB (10 mg/l) can reach upto 90%. The results reveal that the as-prepared GF exhibits excellent removal performance for MB dyes. The recombination rate of α-Fe_2O_3 is much higher, when it acts independently [10]. With the introduction of GO the recombination rate became quite lowered so higher the photocatalytic activity.

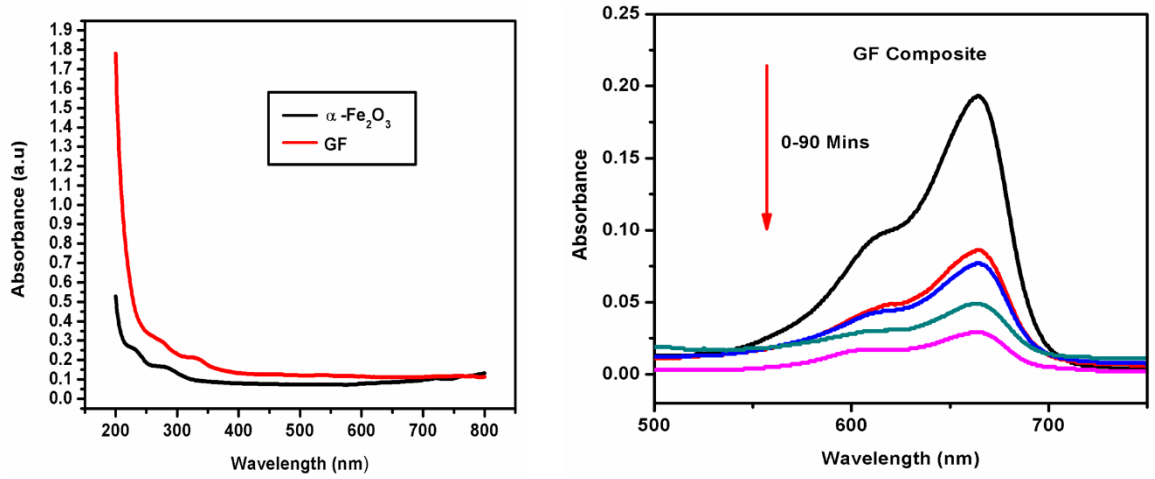

Fig. A3. (a) UV-VIS absorption spectra of α-Fe_2O_3 and GO@α-Fe_2O_3 (b) UV-VIS absorption spectral change of MB dye by GO@α-Fe_2O_3.

In brief, we have successfully synthesized GO@ α-Fe_2O_3 by co-precipitation method. The structure and morphology of GF are examined by PXRD, FESEM and TEM. The nanocomposite showed higher intensity of UV-VIS spectra compared to α-Fe_2O_3. So, we used GF as photo catalyst for the degradation of MB. In our work, the efficiency for degradation of GF has been found to be 90%

References

1. D.S. Bohle, C.J. Spina, “Cationic and anionic surface binding sites on nanocrystalline zinc oxide: surface influence on photoluminescence and photocatalysis”. J. Am. Chem. Soc. 131 4397–4404(2009).

2. K. Geim, K. S. Novoselov, “The rise of graphene”. Nat Mater 6,183–191 (2007).

3. S. Mukherjee, T. P. Kaloni, “Electronic properties of boron and nitrogen-doped graphene: a first principles Study”.J Nanopart Res 14, 1059 (2012).

4. K. S. Novoselov, D.Jiang, F. Schedin, “Two-dimensional atomic crystals”. J Proc National Acad Sci 102,10451–10453 (2005)

5. Y. Y. Liang, H. H. Wang, H. S. Casalongue, Z. Chen, “TiO2 nanocrystals grown on graphene as advanced photocatalytic hybrid materials”. Nano Res 3,701–705(2010).

6. S. Park, R. S. Ruoff, “Chemical methods for the production of graphenes”. Nat Nanotechnol 4,217–224 (2009)

7. W. S. J. R. Hummers and R. E. Offeman, “Preparation of Graphitic oxide”. J. Am. Chem. Soc. 80, 1339(1958).

8. J. Hua, J. Gengsheng, “Hydrothermal synthesis and characterization of monodisperse α-Fe2O3 nanoparticles”. Mater let. 63, 2725-2527 (2009).

9. Q. Wu, L. Cheng, J. Li, K. Wu, “Synergetic signal amplification of graphene–Fe2O3 hybrid and hexadecyltrimethylammonium bromide as an ultrasensitive detection platform for bisphenol A”. Electrochim. Acta, 115, 434–439. (2014).

10. B. Li, T. Liu, Y. Wang and Z. Wang: “ZnO/graphene-oxidenanocomposite with remarkably enhanced visiblelight-drivenphotocatalytic performance”. J. Colloid Interface Sci., 377,114–121. (2012

APPENDIX II

List of Publications and Conference Presentation

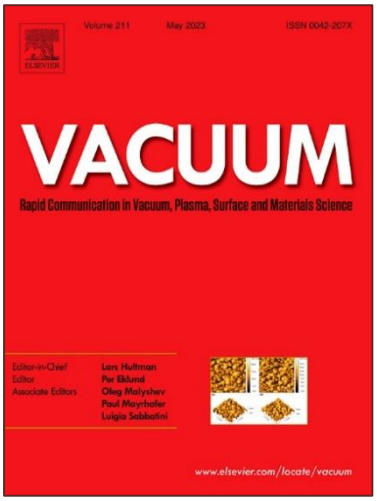

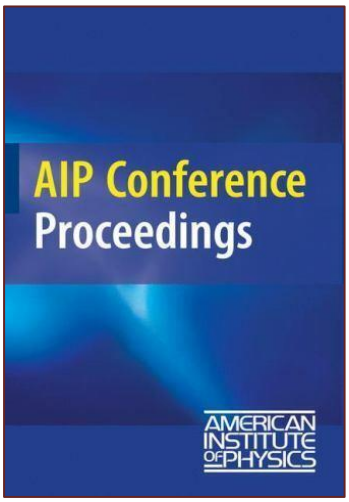

Publications related to this thesis work

1. *$MnFe_2O_4$ decorated reduced graphene oxide heterostructures: Nanophotocatalyst for methylene blue dye degradation.* **B. Mandal**, J. Panda , P. K. Paul , R. Sarkar , B. Tudu. **Vacuum** 173 (2020) 109150. (IF- 4)

2. *Supercapacitor performance of nitrogen doped graphene synthesized via DMF assisted single-step solvothermal method*. **B. Mandal**, S. Saha, D. Das, J. Panda, S.Das, R.Sarkar, B.Tudu. **FlatChem** 34 (2022) 100400. (IF- 6.2)

3. *Synthesis and Characterization of Nanocomposite GO@α-Fe_2O_3 : Efficient Material for Dye Removal*. **B. Mandal,** J. Panda, and B. Tudu. **AIP Conference Proceedings** 1953, 030173 (2018).

Manuscript under review in International Journals

1. *Enhanced electrochemical properties of $MnFe_2O_4$/reduced graphene oxide nanocomposite with a potential for supercapacitor application*. **B. Mandal,** K Ghorui, S. Saha, S.Das, R.Sarkar, B.Tudu. (Under review in **Material Research Bulletin**).

2. *Time-dependent adsorptive removal of Methylene Blue dye by $CoFe_2O_4$/rGO nanocomposite*. **B.Mandal**, K Ghorui, R.Sarkar, B.Tudu. (Under review in **Applied Physics A).**

Publication not related to this thesis work

1. *Anticancer Potential of Docetaxel Loaded Cobalt Ferrite Nanocarrier: An in vitro Study on MCF-7 and MDA-MB-231 Cell Lines.* J. Panda , B. S. Satapathy , **B. Mandal ,** R. Sen, B. Mukherjee , R. Sarkar & B. Tudu. **Journal of Microencapsulation** 38(1) (2021).

List of Conferences/Seminars attended

1. "2nd International Conference on Condensed Matter and Applied Physics (ICC-2017)" held at Bikaner, Rajasthan, India during 24th -25th November, 2017, organized by Govt. Engineering College, Bikaner.

2. One day National Seminar on "Energy Storage and Conversion (NSESC-2018) " Organized by the Department of Instrumentation Science, Jadavpur University, Kolkata-700032 on 6th December, 2018.

3. National seminar on “Physics at surfaces and Interfaces of soft materials (PSISM-2019) ” Organised by Condensed matter Physics Research Center, Department of physics, Jadavpur University, Kolkata -700032, during 26-27th September, 2019

4. “India International Science Festival.-2019”, Kolkata. Held at Biswa Bangla Convention Center during 5-8th November, 2019.

APPENDIX III

Reprints of the published papers (First page only)

Vacuum 173 (2020) 109150

Contents lists available at ScienceDirect

Vacuum

journal homepage: http://www.elsevier.com/locate/vacuum

$MnFe_2O_4$ decorated reduced graphene oxide heterostructures: Nanophotocatalyst for methylene blue dye degradation

Bidisha Mandal [a], Jnanranjan Panda [a], Pabitra Kumar Paul [a], Ratan Sarkar [b,**], Bharati Tudu [a,*]

[a] Department of Physics, Jadavpur University, Kolkata, 700 032, India
[b] Department of Physics, Jogesh Chandra Chaudhuri College, Kolkata, 700 033, India

ARTICLE INFO

Keywords:
Manganese ferrite
Graphene oxide
Heterostructures
Photocatalysis
Degradation
Methylene blue

ABSTRACT

The photocatalytic degradation of methylene blue dye (MB) has been investigated using bare manganese ferrite ($MnFe_2O_4$) nanoparticles and $MnFe_2O_4$ nanoparticles-decorated reduced graphene oxide heterostructures ($MnFe_2O_4$/rGO) under ultra-violet irradiation. The $MnFe_2O_4$ nanoparticles prepared using a facile co-precipitation method showed single-phase cubic spinel structure and superparamagnetic property. The $MnFe_2O_4$/rGO heterostructures showed the formation of sphere-like $MnFe_2O_4$ nanoparticles well-attached on rGO nanosheets with reduced agglomeration. The photocatalysis study shows that $MnFe_2O_4$/rGO had higher photocatalytic activity compared to bare $MnFe_2O_4$ nanoparticles. MB degraded by 84% in presence of $MnFe_2O_4$ after UV irradiation of 290 min, while 97% of it degraded in merely 60 min in case of $MnFe_2O_4$/rGO heterostructures. This is further confirmed by the well-fitted Langmuir-Hinshelwood Kinetics equation. This improvement in the photocatalytic activity of the heterostructure is attributed mainly to the retardation of the recombination process of photo-generated charge carriers. Hydroxyl radicals play the crucial role in the $MnFe_2O_4$-graphene system for MB photodegradation. Thus, $MnFe_2O_4$ nanoparticles-decorated reduced graphene oxide heterostructures can act as potential photocatalyst for degradation of hazardous organic dyes present in water.

1. Introduction

One of the major environmental concerns in pollution control is the removal of hazardous materials from water resources. The pollution of water resources by industrial effluents containing toxic dyes like, Congo red, Methyl orange, Methyelene Blue etc. have been a serious problem to the human health and environment. Most of the dyes are harmful due to the high toxicity and carcinogenicity due to their non-biodegradable aromatic structure [1]. Therefore, to control the pollution of water, elimination of these dyes from water is of utmost importance. Several methods and technologies have been developed to remove such organic dyes which include membrane treatment [2], adsorption [3], electrochemical [4], biological method [5], ion-exchange method [6], photocatalysis [7] etc. Among all these methods, photocatalysis has gained a huge interest in last few decades due to its low cost and simple execution [8]. Photocatalytic water treatment is a well-known advanced oxidation process in which the photocatalyst material with the production of electron-hole pair upon the irradiation with light, mineralize complex organic compound to mainly CO_2, H_2O, and other non-harmful inorganic materials [9].

Nowadays, spinel ferrite magnetic nanoparticles (with formula MFe_2O_4: M = Zn, Co, Mn, Ni, etc.) have emerged as potential candidates for various applications such as energy storage, pollution control, drug delivery etc. [10–12], due to their excellent catalytic and magnetic properties and ease of fabrication [13,14]. Several different types of magnetic ferrites such as copper ferrite ($CuFe_2O_4$) [15], cobalt ferrite ($CoFe_2O_4$) [16] and manganese ferrite ($MnFe_2O_4$) [17] have been reported to exhibit excellent catalytic and photocatalytic activity. The spinel ferrites have a relatively narrow band gap (~2.0 eV) which makes them suitable photocatalyst candidates for degradation processes [18]. In addition, they can be easily separated from the polluted aqueous solution or reaction system with the application of an external magnetic field which has the added advantage of its repetitive use which is of great interest in wastewater management. Among all spinel ferrites, $MnFe_2O_4$ has attracted huge attention for application in pollution control because of its low cost, non-toxicity, and high chemical stability

* Corresponding author.
** Corresponding author.
E-mail addresses: dr.ratansarkar@jogeshchaudhuricollege.org (R. Sarkar), bharati.tudu@jadavpuruniversity.in (B. Tudu).

https://doi.org/10.1016/j.vacuum.2019.109150
Received 19 July 2019; Received in revised form 18 December 2019; Accepted 19 December 2019
Available online 24 December 2019
0042-207X/

FlatChem 34 (2022) 100400

Contents lists available at ScienceDirect

FlatChem

journal homepage: www.sciencedirect.com/journal/flatchem

Supercapacitor performance of nitrogen doped graphene synthesized via DMF assisted single-step solvothermal method

Bidisha Mandal [a], Samik Saha [a,b], Dipanwita Das [a], Jnanranjan Panda [a], Sachindranath Das [b], Ratan Sarkar [c,*], Bharati Tudu [a,*]

[a] Department of Physics, Jadavpur University, Kolkata 700 032, India
[b] Department of Instrumentation Science, Jadavpur University, Kolkata 700 032, India
[c] Department of Physics, Jogesh Chandra Chaudhuri College, University of Calcutta, Kolkata 700033, India

ARTICLE INFO

Keywords:
Solvothermal
Nitrogen doping
Graphene
Complex capacitance
Relaxation time

ABSTRACT

We report a single step dymethyleformamide (DMF) assisted solvothermally synthesized nitrogen-doped reduced graphene oxide (N-RGO) as a novel electrode material. DMF effectively acts as a nitrogen dopant cum reducing agent for graphene which remarkably enhances its electrochemical properties. X-ray diffraction (XRD), scanning electron microscopy (SEM), Raman spectroscopy, FTIR spectroscopy and X-ray photoelectron spectroscopy (XPS) were employed to characterize the structure and properties of the N-RGO. XRD study confirms effective reduction of GO in the N-RGO. SEM image shows the formation of fluffy and highly porous N-RGO. EDX, XPS and FTIR spectroscopic studies confirm the doping of nitrogen atom into the resultant material (N-RGO). The highest specific capacitance of N-RGO is found to be 516 Fg^{-1} at a scan rate of 2 mVs^{-1} along with a good cyclic stability and stable coulombic efficiency. Such a remarkable capacitive performance is attributed to its porous structure and effective nitrogen doping which facilitates the migration of electrolyte ions and provides abundant active sites for such electrochemical behaviour. The electrochemical impedance spectroscopy study showed a typical capacitive behavior of the N-RGO and a faster frequency response with a relaxation time constant of 0.4 s. Thus, the synthesized N-RGO using this simple, cost-effective, environment friendly method could be a potential candidate for high performance energy-storage applications.

1. Introduction

Today, the demand for a very fundamental requirement of mankind, energy is expected to increase significantly. The world energy assessment report estimates that consumption of global energy is going to reach about 27.6 terawatts (TW) by 2050 due to the population explosion and change in present lifestyle [1]. To achieve ever-increasing desired energy due to the fast gradual decrement of fossil fuel, global warming and pollution, researchers are forced to explore sustainable energy and efficient energy storage devices [2,3]. One of the different energy storage systems, supercapacitors are drawing huge attention because of their high power density, environmental friendliness, long operating life and product safety [2,4–6]. With respect to the process of charge storage and usage of the material for electrodes, supercapacitors are categorized mainly into two parts: electrical double-layer capacitors (EDLCs) and pseudo-capacitor. Generally, carbonaceous materials having excellent conductivity and large specific surface area are utilized as EDLC material in which the charge storage process occurs through the physical accumulation of charges electrostatically via non Faradaic process at the interfaces of electrode and electrolyte where there is no transfer of electrons. As this category is a surface process, it strongly depends on the electrode surface area which can be accessible to the electrolyte. On the contrary, redox operative metal oxides/sulfides/hydroxides including conductive polymer composite materials have been employed as electrode material for Pseudo capacitors in which charge storage arises due to rapid electrochemical Faradaic reactions [7–11].

Graphene, a single atom thick sheet having a hexagonal honeycomb sp^2-hybridized carbon atom network has been extensively used as EDLC material as it possesses good conductivity and a large surface area of approximately 2600 m^2/g [12,13]. By and large, graphene-based supercapacitors are effective to attain capacitance of 550 Fg^{-1} theoretically when the complete surface area is employed [14,15]. In a practical situation, graphene electrode exhibits a specific capacitance of 130–200 Fg^{-1} which is considerably lower than that of the theoretical value as

* Corresponding authors.
E-mail addresses: ratansarkar.jccc@gmail.com (R. Sarkar), bharati.tudu@jadavpuruniversity.in (B. Tudu).

https://doi.org/10.1016/j.flatc.2022.100400
Received 3 April 2022; Received in revised form 11 June 2022; Accepted 26 June 2022
Available online 3 July 2022

JOURNAL OF MICROENCAPSULATION
https://doi.org/10.1080/02652048.2020.1842529

Anticancer potential of docetaxel-loaded cobalt ferrite nanocarrier: an in vitro study on MCF-7 and MDA-MB-231 cell lines

Jnanranjan Panda[a], Bhabani Sankar Satapathy[b], Bidisha Mandal[a], Ramkrishna Sen[c], Biswajit Mukherjee[c], Ratan Sarkar[d] and Bharati Tudu[a]

[a]Department of Physics, Jadavpur University, Kolkata, India; [b]School of Pharmaceutical Sciences, Siksha 'O' Anusandhan (Deemed to be University), Bhubaneswar, India; [c]Department of Pharmaceutical Technology, Jadavpur University, Kolkata, India; [d]Department of Physics, Jogesh Chandra Chaudhuri College, Kolkata, India

ABSTRACT

Aim: To develop a biocompatible cobalt ferrite (CF-NP) nanodrug formulation using oleic acid and poly (D,L-lactide-*co*-glycolic) acid (PLGA) for the delivery of docetaxel (DTX) specifically to breast cancer cells.

Methods: The CF-NP were synthesised by hydrothermal method and conjugated with DTX in a PLGA matrix and were systematically characterised using XRD, FE-SEM, TEM, DLS, FTIR, TGA, SQUID etc. The drug loading, in vitro drug release, cellular uptake, cytotoxicity were evaluated and haemolytic effect was studied.

Results: The CF-NP showed good crystallinity with an average particle size of 21 nm and ferromagnetic nature. The DTX-loaded CF-NP (DCF-NP) showed 8.4% (w/w) drug loading with 81.8% loading efficiency with a sustained DTX release over time. An effective internalisation and antiproliferative efficiency was observed in MCF-7 and MDA-MB-231 breast cancer cells and negligible haemolytic effect.

Conclusion: The DCF-NP can have the potential for the effective delivery of DTX for breast cancer treatment.

ARTICLE HISTORY
Received 16 May 2020
Accepted 21 October 2020

KEYWORDS
Cobalt ferrite nanoparticles; breast cancer; docetaxel; cytotoxicity; biocompatibility

1. Introduction

In recent times, magnetic nanoparticles have received immense attention among the scientific community owing to their distinct applications in magnetically assisted wastewater treatment (Mandal *et al.* 2020), biosensors (Rocha-Santos 2014), magnetic recording media (Mohtasebzadeh *et al.* 2015) along with various biomedical applications such as magnetic resonance imaging (Wabler *et al.* 2014), hyperthermia (Mazario *et al.* 2013), and drug delivery (Wang *et al.* 2012, Tietze *et al.* 2015, Jauhar *et al.* 2016). Among various types of magnetic nanoparticles, cobalt ferrite based nanodrug delivery system has emerged as an attractive drug delivery technique for improved cancer treatment (Ansari *et al.* 2016, Dey *et al.* 2018). This is because cobalt ferrite nanoparticles (CF-NP) have the advantages of excellent biocompatibility, tuneable particle size, ease of surface functionalization, moderate saturation magnetisation, large magnetic anisotropy along with minimal toxicity (Ansari *et al.* 2016).

Recently, cancer has been identified as the most fatal disease with an alarming mortality rate across the globe. Based on the latest report from the International Agency for Research on Cancer (IARC), in 2018, more than 18.1 million new cancer cases have been diagnosed all over the world, with around 9.6 million deaths (Bray *et al.* 2018). Among all cancers, breast cancer tops the list with the highest morbidity and mortality counts among the women in western countries. Even in India, breast cancer has secured 1st rank among Indian females, with a mortality rate of nearly 12.7 per 100,000 women (Malvia *et al.* 2017). These figures signify the inefficiency of currently available treatment strategies to tackle the disease. Multimodal treatment strategies including a combination of surgery, radiation therapy, chemotherapy have failed to improve treatment outcomes in metastatic breast cancer cases. Conventional chemotherapy has the limitation due to the non-selective distribution of anticancer drugs between cancer cells and healthy cells, which in turn produces severe toxic effects

CONTACT Bharati Tudu bharati.tudu@jadavpuruniversity.in Department of Physics, Jadavpur University, Kolkata 700032, India; Ratan Sarkar dr.ratansarkar@jogeshchaudhuricollege.org Department of Physics, Jogesh Chandra Chaudhuri College, Kolkata 700033, India

RESEARCH ARTICLE | MAY 08 2018

Synthesis and characterization of nanocomposite GO@α-Fe_2O_3:Efficient material for dye removal

B. Mandal ✉; J. Panda; B. Tudu

+ Author & Article Information
AIP Conf. Proc. 1953, 030173 (2018)
https://doi.org/10.1063/1.5032508

In this work a composite of Graphene Oxide (GO) supported α-Fe_2O_3 nanoparticles (GF) has been synthesized via a simple co-precipitation method. Structural, and morphological study of nanocomposite (GF) are examined by powder X-ray diffraction (PXRD), field emission scanning electron microscopy (FESEM) and Transmission electron microscopy (TEM). The XRD study indicates that Graphene oxide is implanted with well crystalline α-Fe_2O_3 which has pure rhombohedral phase. Surface morphological study of SEM depicts sphere-like shaped α-Fe_2O_3 particles with formation of clusters have been embedded on Graphene oxide nano sheet. TEM image reveals that GO sheet acts as a good supporting material for anchoring nano sized α-Fe_2O_3 particles. Efficiency of dye removal of the prepared GF composite has been measured by the degradation of methylene blue (MB) in an aqueous solution under visible light irradiation. The degradation of the dye has been evaluated by a UV-visible spectroscopy, by decrease in the intensity of absorbance and concentration. The degradation efficiency of GF is found to be 90% towards MB.

Topics
Transmission electron microscopy, X-ray diffraction, Nanocomposites, Nanomaterials, Optical properties, Transition metal oxides, Methylene blue, Precipitation method, Visible spectroscopy

REFERENCES

1. D.S. Bohle, C.J. Spina, "Cationic and anionic surface binding sites on nanocrystalline zinc oxide: surface influence on photoluminescence and photocatalysis". *J. Am. Chem. Soc.* 131 4397–4404 (2009). https://doi.org/10.1021/ja808663b
Google Scholar Crossref PubMed

2. K. Geim, K. S. Novoselov, "The rise of graphene". *Nat Mater* 6, 183–191 (2007). https://doi.org/10.1038/nmat1849
Google Scholar Crossref PubMed

3. S. Mukherjee, T. P. Kaloni, "Electronic properties of boron and nitrogen-doped graphene: a first principles Study". *J Nanopart Res* 14, 1059 (2012). https://doi.org/10.1007/s11051-012-1059-2
Google Scholar Crossref

4. K. S. Novoselov, D. Jiang, F. Schedin, "Two-dimensional atomic crystals". *J Proc National Acad Sci* 102, 10451–10453 (2005) https://doi.org/10.1073/pnas.0502848102
Google Scholar Crossref

5. Y. Y. Liang, H. H. Wang, H. S. Casalongue, Z. Chen, "TiO_2 nanocrystals grown on graphene as advanced photocatalytic hybrid materials". *Nano Res* 3, 701–705 (2010). https://doi.org/10.1007/s12274-010-0033-5
Google Scholar Crossref

6. S. Park, R. S. Ruoff, "Chemical methods for the production of graphenes". *Nat Nanotechnol* 4, 217–224 (2009) https://doi.org/10.1038/nnano.2009.58
Google Scholar Crossref PubMed

7. W. S. J. R. Hummers and R. E. Offeman, "Preparation of Graphitic oxide". *J. Am. Chem. Soc.* 80, 1339 (1958). https://doi.org/10.1021/ja01539a017
Google Scholar Crossref

8. J. Hua, J. Gengsheng, "Hydrothermal synthesis and characterization of monodisperse α-Fe_2O_3 nanoparticles". *Mater let.* 63, 2725–2527 (2009). https://doi.org/10.1016/j.matlet.2009.09.054
Google Scholar Crossref

9. Q. Wu, L. Cheng, J. Li, K. Wu, "Synergetic signal amplification of graphene–Fe_2O_3 hybrid and hexadecyltrimethylammonium bromide as an ultrasensitive detection platform for bisphenol A". *Electrochim. Acta*, 115, 434–439. (2014). https://doi.org/10.1016/j.electacta.2013.10.188
Google Scholar Crossref

10. B. Li, T. Liu, Y. Wang and Z. Wang: "ZnO/graphene-oxidenanocomposite with remarkably enhanced visible-light-drivenphotocatalytic performance". *J. Colloid Interface Sci.*, 377, 114–121. (2012). https://doi.org/10.1016/j.jcis.2012.03.060
Google Scholar Crossref PubMed